Synthesis and Characterisation of Layered Oxypnictides and Oxychalcogenides

Xiaoyu Xu

A thesis submitted in part fulfilment of the requirements for the degree of Doctor of Philosophy at the University of Oxford

Brasenose College

University of Oxford

August 2019



Abstract

Synthesis and Characterisation of Layered Oxypnictides and Oxychalcogenides

Xiaoyu Xu — Brasenose College

D.Phil Thesis — August 2019

This thesis reports the synthesis and characterisation of a series of layered oxyarsenides $A_2M_3As_2O_2$ (A=Sr, Ba and M = Cr, Mn) and layered oxychalcogenides Sr_2MO_3CuX (M = Cr, Mn, Fe and X= S, Se). These materials are synthesised with different choices of the transition metal cations and it has been demonstrated that the nature of the metals can strongly influence the magnetic properties of these layered solids.

Variable temperature powder neutron diffraction on $Ba_2CrO_2Cr_2As_2$ has revealed long range antiferromagnetic ordering of the Cr^{2+} ions in both oxide and arsenide layers below 248 K and 470 K and the magnetic moments in both layers are aligned along the *c*-axis, where the two independent Cr^{2+} sublattices order with two different propagation vectors k = (½ ½ 0) in the oxide layer and k = (1 1 1) in the arsenide layer. The system has similarities and differences with the Sr analogue.

The partial substitution of Cr^{2+} by Mn^{2+} in $Sr_2CrO_2Cr_2As_2$ and $Ba_2CrO_2Cr_2As_2$ has been shown to change their crystal structures and magnetic properties depending on the Mn:Cr ratio. Variable temperature neutron powder diffraction enabled the magnetic structures to be determined and the compounds with substitution all show antiferromagnetic ordering, analogous to those seen in their parent samples. The most characteristic feature of the magnetic properties in these compounds is the appearance of two similar magnetic structures, with the magnetic spins in adjacent arsenide (oxide) layers aligned either parallel or antiparallel. Similar to $Sr_2CrO_2Cr_2As_2$, a spin-reorientation of the moments is found in the arsenide layer of $Sr_2Cr_{0.93}Mn_{0.07}O_2Mn_{0.92}Cr_{1.08}$.

PND measurements have revealed long-range AFM ordering in the oxide layers of Sr_2MnO_3CuSe. In replacing Se^{2-} by S^{2-}, a new magnetic structure is found in Sr_2MnO_3CuS which is different in detail to that of the selenide analogue. The deintercalation of a small amount of Cu in Sr_2MnO_3CuS results in adoption of the same magnetic structure as found for the selenide analogue and leads to a much larger ordered moment (3.60(4) μB/Mn^{3+}) than in stoichiometric Sr_2MnO_3CuS (2.83(6) μB/Mn^{3+}), with a value approaching that of Sr_2MnO_3CuSe (3.76(2) μB/Mn^{3+}). The different magnetic behaviour between Sr_2MnO_3CuSe and Sr_2MnO_3CuS suggests that the Mn^{3+} ions in sulfide are slightly reduced and this introduces some Mn^{2+} ions and leads to moment reduction due to frustration. The neighbouring moments in all cases are found to be antiferromagnetically coupled in a checkerboard fashion with their moments directed perpendicular to the *ab*-plane.

Investigations into Sr_2FeO_3CuSe have revealed a spin reorientation transition of Fe moments between 1.5 K and 230 K with the tilted Fe^{3+} spins in the oxide planes gradually reorienting to lie in the *ab* plane. Similarly, Sr_2CrO_3CuSe demonstrates antiferromagnetic ordering of Cr^{3+} in the oxide layers at 4 K with their moments aligned within the *ab*-plane.

Finally, the synthesis of a novel and challenging compound Sr_2CrO_3CrAs has been successful. Variable temperature powder neutron diffraction reveals long range antiferromagnetic ordering of the Cr^{2+} ions in the arsenide layer below 478 K, with their moments directed along the *c*-axis. In contrast to other Sr_2CuGaO_3S-type compounds, there is no evidence for long range magnetic ordering in the oxide layers of Sr_2CrO_3CrAs.

Acknowledgements

First and foremost I would like to thank my supervisor Prof. Simon Clarke for all his guidance, ideas and enthusiasm throughout my DPhil in the group. I am particularly grateful for the opportunity to join his research group after the “difficult moments” at the beginning of my time in Oxford.

I have been so lucky to work with some great people over the last three years. In particular, thanks must go to Dr Simon Cassidy for his magic on TOPAS, and his invaluable help and support throughout my DPhil; to Dr Jack Blandy for his encouragement and keeping me company both in and out of the lab; To Dr Daniel Woodruff for his endless patience, knowledge and board games; To Dr Midori Amano Patiño for answering all my questions at the beginning of this journey. I would also like to thank past and present members of the Clarke group for making the experience so enjoyable and memorable: Sophie, Tom, Abi, Michael, Jamie, Dom, Toby, Rob, Sonja, Jamie, Ella, Louise, Nicola, Penny, Brad, Mahmoud, Ben, Cristina, Partha, Drs Bertold Rasche and Machteld Kamminga. Thank you all for creating a great atmosphere throughout my time in the group.

I am also grateful to a number of instrument scientists who have provided assistance with X-ray and neutron diffractometers: Prof. C. Tang, Dr A. Baker and Dr C. Murray (I11) from Diamond; Drs P. Manuel and F. Orlandi (WISH), Dr. R. Smith (Polaris and GEM Xpress) and Dr F. Demnel (OSIRIS) from ISIS; Dr E. Suard (D2B) from ILL. Thanks also go to Prof. J. Hadermann for performing the electron diffraction and microscopy measurements; to Drs P. Wiseman and Amber Thompson for maintenance of the powder X-ray diffractometers and SQUID magnetometers in the ICL; to Dr Bertold Rasche for his help with TGA measurements.

Finally, thanks to my family, friends and Isabel for their support and good company throughout my time in Oxford.

Contents

Chapter 1 Introduction 1

1.1 Solid state chemistry 1

1.2 Non-oxide and mixed-anion solids 3

1.3 Oxypnictides and oxychalcogenides 4

1.3.1 ZrCuSiAs structure 4

1.3.2 $Sr_2Mn_3O_2Sb_2$ structure 6

1.3.3 Sr_2CuGaO_3S structure 9

1.4 Magnetic behaviour of solids 11

1.4.1 Diamagnetism 11

1.4.2 Paramagnetism 11

1.4.2.1 Curie paramagnetism 12

1.4.2.2 Curie-Weiss paramagnetism 14

1.4.2.3 Pauli paramagnetism 14

1.4.3 Ferromagnetism 15

1.4.4 Antiferromagnetism 17

1.4.5 Spin glass behaviour 18

1.5 Models of magnetic exchange 20

1.5.1 Direct exchange 20

1.5.2 Superexchange 20

1.5.3 Double exchange 22

1.6 Aims of this thesis 24

Chapter 2 Experimental techniques 27

2.1 Synthetic methods 27

2.1.1 Solid state synthesis 27

2.1.2 Argon-filled dry glove box 29

2.1.3 Preparation of starting materials 29

2.1.3.1 Synthesis of SrO 29

2.2 Characterisation techniques 30

2.2.1 Diffraction 30

2.2.2 X-ray diffraction 31

2.2.3 Powder X-ray diffraction 36

2.2.4 Powder neutron diffraction 38
2.2.5 Laboratory powder X-ray diffractometers 40
2.2.6 Synchrotron powder X-ray diffraction 44
2.2.6.1 I11 (DIAMOND) 47
2.2.7 Neutron powder diffractometers 49
2.2.7.1 OSIRIS (ISIS) 54
2.2.7.2 GEM (ISIS) 55
2.2.7.3 POLARIS (ISIS) 55
2.2.7.4 WISH (ISIS) 55
2.2.7.5 D2B (ILL) 56
2.2.8 Rietveld refinement 57
2.2.9 Pawley refinement 60
2.2.10 DC SQUID magnetometry 61

Chapter 3 Synthesis and characterisation of $Ba_2CrO_2Cr_2As_2$ 64
3.1 Introduction 64
3.2 Synthesis and characterisation of $Ba_2CrO_2Cr_2As_2$ 66
3.2.1 Powder X-ray diffraction 69
3.2.2 Magnetic susceptibility measurements 73
3.2.3 Powder neutron diffraction 74
3.2.3.1 Low temperature PND 74
3.2.3.2 Variable temperature PND 75
3.3 Discussion 82
3.3.1 Crystal structure 82
3.3.2 Magnetic ordering 85

Chapter 4 Synthesis and characterisation of $Sr_2Cr_{3-x}Mn_xAs_2O_2$ and $Ba_2Cr_{3-x}Mn_xAs_2O_2$ 89
4.1 Introduction 89
4.2 Synthesis and characterisation of $Sr_2Cr_{0.79}Mn_{0.21}O_2Mn_{1.76}Cr_{0.24}As_2$ 90
4.2.1 Powder X-ray diffraction 91
4.2.2 Room temperature PND 93
4.2.3 Magnetic susceptibility measurements 95
4.2.4 Variable temperature PND 97

4.3 Synthesis and characterisation of $Sr_2Cr_{0.93}Mn_{0.07}O_2Mn_{0.92}Cr_{1.08}As_2$ 107
4.3.1 Powder X-ray diffraction 108
4.3.2 Room temperature PND 110
4.3.3 Magnetic susceptibility measurements 112
4.3.4 Variable temperature PND 113
4.3.4.1 POLARIS 113
4.3.4.2 WISH 115
4.4 Synthesis and characterisation of $Ba_2CrO_2Cr_{1.02}Mn_{0.98}As_2$ 124
4.4.1 Powder X-ray diffraction 125
4.4.2 Room temperature PND 126
4.4.3 Magnetic susceptibility measurements 128
4.4.4 Variable temperature PND 129
4.5 Discussion 138
4.5.1 Crystal structures 138
4.5.2 Magnetic ordering 141

Chapter 5 Synthesis and characterisation of Sr_2MnO_3CuSe, Sr_2MnO_3CuS and $Sr_2MnO_3Cu_{0.94}S$ 154
5.1 Introduction 154
5.2 Synthesis and characterisation of Sr_2MnO_3CuSe 156
5.2.1 Powder X-ray diffraction 156
5.2.2 Magnetic susceptibility measurements 159
5.2.3 Room temperature PND 161
5.2.4 Variable temperature PND 163
5.3 Synthesis and characterisation of Sr_2MnO_3CuS 172
5.3.1 Powder X-ray diffraction 173
5.3.2 Room temperature PND 176
5.3.3 Magnetic susceptibility measurements 178
5.3.4 Variable temperature PND 179
5.4 Synthesis and characterisation of $Sr_2MnO_3Cu_{0.94}S$ 184
5.4.1 Deintercalation of Sr_2MnO_3CuS 184
5.4.2 Powder X-ray diffraction 185
5.4.3 Room temperature PND 187
5.4.4 Magnetic susceptibility measurements 189

5.4.5 Variable temperature PND 192
5.5 Discussion 195

Chapter 6 Synthesis and characterisation of Sr_2FeO_3CuSe and Sr_2CrO_3CuSe 198
6.1 Introduction 198
6.2 Synthesis and characterisation of Sr_2FeO_3CuSe 199
6.2.1 Powder X-ray diffraction 200
6.2.2 Room temperature PND 202
6.2.2 Magnetic susceptibility measurements 205
6.2.3 Variable temperature PND 206
6.2.3.1 Low temperature magnetic structure 207
6.2.3.2 High temperature magnetic structure 213
6.3 Synthesis and characterisation of Sr_2CrO_3CuSe 218
6.3.1 Powder X-ray diffraction 219
6.3.2 Room temperature PND 221
6.3.3 Magnetic susceptibility measurements 225
6.3.4 Variable temperature PND 227
6.4 Discussion 230

Chapter 7 Synthesis and characterisation of Sr_2CrO_3CrAs 238
7.1 Introduction 238
7.2 Synthesis and characterisation of Sr_2CrO_3CrAs 240
7.2.1 Powder X-ray diffraction 242
7.2.2 Room temperature PND 244
7.2.3 Magnetic susceptibility measurements 246
7.2.4 Variable temperature PND 246
7.3 Discussion 252
7.3.1 Crystal structures 252
7.3.2 Magnetic ordering 253

Chapter 8 Summary 257

References 262

Appendix A: Units in magnetometry i
Appendix B: Variable temperature PND (WISH) on $Sr_2CrO_2Cr_2As_2$ iii
Appendix C: Bond valence calculations.....v
Appendix D: 3 T/4 T subtraction.....vi
Appendix E: Variable temperature powder X-ray diffraction on Sr_2MnO_3CuSe ...viii

Chapter 1 Introduction

1.1 Solid state chemistry

Interest in solid-state chemistry in the last few decades has been fuelled by the discoveries of many solid-state materials with unusual properties including semi-conductivity, superconductivity, ferromagnetism, ferroelectricity, etc., which all have vital technological uses. To understand these solid-state materials, it is important to have some insight into their structures and properties. The development of the technique of X-ray crystallography by Max von Laue[1] and W.H. and W.L. Bragg[2] in the early 20th century allowed the structural analysis of crystalline materials. The resulting diffraction patterns can be interpreted to provide the internal positions of the atoms in the crystal very precisely, and thus enable the properties of a solid to be related to the arrangement of atoms. This powerful technique has since accelerated the synthesis and investigation of new solid-state compounds with interesting chemical and physical properties and potential technological applications, which have been driving the research in this field.

One of the most exciting scientific breakthroughs for technological applications of these materials was the discovery of high-temperature superconductivity in layered perovskite-based cuprates $La_{2-x}Ba_xCuO_{4-\delta}$ (T_c = 35 K),[3] for which J. G. Bednorz and K. A. Müller were awarded the Nobel Prize in Physics in 1987. In the space of a few months, T_c was raised above the boiling point of liquid nitrogen in $YBa_2Cu_3O_{7-\delta}$ (T_c = 93 K).[4] The current maximum T_c is 138 K in $Hg_{0.8}Tl_{0.2}Ba_2Ca_2Cu_3O_{8.33}$.[5] Prior to these discoveries, superconductivity was first reported in elemental mercury (T_c = 4.2 K) and many other metals

and alloys at low temperatures.[6] During the last three decades, superconductivity has changed from a low-temperature curiosity that is out of reach of normal laboratory conditions to a readily accessible phenomenon with many exciting possibilities for new developments and applications. Appearance of high-temperature superconductors (cooled with liquid nitrogen) offers huge potential for their technological applications, e.g., in magnetic resonance imaging (MRI), nuclear magnetic resonance (NMR) machines and maglev trains. In 2008 Hosono and co-workers at the Tokyo Institute of Technology reported superconductivity in an iron-based compound LaOFeAs when O is partially substituted by F,[7] after which several others in this class of superconductors[8] were synthesised and although they had lower critical temperatures than those of the cuprates, some of them have favourably high critical fields and critical currents. This has led to the huge interests of scientists in the preparation of new iron-based superconductors and investigation of similarities and differences between the cuprates and iron-based compounds.

Another important scientific breakthrough was the discovery of rechargeable lithium-ion battery, which has emerged as the dominant energy storage source for consumer electronics, and is being explored for automotive and stationary storage applications.[9] The first commercial lithium-ion battery was made by Sony in 1990, which utilized $LiCoO_2$ as the cathode material in the portable electronic devices due to its high structural stability and the ability to reversibly intercalate Li ions in the charge/discharge cycles.[10] Since then, several other cathode materials ($LiCoO_2$[11], $LiNi_xMn_yCo_zO_2$[12], $LiMn_2O_4$[13] and $LiFePO_4$[14]) have also been prepared and investigated to improve stored energy density, charge/discharge rates, cost and safety issues and service life of batteries for the development of new Li batteries in the huge potential market for electric vehicles which can alleviate distributed CO_2 emissions and air pollution from fossil fuels.[15]

Solid state materials are also commonly found in the electronics industry. Ferromagnetic materials (e.g. γ-Fe_2O_3[16] and CoPtCr[17]) are used in hard disks for computer memory storage. Some dielectric materials (e.g. $BaTiO_3$ and $PbTiO_3$)[18], which are also classic examples of ferroelectric perovskites, have very low conductivity and usually used in a wide variety of electronic devices in the industry. Furthermore, three-dimensional porous materials (e.g. aluminophosphates[19], metal-organic frameworks[20] and zeolites[21]) are found to have applications in the heterogeneous catalysis and absorption.

1.2 Non-oxide and mixed-anion solids

The investigation of the structures and properties of oxide materials has dominated much of solid-state chemistry, due to the oxidising nature of ambient air. More complicated techniques are required to exclude atmospheric oxygen and moisture for the synthesis of non-oxide materials (e.g. nitrides and sulphides which contain readily oxidisable N^{3-} and S^{2-} respectively), making the study of these compounds fall behind those well-developed oxides. However, nowadays the more widely available techniques (Ar or N_2 filled dry glovebox) for handling air and moisture sensitive solids have facilitated the synthesis and exploration of compounds containing non-oxide anions. Two well-known examples of these non-oxide compounds are GaN and MgB_2. GaN has been widely used in blue lasers and LEDs,[22] and MgB_2 is a superconductor with a high T_c at 39 K.[23] Moreover, the investigation of mixed-anion solids (oxynitrides and oxyhalides) has also attracted a lot of attention because of their interesting magnetic, electronic and optical properties.[24-26]

1.3 Oxypnictides and oxychalcogenides

In this thesis, mixed-anion chemistry will be described with a particular focus on the areas of oxypnictide and oxychalcogenide chemistry, where the compounds contain both oxide anions and pnictide (phosphide, arsenide, antimonide, or bismuthide) or chalcogenide (sulfide, selenide, or telluride) anions, with one or more cations derived from the metallic elements. The polarizability and sizes of oxide and pnictide or chalcogenide anions are different, suggesting that long-range anion ordering may be expected with their bonding preferences to different metals also determining the crystal structures. In these compounds, the distinct crystallographic sites are usually occupied by different ions and layered crystal structures are generally adopted.[27]

1.3.1 ZrCuSiAs structure

ZrCuSiAs is a representative of the compounds (oxypnictides, oxychalcogenides and halide pnictides) which adopt the ZrCuSiAs structure type (Figure 1.1)[28] and are composed of alternating PbO-type layers and anti-PbO-type layers in a tetragonal unit cell with the *P*4/*nmm* space group. $ThCu_{1-x}PO$ was the first reported oxypnictide (prepared by Albering et al. in 1996) with the ZrCuSiAs structure[29] and now this class of compound constitutes the largest family of layered *d*-metal oxypnictides, including some of the Fe-based superconductors. In ThCuPO, the two alternating layers are viewed as $[CuP]^{2-}$ and $[ThO]^{2+}$, where O^{2-} is in the tetrahedral coordination with four Th^{4+} ions and Cu^{+} is coordinated by four P^{3-} anions.

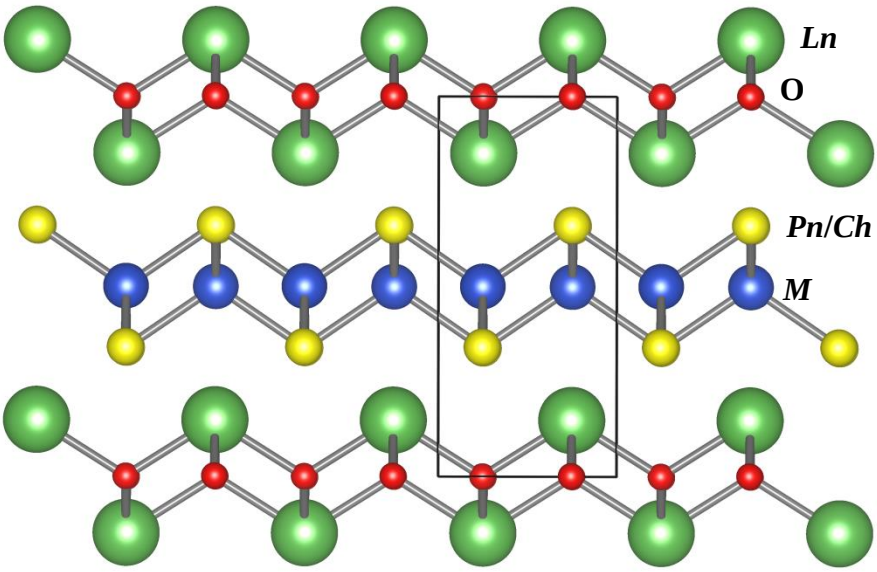

Figure 1.1: The crystal structures of *Ln*O*MCh* and *Ln*O*MPn*, which adopt the ZrCuSiAs structure

The ZrCuSiAs structure type is often observed in oxychalcogenides. One such group of layered oxychalcogenides are those with the composition of *Ln*OCu*Ch* (where *Ln* = lanthanide La – Nd and *Ch* = S, Se, and Te), discovered by Palazzi in 1981.[30, 31] These compounds contain separate layers of $[Ln_2O_2]^{2+}$ and $[Cu_2Ch_2]^{2-}$, making it possible to synthesise numerous compounds with different ions in the two distinct layers and thus to modify the physical properties of the solids through chemical substitution. *Ln*OCu*Ch* has been of great interest because of its transparent *p*-type semiconductor properties,[32] leading to the development of application of LaOCuSe in light-emitting diodes (LEDs).[33] In addition, a family of rare earth pnictide oxides (*Ln*OFeAs materials) with this structure type has also been under intense investigation since the recent discovery of superconductivity.[34]

1.3.2 $Sr_2Mn_3O_2Sb_2$ structure

This structure type was first described for the oxide antimonide $Sr_2Mn_3O_2Sb_2$ by Brechtel *et al.* in 1979,[35] after which several other compounds possessing the composition of $A_2M_3Pn_2O_2$ (*A*=Sr, Ba, *M* = 1st-row transition metal and *Pn*=As, Sb, Bi) were also reported.[36, 37] These compounds showed the segregation of layers along the *c* axis where perovskite-based metal oxide sheets are sandwiched by tetrahedrally-coordinated metal pnictide layers with alkaline earth cations interspersed between them (Figure 1.2). The anti-PbO type $[M_2As_2]^{2-}$ layers are structurally similar to those pnictide layers in the ZrSiCuAs-structure-type compounds.

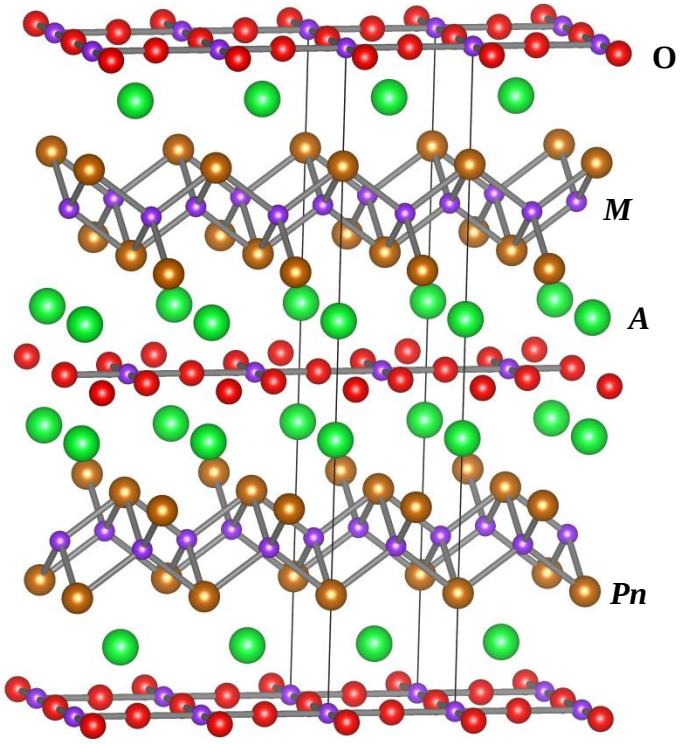

Figure 1.2: The crystal structure of $Sr_2Mn_3O_2Sb_2$-type compounds

However, the properties of these compounds were not fully investigated until the mid-1990s, during which time they were of great interest to chemists again because of the MO_2 planes,

with their structural similarities to CuO_2 planes in high-temperature superconductors. As the discovery of new high-temperature superconducting materials with Fe_2X_2 layers (X = As, Se) in 2008, a second resurgence in the interest of these oxide pnictides, and related oxide chalcogenides occurred. Additionally, the magnetic properties of some of these layered oxypnictides were also found interesting. Neutron diffraction studies of $Sr_2MnO_2Mn_2Sb_2$ and $Sr_2MnO_2Mn_2As_2$ revealed that the manganese atoms in the pnictide layers order antiferromagnetically below 300 K and 340 K respectively with the moments adopting a checker-board arrangement with the antiferromagnetic coupling of nearest neighbours and with the moment directed along the *c* direction perpendicular to the layers.[38] Furthermore, the $[Mn_2Pn_2]^{2-}$ and $[MnO_2]^{2-}$ layers in these structures behave as nearly independent two-dimensional magnetic systems. For $Sr_2MnO_2Mn_2Sb_2$, the manganese ions in the $[MnO_2]^{2-}$ layers order antiferromagnetically below 65 K, with a checker-board-type array and the magnetic moments are oriented in the *ab* plane, perpendicular to those in the antimonide layers. But in the case of $Sr_2MnO_2Mn_2As_2$, only short-range ordering of the magnetic moments in the MnO_2 layer of the oxyarsenide was observed. The reasons for the appearance of these different magnetic behaviours of these layered oxypnictides are not entirely clear. Related compounds are discussed in Chapter 3 and Chapter 4.

Numerous other transition-metal compounds were also prepared with this layered structure, by incorporating the metals into both oxide and pnictide layers. $A_2Zn_3As_2O_2$ (A = Sr, Ba) was synthesized by Brock *et al.* in 1994,[39] which provided the first evidence that $Sr_2Mn_3As_2O_2$-structure-type can accommodate a range of metal ions promising a range of electronic properties. This is a rare example because this structure accommodates Zn with a square planar geometry in an extended structure. A few years later, another $Sr_2Mn_3As_2O_2$-structure-type compound, $Ba_2MnO_2Zn_2As_2$, was reported by Ozawa *et al.* in 1997. This compound is composed of alternating layers of $[Zn_2As_2]^{2-}$ and $[MnO_2]^{2-}$ anionic network

separated by the Ba cations, and the ordering of Zn and Mn ions in two sublattices were confirmed by powder neutron diffraction in their original paper.[40] This indicates that crystallographically ordered mixed metal phases can be obtained in this structure type with the coordination preferences of Mn and Zn as the driving force. Similar to those *Ln*O*MPn* compounds, the ordering in the structure arises from their differences in the size and polarisability of the ions, leading to the generation of separate layers. The successful synthesis of these compounds offered a logical starting place to chemists for the exploration of new possibilities of this $Sr_2Mn_3As_2O_2$ structure with other transition metals.

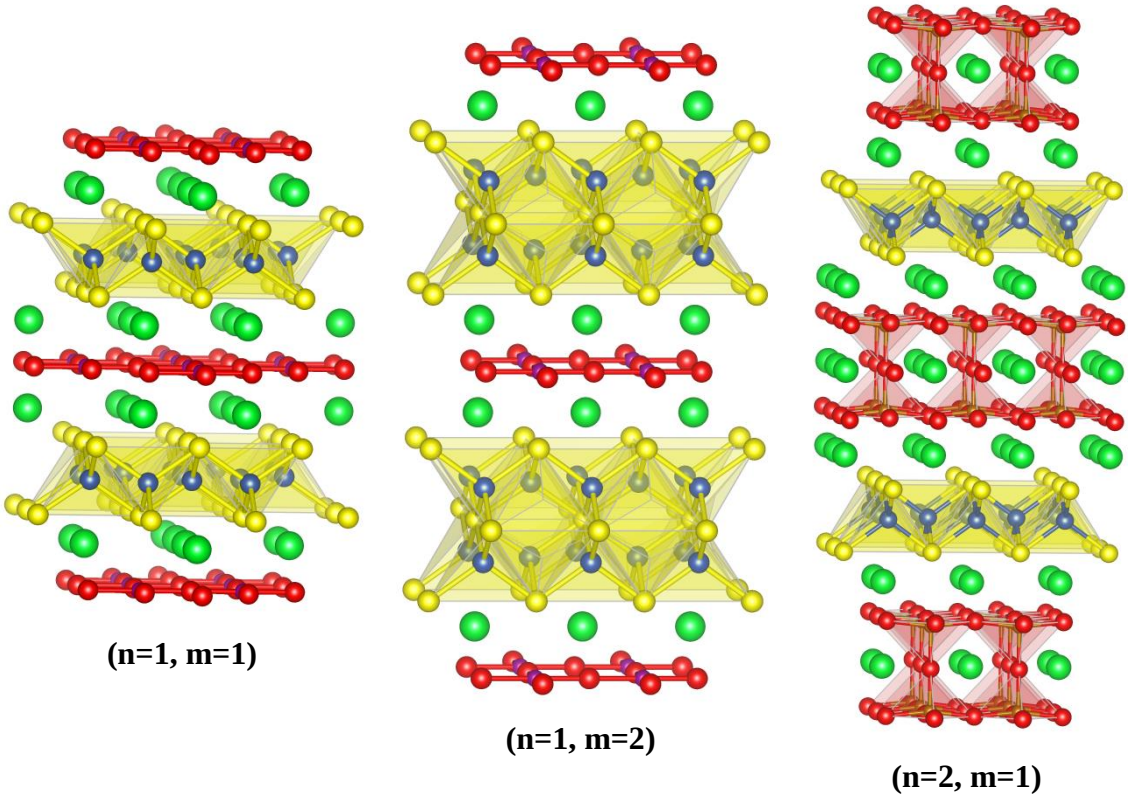

Figure 1.3: The crystal structures of $Sr_2Mn_3Sb_2O_2$-type oxychalcogenides with thicker oxide or chalcogenide layers: $Sr_2MnO_2Cu_{1.5}S_2$,[41] $Sr_2MnO_2Cu_{3.5}S_3$[42] and $Sr_3Fe_2O_5Cu_2S_2$[43] (from left to right)

The isostructural oxychalcogenides with the $Sr_2Mn_3Sb_2O_2$ structure type were first discovered in the synthesis of $Sr_2ZnO_2Cu_2S_2$ and $Sr_2MnO_2Cu_2S_2$ by Zhu and Hor in 1997,[41] since which time many solids of this structure type have been found. Furthermore, compounds with different thicknesses of the perovskite oxide layers and anti-PbO type chalcogenide layers have also been reported by applying various element ratios and synthesis conditions. Figure 1.3 shows the crystal structures of these compounds with thicker layers, in which *n* represents the number of oxide layers and *m* represents the number of chalcogenide layers.[27]

1.3.3 Sr_2CuGaO_3S structure

The Sr_2CuGaO_3S structure type crystallises in a tetragonal unit cell with the *P*4/*nmm* space group. The first compound of this structure was the Sr_2CuGaO_3S synthesized and characterised by Zhu and Hor in 1997,[44] together with some other similar materials with different metals (Sr_2MO_3CuS (*M* = Cr, Mn, Fe and In).[43, 45] This family contains anti-PbO-type CuS layers separated by the thick oxide layers where the *M* metal cations are in an unusual square pyramidal geometry (Figure 1.4a). The layered structure of these compounds is similar to that of the $n = 2$ members of the $A_{n+1}M_nO_{3n-1}Cu_2S_2$ perovskite-type materials (e.g. $Sr_3Fe_2O_5Cu_2S_2$ in Figure 1.4b), but the oxide layers in Sr_2MO_3CuS solids are slightly thicker than those in $Sr_3Fe_2O_5Cu_2S_2$. In addition, the connectivity of the transition metal polyhedra is also different. There is an extra layer of Sr/O inserted between the double layers of MO_5 polyhedra in Sr_2MO_3CuS and this leads to the absence of the body centring. Figure 1.4c compares the oxide-layer structures in Sr_2MO_3CuS and $Sr_3Fe_2O_5Cu_2S_2$.

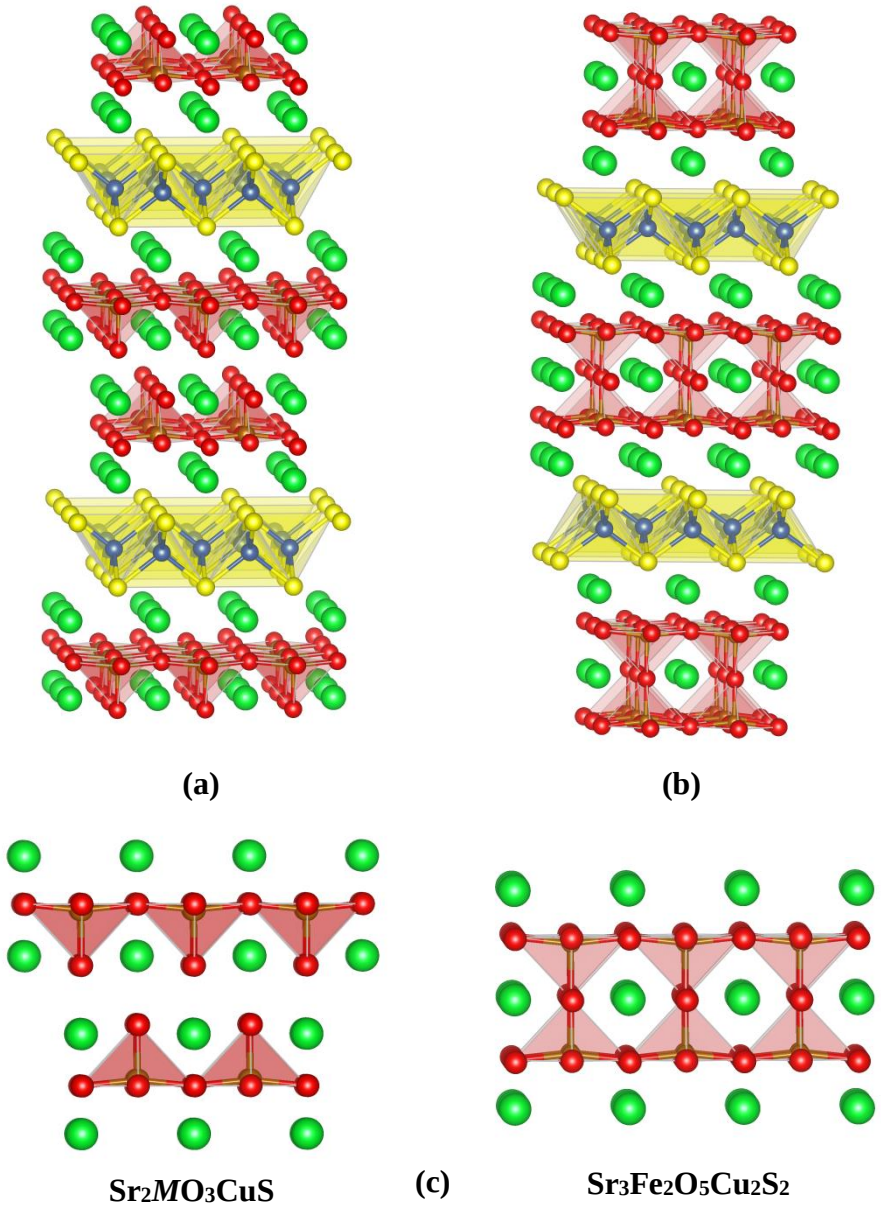

Figure 1.4: (a) The crystal structure of Sr_2CuGaO_3S-type oxychalcogenides with thicker oxide layers; (b) The crystal structure of $Sr_3Fe_2O_5Cu_2S_2$; (c) The comparison between the oxide layers in Sr_2MO_3CuS and $Sr_3Fe_2O_5Cu_2S_2$

1.4 Magnetic behaviour of solids

1.4.1 Diamagnetism

Diamagnetism is the phenomenon present in all materials where paired electrons work to repel the applied magnetic field. This type of diamagnetism is actually a very weak phenomenon and only observed when all the atomic shells are filled or empty, with no net magnetic moment. The diamagnetism is usually overshadowed in the solids by some other stronger magnetic interactions such as paramagnetism or ferromagnetism. The origin of diamagnetism is due to the orbital motion of electrons around the nuclei of atoms, which generates some small currents in the magnetic field by electromagnetic induction. These small currents in turn give the induced magnetic moments with their directions opposed to the applied field, as described in Lenz's law. The diamagnetic susceptibility is always negative with a magnitude around 10^{-6} emu mol^{-1}, which is much smaller than that of other types of magnetic interactions. Therefore it can usually be ignored when measuring the solids with unpaired electrons showing paramagnetism or ferromagnetic and antiferromagnetic orderings. Diamagnetism is a property of closed-shell systems and it is the most common magnetic behaviour for a compound to show.

1.4.2 Paramagnetism

The phenomenon of paramagnetism occurs in solids with unpaired spins or partially filled bands, which are weakly coupled to each other and have a disordered arrangement in the absence of an external magnetic field due to their thermal motions. These randomly orientated moments tend to align with an applied magnetic field *H* and display a positive magnetic susceptibility. Paramagnetism is often observed in transition-metal compounds

since the partially filled d-orbitals of metal cations give the magnetic moments and the anions in those compounds ensure enough space between cations to generate relatively weak interactions between each magnetic moment. Oxygen is also paramagnetic because of the presence of two unpaired π^* electrons. Paramagnetic solids can be further categorized into three different types:

1.4.2.1 Curie paramagnetism

For a paramagnetic system with non-interacting spins, the coupling between adjacent moments on atomic sites is very weak and the spins will tend to align with an applied external field. However, the thermal energy of the system will tend to make these spins randomly oriented, away from their alignment in the field. The magnetization of the spin in the applied magnetic field can then be expressed:

$$\boldsymbol{M} = \frac{Nm^2}{3k_B}\frac{\boldsymbol{H}}{T} \tag{1.1}$$

where N is Avogadro's constant, m is the magnitude of the magnetic moment, k_B is the Boltzmann constant, $\boldsymbol{H}$ is the applied magnetic field and T is the temperature in Kelvin. The magnetization is proportional to the applied field and inversely proportional to the temperature. This gives the susceptibility:

$$\chi = \frac{M}{H} = \frac{Nm^2}{3k_BT} = \frac{C}{T} \tag{1.2}$$

where $C = \frac{Nm^2}{3k_B}$ is the Curie constant. This expression of susceptibility is obtained if one assumes the magnetic moments in the system can have all possible orientations in the applied field. However, they can only align along discrete orientations because of spatial quantization. Thus the quantum mechanical expression for the susceptibility is:

$$\chi = \frac{N\mu_{\text{eff}}^2\mu_B^2}{3k_BT} = \frac{C}{T} \tag{1.3}$$

where μ_{eff} is the effective magnetic moment and μ_B is the Bohr magneton. Substitution of the actual values for these constants in *eqn* 1.3 gives:

$$\mu_{\text{eff}} = 2.84\sqrt{C} \tag{1.4}$$

This effective magnetic moment is related to the total angular momentum *J* (which is the sum of the orbital momentum *L* and spin momentum *S*) and the Landé *g*-factor:

$$\mu_{\text{eff}} = \text{g}\sqrt{J(J+1)} \tag{1.5}$$

$$\text{g} = 1 + \frac{J(J+1) + S(S+1) - L(L+1)}{2J(J+1)} \tag{1.6}$$

For the first-row transition metals, the orbital angular momentum is largely quenched with the presence of a ligand field which removes the 3*d*-orbital degeneracy and the spin-only angular momenta can be calculated ($L = 0$ thus $S = J$ and $g = 2$) from *eqn* 1.6:

$$\mu_{\text{eff}} = 2\sqrt{S(S+1)} \tag{1.7}$$

The spin-only values are in much better agreement with the experimental results for first-row transition metals than the values derived using the total angular momentum, although there are many exceptions. Combination of *eqn* 1.4 and *eqn* 1.7 gives:

$$C = \frac{S(S+1)}{2} \tag{1.8}$$

Thus the number of unpaired electrons (2*S*) can be calculated using Curie constant which is extracted from the gradient of a plot of $1/\chi$ against T. For a Curie paramagnet, the typical room-temperature susceptibility value is of the order 10^{-3} emu mol^{-1}.

1.4.2.2 Curie-Weiss paramagnetism

In order to obey the Curie Law, the magnetic moments in the solid must be non-interacting (i.e. the system is magnetically dilute and the externally applied field is the only perturbation to the system of moments). More commonly, many paramagnetic solids do not obey the Curie law, but instead follow a more general temperature-dependent Curie-Weiss Law:

$$\chi = \frac{C}{T - \theta} \tag{1.9}$$

where the interactions between the moments in the materials (molecular field) have the tendency to align parallel (ferromagnetically) or antiparallel (antiferromagnetically) at low temperatures. The size of the Weiss constant gives an indication of the strength of the average interactions between neighbouring moments and it can be comparable in size to the transition temperatures of ferromagnetic (FM) (T_C) and antiferromagnetic (AFM) (T_N) ordering. A positive value of θ indicates these interactions are predominantly ferromagnetic. Conversely for a solid displaying a negative Weiss constant, antiferromagnetic interactions are predominant. For a Curie-Weiss paramagnet, the accurate determination of Curie constant requires data points at temperatures well above the absolute value of the Weiss temperature.

1.4.2.3 Pauli paramagnetism

In the previously discussed Curie paramagnet, the electrons in the partially occupied valence shells are fully localised on their atoms. However, there is another type of system, the Pauli paramagnet, where the electrons are delocalised through the lattice and give rise to electrical conductivity (i.e. metallic systems). With the help of the external magnetic field, the original "spin-down" and "spin-up" arrangements of these electrons become non-degenerate. The

energy levels of those spins aligning to the field are thus lowered and are preferentially occupied in the ground state to form an overall magnetisation, the size of which is proportional to the density of states at the Fermi level, $N(E_F)$:

$$\chi = 2\mu_0\mu_B^2 N(E_F)$$

where μ_0 is the vacuum permeability. Therefore the $1/T$ susceptibility dependence of Curie system is not found in the Pauli paramagnet, and instead its susceptibility is actually independent of temperature. The size of the Pauli paramagnetic susceptibility is usually several orders of magnitude smaller than the Curie susceptibility, and in these cases the corrections of core diamagnetism need to be performed; it is also often hard to avoid the presence of small amounts of ferromagnetic impurities which can complicate the interpretation of the magnetic susceptibility of these weakly magnetic system.

1.4.3 Ferromagnetism

Ferromagnetism can arise from localised magnetic moments (e.g. Rb_2CrCl_4) or from delocalised electrons (band ferromagnetism) like in CrO_2 or elemental Fe. For a ferromagnetic material, the interactions between adjacent spins of unpaired electrons are large enough to give long-range magnetic ordering even in the absence of an external field, and below a certain temperature, T_C (Curie temperature), the spins can align parallel to each other and display a large susceptibility up to the order of 10^5 emu mol^{-1}. Above T_C the strong interaction between spins can be disrupted by the thermal energy and the solid is then observed to be paramagnetic. The change in susceptibility χ of a typical ferromagnetic material as a function of T is shown in Figure 1.5, where the susceptibility rises rapidly at the Curie temperature.

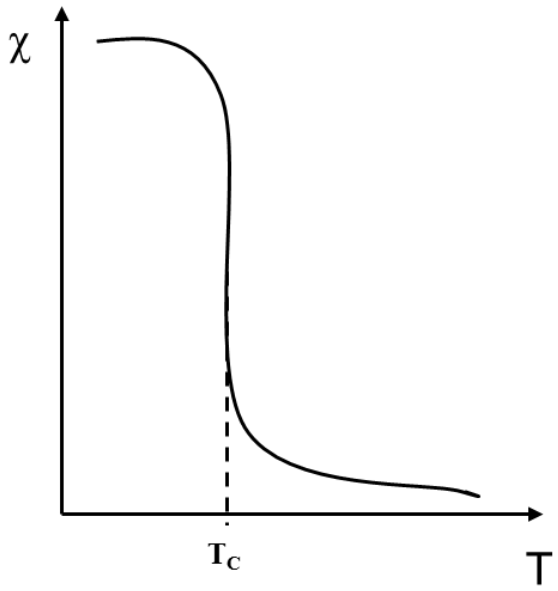

Figure 1.5: Schematic of the change in susceptibility with temperature for a ferromagnetic material

In a ferromagnetic solid, the spins are usually aligned in separate magnetic domains. The spin orientation for each domain is random and hence the overall magnetisation of the bulk material can be zero without the external magnetic field. However, the alignment of domains will be reached in an applied field, to give a net magnetisation. In order to characterise a ferromagnet, the measurement of magnetisation versus the field, *M* vs *H*, is always measured below T_C, in which the magnetisation of the solid will remain even when the external field is removed. This behaviour is called magnetic hysteresis, as shown in Figure 1.6. In the beginning, the material follows a non-linear magnetization curve when the field is raised from zero. A maximum of magnetization value will then be reached in a strong external field, where the ferromagnet is saturated with the alignment of domains. When the driving magnetic field drops to zero, the material will retain a considerable degree of magnetization, and this magnetic behaviour is often used to produce a magnetic memory device. Additionally, the net magnetization in zero applied field can usually be driven to zero again if the external magnetic field is reversed and increased to a very large value.

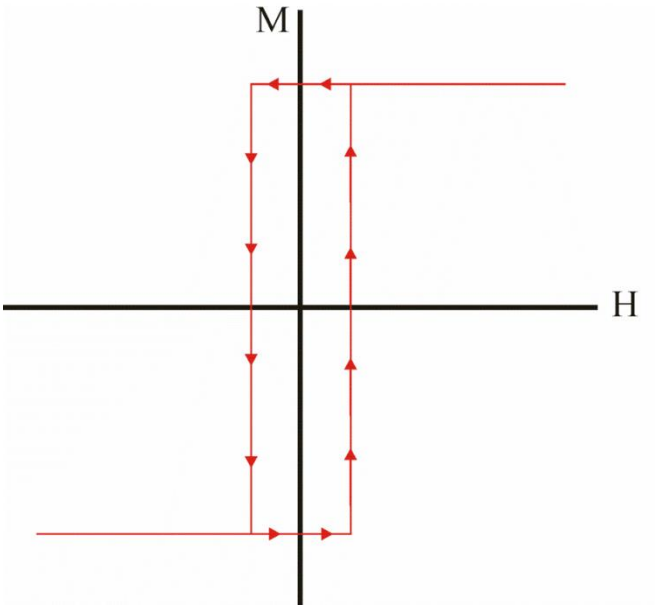

Figure 1.6: The hysteresis of a ferromagnetic material

1.4.4 Antiferromagnetism

In antiferromagnetic materials, the adjacent spins of unpaired electrons tend to align antiparallel to each other below the critical Néel temperature T_N, giving rise to a zero value of net magnetisation. At low temperatures, the spins in the material are locked in the antiferromagnetic arrangement and there is no net spontaneous magnetisation in the presence of an external magnetic field. When the temperature is increased, some locked spins become free to align with the applied field due to the thermal energy, generating a small magnetisation in the material. The value of magnetisation will reach a maximum at the Néel temperature, T_N, above which the thermal energy is big enough to overcome the antiparallel interactions between the spins and the temperature dependence of the susceptibility is similar to that of a paramagnet (the magnitude of susceptibility is much lower than that of a paramagnetic material close to the transition). A sharp cusp (Figure 1.7) can be observed at T_N in the susceptibility measurement of a three-dimensional ordering antiferromagnet, and this will be broader in the case of low-dimensional ordering. Generally, the materials only

display their antiferromagnetic ordering at very low temperatures. However, in this thesis, most compounds were found to be antiferromagnetically ordered at the temperatures that are much higher than room temperature.

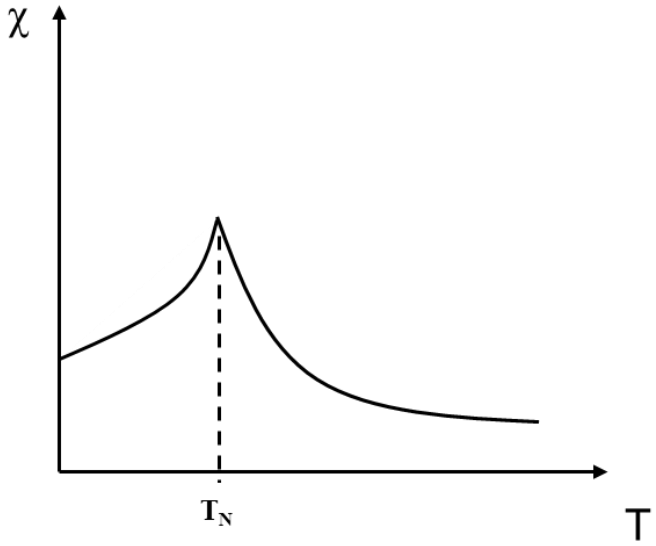

Figure 1.7: Schematic of the change in susceptibility with temperature for an antiferromagnetic material

1.4.5 Spin glass behaviour

Spin glass behaviour is a magnetic phenomenon due to the frustration and disorder of interactions between magnetic spins. The spin frustration can arise if there is competition between AFM and FM interactions or it is impossible to satisfy all magnetic spins simultaneously. This can be shown in a triangular arrangement of magnetic spins (Figure 1.8) where the adjacent spins prefer to align antiparallel with each other, but it is not possible for all three spins to be antiferromagnetically ordered in a triangle.

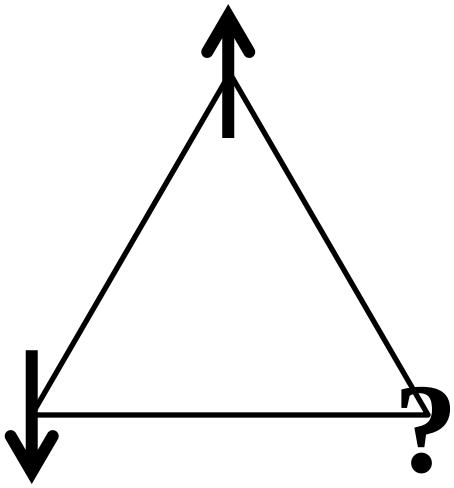

Figure 1.8: Schematic of the magnetic frustration in a triangular antiferromagnet

Different from typical ferromagnetic and antiferromagnetic materials, several possible magnetic configurations can be found in the spin-glass materials with magnetic frustration. At high temperatures, the thermal energy is greater than the interaction between spins and the spin-glass materials usually display paramagnet-like behaviour. As the temperature is decreased, the spins start to be locked, however, because of the random orientation of those frozen spins, the long-range magnetic ordering cannot be observed even if the temperature is lower than the freezing temperature, T_g. The arrangement of spins will also be affected by whether the solid is previously cooled with the applied field (FC) or without the field (ZFC). Thus below a spin-glass freezing temperature (T_g), the measurement of the magnetic susceptibility after cooling in the applied field will not coincide with the measurement made without the field. This is always used to identify if a material gives spin-glass or antiferromagnetic behaviour since for antiferromagnet, it does not matter if the applied field is on or off during cooling through $T_{N;}$ but for a spin-glass material, a clear divergence can be seen in its ZFC and FC curves below T_g, especially in a small measuring field. Moreover, the magnetisation isotherm of a spin-glass material will display a hysteresis that is

superficially similar looking to that of a ferromagnet, expect that the spin-glass hysteresis can be displaced from the origin and its isotherm may not close up.

1.5 Models of magnetic exchange

1.5.1 Direct exchange

The direct-exchange interaction involves the overlap between the adjacent metal orbitals containing the unpaired electrons, leading to alignment or anti-alignment of the magnetic moments. This mechanism is usually only significant between electrons in the nearest neighbour magnetic ions, which gives sufficient direct orbital overlap. However, this interaction falls off rapidly with distance and thus it is less important in most complex solids where the metal ions are too far apart to form direct interactions, but in most compounds described in this thesis, it is an important interaction in the CrAs layers since the Cr ions are quite close. Therefore, it is found that an indirect mechanism is useful to explain the exchange coupling between the metal ions through the simultaneous covalent bonding with their bridging ligands. Such anion-mediated interaction is known as "superexchange".

1.5.2 Superexchange

Superexchange is usually seen in many transition-metal oxides and related compounds, in which the magnetic interactions between the transition-metal ions are mediated by the intermediate anions. This indirect interaction leads most commonly to antiferromagnetic ordering. Figure 1.9 illustrates the antiferromagnetic superexchange interaction between two metal $d(e_g)$ orbitals via the oxygen $2p(\sigma)$ orbital in a linear array of M^{n+}-O-M^{n+}, if assuming the indirectly coupled metal ions both possess only one e_g electron. The overlap between

each metal *d*-orbital and the filled *p*-orbital of O leads to the partial donation of electron density to the metal site. If the unpaired electron on *M*(1) has its spin "up" then the electron density transferred from the O *p*-orbital must have the opposite spin "down" in accordance with the Pauli exclusion principle. To keep the spin neutrality on O, the electron density donated simultaneously to the other metal ion must have "up" spin and this is possible only if the electron on *M*(2) has its spin "down". This arrangement allows the electrons to be delocalised and lowers the energy of the system. The superexchange interaction is also significantly influenced by the covalency between the orbitals and there is an overall trend of increasing T_N across the first transition series (e.g. T_N(VO)= 117 K, T_N(MnO)= 122 K, T_N(FeO)= 198 K, T_N(CoO)= 291 K and T_N(NiO)= 523 K)[46] as the nuclear charge *Z* increases and the *d*-orbital energies decrease to be a better energy match with the anion orbitals.

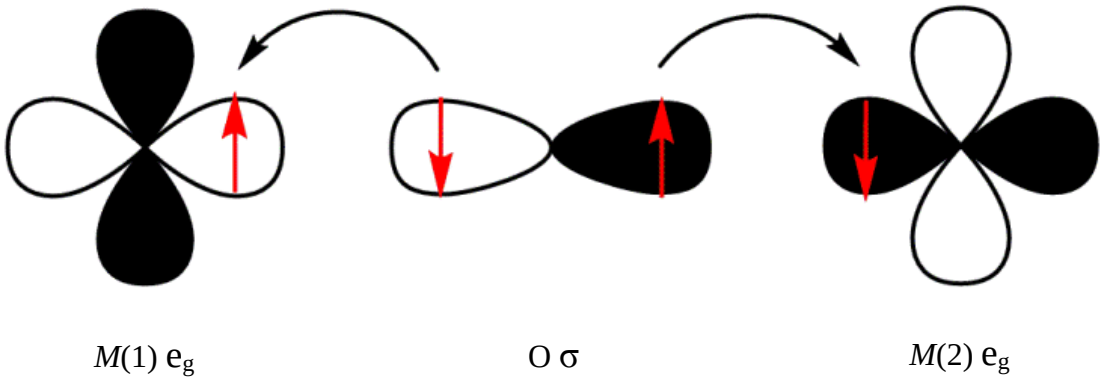

Figure 1.9: AFM superexchange interaction between two metal ions via an intermediate O ligand

The superexchange mechanism can also lead to a FM interaction between cations via the 90° *M* -*L*- *M* configuration (Figure 1.10), where the $d(e_g)$ orbitals overlap with different *p*-orbitals on the ligand. Similar to Figure 1.17, if the unpaired electron on *M*(1) has its spin "up" then the overlap (σ-bonding) between *d*-orbital of *M*(1) and the filled *p*-orbital (p_A) of *L* results in the transfer of electron density with spin "down" to the metal site. Since spin correlation in the ligand always favours the parallel alignment of spins in different orbitals,

thus the donation of electron density from the second orthogonal *p*-orbital (p_B) to *M*(2) has the same spin "down" configuration as that transferred to *M*(1). The Pauli exclusion principle also requires that the electron on *M*(2) has its spin "up" to give an antiparallel spin arrangement to that of the incoming electron density, which then generates the ferromagnetic coupling between *M*(1) and *M*(2).

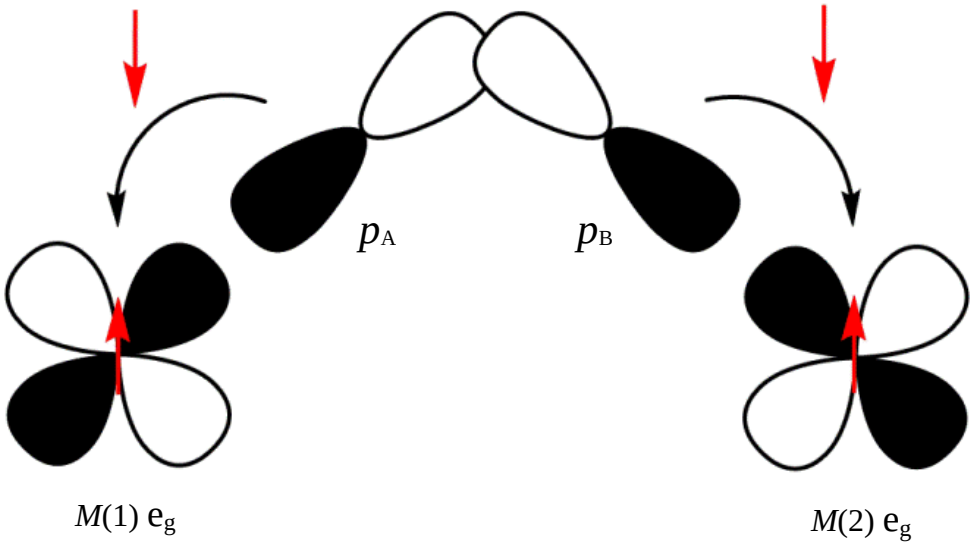

Figure 1.10: FM superexchange in a 90° σ-type array

Furthermore, ferromagnetic superexchange is also found in the case of a linear *M*-*L*-*M* array, in which the $M(2) - d_\sigma$ orbital is empty but has an occupied orthogonal partner. Spin correlation drives the electron spin in the occupied *M*(2) orbital parallel to that of the transferred ligand p_σ density and therefore parallel to that on *M*(1). One known example of this situation is found in Rb_2CrCl_4, where the Cr ion is in the square plane with the Jahn-Teller distortion.

1.5.3 Double exchange

Ferromagnetism can also occur via "double exchange" in compounds in which the magnetic ions have mixed valence. Figure 1.11 shows the ferromagnetic ordering of Mn^{3+} and Mn^{4+}

ions observed in rare-earth manganites $Ln_{1-x}A_xMnO_3$ (*Ln* is a trivalent rare earth metal ion and *A* is a divalent alkaline earth metal ion), where d^4 Mn^{3+} ion has a high-spin configuration with one unpaired electron in the e_g orbital and three unpaired electrons in the t_{2g} orbital, but d^3 Mn^{4+} ion has the empty e_g orbital and three unpaired electrons in the t_{2g} orbital. The e_g electron on Mn^{3+} may transfer to the empty e_g orbital on Mn^{4+} ion without changing its spin, and this can happen only if the spins of t_{2g} electrons on both Mn^{3+} and Mn^{4+} are directed parallel, which is in accordance with the Hund's rule that the electrons in partially filled orbitals have the same spin. In addition, the concentrations of Mn^{3+} and Mn^{4+} must be high enough in the system to form sufficient paths for Mn^{3+} - Mn^{4+} exchange and therefore leading to the ferromagnetic alignment between two cations. In this case the electronic conductivity is much higher in the ferromagnetic state and the phenomenon of magnetoresistance is important in these compounds. [47]

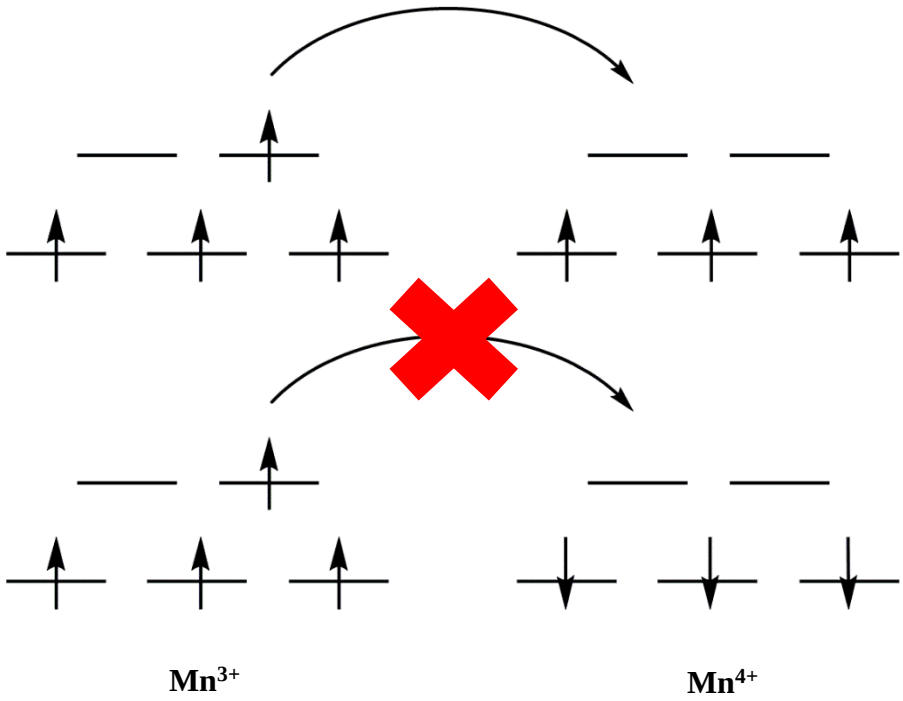

Figure 1.11: Schematic of the double exchange mechanism in a mixed Mn^{3+} and Mn^{4+} compound

1.6 Aims of this thesis

Layered transition metal oxides, pnictides and chalcogenides have been well studied so far for their unusual physical properties which include interesting magnetic and electronic properties. The groups of layered oxypnictides $A_2MO_2M_2As_2$ (A = Sr, Ba and M = Cr, Mn) and layered oxychalcogenides $Sr_2M(1)O_3M(2)X$ ($M(1)$ = Cr, Mn, Fe; $M(2)$ = Cr, Cu; X= S, Se, As) are investigated in this thesis. For $A_2MO_2M_2As_2$, the transition metals are located in the square-planar MO_2 sheets that are separated by tetrahedrally-coordinated metal arsenide layers, but for $Sr_2M(1)O_3M(2)X$, thicker square-pyramidal oxide layers are present between the anti-PbO-type MAs layers. Despite the similarities in the structural blocks of these solids, it has been found that their physical properties are significantly dependent on the identity of the transition metal M. Therefore, the work described in this thesis focuses on the synthesis of novel compounds of these types with different transition metals, controlling their compositions and crystal structures, and hence understanding their physical properties.

Chapter 3 describes the synthesis and characterisation of a novel $Sr_2Mn_3O_2Sb_2$-structure-type compound, $Ba_2CrO_2Cr_2As_2$. The structure and magnetic properties of this compound are then assessed by powder X-ray diffraction, SQUID magnetometry and powder neutron diffraction. It shows that although $Ba_2CrO_2Cr_2As_2$ is isostructural with its Sr analogue, the different structural parameters when the barium cation is incorporated result in significant differences in the separation of the two sublattices and thus the corresponding exchange interactions, which can then make the nature of the magnetic ordering different from the Sr case.

In chapter 4 the substitution of Cr in $Sr_2CrO_2Cr_2As_2$ and $Ba_2CrO_2Cr_2As_2$ by Mn has been performed to successfully synthesize three novel mixed-metal compounds with the same $Sr_2Mn_3O_2Sb_2$-structure. It is found the more oxophilic Cr^{2+} prefers to occupy the *M*(1) sites in the oxide layers and the mixture of Mn^{2+} and Cr^{2+} occupies the *M*(2) sites in the arsenide layers, depending on the Mn:Cr ratio. PND measurements made at variable temperatures have shown unusual magnetic ordering of these compounds with spin-reorientation transition and the appearance of two magnetic structures in a certain range of temperatures.

Chapter 5 reports the synthesis and magnetic behaviours of Sr_2MnO_3CuSe, Sr_2MnO_3CuS and $Sr_2MnO_3Cu_{0.94}S$, where Sr_2MnO_3CuSe has been synthesised with high purity for the first time. Low-temperature PND has revealed the long-range antiferromagnetic ordering in all these compounds, with their magnetic moments of Mn^{3+} ordered along the *c*-axis. $Sr_2MnO_3Cu_{1-\delta}S$ has been found to have a Cu-deficiency of just about 0.06%, but with a different magnetic unit cell compared to its parent compound Sr_2MnO_3CuS, showing the importance of small compositional changes on the physical properties.

Chapter 6 details the synthesis and characterisation of a phase-pure sample of Sr_2FeO_3CuSe. The structural and magnetic behaviours are studied using various characterisation methods, from which an interesting spin-reorientation of the Fe^{3+} magnetic moments is found by analysing the variable-temperature PND data. A novel compound with the composition of Sr_2CrO_3CuSe is also synthesised in this chapter, although with the presence of some impurity phases. Both room-temperature PXRD and PND measurements were used to study its structure and composition. The magnetic susceptibility measurements and low-temperature PND were also performed to probe its magnetic behaviour.

In chapter 7, the synthesis and characterisation of a novel compound, Sr_2CrO_3CrAs, is discussed. Low-temperature PND has revealed the appearance of long-range

antiferromagnetic magnetic ordering in Sr_2CrO_3CrAs, which is very different from those magnetic properties previously reported in Sr_2CrO_3FeAs and some other Sr_2CuGaO_3S-structure-type solids.

The final chapter concludes all the work in this thesis.

Chapter 2 Experimental techniques

2.1 Synthetic methods

2.1.1 Solid state synthesis

The traditional and most common method of preparing solid-state compounds is the ceramic synthesis, where stoichiometric amounts of starting materials are accurately weighed and ground together in an agate pestle and mortar to obtain well-mixed starting materials. The mixture is then placed in an alumina crucible and heated in a furnace at high temperature, typically between 500 and 1300 °C, for a period of time varying between a few hours and several weeks. The high temperatures are used in this method because, for solid-state compounds, it usually takes a lot of energy for ions to overcome the activation barrier to leave their original positions and diffuse to the interface where two solids react. Once the solids at the interface have reacted completely, more reactants will diffuse from the bulk of the solid to the interface. Running the reactions at high temperatures can accelerate the diffusion of reactants (limiting step) and thus make the reactions at the interface faster. Additionally, in order to get a high-purity product, it is also important that the reactants are mixed and ground adequately to give small and homogeneous particles, which minimises the distance between reactant particles and enables the contact area between particles to be maximised. The complete reaction can also be improved by pelletizing the ground mixtures to further increase the surface contact area. It is common that the reactants are heated in the furnace several times and are reground after each heating process to expose new reactive surfaces until a phase-pure product is achieved.

Most starting materials used in this thesis are air-sensitive at room temperature and their products (oxypnictides and oxychalcogenides) can also be easily oxidised in the air at high synthesis temperature (e.g. selenides can be oxidised to selenites). Thus all the samples used in this work and their preparation were performed in an inert atmosphere. The starting materials were stored, weighed and ground in an argon-filled dry glove box. To prepare a pellet, the ground reactants were pelletized using a 13 mm pellet die which was sealed in two polythene bags inside the glovebox and pressed with a force of 3 tonnes outside the glovebox. This was then returned to the glove box and the pellet was placed in a clean alumina crucible which was loaded into a silica tube with a closed end and a short silica spacer at the bottom. A Young's tap was attached to the open end of the tube via a brass adaptor to ensure the atmosphere inside was full of argon. After this, the tube was removed from the glove box and attached to a dynamic vacuum line with a vacuum of approximately 10^{-2} mbar. The tube was then evacuated and carefully sealed using a methane/oxygen blowtorch, giving an evacuated silica ampoule, which was placed in the furnace to run the heating programme.

An alumina crucible was used to avoid the potential reaction between the starting materials (such as the basic Ba and Sr oxides used in this thesis) and the acidic silica tube. Placing a silica spacer below the crucible prevents the cracking of the bottom of the silica tube because the alumina crucible will expand relative to the silica at the high temperature. Before use the silica tubes were pre-dried by heating under a dynamic vacuum using a methane/oxygen blowtorch for 5 to 10 minutes to remove the moisture in the silica tube before loading inside the glovebox, which avoids the possibility of hydrolysis of starting materials and products at a high temperature by water absorbed on the surface of the silica tube.

2.1.2 Argon-filled dry glove box

Throughout this thesis, to avoid oxidation or hydrolysis of the reactants and products, all samples were stored and handled in a Glovebox Technology argon-filled dry box. The argon atmosphere was continually circulated through several columns containing both Dow Chemical copper catalysts and molecular sieves to remove the potential O_2 and H_2O respectively. An oxygen sensor was used to monitor the O_2 concentration inside the glove box, which should read below 1 ppm under the normal working conditions. The quality of the argon atmosphere could also be checked by observing the oxidation rate of the fresh surface of sodium metal. If the surface remained shiny for more than 30 minutes, the working atmosphere was indicated to be acceptable. In order to maintain a good-quality atmosphere in the glovebox, everything to be taken inside was dried in an oven beforehand.

2.1.3 Preparation of starting materials

2.1.3.1 Synthesis of SrO

SrO was used for all the compounds containing Sr in this thesis and it was synthesised by the thermal decomposition of $SrCO_3$ (Alfa, 99.99 %,)[48] shown in *eqn*. 2.1:

$$SrCO_3 \xrightarrow{900°C \text{ for } 18h \text{ and } 1100\ °C \text{ for } 4h} SrO + CO_2\uparrow \qquad (2.1)$$

Approximately 8 g of the starting material $SrCO_3$ was placed in two 13 mm deep alumina boats and loaded into a 25 mm diameter silica tube, which had been pre-heated in the drying oven to avoid the adsorbed water. Ultratorr endcaps (one of them with a Young's tap attachment) were attached to the two open ends of the silica tube. The whole assembly was then put inside the split-tube furnace and under a dynamic vacuum < 10^{-2} mbar, with two

fans below each endcap to avoid the overheating of the rubber O-rings, as shown in Figure 2.1.

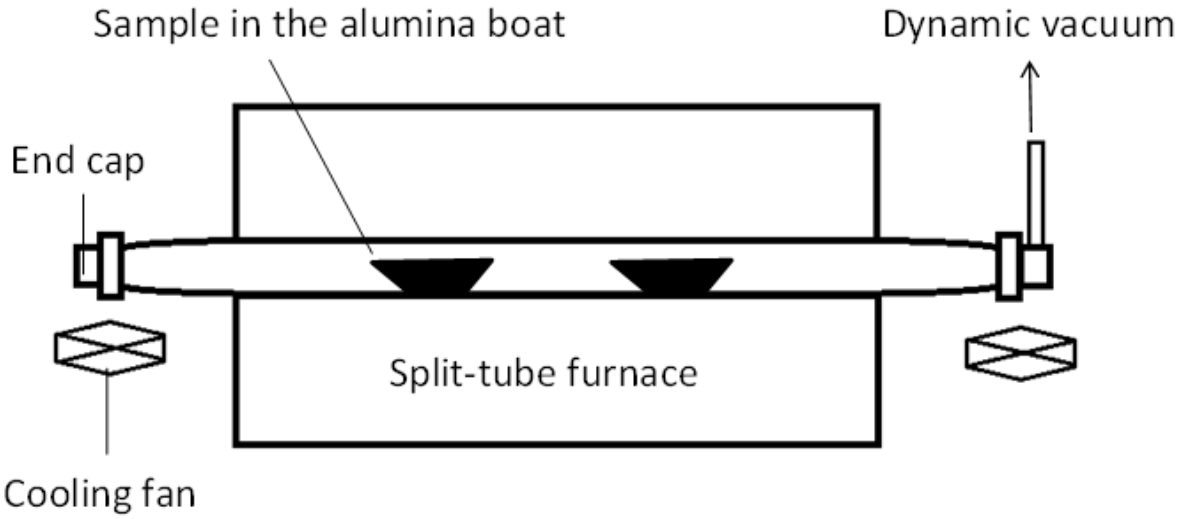

Figure 2.1: The setup used for thermal decomposition of $SrCO_3$ to SrO

The tube was heated to 900 ºC at a rate of 10 °C min^{-1} and this temperature was maintained for 18 h and it was then heated for a further 4 h at 1100 ºC to ensure complete decomposition. CO_2 was collected in the trap of the vacuum line and was not allowed to pass through the vacuum pump. The whole assembly was then transferred into the glove box and the SrO was ground and analysed using lab X-ray powder diffraction to check the purity (the change in mass could be checked as well).

2.2 Characterisation techniques

2.2.1 Diffraction

If an object such as a liquid, gas or amorphous material is illuminated by an incident beam (e.g. X-rays), the radiation can be scattered in all directions by the object and actually very little detail (apart from local structural information) can be obtained from such scattering,

which is usually collected as an apparently featureless background. However, when the material is a crystal, the resultant scattering is no longer featureless. This is because the scattering of radiation from a single point scatterer doesn't give you very much information, but when there is a periodic array of these scatterers in a crystal, the interference of the scattered beams gives constructive interference in a few special directions which allows the determination of the periodicity and the relative positions of the scattering objects. If the scattered waves are completely in-phase with one another, they will interfere constructively giving intensity above the background on the detector. But if they are completely out-of-phase with one another, only the background intensity will be measured. Diffraction is an important tool to detect the structure of crystalline material, giving information about the positions of all the constituent atoms in the diffracting crystal.

2.2.2 X-ray diffraction

X-ray diffraction is a fundamental method that is used to determine the arrangement of atoms in a crystalline material in three-dimensional space. This method takes advantage of the phenomenon that the crystalline solids are usually composed of atoms with interatomic spacings of ~ 1 – 2 Å, comparable to the range of the wavelength (0. 1 Å – 10 Å) for X-ray light. Therefore the regular atomic arrangement in a crystal can act as a diffraction grating, which can scatter the incident X-ray waves along certain directions. In order to diffract the X-ray beams, it was considered that the arrangement of the atoms in the materials needed to be in an ordered, periodic and three-dimensional space. This theory can be illustrated using a hypothetical one-dimensional crystal with a row of atoms shown in Figure 2.2.

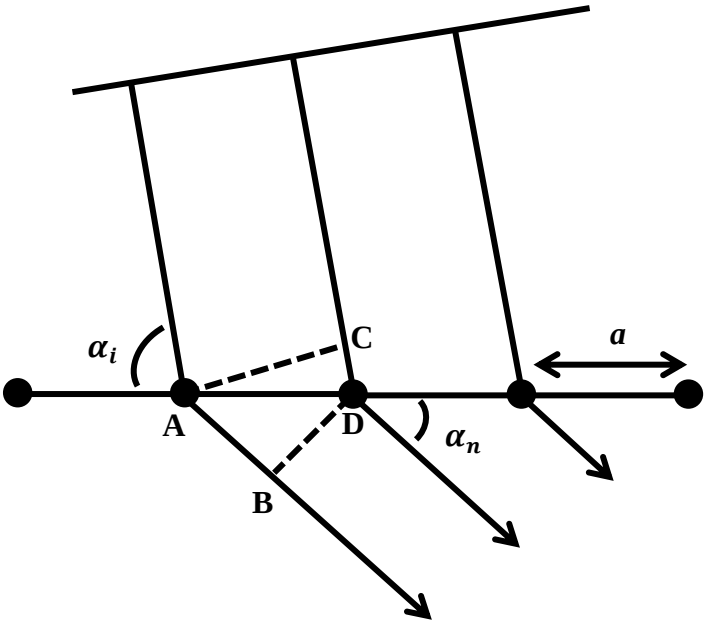

Figure 2.2: Laue scattering of monochromatic radiation by a one-dimensional lattice

Three parallel monochromatic X-ray beams hit a row of atoms in a 1D crystalline lattice with an angle α_i. The total path difference between the first two beams is AB – CD. To observe a diffracted wave of high intensity (the interference between the scattered beams is constructive) at the angle α_n, the difference AB – CD must equal to an integer number (n) of the wavelengths (λ):

$$AB - CD = a(\cos\alpha_n - \cos\alpha_i) = n\lambda \tag{2.2}$$

In a real three-dimensional crystal system, three Laue equations can be defined, which correspond to the rows of atoms along orthogonal x, y, and z-axes. All of them must be satisfied simultaneously for constructive interference:

$$b(\cos\beta_n - \cos\beta_i) = n_y\lambda \tag{2.3}$$

$$c(\cos\gamma_n - \cos\gamma_i) = n_z\lambda \tag{2.4}$$

The calculation of Laue equations requires the determination of three lattice spacings, six diffracted and incident angles and three integers, which limits their practical use in crystallography. Bragg suggested an alternative method to predict the diffracted beam with much less information. Due to the periodically ordered crystalline in a solid material, it is reasonable to describe the whole structure as a series of planes with an equal interplanar distance. These sets of reflecting planes are defined by the Miller indices *h k l*, which intersect the edges of the unit cell *a*/*h*, *b*/*k* and *c*/*l*, respectively. As the X-ray beams hit the surface at an angle θ, some of the beams are diffracted away from the material at the same angle. The rest of the beams will go into the material and part of them can be diffracted again by the second plane of atoms at the same angle θ. This process will be repeated on many planes in the crystal, as shown in Figure 2.3. The X-ray beams actually travel different pathlengths both before and after the scattering on various planes. For constructive interference to occur the beams that reach the detector must be in phase, therefore the path length difference must be a whole number of wavelengths. In the figure below, the difference between path lengths (AB+BC), the incident angle of the beam (θ), the *d*-spacing between the adjacent planes and the wavelength of X-rays can be related by Bragg's Law, which was discovered by W. H. Bragg and his son, W. L. Bragg in 1912:[49]

$$(AB + BC) = 2d_{hkl} \sin\theta = n\lambda \tag{2.5}$$

As there are many different sets of planes in the crystal lattice, there are many opportunities to satisfy Bragg's Law for the same crystal (but the condition is really quite stringent and means that diffracted intensity is only produced in a few special directions). In the diffraction pattern, each reflection occurs when the angle made by a set of planes to the X-ray beam direction (θ) satisfies Bragg's law.

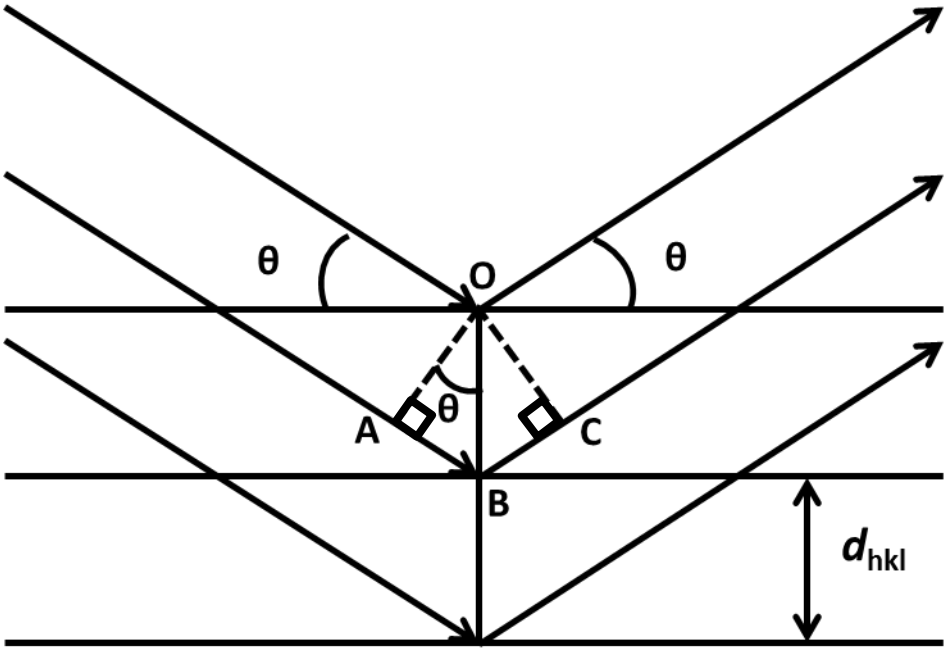

Figure 2.3: Bragg diffraction from the Miller planes in one dimension

The measurement of an X-ray diffraction pattern gives the intensity of the diffracted beams as a function of 2θ, which provides information about the regular arrangement of atoms in the crystal structure. The *d*-spacing of the (*hkl*) reflection can be related to unit cell parameters using Bragg's Law and thus if one can assign (*hkl*) values to the measured peaks, the unit cell parameters can be determined. This process is called indexing. Additionally, the presence of further translational symmetry within the unit cell leads to the systematic absences of certain reflections, which is then used to determine the lattice type of the crystal, and obtain possible space groups. The intensities of the Bragg reflections in the diffraction pattern are related to the structure factor F_{hkl}:

$$I_{hkl} \propto |F_{hkl}|^2 \tag{2.6}$$

The structure factor for a peak (*hkl*), F_{hkl}, is the resultant of the waves scattered by all of the atoms in the unit cell in the $2\theta_{hkl}$ direction, which can be defined:

$$F_{hkl} = \sum_{n=1}^{N} f_n(\theta)\,[\cos 2\pi\,(hx_n + ky_n + lz_n)]q +$$

$$i\sum_{n=1}^{N} f_n(\theta)\,[\sin 2\pi\,(hx_n + ky_n + lz_n)]q \qquad (2.7)$$

where *N* is the number of atoms in the unit cell, $f_n(\theta)$ is the atomic scattering factor of atom n, x_n, y_n, z_n are the Cartesian coordinates of atom *n* in the unit cell and q is the Debye-Waller term. The Debye-Waller factor q indicates the temperature effect on the intensities of the diffraction pattern. As the temperature rises, the atoms are not stationary and have increased displacement from their average positions. This can also lead to a dispersion of electron density in the atoms, resulting in a fall of intensities of the diffraction pattern with θ as destructive interference increases due to the greater phase difference between scattered X-ray beams. The Debye-Waller factor for isotropic thermal motion, q_{iso}, can be given by:

$$q_{iso} = \exp\left[\frac{-8\pi^2 U_{iso} sin^2(\theta)}{\lambda^2}\right] \qquad (2.8)$$

where U_{iso} is the experimentally determined isotropic temperature factor. *eqn* 2.8 can also be represented below with $B_{iso} = 8\pi^2 U_{iso}$.

$$q_{iso} = \exp\left[\frac{-B_{iso} sin^2(\theta)}{\lambda^2}\right] \qquad (2.9)$$

The atomic scattering factor is dependent on the angle of scattering (2θ) and the atomic number, *Z*:

$$f_n(\theta) \propto \frac{Z}{2}(1 + \cos 2\theta) \qquad (2.10)$$

The proportional relationship between Z and $f_n(\theta)$ makes it hard to obtain useful information for the lighter atoms since the small number of electrons around light atoms

scatter X-ray beams weakly. Furthermore, for the atoms with similar atomic numbers, it will be difficult to distinguish between them using X-ray diffraction. This is particularly relevant to the investigation of the Cr/Mn crystallographic sites discussed in chapter 4. *Eqn* 2.10 also shows the angular dependence of the atomic scattering factor, where the reduced intensity of the scattering from an atom is observed at high scattering angles 2θ. This is due to the similar size of the electron cloud within the atom compared to the wavelength of X-rays. The X-ray beams can travel different path lengths after scattering from slightly different regions of the same atom, which results in the destructive interference with reduced intensity as scattering angle 2θ increases.

In order to investigate the details of the structural parameters of a crystal, one can apply the structure factors in *eqn* 2.7 to obtain the exact atom locations. However, F_{hkl} is a complex number, composing of both amplitude and phase, and only the amplitude can be measured from the intensities of reflections in the diffraction pattern (see *eqn* 2.6). Thus there is not enough information to calculate F_{hkl} and this is called phase problem. Several computational techniques such as direct methods[50, 51], Patterson method[52] and charge-flipping[53] have been designed to solve this problem.

2.2.3 Powder X-ray diffraction

A powder sample of a single material consists of a large number of randomly orientated crystallites, from which a number of crystallites at the correct orientation will satisfy Bragg's Law to give a cone of diffracted X-rays (this will only be true for scattering angles where Bragg's law can be satisfied for one of the *hkl* reflections, but at most angles there will be no intensity in the diffraction pattern). These cones can intersect a flat detector as circles, known as Debye-Scherrer cones, as shown in Figure 2.4.

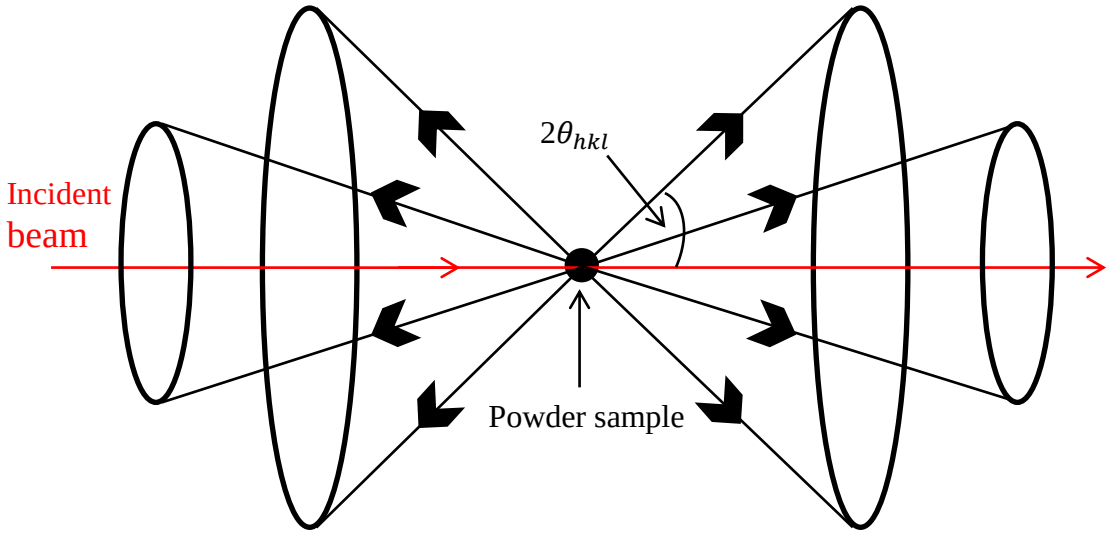

Figure 2.4: Debye-Scherrer cones of X-ray diffraction of a powder sample

In the PXRD experiment, these cones are intercepted by the detector of X-ray diffractometer, giving a one-dimensional diffraction pattern with the diffracted intensity as a function of the scattering angle 2θ. The reflections with identical *d*-spacing but different (*hkl*) values are coincident and they will overlap with each other to contribute intensity to the same peak. Thus the intensity for powder X-ray diffraction also needs a multiplicity term to represent the symmetry-equivalent reflections. Furthermore, the scattered reflections with similar *d*-spacings may also overlap partially because of the finite width of peaks, making it difficult to deconvolve the intensities of specific reflections. The partial overlap of the scattered reflections will be more common in the crystals with low symmetry, where there are more reflections.

The peak overlap, as well as the phase problem, often makes the solution of the crystal structure from PXRD data difficult. However, powder X-ray diffraction is still one of the most powerful techniques in the laboratory, which is used as a fingerprinting tool to examine the purity of product with the comparison of the diffraction patterns collected on the known compounds from the ICSD database. In addition, the increasing availability of synchrotron

techniques and better lab diffractometers, together with the implementation of computational methods such as charge flipping, allow the easier solution of crystal structures since the higher resolution reduces partial peak overlap and the higher signal to noise ratio means that small reflections become visible. The application of Rietveld refinement (see section 2.2.10) enables accurate refinement of the crystal structure.

2.2.4 Powder neutron diffraction

Neutrons interact with the nucleus via the short-range strong nuclear force. They have a wavelength that can be formalised via the de Broglie relationship:

$$\lambda = \frac{h}{p} = \frac{h}{m_n v} \tag{2.11}$$

where h is Planck's constant (= 6.626×10^{-34} Js), p is momentum, m_n is the mass of the neutron (=1.675×10^{-27} kg) and v is the velocity of the neutron. For neutron diffraction, neutron scattering length, b, is used in the equation for the structure factor (*eqn* 2.7). The nucleus acts as a point scatterer (unlike the electron cloud in X-ray scattering), which has negligible size compared to the wavelength of neutrons. Therefore, the scattering length b is independent of scattering angle and information at shorter d-spacings can be measured with a high signal-to-noise ratio in a neutron experiment. Moreover, the scattering length is a property of the nucleus, varying randomly with atomic number, and for a given element, its isotopes usually have different neutron scattering lengths. This can be used to distinguish different isotopes or atoms with very similar electron counts, which is very helpful in the investigation of mixed transition metal compounds (e.g. the Cr/Mn oxypnictides discussed in chapter 4). Neutrons can also be used to probe the light elements (which do not make a significant contribution to X-ray diffraction), as the heavy elements do not scatter on average

very much more than lighter ones. Table 2.1 lists the values for the neutron scattering lengths of a few atoms together with their atomic numbers, which are mostly from the compounds studied in this thesis.

Element (*Z*)	Scattering length *b* / fm	Element (*Z*)	Scattering length *b* / fm
H	-3.7390	Cr	3.635
D	6.671	Mn	-3.73
Sr	7.02	Fe	9.45
Ba	5.07	Cu	7.718
O	5.803	Se	7.970
As	6.58	S	2.847

Table 2.1: Neutron scattering lengths with their atomic numbers for most elements used in this thesis, values were taken from the National Institute of Standards and Technology (NIST)[54]

A further important feature of neutrons is that the spin of the neutron may interact with the spin of any unpaired electrons of an atom, which leads to so-called magnetic scattering. Neutrons can be diffracted by the magnetic lattice of a material with magnetic ordering and the intensity of the diffracted beam of neutrons is proportional to the square of the magnitude of the ordered moment. This interaction can give a second diffraction pattern superimposed on the nuclear scattering pattern with comparable intensities. Similar to X-rays, the magnetic scattering form factor is dependent on the scattering angle, where the intensities of peaks fall off fast with increased 2θ. This is because the neutrons are scattered by the outermost unpaired electrons.

The magnetic peaks may coincide with the nuclear peaks, or they may appear in new positions depending on the periodicity of the magnetic structure. Further analysis and refinement of the magnetic structure were performed by Rietveld refinement using Topas

Academic Version 5[55] in conjunction with the web-based software ISODISTORT [56] to determine the orientation and magnitude of ordered magnetic moments.

2.2.5 Laboratory powder X-ray diffractometers

The in-house PXRD measurements described in this thesis were performed on a daily basis by using three laboratory diffractometers with the monochromatic X-ray radiation ($K_{\alpha 1}$) on both X'pert and Empyrean diffractometers and a mixture of $K_{\alpha 1}$ and $K_{\alpha 2}$ radiation on the Bruker diffractometer. For these diffractometers, a tungsten filament is heated to produce electrons which are then accelerated under vacuum by a voltage of 40 kV towards a Cu target (this is also called the anode). The incident electron beam is sufficiently energetic to ionise the 1*s* electrons, which are ejected from Cu producing core holes. These core holes are then filled by the electrons from higher-energy orbitals and thus the energy loss results in the emission of X-rays with characteristic λ. When the transition is between the *L* and *K* shells, the X-ray emission is called K_{α} and when the transition is between the *M* and *K* shells, the spectrum is called K_{β}. The transition energy for β is bigger than α (i.e. $\Delta E_{\beta} > \Delta E_{\alpha}$), thus $\lambda_{\beta} < \lambda_{\alpha}$. Figure 2.5 shows the example of the production of X-rays with the empty 1*s* orbital occupied by the electrons from *M*-shell electrons.

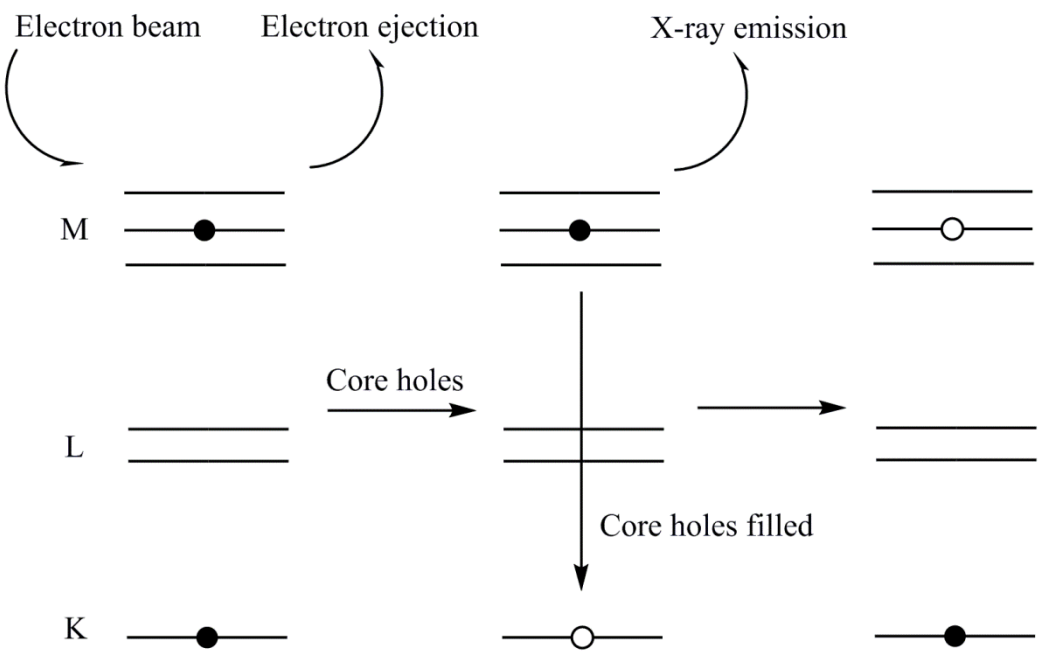

Figure 2.5: Schematic of the process of X-ray emission

In the copper X-ray spectrum, the intensity of the K_α radiation is approximately 5 times bigger than that of K_β and hence the K_α is more frequently selected for use. At higher resolution the K_α transition is seen to be a doublet ($K_{\alpha1}$ and $K_{\alpha2}$) due to spin-orbit coupling, giving two different spin states ($^2P_{3/2}$ and $^2P_{1/2}$) of the electrons in the 2*p* orbital. The intensity of $K_{\alpha1}$ and $K_{\alpha2}$ transitions are in a ratio of 2:1 and their wavelengths are 1.54051 Å ($K_{\alpha1}$) and 1.54433 Å ($K_{\alpha2}$). In order to have the monochromatic radiation from Cu X-ray spectrum (a single X-ray wavelength), a nickel filter with an appropriate thickness can sometimes be used to reduce the intensity of K_β X-rays (energy-discriminating detectors are also used in the current diffractometers). A monochromator crystal can also be used in the path of the incident beam to isolate just the $K_{\alpha1}$ radiation.

All the in-house diffractometers used in this thesis have the Bragg-Brentano reflection geometry, where the divergent beam can be focussed at a fixed radius from the sample position. Figure 2.6 shows that the position of the incident beam is fixed and the sample

holder and detector are rotated by θ and 2θ respectively. Another common setup is to fix the sample in the horizontal position and rotate the X-ray source and detector by - θ and θ.

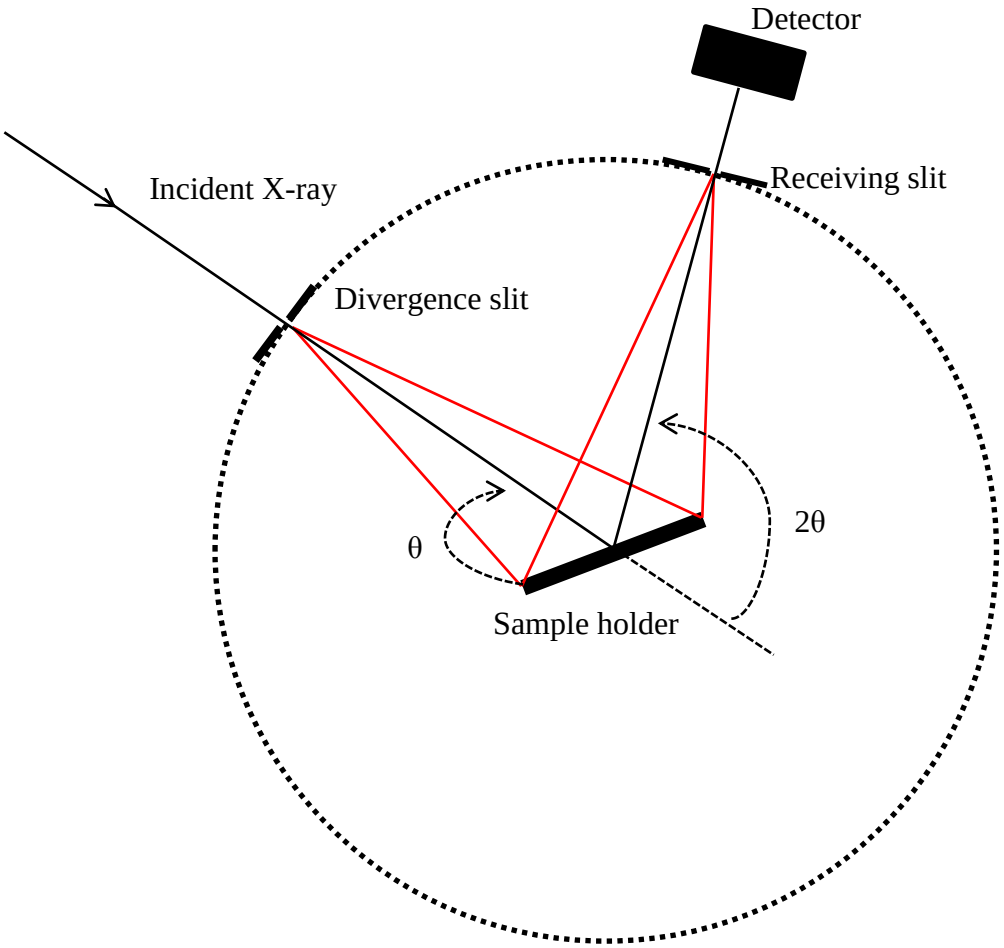

Figure 2.6: Schematic of the Bragg-Brentano geometry with the X-ray source fixed

2.2.6.1 PANalytical X'pert Diffractometer

The PANalytical X'pert diffractometer has high resolution and intensity to collect high-quality lab PXRD for checking the purity of phases and analysing the structures and lattice parameters before further measurements are performed on I11(synchrotron). The Bragg-Brentano reflection geometry is applied for PANalytical X'pert with a setup using a fixed X-ray source (I = 40 mA and V = 45 kV) and a rotatable sample holder and detector. A germanium crystal (111) monochromator is also used to select only the Cu $K_{\alpha 1}$ radiation,

which improves the resolution and peak shape collected on this diffractometer. Air-stable samples are placed on a very lightly greased silicon wafer that is cut along the (110) direction. The sample is then mounted on a spinner-plate stage, rotating at 60 rpm to improve the powder average. For air-sensitive compounds, the samples are mounted on a flat stage using the air-tight sample "cell".

2.2.6.2 PANalytical Empyrean diffractometer

The PANalytical Empyrean diffractometer used in the laboratory is a relatively new model by comparison with the X'pert diffractometer. Similar to the X'pert, the Bragg-Brentano reflection geometry is utilised (with a fixed X-ray source) and a germanium crystal (111) monochromator in the path of incident beam eliminates the Cu $K_{\alpha 2}$ radiation from the X-ray source. All samples are mounted in the same way used in that of X'pert diffractometer.

2.2.6.3 Bruker D8 Advance Eco diffractometer

The Bruker D8 Advance Eco diffractometer also uses Bragg-Brentano geometry, but with a setup where the sample position is fixed and the X-ray source and detector are rotated. The incident X-ray is not monochromated, with both $K_{\alpha 1}$ and $K_{\alpha 2}$ radiation, reducing the resolution in this instrument. However, the relatively increased intensity of the X-ray and a position-sensitive detector capable of measuring simultaneously over a 2θ range of 3° allows reasonable diffraction patterns to be collected in a short time (25 mins) with a good signal-to-noise ratio to assess the purity of product phases.

2.2.6 Synchrotron powder X-ray diffraction

Synchrotron radiation is a very intense electromagnetic radiation that is generated by the acceleration of electron particles in the magnetic fields. A synchrotron source is typically comprised of 5 main components (see Figure 2.7): An electron gun, a linear accelerator (*linac*), a booster synchrotron, a large storage ring and beamlines. First, the electron gun produces low-energy electrons by heating a cathode with a high voltage under the vacuum. After this, some electrons have sufficient thermal energy (keV) to escape by a process known as thermionic emission. Those electrons are then fed into the linear accelerator (*linac*) and accelerated to a range of MeV. Before the electrons go to the storage ring, a small booster synchrotron is used to fill the energy gap between the output-MeV range of the linac and the input-GeV range required of the storage ring. The storage ring contains both straight and curved sections to make electrons circulate inside the ring (e.g. 48 straight sections together with 48 bending magnets giving a ring of 560 m at Diamond Light Source), where the synchrotron radiation is produced.

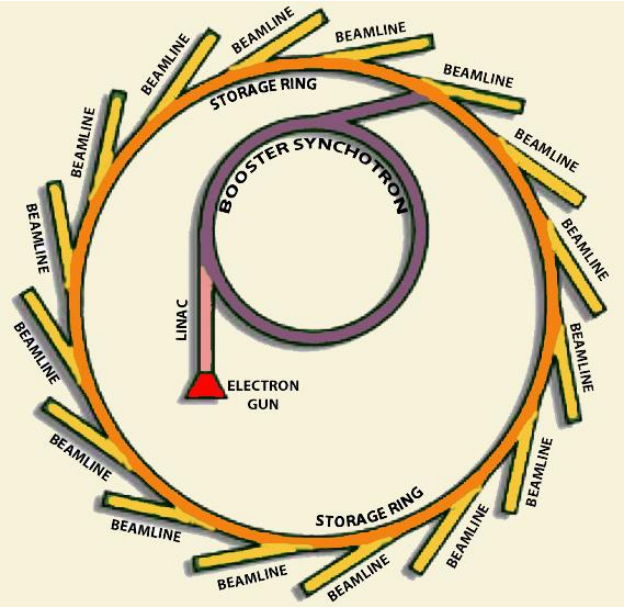

Figure 2.7: Schematic of a synchrotron[57]

The electrons injected in the storage ring are in discrete pulses and they are distributed as bunches inside the whole ring. A radio-frequency cavity (kicker magnets) is used in the storage ring (Figure 2.8), in which oscillating electromagnetic fields can replenish the energy lost to the electron bunches as circulating electrons give off synchrotron radiation. Furthermore, the electron bunches will also slowly decay with time because of the collisions between the electrons and other molecules even under very high vacuum (< 10^{-10} mbar), and thus the storage ring needs to be refilled about every 12-24 hours (by comparison, modern synchrotrons have a continuous filling system) to provide a stable radiation flux.

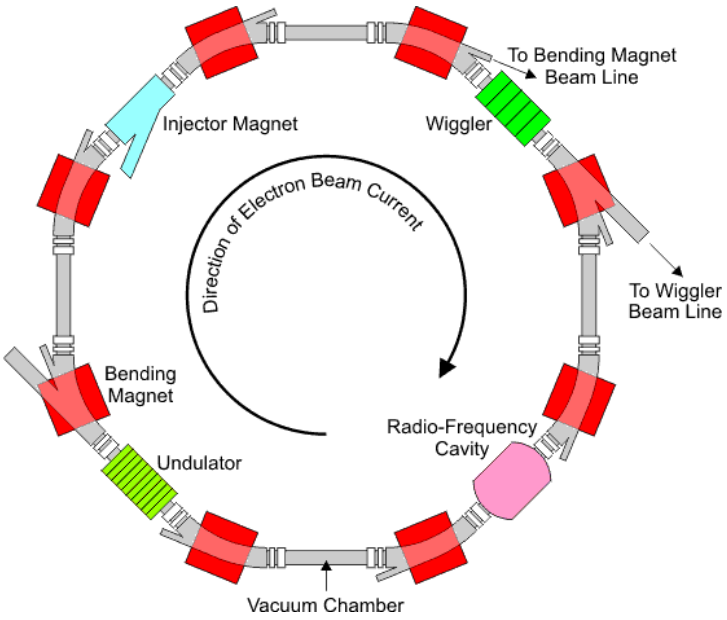

Figure 2.8: Schematic of a typical storage ring[58]

Synchrotron radiation can be generated inside the storage ring using two types of magnets: bending magnets and insertion devices (Figure 2.8). The bending magnets force the electron beam to follow the curve and the deflection of the electron path gives the emission of radiation. For the insertion devices (e.g. Diamond Light Source), two magnets wigglers and undulators are equipped in the straight sections in the storage ring to give off synchrotron

radiation. Electron beams superimpose on each other in the wigglers to produce harder X-rays (shorter wavelengths) and their intensities can increase with the number of bends. An undulator consists of about 20-30 alternating low-field magnets with individual radiation emitted from each magnet. The very intense beam can be generated at a certain wavelength if the radiation emissions can constructively overlap with each other. Figure 2.9 shows the wiggler and undulator used in the synchrotron source.

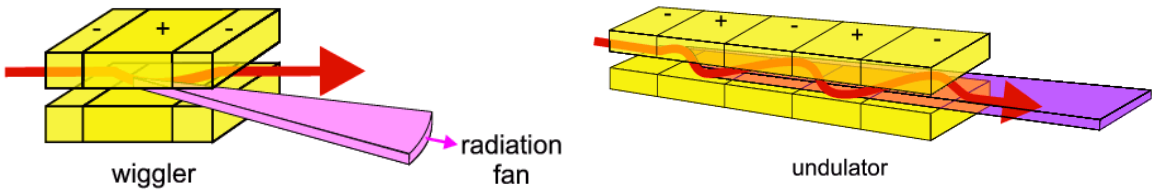

Figure 2.9: Schematic of a wiggler and an undulator[59]

The emitted synchrotron radiation is finally directed to the individual beamlines, which serve as radiation sources for different types of apparatus (e.g. XRD and EXAFS). The monochromators and filters are often used as most techniques require monochromatic radiation or narrow bandwidth.

Synchrotron radiation has several unique features in comparison with the laboratory sources: it has very high intensity over a broad range of wavelengths, which enables the study of smaller samples, weaker phenomena and faster experiments. It also possesses good tunability, a certain wavelength of interest can be selected by choice of monochromators and filters. Moreover, the synchrotron beam is highly collimated with narrow angular divergence.

In this thesis, the synchrotron X-ray powder diffraction data were collected on I11 at the Diamond Light Source (Diamond), Harwell Science and Innovation Campus, UK (3 GeV storage ring).

2.2.6.1 I11 (DIAMOND)

I11 is a high-resolution powder diffraction beamline at the Diamond Light Source (Diamond).[60] High brightness radiation is generated from in-vacuum undulator in the storage ring with the wavelength in the range of 0.5-2.1 Å (X-ray beam energy is at 6-25 keV). The monochromatic X-ray beam is produced by a double-bounce Si(111) monochromator and harmonic rejection mirrors (filtering high energy harmonic photons), after which the beam is delivered into the centre of the diffractometer in the experimental hutch (Figure 2.10) for measurement.

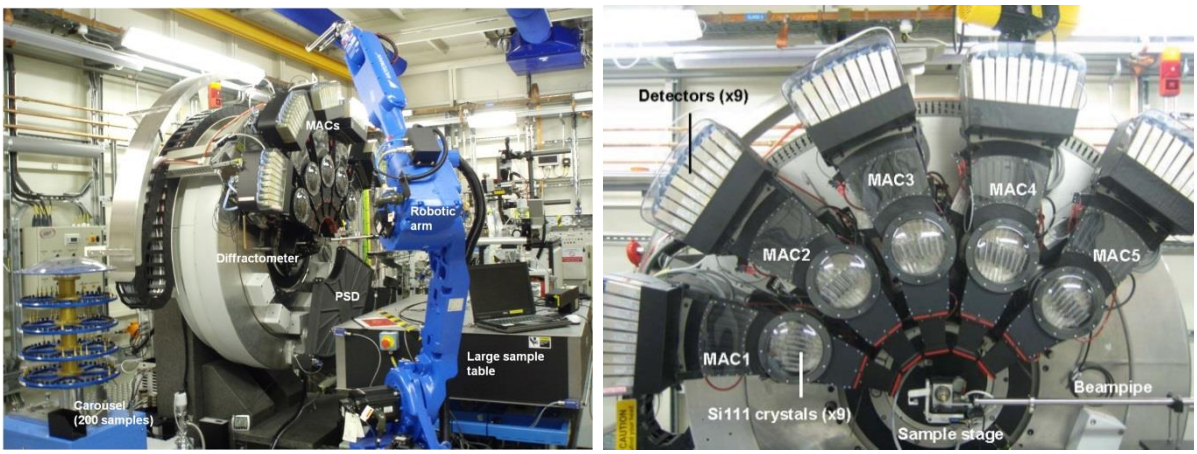

Figure 2.10: Left. a photograph of I11 experimental hutch; Right. MAC arms in the range of 5-150 °, each with 9 Si (111) analyser crystals and 9 individual detectors[60]

I11 beamline has both a Multianalysing Crystal detector (MAC) and a wide-angle position sensitive Mythen detector (PSD). The MAC detector is usually used for high-resolution measurements. It is comprised of 45 Si (111) analyser crystals on 5 separate arms with 9 individual detectors on each arm, as shown in Figure 2.10. A full scan with a 2θ range of 5-150 ° can be achieved by 40 ° of motion with the overlap between adjacent detectors. The results from a total of 45 detectors are then integrated to give the final diffraction pattern. The lower-resolution PSD detector is used for time-resolved (t ~ 1 s for each sample)

measurements, where a 90 ° aperture allows the diffraction patterns to be collected fast with an angular resolution of 0.01 °.

0.5 mm diameter borosilicate capillaries are used to mount the samples on the I11 diffractometer. All the samples are prepared in the in-house glovebox, ground with glass powder in a mass ratio of 1:1 to reduce preferred orientation and X-ray absorption of the sample. The sealed capillaries are then taken into the chemistry laboratory at I11 beamline and glued into a brass holder. The whole assembly (Figure 2.11) is then placed in a carousel and automatically selected for mounting on the rotatable sample stage using a programmable robot arm. Furthermore, several measuring environments are allowed on I11: the sample can be measured in a temperature range of 100 K to 500 K using a nitrogen cryostream; A higher temperature up to 1800 K is available through a furnace or hot-air blower.



Figure 2.11: a photograph of the magnetic brass holder containing the capillary[61]

2.2.7 Neutron powder diffractometers

By contrast to synchrotrons, the production of neutrons for experiments is both expensive and hazardous. There are two main types of neutron sources for diffraction measurements in the world today: steady-state neutron sources and pulsed neutron sources. The steady-state neutron sources involve using the nuclear reactors that generate intense beams of neutrons for research use. The more environmentally-friendly (because large quantities of nuclear waste are not generated) alternative to reactor sources is the pulsed spallation source. Both of them were used in this thesis to perform the neutron powder diffraction measurements.

The PND experiments using reactor neutron source were made on the D2B instrument at the Institut Laue Langevin (ILL) in Grenoble, France. The nuclear reactor utilises the fission reaction of highly-enriched ^{235}U to provide extremely high-intensity neutron beams. To keep the fission reaction going, the neutrons need to be slowed in the moderator using the heavy water D_2O, which then produces a thermal neutron beam with a peak flux at 1.2 Å, a wavelength suitable for solid-state-compounds diffraction. The white neutron beam generated by a nuclear reactor contains a broad range of wavelengths and the beam needs to be monochromated before delivering to the diffraction experiment. The resultant PND pattern is measured as a function of 2θ by non-fixed detectors.

Another way of producing neutrons for diffraction experiments is to use spallation neutron sources. In this thesis, measurements with pulsed neutrons were carried out on OSIRIS, GEM, POLARIS and WISH diffractometers at the ISIS facility at the Rutherford-Appleton Laboratories (RAL). Similar to a synchrotron source, the pulsed neutron source utilises a beam of H^- ions that are first accelerated in a linear accelerator (*linac*) to the energy of 70 MeV. After this, a gold foil is used to strip off the electrons from the H^- ions and the medium-energy proton beam is then further accelerated in the synchrotron ring to 800 MeV, which

is bombarded into a water-cooled tungsten target with a fixed frequency of 50 Hz. The collision of the proton beam with the nuclei of the tungsten atoms gives off intense pulses of high-energy neutrons with a wide range of wavelengths, which are then extracted to experimental beamlines through a neutron moderator (solid hydrogen or solid methane) to slow down the neutrons to the desired range of wavelengths for diffraction studies (Figure 2.12).

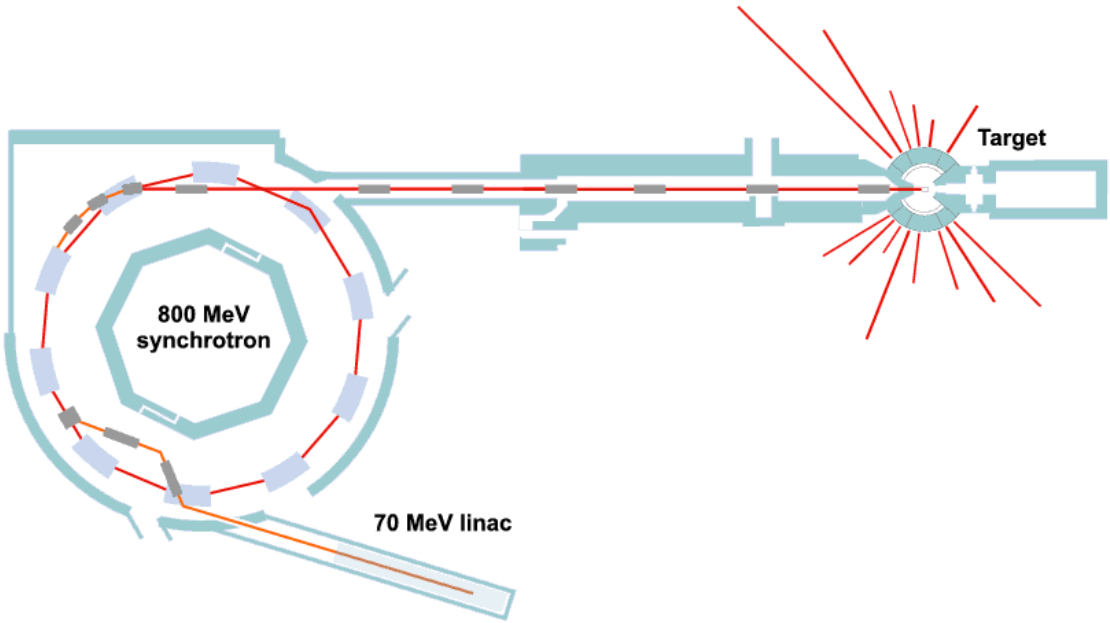

Figure 2.12: Schematic of the generation of neutron beams in a spallation neutron source (ISIS)[62]

The experimental samples at beamlines are measured by the pulsed neutron beam (white) containing dispersive energies, which are then detected by fixed-scattering-angle detectors to give the PND pattern with the intensities as a function of time-of-flight (TOF). In the TOF diffraction experiments, the wavelength of a neutron is related to its velocity via de Broglie equation (see *eqn* 2.11)

The single neutron travels from the moderator to detector with a fixed path length *L* and the time taken for a neutron to reach the detector is the time-of-flight, *t*. The de Broglie equation relates the wavelength of a neutron to its momentum by the relationship:

$$\lambda = \frac{h}{m_n v} = \frac{ht}{m_n L} \tag{2.12}$$

A large number of detectors are usually grouped together as banks to reduce the count time of neutron beams. Each bank gives a characteristic count rate, *d*-spacing range and resolution. As the detectors are fixed at angle 2θ, the neutron time-of-flight is now related to the *d*-spacing of the measured sample via both equation 2.12 and Bragg equation (*eqn*.2.5):

$$\frac{ht}{m_n L} = 2d_{hkl} \sin\theta \tag{2.13}$$

For a given value of path length *L* and the fixed 2θ positions, the values of *d*-spacing are proportional to the time-of-flight.

For nuclear-reactor neutron source (ILL) with a constant wavelength, the shortest measured *d*-spacing can be achieved if the angle of the detector is at $2\theta = 180°$ ($\sin\theta = 1$). Thus the minimum observable *d*-spacing can be calculated as $\lambda/2$ via the Bragg's Law (*eqn*.2.5), which gives a limit for the short-*d*-spacing diffraction experiments. However, for the spallation neutron source (ISIS), a high flux of neutron beams with different short wavelengths can be generated from the moderator, allowing diffractions with very short *d*-spacings to be measured.

There are several factors that can affect the resolution of reflections measured on the TOF diffractometers. The relative uncertainty in *d*-spacing is determined by the equation:[63]

$$\frac{\Delta d}{d} = \left[\left(\frac{\Delta t}{t}\right)^2 + \left(\frac{\Delta L}{L}\right)^2 + (\Delta\theta \cot\theta)^2\right]^{\frac{1}{2}} \quad (2.14)$$

where Δd is the width of a reflection at position *d*, Δt is the uncertainty of time, ΔL is the uncertainty of flight-path and $\Delta\theta$ is the uncertainty of scattering angle. Given the above equation, high *d*-spacing resolution can be achieved by either using a long flight-path or moving the detectors at high scattering angle 2θ, as Δt is approximately constant for a given moderator. The uncertainty in flight-path is a function of the finite size of the moderator, sample and the detector. Increasing the length of the flight-path (time-of-flight of neutron also increased) can reduce the uncertainty in both time and flight-path. The uncertainty in the scattering angle is due to the finite angular widths of the sample and the detector aperture, which can be reduced by increasing the distance between the sample and detector. Moreover, this uncertainty tends to be 0 as 2θ goes to 180 °. Therefore, the detector banks at higher angles would have higher resolution (at ISIS, the HRPD diffractometer is a good example for high-resolution measurement that has a long flight-path (100 m) and a detector with a scattering angle at 168 °). The low-angle banks are used to measure those reflections at higher *d*-spacings, especially for analysing magnetic reflections and superstructure peaks. Some intermediate detector banks are also utilized to give a balance between the resolution and *d*-spacing range to improve statistics. For each detector on the diffractometer at ISIS, the uncertainty in *d* spacing is approximately constant across the whole *d*-spacing range, which reduces the Bragg peak overlap in the diffraction pattern and also gives narrow peaks at low *d*-spacings. The resolution on D2B is however poorer at higher *d*-spacings, although its improved resolution at low *d*-spacings allows structural and magnetic investigations to

be performed simultaneously. Furthermore, the absorption is wavelength dependent so for a single wavelength source it just mimics a displacement parameter, while for the TOF system it needs to be taken into account in the refinements.

At ILL, the D2B diffractometer has a constant wavelength and the resolution is θ-dependent, which can be described by a Caglioti relationship:[64]

$$\sigma^2 = \frac{FWHM^2}{8log_e 2} = Utan^2\theta + Vtan\theta + W \qquad (2.15)$$

where FWHM is the full width at half maximum, and parameters *U*, *V* and *W* are dependent on both instrument and sample. Different to the resolution measured at TOF diffractometers, as *U* is positive and *V* is negative in this equation when θ increases the width of reflections will decrease to a minimum, after which it will increase towards the high angles (low *d*-spacings). The changes of resolution as a function of *d*-spacings for the high resolution (HRPD) and high flux (POLARIS) ToF diffractometers at the pulsed source ISIS and that of the now-retired high resolution diffractometer (D1A) at the ILL reactor source are shown in Figure 2.13.[65]

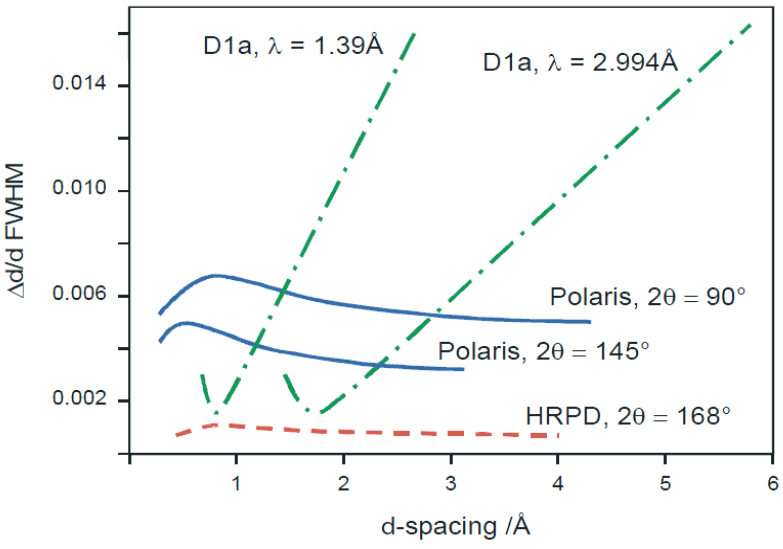

Figure 2.13: The resolution as a function of *d*-spacings for several diffractometers; Taken from ISIS Neutron Training Course booklet 2017[65]

All the neutron samples described in this thesis were placed in airtight vanadium cans with a diameter of 6 or 8 mm due to its weak coherent scattering of neutrons, thus the peaks seen by the PND pattern are from the sample rather than the sample holder. For low-temperature PND measurements, samples were measured in a helium cryostat and the vanadium can was sealed with an indium wire gasket under the argon atmosphere in the glovebox to give the sample an air-tight environment. For those measurements above room temperature, samples were heated in a resistance furnace and the indium wire gasket was not used (It would melt) since the samples measured in this thesis were not sufficiently air sensitive to need one.

2.2.7.1 OSIRIS (ISIS)

OSIRIS is used as a high-resolution, long-wavelength TOF diffractometer at ISIS with a primary instrument flight-path of 34 m. The neutron beams are cooled to 25 K through a liquid hydrogen moderator, generating a large flux of long-wavelength cold neutrons.[66] Neutrons are transported from moderator to sample stage using a curved neutron guide, which only allows the neutrons with a wavelength more than 1.5 Å to go through. By contrast, the beam flux on HRPD is much lower for cold neutrons, but with access to shorter wavelengths since HRPD views the liquid methane moderator at 100 K, giving an intensity maximum around 2Å. The neutron spectrum on OSIRIS makes it particularly useful for magnetic structure determination giving high signal to noise and high resolution at long *d*-spacings.[66]

2.2.7.2 GEM (ISIS)

The General Materials Diffractometer (GEM) is used to study the structure of crystalline powders and amorphous materials with high resolution. The neutron beam is rectangular with a maximum size of 40 mm high and 20 mm wide, which can be changed by using a set of adjustable apertures. GEM is equipped with 7 fixed-angle detector banks at 5-12 °, 13-21 °, 24-45 °, 50-74 °, 79-106 °, 106-114 ° and 142-171 ° respectively, covering a very wide range in scattering angle. The relative count rates of 7 detector banks are collected by measuring the diffraction from a 6 mm diameter rod of vanadium due to its entirely incoherent scattering.[67]

2.2.7.3 POLARIS (ISIS)

POLARIS is a high intensity and medium resolution diffractometer at ISIS. The intense incident neutron flux generated from the H_2O moderator and solid-angle detectors give a high count rate, allowing the PND experiments to be measured with short counting times or very small sample volumes. It is equipped with four separate banks, each having a constant $\Delta d/d$ resolution, at the 2θ ranges of 13-15 °, 28-42 °, 83-97 ° and 130-160 °. A variety of sample environment is accepted at POLARIS for experiments: cryostats, furnaces and pressure cells are available to collect data under non-ambient conditions.[68]

2.2.7.4 WISH (ISIS)

The WISH diffractometer operating at the second target station at ISIS is a long-wavelength diffractometer designed for powder diffraction at long *d*-spacing in magnetic and large unit cell systems, which gives high-resolution data in a *d*-spacing range of 0.7- 17 Å. WISH has an array of 10 position sensitive detector banks with their positions in two semi-cylindrical

annuli around a central sample stage at a radius of 2.2 m. The detectors from each side cover an angular range of 160 ° and the measured data from corresponding angles on the two sides are combined together to improve the signal-to-noise ratio.[69]

2.2.7.5 D2B (ILL)

D2B is a high-intensity powder neutron diffractometer at the ILL. The rotation of a germanium crystal (115) monochromator with various *hkl* planes allows that wavelengths can be easily changed under computer control. A schematic of the set-up of the D2B is shown in Figure 2.14. The high resolution is achieved by having a very high take-off angle (135 °) for the monochromator, which maximises the differentiation between λ of radiation diffracted by *hkl* planes and thus obtains the best monochromation. The two most frequently used wavelengths on D2B are 1.59 and 2.39 Å. The neutron beam with a shorter wavelength is good for the PND measurements with optimum intensity for crystal structural analysis. The longer wavelength is useful to probe the high *d*-spacing peaks generated from magnetic ordering. In this thesis, all the measurements were performed by using a wavelength of 1.59 Å on D2B.

The D2B detector bank is comprised of 128 ^{3}He counting tubes spaced at 1.25 ° interval. This enables the detector to cover an angular range of $5\ ^{o} \leq 2\theta \leq 165\ ^{o}$ and thus measure the *d*-spacing of the sample in a range of 0.8 - 18 Å with a wavelength of neutron beam at 1.59 Å. A pseudo-2D detector allows measurements to be collected in a few hours by using a small sample with only 500 milligrams.[70]

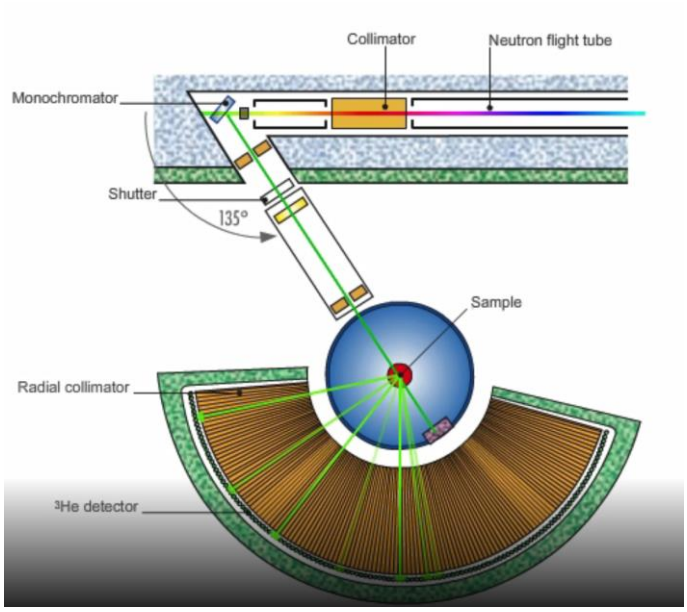

Figure 2.14: Schematic of neutron powder diffractometer D2B with constant wavelength[71]

2.2.8 Rietveld refinement

Refinement is a process where a structural model is refined against diffraction data to obtain a good agreement between the observed and calculated pattern. Before the Rietveld method was published in 1969, attempts were performed at using powder diffraction data to refine structural models. However, due to the relatively poor resolution of early collected powder diffractometer data, the use of the least-squares method was limited until Hugo Rietveld developed the new Rietveld procedure (which is also a least-squares refinement technique).[72, 73] Rietveld realized that the diffraction pattern could be fitted on a point by point basis (rather than peak by peak) using the Gaussian peak-shape function without determining the intensities of individual reflections. The calculated intensity y_{ci} at point *i* in the diffraction pattern can be written as the summation of all the contributions of Bragg reflections within a fixed range:

$$y_{ci} = s \sum_{hkl} L_{hkl} P_{hkl} A |F_{hkl}|^2 \phi(2\theta_i - 2\theta_{hkl}) + y_{bi} \qquad (2.16)$$

Where *s* is the scale factor, L_{hkl} is the Lorentz polarisation factor, P_{hkl} is the preferred orientation function, *A* is the absorption factor, F_{hkl} is the structure factor, ϕ is the reflection profile function and y_{bi} is the background intensity at point *i*. The difference between the calculated intensities *yci* and observed intensities *yi* is then determined using the residual *Sy*:

$$S_{y=\sum_{i=1}^{n} w_i(y_i - y_{ci})^2} \tag{2.17}$$

where y_i is the observed intensity at point *i* and w_i is a weight attributed to each observation, defined by $1/y_i$ so that each point contributes equally to the residual. The least-squares minimisation is then used to refine the above parameters until S_y is minimised. This procedure can be repeated by refining different parameters until the resultant model is no longer improved where the stable solution of the refined structure is obtained. In order to run a successful refinement, the lattice parameters, zero point correction, background and scale factors are usually first refined to have a good match between the calculated model and measured peak positions. The parameters that control the peak intensities can then be refined by introducing the atomic positions, atomic occupancies, thermal displacement parameters, peak functions and absorption factors. The quality of the refinement can be assessed by visually comparing the fit between the calculated and observed diffraction patterns. The statistical parameters (*R*-factors) are also used to numerically evaluate the quality of a refinement. The *R*-structure factor R_F is based on the Bragg intensities of the calculated peaks and it is not sensitive to the full pattern:

$$R_F = \left[\frac{\sum_K \left| I_{K_{obs}} - I_{K_{calc}} \right|}{\sum_K I_{K_{obs}}}\right]^{\frac{1}{2}} \tag{2.18}$$

where $I_{K_{obs}}$ and $I_{K_{calc}}$ are the observed and calculated intensities of the reflection *K*, respectively. R_F is a useful structure factor to check how good the resultant model is for a

product phase without considering the presence of other impurity phases and the influence of background. By contrast, the profile *R*-value R_p and the weighted profile R-value R_{wp} are more commonly used to examine the quality of the fit to the full diffraction pattern:

$$R_p = \frac{\sum_i |y_i - y_{ci}|}{\sum_i y_i} \tag{2.19}$$

$$R_{wp} = \left[\frac{\sum_i w_i (y_i - y_{ci})^2}{\sum_i w_i {y_i}^2}\right]^{\frac{1}{2}} = \left[\frac{S_y}{\sum_i w_i y_i}\right]^2 \tag{2.20}$$

where R_{wp} is the most mathematically meaningful *R*-factor since it contains the residual S_y, the value needed to be minimised in *eqn* 2.17. The final R_{wp} should approach the statistically expected *R*-value R_{exp} :

$$R_{exp} = \left[\frac{N_{obs} - N_{var}}{\sum_i w_i {y_i}^2}\right]^{\frac{1}{2}} \tag{2.21}$$

where N_{obs} and N_{var} are the numbers of observations and refined parameters, respectively. In a common powder diffraction measurement, Nobs is around 2000, which is much bigger than the value of N_{var}. The ration between these *R*-values, R_{wp}/ R_{exp} can also be used as a goodness-of-fit parameter (*gof)* or χ^2:

$$\chi^2 = \left(\frac{R_{wp}}{R_{exp}}\right)^2 \tag{2.22}$$

Generally, the smaller values of these above parameters correspond to the better fit between the calculated and observed data. A good fit is usually obtained if $\chi^2 < 2$, $R_{wp} < 0.05$, although sometimes a too large R_{exp} value may give a misleadingly low value of χ^2 ($\chi^2 < 1$) if the counting time in the diffraction experiment is insufficient or there are too many

variables to refine. On the contrary, a high value of χ^2 can be calculated due to the presence of very small R_{exp} if too many data points are collected in the diffraction pattern or the measuring time is too long. Additionally, an over-fitted background can also give much lower calculated R_{wp} together with low χ^2. Therefore, it is important to assess the quality of the refined model by not only using the numerical *R*-factors but also visually checking the difference between the calculated result and the observed pattern until the fit to the pattern looks good, the *R*-factors are reasonable and the structural model makes chemical sense.

In this thesis, the TOPAS academic version 5 refinement software was used to perform Rietveld refinements on both powder X-ray diffraction and powder neutron diffraction data.[55]

2.2.9 Pawley refinement

Pawley refinement is a structure-independent method where a model with only the parameters of the unit cell (crystal structure is not required) are used to fit a powder diffraction pattern.[74] The procedure of Pawley refinement involves fitting the Bragg reflections in the diffraction pattern by utilising arbitrary intensities, and refining the following parameters: *I*(*hkl*) – the intensity of each reflection with indices *hkl*, the unit cell parameters, the instrumental zero error, and peak-shape functions and background. This method is not used to refine the structure and composition of a solid material; however, it is very helpful when one needs to confirm the space group for a novel compound, by running the Pawley refinement to compare which space group gives the better fit. In this thesis, TOPAS academic version 5 refinement software was also used to perform Pawley methods on PXRD and PND data.

2.2.10 DC SQUID magnetometry

The DC magnetic susceptibility measurements described in this thesis were performed using a Quantum Design MPMS-XL SQUID magnetometer. A SQUID device is a closed ring consisting of two superconductors, which are separated by two thin insulating layers to form two parallel Josephson junctions (see Figure 2.15[75]). When a small current is applied to the ring, Cooper pairs of electrons can tunnel through the insulating junction without resistance. However, if the applied current exceeds the critical current available for tunnelling through the Josephson junctions, the ring can have a non-zero resistance and a voltage is established across the junctions. The critical current of the Josephson junctions is affected by the presence of the external magnetic field and thus an applied magnetic field can be easily measured by detecting the changes in the voltage across the device.[76]

An approximately 30 – 50 mg of sample is placed inside a gelatin capsule, which is then loaded into a plastic straw squeezed with several other empty capsules to ensure the position of the sample is stable. The straw is then connected to the end of a long stick and mounted within an induction coil and magnetised by a helium-cooled superconducting magnet, which can generate a magnetic field in the range of -5 T to +5 T. The vertical translation of the magnetised sample induces a current in the induction coil, which is coupled to the SQUID and therefore an output SQUID voltage can be monitored and it is proportional to the magnetic moment of the measured sample.

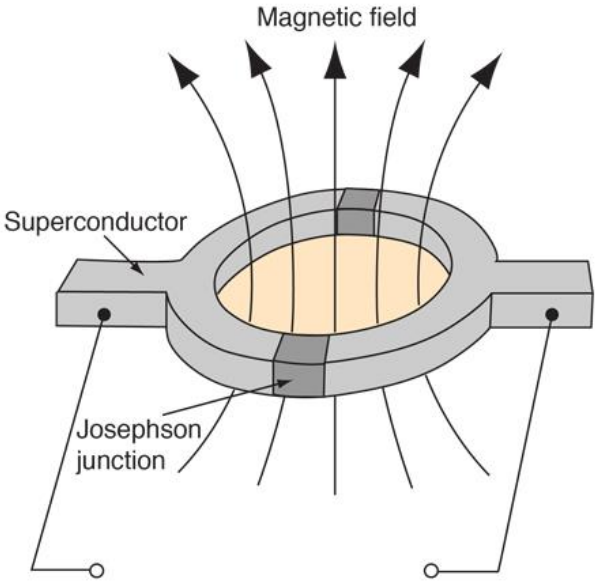

Figure 2.15: Schematic of the experimental set-up for Josephson junctions[75]

When an external magnetic field *H* is applied to a compound, the response of the material is its magnetic induction *B*. The relationship between *B* and *H* can be expressed:

$$B = H + 4\pi M \tag{2.23}$$

where *M* is the magnetization of the material. Apart from the magnetization and magnetic induction, the properties of a material can also be defined by the magnetic susceptibility. The molar susceptibility χ_{mol} is defined by:

$$\chi_{mol} = \frac{m}{B_0 n} \tag{2.24}$$

where B_0 is the applied magnetic flux density in gauss and n is the number of moles. More details on the units used in magnetism are shown in Appendix A. The sample measured on a SQUID magnetometer is kept under a helium atmosphere and can be cooled from 330 K to 2 K. Therefore, the magnetisation of a compound can be measured as a function of both temperature and applied field.

A linear magnetisation curve was usually observed in the *M vs H* measurement at 300 K, indicating the absence of room temperature ferromagnetic impurities. The magnetisation was measured as a function of temperature in a fixed applied field at 0.01T in this thesis. The sample was first cooled without an applied field (zero-field cooled (ZFC)) and then it was cooled in the applied field (field-cooled (FC)). Differences between the zfc and fc curves provided additional information about the magnetic behaviour of the sample. A hysteresis loop was typically also performed with an applied field range of -5 T to +5 T. This was usually measured at 5 K with field cooling in the 5T field to check the appearance of the spin-glass behaviour. The spin-glass magnetisation isotherm will show a ferromagnet-like hysteresis, but with the curve displaced from the origin and often the isotherm will not close up. Furthermore, below the spin-glass freezing temperature T_g, the magnetic susceptibility in an applied field will not coincide with the measurement in zero applied field and a divergence between the fc and zfc susceptibility curves is often observed below T_g.

Chapter 3

Synthesis and characterisation of $Ba_2CrO_2Cr_2As_2$

3.1 Introduction

In 2015, a new layered oxypnictide, $Sr_2CrO_2Cr_2As_2$, belonging to the family of compounds with the $Sr_2Mn_3As_2O_2$ structure type was reported for the first time.[77] This was also the first reported chromium-containing oxypnictide with a layered structure. Jiang *et al.* observed a magnetic transition at approximately 291 K, which they attributed to antiferromagnetic ordering in the Cr_2As_2 layers. Furthermore, they predicted the magnetic transition temperature of the oxide-layer Cr(1) sublattice to be relatively low, as in the manganese analogue, to which they attributed a broad transition at around 38 K in the magnetic susceptibility data. They also suggested that neutron diffraction would help to clarify these preliminary conclusions. Our group has recently synthesized several phase-pure samples of $Sr_2CrO_2Cr_2As_2$ allowing variable temperature neutron powder diffraction studies to be performed, which confirms that the qualitative predictions as to temperature in Jiang's work were correct, but their assignment of features in the susceptibility to the main magnetic ordering transitions were not. The strong magnetic interactions mean that the transition temperatures are much higher than those in the Mn analogue. PND data reveals an antiferromagnetic ordering of the Cr ions in the Cr_2As_2 layers below 600 K with the moments directed along the *c* axis in the magnetic unit cell. As the temperature decreases to about 330

K, a long-range antiferromagnetic ordering of the Cr ions in the CrO_2 plane is observed with the moments oriented with their main component in the *ab*-plane. A spin reorientation transition (Figure 3.1) is also observed around room temperature in which the moments of Cr ions in the Cr_2As_2 layers reorient to align in the ab-plane, while the Cr moments in the CrO_2 plane reorient to lie along the *c* axis. This behaviour has also been reported recently by Liu *et al.*, although without any rationalisation.[78]

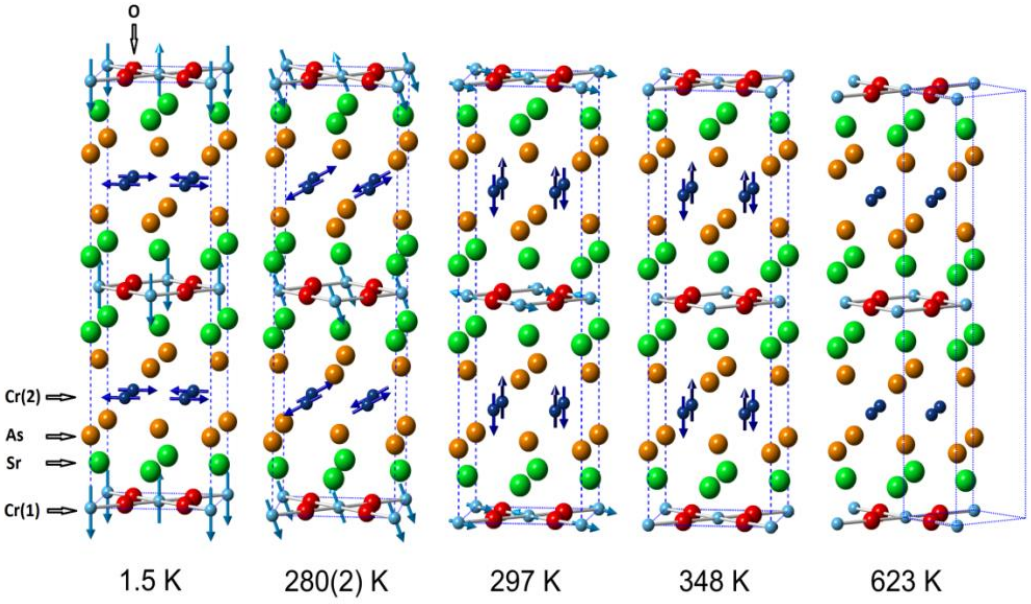

Figure 3.1: Magnetic unit cells of $Sr_2CrO_2Cr_2As_2$ at different temperatures, showing the magnitude and direction of magnetic moments for the two chromium sublattices; Sr, O and As atoms are represented in the models by green, red and orange balls, respectively. Cr(1) and Cr(2) atoms are represented by blue balls

In this chapter, the successful synthesis of $Ba_2CrO_2Cr_2As_2$ is reported, which is isostructural with its Sr analogue. However, the different structural parameters of this compound when the barium cation is incorporated means that there will be significant differences in the exchange interactions and the separation of the two sublattices is larger, which can then make the nature of the magnetic ordering different from the Sr case. The detailed analysis to compare its behaviour with the Sr analogue and other related compounds is discussed in this chapter.

3.2 Synthesis and characterisation of $Ba_2CrO_2Cr_2As_2$

Synthesis of phase-pure $Ba_2CrO_2Cr_2As_2$ was difficult to achieve, with many attempts yielding a large number of impurity phases such as $BaCr_2As_2$ and various chromium arsenide phases. Thus many different reaction conditions were tried in an effort to optimise the synthesis.

A polycrystalline sample of $Ba_2CrO_2Cr_2As_2$ was prepared by solid-state-reaction techniques using BaO (Aldrich, 99.99 %), Cr (Alfa, 99.95 %) and As (Alfa, 99 %) as starting materials in stoichiometric amounts. A pellet of the ground mixtures of the starting materials was placed in an Al_2O_3 crucible which was then sealed inside a pre-dried evacuated silica tube (see section 2.1.1). Firstly, the sample was heated to 800 °C for 24 hours at a slow rate of 2 °C/min, in which the As was reacted completely before it reached a high vapour pressure in the tube (the boiling point of As is 613 °C).[79] The mixture was then reground for homogenization, pressed into a pellet and sintered at 1100 °C for another 20 hours (10 °C/min) followed by quenching the reaction in an ice bath. However, the reacted sample only consisted partially of the $Ba_2CrO_2Cr_2As_2$ phase, with a large amount of $BaCr_2As_2$ and some other unidentified impurity phases (Figure 3.2). Further reheats of the product at 1100 °C did not improve the purity but made all the $Ba_2CrO_2Cr_2As_2$ phase decompose to $BaCr_2As_2$ and other oxide products (Figure 3.3).

Attempts to increase purity by changing the temperature of the reheating stage were made. The samples were reheated to 900, 1000 and 1100 °C (10 °C/min) for 20 hours. The amount of the impurity phase ($BaCr_2As_2$) in the product tended to decrease from 900 °C to 1100 °C while the amount of the $Ba_2CrO_2Cr_2As_2$ target phase increased at the same time. In order to see how the purity improved at a higher temperature, another sample was sintered at the

reheating stage for 20 hours at 1200 °C (10 °C/min). However, this didn't give the expected purer result, leading instead to the decomposition of the product phase, notably to Cr_2As.

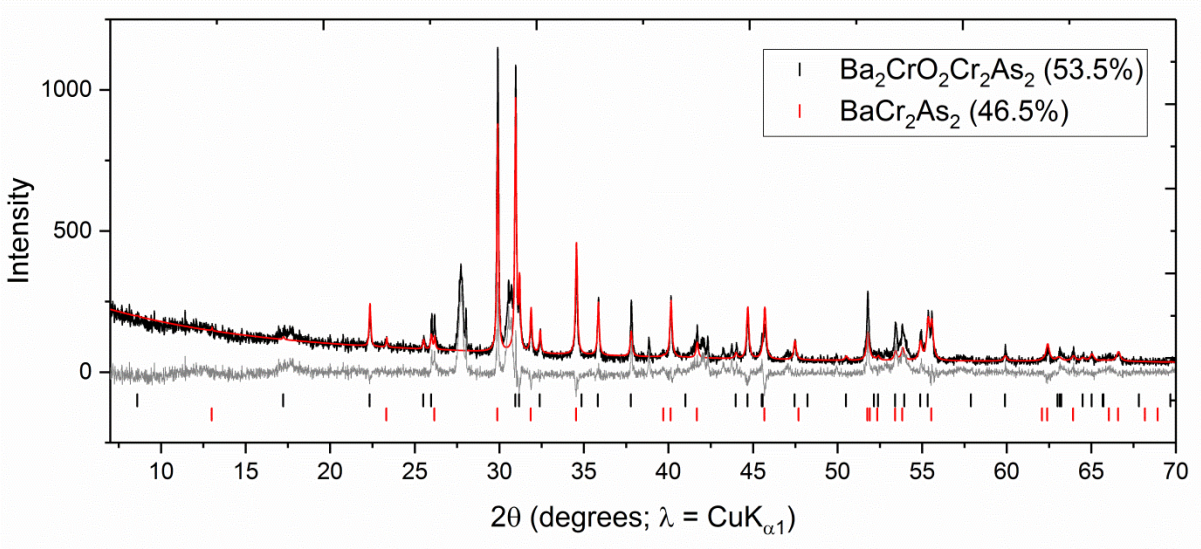

Figure 3.2: Rietveld plot of $Ba_2CrO_2Cr_2As_2$ (XX031B) measured at RT using the PANalytical X'Pert Pro diffractometer

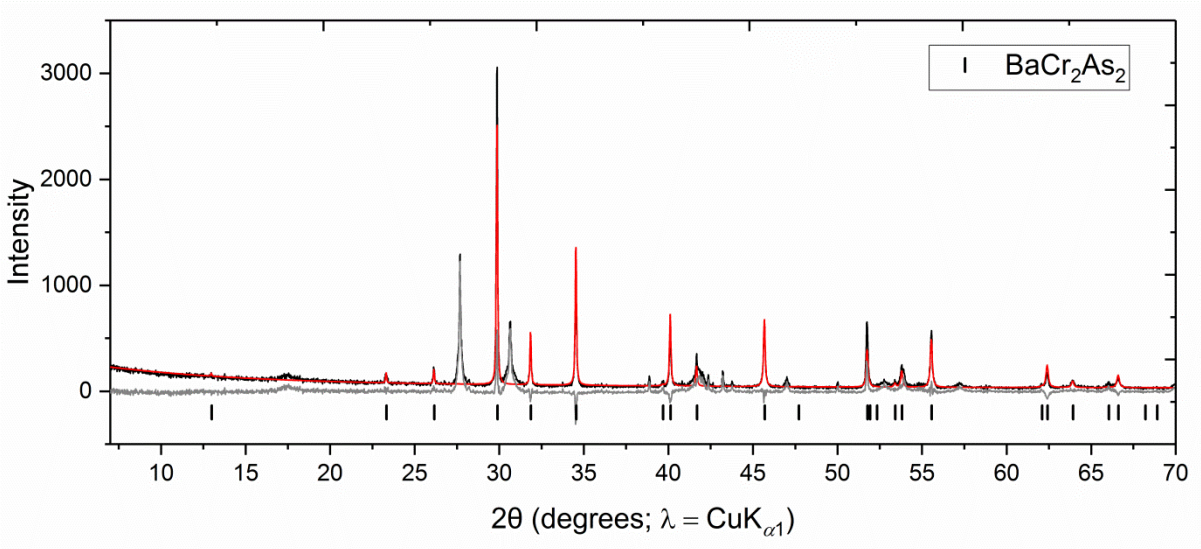

Figure 3.3: Rietveld plot of $Ba_2CrO_2Cr_2As_2$ (XX031C) measured at RT using the PANalytical X'Pert Pro diffractometer

Optimizing the reaction time of the reheating step was then attempted in this work. The samples were reheated to 1100 °C and 1200 °C (10 °C/min) for 1 h, 3 h, 5 h, 10 h, 24 h and 4 days respectively. The samples sintered at 1100 °C had a large number of impurities and very little of the $Ba_2CrO_2Cr_2As_2$ target phases. For the reactions at 1200 °C, relatively pure

$Ba_2CrO_2Cr_2As_2$ samples (about 90 % by mass) were obtained after reheating for 3 and 5 hours, with a small amount of $BaCr_2As_2$ and Cr_2As included as minor impurity phases. There was no obvious $Ba_2CrO_2Cr_2As_2$ phase after a one-hour-heating reaction, in which the $BaCr_2As_2$ was the main product and some other unidentified impurity phases were also observed. Furthermore, the $Ba_2CrO_2Cr_2As_2$ phases did not survive if the samples were heated to 1200 °C for a long time (10 h, 24 h and 4 days), with a trend towards forming different types of chromium arsenides as the reaction time was increased. Therefore, the time of the reheating stage played a very important role in this synthesis and the short-duration reactions gave the most promising results.

Flux methods which worked very well in the synthesis of $Sr_2CrO_2Cr_2As_2$ were also employed for this synthesis. This involved grinding the stoichiometric amount of the target compound with an equimolar ratio of CsI (Aldrich, 99.999 %) inside an Ar-filled glove box. The powder mixture (it was not necessary to press a pellet) was then heated at 1100 °C for 48 hours at a rate of 2 °C/min, in which the slow heating rate avoided the high vapour pressure of As in a sealed tube. Removal of the flux by washing with distilled water and acetone was performed under inert conditions using the Schlenk line (although later $Ba_2CrO_2Cr_2As_2$ proved not to be air sensitive, all samples were treated as air-sensitive at all stages). PXRD of the sample revealed, together with the intended phase, the presence of the competing $BaCr_2As_2$ phase and some other chromium arsenide phases such as Cr_2As, Cr_4As_3 and CrAs. The high-temperature reactions (1200 °C) were also tried by using the CsI flux, however, 1200 °C seemed too high for this flux method, where the silica tubes all cracked in the furnace even when they were cooled slowly. The alternative flux mixture (NaI and CsI) was used as well, which was separately prepared by grinding together NaI (Alfa, 99.98 %) and CsI (Aldrich, 99.999 %) in the molar ratio 0.44:0.56. The prepared "$Ba_2CrO_2Cr_2As_2$" and flux mixture were then ground together in a 1:1 molar ratio and heated

at 1100 °C for 48 hours. However, this produced very little of the desired product. The attempts at optimizing fluxes by use of quenching also failed to bring an improvement in product purity.

The purest samples of $Ba_2CrO_2Cr_2As_2$ were obtained by increasing the temperature of the reheating step to 1200 °C at a rate of 10 °C/min followed by quenching the reaction in an ice bath after about 3-4 hours, which was found to be the optimum time and temperature for this synthesis. Higher temperatures (1250 °C and 1280 °C) were also attempted and they produced samples of similar purity to 1200°C. Surprisingly, the reaction scale seemed to be very important in this synthesis. The product couldn't be made very pure if the sample was heated on a small scale and the impurity phase was different as the reaction scale was changed (see Table 3.1). This may relate to the actual cooling rate in the quench.

Reaction Scale	Main Phase	Impurity Phase
0.5g	Cr_2As	Unidentifiable Impurities
0.8g	$Ba_2CrO_2Cr_2As_2$	Cr_2As
1g	$Ba_2CrO_2Cr_2As_2$	Cr_2As
2g	$Ba_2CrO_2Cr_2As_2$	$BaCr_2As_2$
3g	$Ba_2CrO_2Cr_2As_2$	$BaCr_2As_2$

Table 3.1: Product of the synthesis of $Ba_2CrO_2Cr_2As_2$ on a different reaction scale

3.2.1 Powder X-ray diffraction

High-resolution powder X-ray diffraction was measured at room-temperature on the sample of $Ba_2CrO_2Cr_2As_2$ (XX81, the 1 g sample synthesised above) synthesised by the method described above. A refinement against data collected on the MAC detector of the instrument I11 at the Diamond Light Source is shown in Figure 3.4. Despite many attempts to synthesise a single phase compound of $Ba_2CrO_2Cr_2As_2$, the sample was still contaminated by a significant amount of Cr_2As impurity and the diffraction pattern also contained some

unindexed reflections that were presumed to arise from an unidentified Ba-containing impurity.

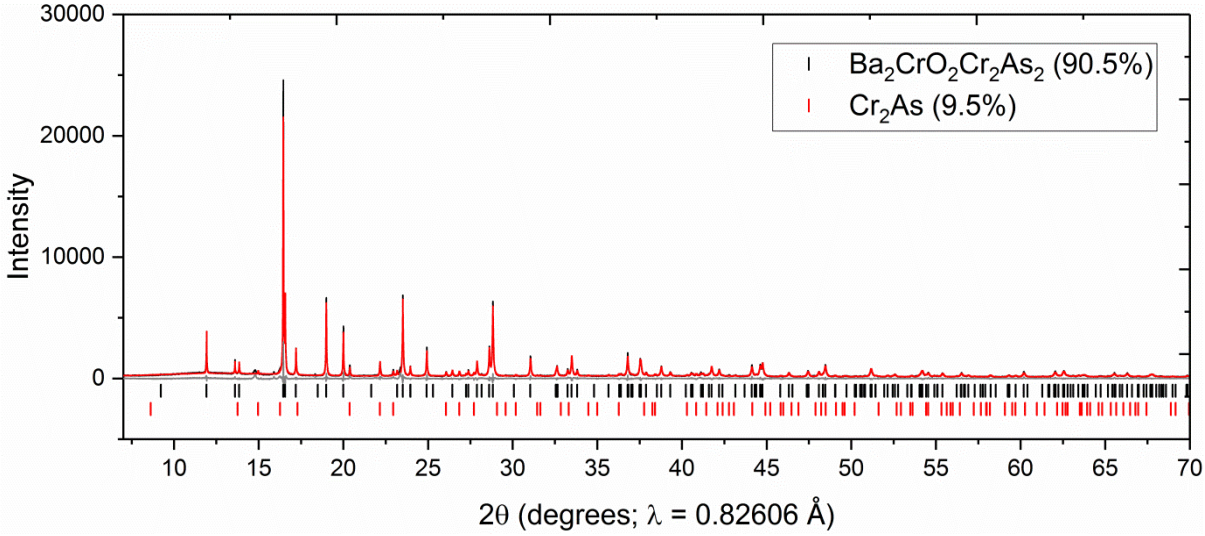

Figure 3.4: Rietveld refinement result of high resolution powder x-ray diffraction data for $Ba_2CrO_2Cr_2As_2$ using the MAC detector of the instrument I11 at the Diamond Light Source

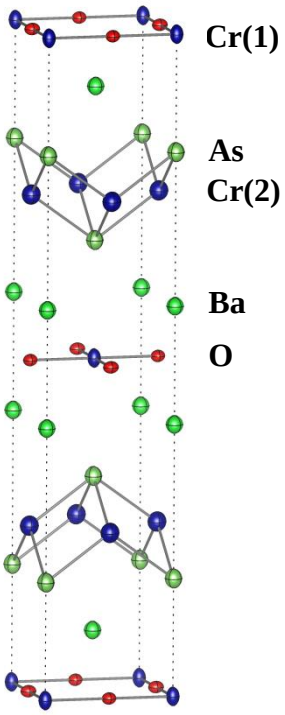

Figure 3.5: The unit cell of $Ba_2CrO_2Cr_2As_2$, showing thermal displacement ellipsoids at room temperature

The crystal structure of $Ba_2CrO_2Cr_2As_2$ is shown in Figure 3.5, which is isotypic to its Sr-analogue $Sr_2CrO_2Cr_2As_2$ in the space group *I*4/mmm.[77] The Ba-containing layers are separated by alternating $Cr_2As_2^{2-}$ and CrO_2^{2-} layers. The CrO_2 layers contain Cr^{2+} in a square planar environment with oxygen atoms. Whereas the $Cr_2As_2^{2-}$ layers consist of a Cr square network with squares of Cr ions capped alternately above and below the plane by As atoms to create an edge-shared tetrahedral network, which is similar to the layers in the anti-PbO structure. In addition, the As atoms in the $Cr_2As_2^{2-}$ layers point directly towards the square-planar Cr atoms, forming distended octahedral CrO_4As_2. The lattice parameters obtained from room-temperature X-ray diffraction are a = 4.05506(2) Å and c = 20.5637(1) Å, and are compared with those of the Sr-analogue $Sr_2CrO_2Cr_2As_2$ in Table 3.2. The cell dimensions a and c of $Ba_2CrO_2Cr_2As_2$ are larger owing to the bigger ionic radius of Ba^{2+} (1.42 Å) as compared with Sr^{2+} (1.26 Å).[80] Structural parameters, selected atomic distances and bond angles from X-ray data are presented in Tables 3.3 and 3.4.

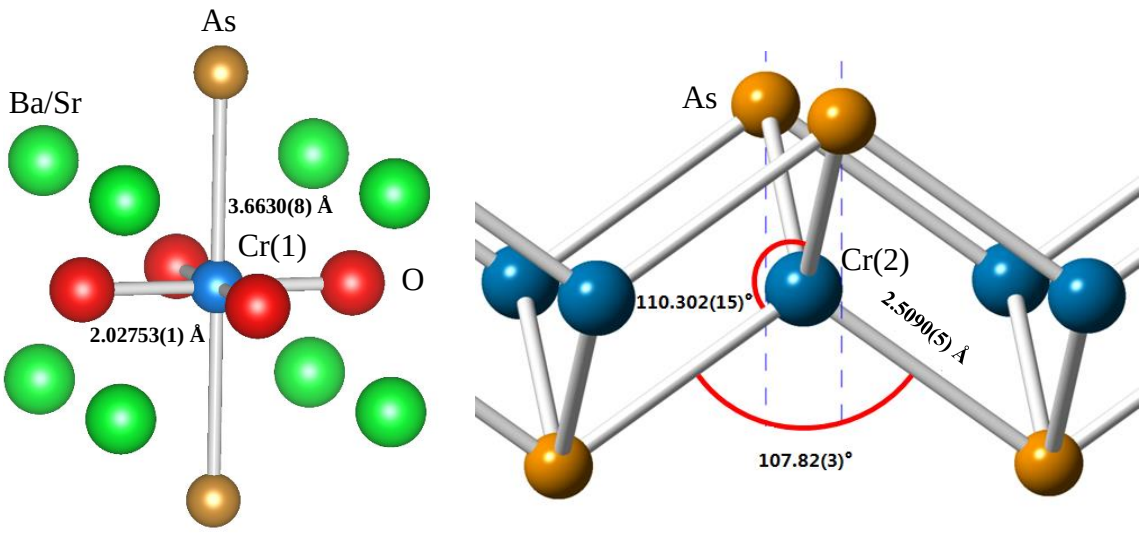

Figure 3.6: Left. CrO_2 coordination environment, showing bond lengths obtained from synchrotron PXRD; Right. Cr_2As_2 coordination environment, showing bond lengths and angles obtained from synchrotron PXRD

	$Ba_2CrO_2Cr_2As_2$ at I11	$Sr_2CrO_2Cr_2As_2$ at I11
Temperature (*K*)	298	298
Space group	*I*4/mmm	*I*4/mmm
a (Å)	4.05506(2)	4.00800(2)
c (Å)	20.5637(1)	18.8214(1)
V (Å^3)	338.140(4)	302.347(4)
R_{wp}	8.05	7.90
χ^2	1.97	2.22

Table 3.2: Lattice Parameters for $Ba_2CrO_2Cr_2As_2$ and $Sr_2CrO_2Cr_2As_2$ from Rietveld Refinement

I11 PXRD of $Ba_2CrO_2Cr_2As_2$ at room temperature

Atom	Site	*x*	*y*	*z*	U_{11} (Å^2)[a]	U_{33} (Å^2)
Ba	4*e*	0	0	0.41073(2)	0.0149(2)	0.0161(3)
Cr(1)	2*a*	0	0	0	0.0090(6)	0.018(1)
Cr(2)	4*d*	0	0.5	0.25	0.0176(5)	0.0199(8)
As	4*e*	0	0	0.17813(4)	0.0152(4)	0.0189(6)
O	4*c*	0	0.5	0	0.012(1)[b] [U_{iso} (Å^2)]	

I11 PXRD of $Sr_2CrO_2Cr_2As_2$ at room temperature

Atom	Site	*x*	*y*	*z*	U_{11} (Å^2)[a]	U_{33} (Å^2)
Sr	4*e*	0	0	0.41229(4)	0.0107(3)	0.0133(5)
Cr(1)	2*a*	0	0	0	0.0098(5)	0.015(1)
Cr(2)	4*d*	0	0.5	0.25	0.0126(4)	0.0098(6)
As	4*e*	0	0	0.17040(4)	0.0155(3)	0.0165(5)
O	4c	0	0.5	0	0.004(1)[b] [U_{iso} (Å^2)]	

[a] $U_{11} = U_{22}$ by symmetry for sites refined anisotropically
[b] O atoms refined isotropically

Table 3.3: Structure parameters for $Ba_2CrO_2Cr_2As_2$ and $Sr_2CrO_2Cr_2As_2$ from the Rietveld Refinement of powder X-ray diffraction data; The results of $Sr_2CrO_2Cr_2As_2$ (ref. 81) were taken from Part II student Michael Jones's thesis[81]

	I11 PXRD of $Ba_2CrO_2Cr_2As_2$	I11 PXRD of $Sr_2CrO_2Cr_2As_2$
Ba(Sr)–O (Å)	2.7351(3)	2.5964(5)
Ba(Sr)–As (Å)	3.4001(5)	3.2333(5)
Cr(1)-As (Å)	3.6630(8)	3.2072(7)
Cr(2)-As (Å)	2.5090(5)	2.5021(4)
Cr(1)-O (Å)	2.02753(1)	2.00400(1)
As–Cr(2)–As (°) [×4]	110.302(15)	111.01(1)
As–Cr(2)–As (°) [×2]	107.82(3)	106.44(3)

Table 3.4: Selected atomic distances and bond angles for $Ba_2CrO_2Cr_2As_2$ and $Sr_2CrO_2Cr_2As_2$ from the Rietveld Refinement of powder X-ray diffraction data (see Figure 3.6)

3.2.2 Magnetic susceptibility measurements

The temperature-dependent ZFC and FC magnetic susceptibilities (χ) of $Ba_2CrO_2Cr_2As_2$ (XX081) was first measured in an applied field of 1000 Oe between 2 K and 350 K (Figure 3.7a). The data below show the sample is paramagnetic at low temperatures from 2 K to 100 K. Above 100 K, χ increases almost linearly with temperature to a maximum at 350 K, at which point there is a hump suggestive of a broad antiferromagnetic transition extending to higher temperatures. The sample was thus then measured in an applied field of 5000 Oe over the temperature range of 300 K-650 K (Figure 3.7b). The furnace in the MPMS5-XL SQUID magnetometer produced noisy data at high temperatures which made it hard to tell whether there was a transition at 350 K but from the high-temperature data, another antiferromagnetic transition is very tentatively suggested at around 540 K. The susceptibility data did not give evidence for long-range magnetic ordering (in low dimensional systems the onset of long-range magnetic order is often not clearly visible in the susceptibility measurements), however, neutron powder diffraction data clearly showed that long-range magnetic ordering occurs below 470 K.

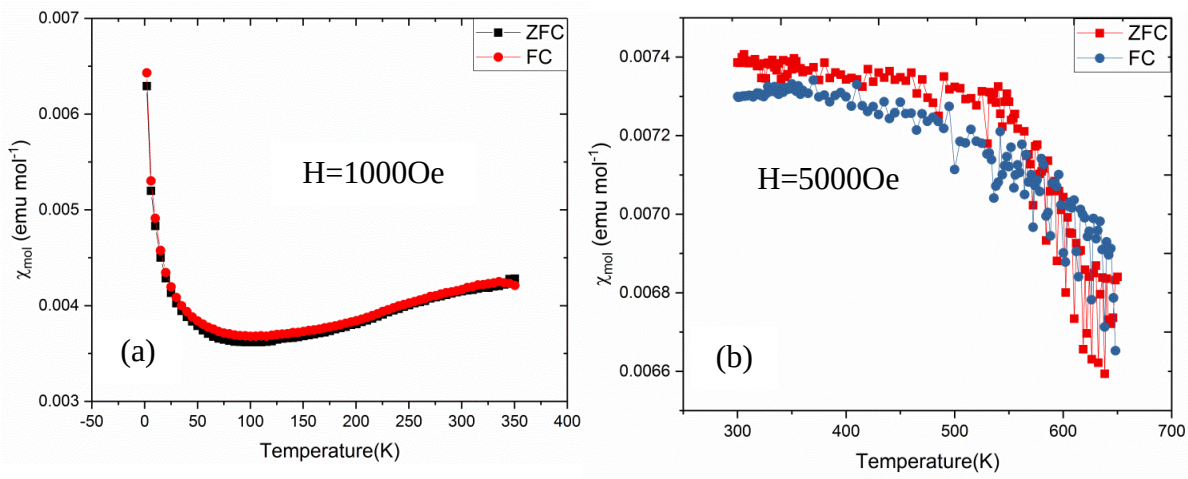

Figure 3.7: (a). SQUID magnetometry data for $Ba_2CrO_2Cr_2As_2$ at 1000 Oe between 2 K and 350 K; (b). High-temperature SQUID magnetometry data for $Ba_2CrO_2Cr_2As_2$ at 5000 Oe between 300 K and 650 K; The two data sets were collected using different sample environments

3.2.3 Powder neutron diffraction

3.2.3.1 Low temperature PND

PND was first performed on $Ba_2CrO_2Cr_2As_2$ (XX081) at low temperatures using the OSIRIS diffractometer. Approximately 700 mg of the sample of $Ba_2CrO_2Cr_2As_2$ was loaded into a vanadium can and sealed with indium wire under an inert argon atmosphere. The sample was then measured on OSIRIS between 5 K and 300 K. Figure 3.8 shows the low-temperature data obtained on $Ba_2CrO_2Cr_2As_2$ and clearly depicts the appearance and growth of magnetic peaks (marked with "*") as the temperature cools. These magnetic reflections are comparable to those of its Sr-analogue $Sr_2CrO_2Cr_2As_2$ at a similar temperature range, which are related to the antiferromagnetic ordering in the oxide layers. Furthermore, in comparison with the PXRD data of $Ba_2CrO_2Cr_2As_2$ at 298 K, it was found that some magnetic peaks were already present at 298 K in the OSIRIS neutron diffraction pattern, labelled with "+" in Figure 3.8. These low *d*-spacing magnetic peaks were also observed in $Sr_2CrO_2Cr_2As_2$ (Appendix B) until very high temperature (600 K), corresponding to the

magnetic ordering in the arsenide layers. The WISH diffractometer was then used at a wider range of temperatures, including temperatures above 300 K, to fully investigate the magnetic ordering in both oxide and arsenide layers of $Ba_2CrO_2Cr_2As_2$.

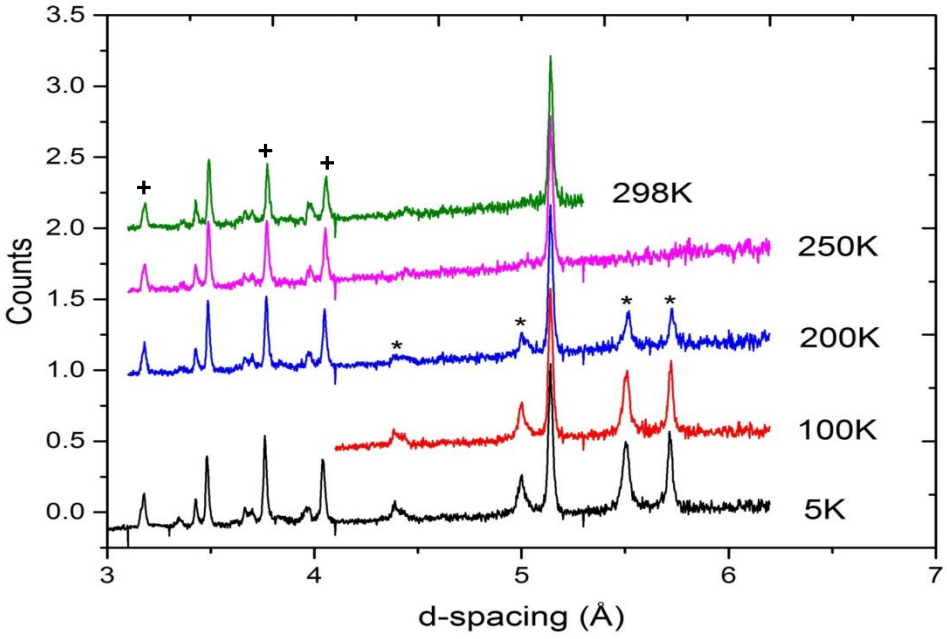

Figure 3.8: OSIRIS PND data of XX081 in the range 5 K to 298 K; The asterisks indicate the magnetic reflections as the sample is cooled

3.2.3.2 Variable temperature PND

On WISH, the 700 mg sample of $Ba_2CrO_2Cr_2As_2$ (XX081) was loaded into a 6 mm vanadium can with the Gd and Cd foil masks (Gd was used to mask the steel part of the can above room temperature, while Cd was used below RT for the same reason; both Gd and Cd absorb neutrons extremely strongly) and measured in a closed cycle refrigerator equipped with a heating stage insert that enabled measurements at variable temperatures below and above room temperature. Data were collected from a minimum temperature of 5.5 K to a maximum temperature of 593 K, from which several intense magnetic reflections are present below 473 K and their intensities changed continuously as a function of temperature. All of the

magnetic reflections can be well indexed by using a $\sqrt{2}\,a \times \sqrt{2}\,a$ expansion of the unit cell in the *ab* plane, although for the ones on the Cr moments in the arsenide layer, a smaller magnetic unit cell can be used. The expanded cell was then loaded into ISODISTORT[56] using the *P*1 space group and it was found that those intensities of the magnetic reflections could be well fitted using both $mX2^+$(a) and $mM4^+$(a) magnetic modes. Thus the two Cr sublattices order with different propagation vectors *k* = (½ ½ 0) in the oxide layer and *k* = (1 1 1) in the arsenide layer, which means that in principle they are independent. Figure 3.9 shows the variable temperature data collected from the WISH diffractometer and clearly depicts the appearance and growth of intensities as the temperature cools. Several magnetic peaks marked with (*) and (+) are present at 5.5 K, which all persist on warming to 233 K. At 205 K the peaks with (*) have greatly diminished in intensity and are absent at 233 K (corresponding to the $mX2^+$(a) mode for the oxide layer). The peaks marked with (+) also decrease in intensity over the same temperature range and are completely absent in the pattern at 473 K (corresponding to the $mM4^+$(a) mode for the arsenide layer). In order to refine both magnetic modes together, a new space group *Pbam* (55.353) was then calculated from ISODISTORT. The combination of both $mX2^+$(a) and $mM4^+$(a) magnetic modes gave a new magnetic model to fit all of those magnetic peaks well in the PND data below 233 K, where both oxide and arsenide sublattices were antiferromagnetically ordered with their moments oriented along the *c*-axis. The changes in intensity result from the onset of ordering of the moments on the two Cr sublattices occurring at different temperatures. The quantitative thermal evolution of the reflections in $Ba_2CrO_2Cr_2As_2$ is discussed below.

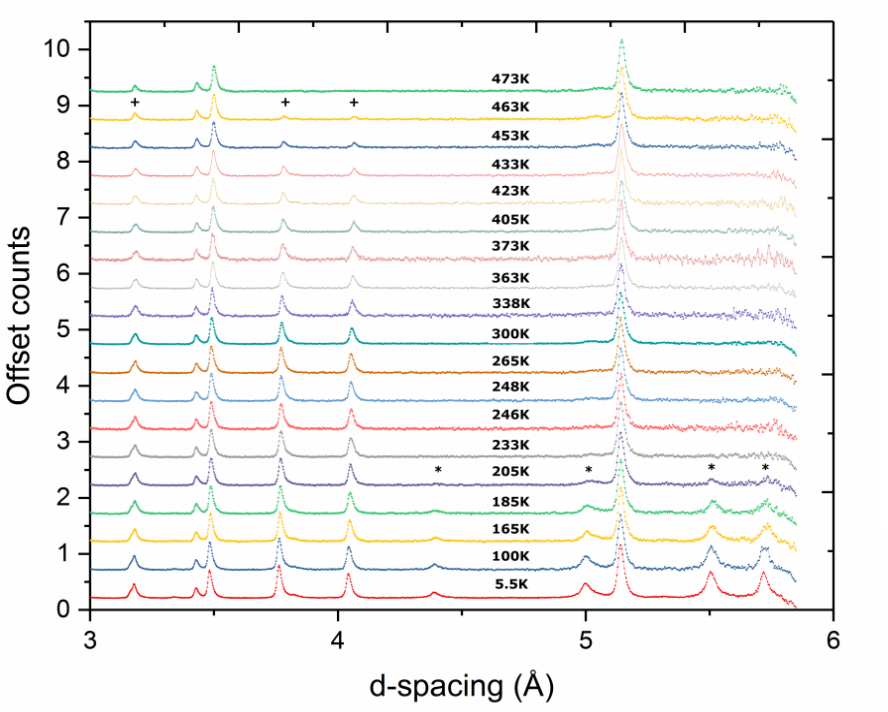

Figure 3.9: WISH PND data of $Ba_2CrO_2Cr_2As_2$ in the range 5.5 K to 473 K from banks 3 and 8, showing all magnetic reflections; The asterisks (*) indicate the sets of magnetic reflections which are present from 5.5 K to 233 K, whereas for crosses (+), the magnetic reflections are present until warming to 473 K

The neutron data can then be divided into three main temperature ranges:

1) Above 473 K, diffraction pattern only shows the scattering from the nuclear crystal structure and there are no magnetic peaks appearing in the PND pattern. Figure 3.10 shows the refinement of the nuclear structure against the data collected in banks 2 and 9 at 593 K. All peaks in the pattern can be accounted for by refinement of the nuclear structures of $Ba_2CrO_2Cr_2As_2$ and Cr_2As.

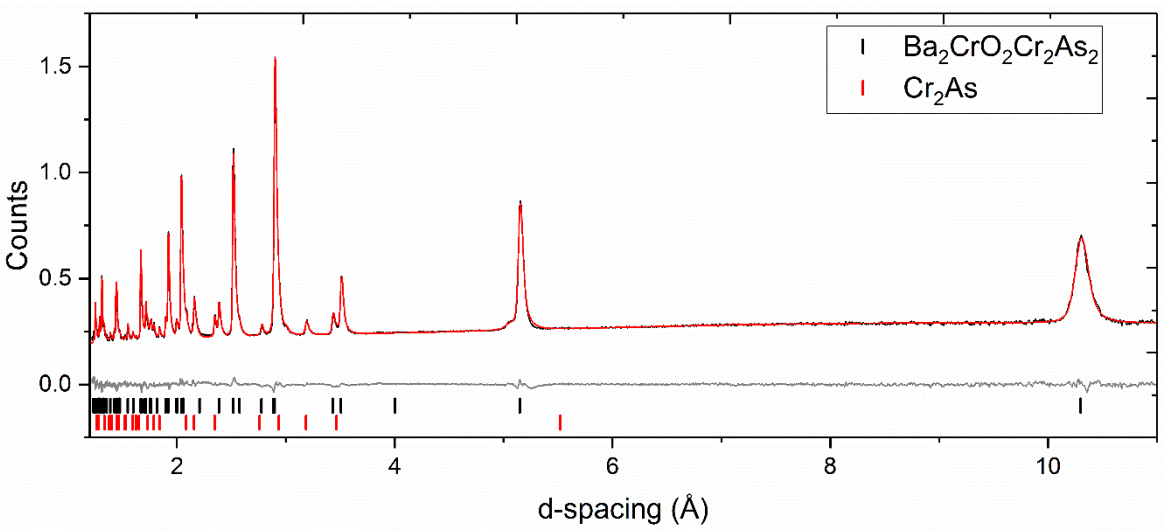

Figure 3.10: Rietveld refinement of PND data collected at 593 K from banks 2 and 9 giving the diffraction pattern of the nuclear structure of $Ba_2CrO_2Cr_2As_2$; Rwp = 2.60

2) Between 473 K and 233 K, a model of the magnetic structure was successfully refined by introducing long-range ordering of the magnetic moments of the Cr^{2+} ions in the Cr_2As_2 layers. The Cr moments are coupled antiferromagnetically in a checkerboard fashion with their moments directed along the *c*-direction perpendicular to the planes in the magnetic unit cell. The ordering scheme is similar to that displayed by the Mn analogues with As or Sb pnictide ions[82] and to the compounds LaCrAsO[83] and $BaCr_2As_2$[84] with similar CrAs layers (Figure 3.11), except that the Cr moments in adjacent layers related by the vector *c*/2 are aligned parallel in $Ba_2CrO_2Cr_2As_2$ rather than antiparallel as in the other compounds. However, in this temperature range, the Cr^{2+} ions in the CrO_2 layers were found not to contribute to the magnetic scattering and the magnetic moments of the Cr^{2+} in the CrO_2 planes remain unordered. The refinement of the PND data and magnetic model at 363 K are shown in Figure 3.12.

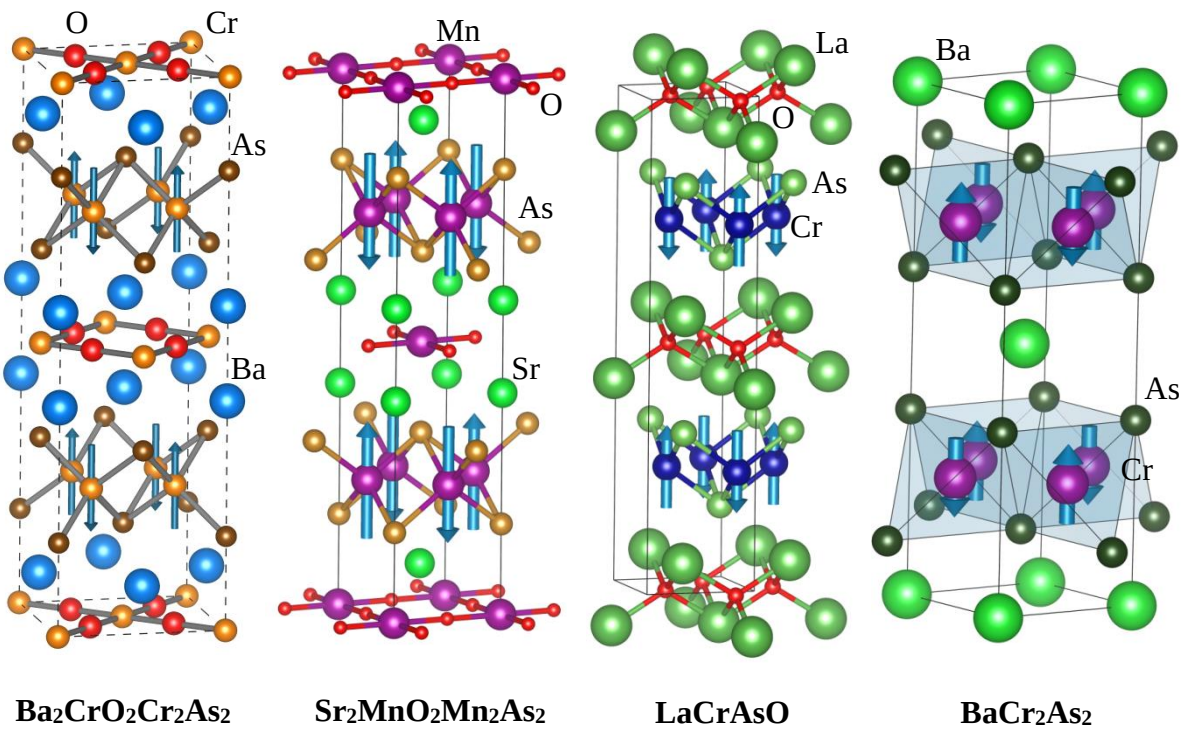

Figure 3.11: The magnetic structures of $Ba_2CrO_2Cr_2As_2$ (between 233 K and 473 K), $Sr_2MnO_2Mn_2As_2$, LaCrAsO and $BaCr_2As_2$

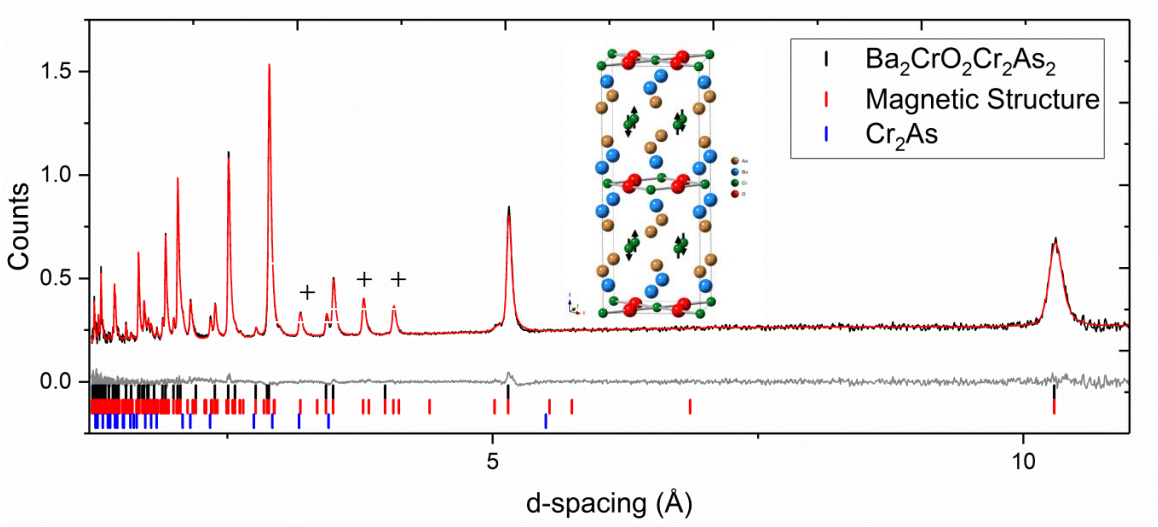

Figure 3.12: Rietveld refinement of PND data collected at 363 K from banks 2 and 9 showing the appearance of magnetic peaks with R_{wp} = 3.95; The crosses (+) indicate the sets of magnetic reflections present in the Cr_2As_2 layers at 363 K; The inset shows the magnetic structure model used in the refinement of PND data at 363 K, consisting of the checkerboard-type antiferromagnetic ordering of Cr^{2+}

3) Below 233 K, the PND measurements showed there were several intense peaks appearing at *d*-spacings from 4.2 to 6 Å, which were successfully modelled as resulting from the antiferromagnetic ordering of Cr^{2+} ions in the CrO_2 planes. In this temperature range, two different propagation vectors were found in the two sublattices and the magnetic moments of the Cr^{2+} are ordering antiferromagnetically in both CrO_2 planes and Cr_2As_2 layers, both with the moments directed along the *c* axis in the magnetic unit cell. On cooling the Cr(1) long-range ordered moment grows in magnitude and becomes larger than the Cr(2) long-range ordered moment below 200 K. At the lowest temperature, both moments are saturated and are directed parallel to the *c* axis. Figure 3.13 shows the Rietveld refinement and the magnetic model at 5.5 K.

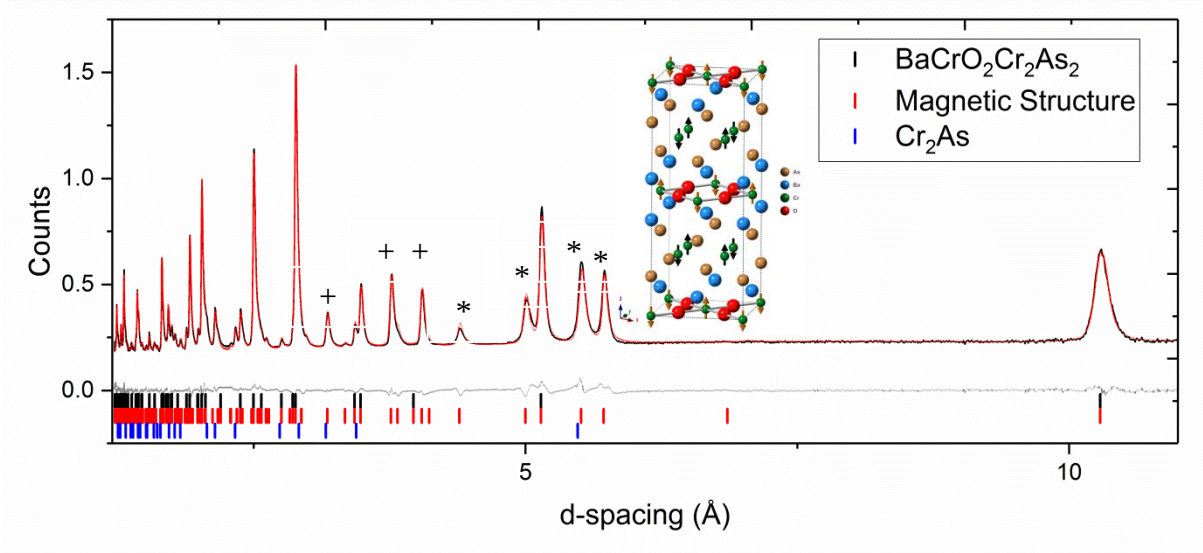

Figure 3.13: Rietveld refinement of PND data collected at 5.5 K from banks 2 and 9 with R_{wp} = 3.77; The crosses (+) and asterisks (*) indicate the sets of magnetic reflections of the Cr^{2+} in the Cr_2As_2 layers and CrO_2 planes respectively; The inset shows the magnetic structure model used in the refinement of PND data at 5.5 K, consisting of antiferromagnetic ordering of the Cr^{2+}(1) and Cr^{2+}(2) moments

This overall magnetic model with ordering on both Cr sublattices is also able to account for all neutron powder diffraction patterns measured for $Ba_2CrO_2Cr_2As_2$ sample. Figure 3.14 shows the changes in the antiferromagnetic ordering of the Cr^{2+} moments in the two sublattices over the whole temperature range. Unlike its Sr analogue, $Ba_2CrO_2Cr_2As_2$ shows no spin-reorientation transition and both Cr(1) and Cr(2) moments are oriented along the *c* direction, which is described in more detail in the discussion.

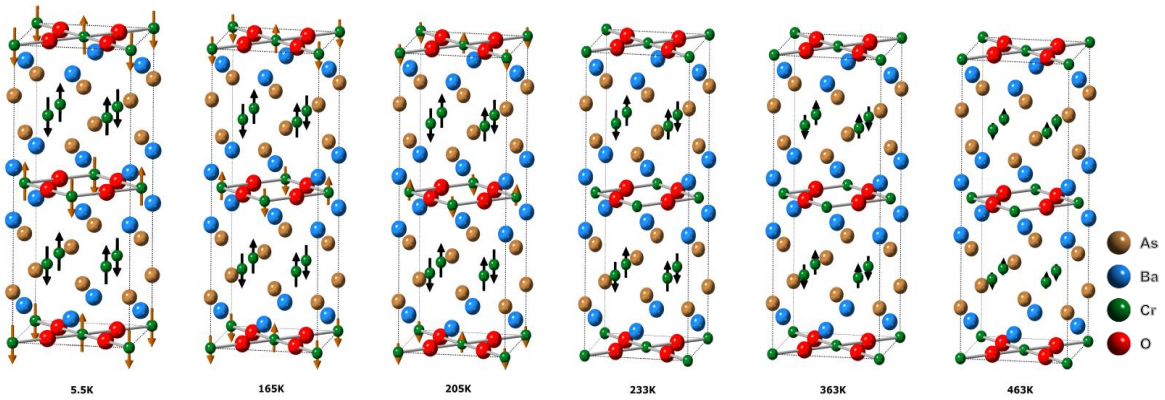

Figure 3.14: Magnetic model of $Ba_2CrO_2Cr_2As_2$ over the temperature range 5.5 K – 593 K, showing the magnitude and direction of magnetic moments for the two chromium sublattices

The ordering temperature for Cr^{2+} in CrO_2 planes is below 248 K while for Cr^{2+} in Cr_2As_2 layers, the Néel temperature (T_N) is around 470 K. The development of the two long-range ordered moments in both magnetic sublattices of $Ba_2CrO_2Cr_2As_2$ is highlighted in Figure 3.15, in which the magnitude of the moments is shown as a function of temperature. The magnetic moments of both chromium layers grow slowly in magnitude as the sample is cooled down to 5.5 K, at which point the moments reach their maxima. Those in the arsenide layers reach a value of 2.298(8) μB/Cr^{2+} at 5.5 K whilst those in the oxide planes reach 3.30(1) μB/Cr^{2+}, both of which are smaller than the saturated spin-only ordered magnetic moment of a Cr^{2+} ion of 4 μB because of the covalency of the Cr–As and Cr–O bonds in both sublattices, decreasing the density of unpaired electrons by delocalisation. And due to the greater

covalency of the bonds between Cr and As, the magnetic moment in the Cr_2As_2 layer has a smaller magnitude compared to the one in the oxide plane.

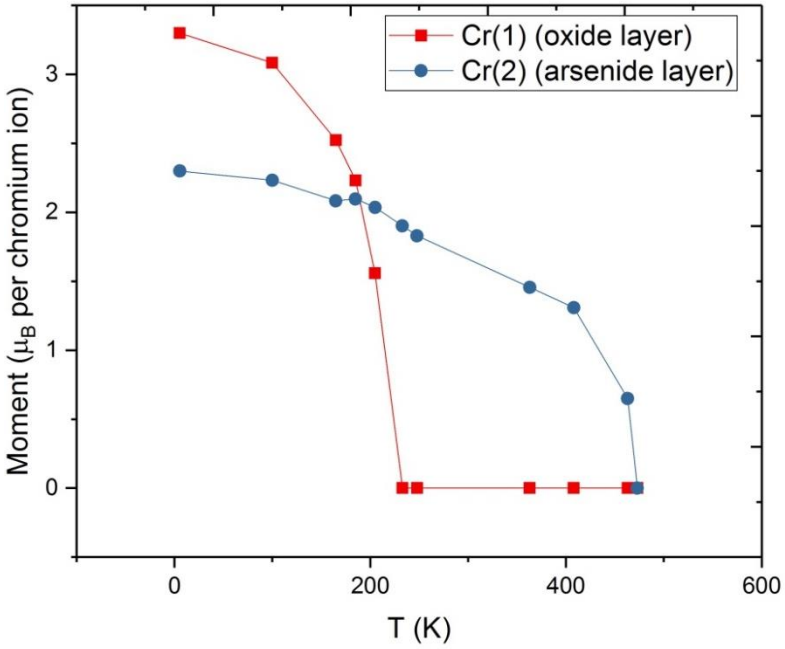

Figure 3.15: Magnitudes of the moments in the two Cr sublattices of $Ba_2CrO_2Cr_2As_2$ as a function of temperature

3.3 Discussion

3.3.1 Crystal structure

Compared to the Sr analogue, The lattice parameters *a* and *c* expand together as the bigger alkaline earth cation Ba^{2+} is substituted in the structure, which is able to change the intraplanar bonding (Table 3.3) as well as the interaction between the oxide and arsenide layers. The lattice parameter *a* and hence the Cr(1)–O and Cr(2)–Cr(2) distances increase by 1.17 % on substituting Sr^{2+} for Ba^{2+}. The Cr(2)–As distance in the arsenide layers increases only marginally (0.3 %) so the $Cr(2)As_4$ tetrahedra which are slightly compressed in the *ab*

plane in $Sr_2CrO_2Cr_2As_2$ become more regular in $Ba_2CrO_2Cr_2As_2$. With the basal plane expansion restricted by maintaining strong Cr(1)–O and Cr(2)–As interactions, the larger Ba^{2+} cation is accommodated disproportionately by the expansion of the cell perpendicular to the basal plane and the *c* lattice parameter increases by 9.3%. Thus the most significant change in the coordination environment for a Cr ion is the 14 % increase in the Cr(1)–As distance, from 3.207(1) Å in $Sr_2CrO_2Cr_2As_2$ to 3.663(1) Å in $Ba_2CrO_2Cr_2As_2$ which makes the already highly distended $Cr(1)O_4As_2$ environment even more distended and in $Ba_2CrO_2Cr_2As_2$, Cr(1) is close to being in a purely square planar CrO_4 coordination environment.

Since Cr^{2+} with the high spin d^4 configuration is strongly Jahn-Teller active when in an octahedral coordination environment, it is worth making a comparison with the crystal structures of other known Ba-containing members of this structural series (Table 3.5). In comparison with the analogous manganese and zinc compounds in the series, trends are observed in the size of the lattice parameters which can be explained in terms of the differing ionic radii of the metals.

The most significant comparison is to be made between $Ba_2CrO_2Cr_2As_2$ and the analogous Mn-containing compound $Ba_2MnO_2Mn_2As_2$. The lattice parameters *a* is significantly shorter in the case of the Cr compound in line with the smaller ionic radius of the d^4 Cr^{2+} ion (0.73 Å) compared with the d^5 Mn^{2+} ion (0.83 Å).[79] But surprisingly, the lattice parameter *c* in $Ba_2CrO_2Cr_2As_2$ is 4.0 % larger than that in $Ba_2MnO_2Mn_2As_2$, which corresponds to evidence that Cr(1)–As distance is 5.9 % longer than the corresponding Mn(1)–As distance in $Ba_2MnO_2Mn_2As_2$. Although Cr^{2+} with the d^4 configuration adopts strongly Jahn-Teller distorted octahedral environments in molecules and solids, the ratio of the Cr(1)–As and Cr(1)–O distances of 1.8 in $Ba_2CrO_2Cr_2As_2$ is even larger than the measured Cr–Cl: Cr–O

ratio of 1.33 in $Cr(H_2O)_4Cl_2$[85], which is elongated along the Cr–Cl bonds (note that Ba–As ~ 3.3 Å [86] and Ba–Cl ~3.2 Å [87] distances are fairly similar, so, for the purposes of comparison, the Cr–Cl distances are used as a proxy for Cr–As distances), and larger than one would expect based on the ratio of axial and equatorial Cr–Cl distances (4 × 2.39 Å and 2 × 2.90 Å) in the crystal structure of $CrCl_2$.[88] So it is not clear that the increased axial distention around the Cr(1) site in $Ba_2CrO_2Cr_2As_2$ compared with the case in $Ba_2MnO_2Mn_2As_2$ is driven by a Jahn-Teller stabilisation and it is probably best to consider it as being a consequence of the crystal structure. Furthermore, in the oxide layers the transition metal ion is forced, by the presence of the intervening Ba^{2+} cation, to occupy a highly distended octahedral environment MO_4As_2 with *M*(1)–As distances that are much larger than in the MAs_4 tetrahedra, reflecting a rather weak interaction between *M*(1) and As. In the arsenide layers the Cr(2)–Cr(2) distance (equal to $a / \sqrt{2}$) across the shared edges of adjacent $CrAs_4$ tetrahedra is 4.5 % shorter than the corresponding distance in $Ba_2MnO_2Mn_2As_2$ and the Cr(2)–As distances in the $CrAs_4$ tetrahedra of 2.5090 Å are 3.2 % shorter than the corresponding Mn(2)–As distances in $Ba_2MnO_2Mn_2As_2$. The result of accommodating a relatively small ion in the arsenide layer and satisfying the coordination requirements of the Ba^{2+} ions results in a CrO_4As_2 coordination environment that is a rather more distended octahedron than that of the corresponding MnO_4As_2 environment. Moreover, as Sr^{2+} is substituted by Ba^{2+}, the distortion becomes much larger in $Ba_2CrO_2Cr_2As_2$ than $Sr_2CrO_2Cr_2As_2$ (Table 3.4).

Compound	$Ba_2CrO_2Cr_2As_2$	$Ba_2MnO_2Mn_2As_2$[38]	$Ba_2ZnO_2Zn_2As_2$[39]	$Ba_2MnO_2Zn_2As_2$[40]
T (K)	298	298	130	295
a (Å)	4.05506(2)	4.248(5)	4.206(1)	4.23369(4)
c (Å)	20.5637(1)	19.77(3)	19.665(6)	19.4780(3)
c/*a*	5.07112(3)	4.653(9)	4.675(2)	4.60071(8)
M (1)–As (Å)	3.6630(8)	3.458(4)	3.4243(13)	3.400(5)
M (1)–O (Å)= *a* / 2	2.02753(1)	2.124(1)	2.1030(6)	2.1158(1)
M (1) Bond Distance Ratio	1.8066(4)	1.628(2)	1.6283(5)	1.606(2)
M (2)–As (Å)	2.5090(5)	2.593(1)	2.5785(6)	2.5848(1)
M (2)–*M* (2) (Å) = *a* /√2	2.86736(2)	3.004(7)	2.9741(8)	2.9923(2)

Table 3.5: Lattice parameters and selected bond distances for all reported Ba- containing oxide oxypnictide with the $Sr_2Mn_3As_2O_2$ structure type containing Mn and Zn; The bond distance ratio given is the *M* (1)–As distance divided by the *M* (1)–O distance

The zinc-containing compound $Ba_2ZnO_2Zn_2As_2$ has a lattice parameter between those of the chromium and manganese compounds. The distance between the Zn (1) and As is 3.4243(13) Å, much longer than the Zn–As bond distance within the arsenide layer of 2.5785(6) Å. The bond distance ratio (see Table 3.5) of the Zn(1)–As and Zn(1)–O distances of 1.6 in $Ba_2ZnO_2Zn_2As_2$ is similar to that in $Ba_2MnO_2Mn_2As_2$ but smaller than $Ba_2CrO_2Cr_2As_2$. In the case of $Ba_2ZnO_2Zn_2As_2$, Zn^{2+} is also in a distorted octahedral geometry, which is enforced by the large Ba^{2+} ions in the crystal structure.

3.3.2 Magnetic ordering

The observation that the Cr(2) moments in the Cr_2As_2 layer of $Ba_2CrO_2Cr_2As_2$ order at a much higher temperature than the Cr(1) moments in the oxide layer is consistent with the observations for its Sr analogue $Sr_2CrO_2Cr_2As_2$. However while the ordering temperature for the Cr(2) moments in the Cr_2As_2 layer is 470 K in $Ba_2CrO_2Cr_2As_2$, the corresponding

Néel temperature (T_{N1}) in $Sr_2CrO_2Cr_2As_2$ is 590 K.[78] Similarly, the Cr(1) magnetic sublattice of the CrO_2 layers of $Ba_2CrO_2Cr_2As_2$ has a Néel temperature (T_{N2}) estimated as 248 K from the PND measurements, whereas in $Sr_2CrO_2Cr_2As_2$ the transition temperature is about 291 K.[78] The lattice parameters *a* and *c* expand together as the bigger Ba cation is substituted in the structure, and both the intraplanar and interplanar distances are increased which results in lower ordering temperatures in both layers of $Ba_2CrO_2Cr_2As_2$.

The orientation of the Cr^{2+} magnetic moments in the oxide layer of $Ba_2CrO_2Cr_2As_2$ can be rationalised on the basis of considerations of spin-orbit coupling in terms of HOMO (highest occupied orbital) – LUMO (lowest unoccupied orbital) interaction between *d*-orbitals, as previously reported by Whangbo *et al*.[89] The Cr^{2+} ions are in the highly distended octahedral environment CrO_4As_2, with the elongated Cr(1)-As bond distance along the *c* axis. In contrast to the perfect octahedral coordination environment, the highly distended octahedral environment around Cr ions results in the loss of degeneracy of the *d*-orbitals but their orbital angular momentum can't be entirely quenched. Thus the split *d*-orbitals of the Cr ions still have the angular momentum behaviour which can be affected by the spin-orbit coupling. The magnetic quantum numbers for the five split *d*-orbitals are: $L_z = 0$ for d_{z^2}, $L_z = \pm 1$ for d_{xz} ,d_{yz} and $L_z = \pm 2$ for d_{xy}, $d_{x^2-y^2}$. If the difference of magnetic quantum number between the HOMO and LUMO orbitals is 0 then the preferred spin orientation of the magnetic ions lies along the principal axis (*c*). If $|\Delta L_z|$ between the HOMO and LUMO orbitals is 1 then the magnetic moment is preferred to lie perpendicular to the principal axis (*c*). In the case of compounds with Cr^{2+} ($3d^4$, $S = 2$) in the oxide layer, the distended octahedral environment gives the nondegenerate *d*-orbitals as shown in Figure 3.16. The split *d*-orbitals are occupied by four unpaired electrons, where the HOMO is the d_{z^2} orbital and the LUMO is the $d_{x^2-y^2}$ orbital. The difference $|\Delta L_z|$ between the two orbitals is 2, suggesting they are not interacting under the spin-orbit coupling. The nearest filled *d*-orbital that can interact with the LUMO

is the d_{xy} orbital. So the new $|\Delta L_z|$ is calculated as 0 between the $d_{x^2-y^2}$ and d_{xy} orbitals, giving that the preferred orientation of the magnetic moments of oxide-layer Cr^{2+} ions lies along the *c*-axis. This result is in a good agreement with the spin orientations observed for oxide-layer Cr^{2+} moments in $Ba_2CrO_2Cr_2As_2$.

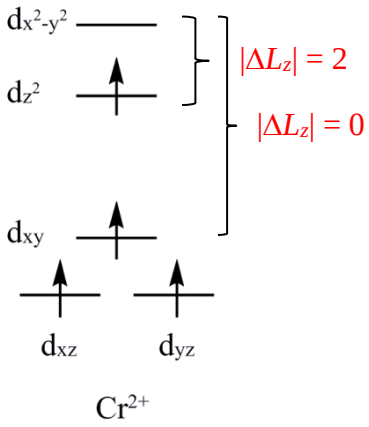

Figure 3.16: The high-spin electron configuration of Cr^{2+} ($3d^4$, $S = 2$) in the axially elongated CrO_4As_2 coordination environment

Experiments reveal that the Cr^{2+} (d^4) moments in the arsenide layers in LaCrAsO and $BaCr_2As_2$[84] all undergo antiferromagnetic ordering with their Cr moments aligned parallel to the *c* axis. This is also the experimentally-observed orientation of the moments corresponding to the Cr (d^4) ions in $Ba_2CrO_2Cr_2As_2$. However, in contrast to all these cases, a spin-reorientation transition was observed in $Sr_2CrO_2Cr_2As_2$ (see Figure 3.1). The Cr moments in the oxide layer are initially oriented with their main component in the *ab* plane. This onset of long-range ordering in the oxide layer precipitates a spin reorientation transition close to ambient temperature which results in the Cr moments in the arsenide layer reorienting to lie in the *ab* plane, while the Cr moments in the oxide layer reorienting to lie along the *c* axis, with the moments on the two sublattices remaining orthogonal through the transition. The reason why this spin-reorientation happens is still under investigation. Electron diffraction studies revealed quite a lot of stacking faults in $Sr_2CrO_2Cr_2As_2$ and it is possible that this is in some way responsible. Furthermore, the neutron diffraction data on

$Sr_2CrO_2Cr_2As_2$ revealed that the magnetic structure was slightly incommensurate with the crystal structure and it may be this which enables communication between the two Cr sublattices and hence the spin reorientation. The new compound $Ba_2CrO_2Cr_2As_2$ presented in this chapter presents less complicated behaviour than the Sr analogue.

Chapter 4

Synthesis and characterisation of $Sr_2Cr_{3-x}Mn_xAs_2O_2$ and $Ba_2Cr_{3-x}Mn_xAs_2O_2$

4.1 Introduction

The synthesis and characterisation of $Ba_2CrO_2Cr_2As_2$ have been described in chapter 3 of this thesis. The substitution of Sr with larger Ba gives a lattice expansion in the directions along both *c*-axis and in the *ab*-plane, which changes distances both in and between the CrO_2 and Cr_2As_2 layers and thus affects the observed magnetic properties in $Ba_2CrO_2Cr_2As_2$. In this chapter, the substitution of Cr in $Sr_2CrO_2Cr_2As_2$ and $Ba_2CrO_2Cr_2As_2$ by Mn has been performed to successfully synthesise three novel mixed-metal compounds (with the compositions $Sr_2Cr_{3-x}Mn_xAs_2O_2$ and $Ba_2Cr_{3-x}Mn_xAs_2O_2$) in the same crystal structure (Figure 4.1), in which more oxophilic Cr^{2+} prefers to occupy the *M* (1) sites in the oxide layers in all three compounds and the mixture of Mn^{2+} and Cr^{2+} occupies the *M* (2) sites in the arsenide layers, depending on the Mn:Cr ratio. The composition, structure and magnetic behaviour of these compounds are investigated using powder X-ray diffraction, neutron powder diffraction and magnetic susceptibility measurements. PND measurements made at variable temperatures have shown unusual magnetic ordering of these compounds with spin-reorientation transition and the appearance of an additional competing magnetic structure in a certain range of temperatures, which will be discussed in detail in this chapter.

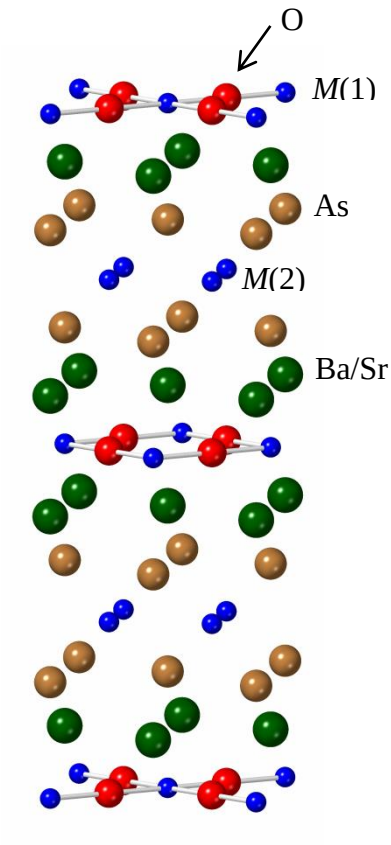

Figure 4.1: Crystal structure of $Sr_2Cr_{3-x}Mn_xAs_2O_2$ and $Ba_2Cr_{3-x}Mn_xAs_2O_2$ with *M* (1) (oxide layer) and *M* (2) (arsenide layer) sites

4.2 Synthesis and characterisation of $Sr_2Cr_{0.79}Mn_{0.21}O_2Mn_{1.76}Cr_{0.24}As_2$

The sample with the composition of $Sr_2CrMn_2As_2O_2$ was synthesised by grinding together SrO (see section 2.1.3.1), Cr (Alfa, 99.95 %), Mn (Aldrich, 99.99 %) and As (Alfa, 99 %) in the molar ratio 2: 1: 2: 2 in the glove box. A pellet of the ground starting materials was sealed in an evacuated silica tube as described in section 2.1.1. The tube was first heated to 800 °C for 24 hours at a slow rate of 2 °C/min, in which the As was reacted completely before it reached a high vapour pressure in the tube (the boiling point of As is 613 °C[79]). The mixture

was then reground for homogenization, pressed into a pellet and sintered at 1200 °C for another 3 hours (10 °C/min) followed by quenching the product in an ice bath.

4.2.1 Powder X-ray diffraction

The crystal structure of $Sr_2CrMn_2As_2O_2$ (XX183) was investigated at room temperature by using high-resolution synchrotron powder X-ray diffraction (MAC detector on the I11 beamline). Rietveld refinement against the collected PXRD pattern is plotted in Figure 4.2, indicating that $Sr_2CrMn_2As_2O_2$ was synthesised almost phase pure with only 1.49(2) weight percentage of CrAs found in the diffraction pattern as an impurity phase. The compound is isotypic to $Ba_2CrO_2Cr_2As_2$ in the space group *I4/mmm*.

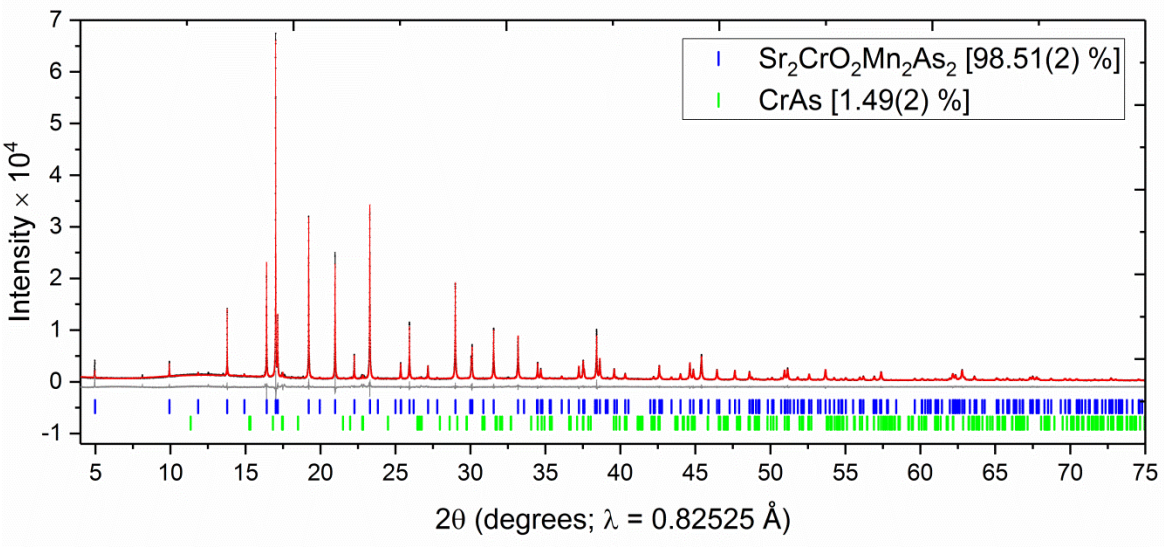

Figure 4.2: Rietveld refinement result of high-resolution powder x-ray diffraction data for $Sr_2CrMn_2As_2O_2$ (XX183) using the MAC detector of the instrument I11 at the Diamond Light Source

The structural parameters, selected atomic distances and bond angles from the refinement of X-ray diffraction data are presented in Tables 4.1, Table 4.2 and Table 4.3. Rietveld refinement against the PXRD data showed that the oxide and arsenide layers were fully

occupied by a mixture of Cr and Mn ions. However, Cr and Mn have very similar electron counts, making it impossible to distinguish the exact distribution of these two transition-metal ions between the $M_2As_2^{2-}$ and MO_2^{2-} layers Neutron powder diffraction was then used to investigate the distribution of transition metals in $Sr_2CrMn_2As_2O_2$ due to the very different neutron scattering lengths of the Cr (+3.64 fm) and Mn (–3.73 fm) nuclei.

	$Sr_2CrMn_2As_2O_2$
Diffractometer	I11 (MAC detector)
Temperature (K)	298
Space group	*I4/mmm*
a (Å)	4.086911(9)
c (Å)	19.05860(5)
V (Å^3)	318.333(2)
Phase density (g cm^{-3})	5.35273(3)
R_{wp}	7.13
χ^2	2.64

Table 4.1: Lattice Parameters of $Sr_2CrMn_2As_2O_2$ from Rietveld Refinement

I11 PXRD of $Sr_2CrMn_2As_2O_2$ at room temperature							
Atom	Site	*x*	*y*	*z*	U_{11} (Å^2)	U_{22} (Å^2)	U_{33} (Å^2)
Sr	4*e*	0	0	0.41419(2)	0.00499(16)	= U_{11}	0.0071(3)
Cr/Mn	2*a*	0	0	0	0.0006(3)	= U_{11}	0.0135(7)
Cr/Mn	4*d*	0	0.5	0.25	0.0023(2)	= U_{11}	0.0055(4)
As	4*e*	0	0	0.16959(2)	0.00485(15)	= U_{11}	0.0056(3)
O	4*c*	0	0.5	0	0.0032(6) [a] [U_{iso} (Å^2)]		

Table 4.2: Structure parameters for $Sr_2CrMn_2As_2O_2$ from the Rietveld Refinement of powder X-ray diffraction data; [a] O atoms were refined with the isotropic thermal displacement parameters

	I11 PXRD of $Sr_2CrMn_2As_2O_2$ at room temperature
Sr–O (Å)	2.6173(3)
Sr–As (Å)	3.3017(3)
M(1)-As (Å)	3.2321(4)
M(2)-As (Å)	2.5543(3)
M(1)-O (Å)	2.04346(0)
As– *M*(2)–As (°) [×4]	111.099(8)
As– *M*(2)–As (°) [×2]	106.263(14)

Table 4.3: Selected atomic distances and bond angles for $Sr_2CrMn_2As_2O_2$ from the Rietveld Refinement of powder X-ray diffraction data

4.2.2 Room temperature PND

A room temperature PND measurement was performed on a 3 g sample of $Sr_2CrMn_2As_2O_2$ (XX183) on the WISH diffractometer at ISIS to investigate the exact ordering of the mixed transition metals unambiguously. A plot of the refinement for $Sr_2CrMn_2As_2O_2$ (XX183) against room temperature PND data is shown in Figure 4.3, which shows a good fit between the observed data and the calculated result (the magnetic reflections observed in this pattern will be discussed in detail in section 4.2.4).

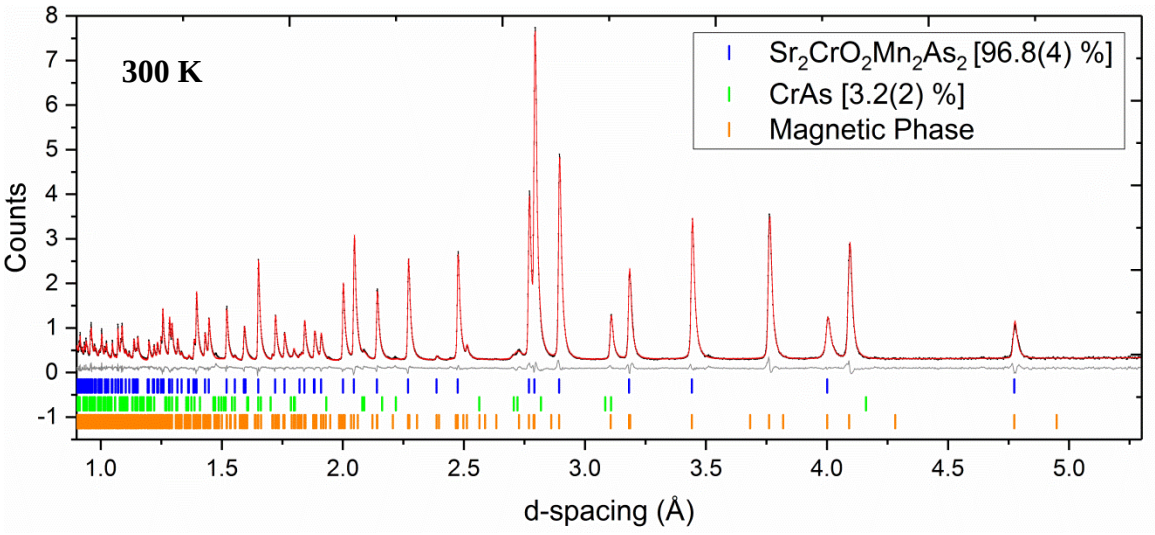

Figure 4.3: Rietveld refinement against the PND pattern of $Sr_2CrMn_2As_2O_2$ (XX183) at 300 K collected from bank 4 and 7 on WISH; R_{wp} = 3.13

The refinement of the structure of $Sr_2CrMn_2As_2O_2$ was carried out assuming that the *M*(1) and *M*(2) sites are fully occupied by a mixture of Mn and Cr in accord with the X-ray analysis. The results of Rietveld refinement show that the $M_2As_2^{2-}$ and MO_2^{2-} layers in $Sr_2CrO_2Mn_2As_2$ are occupied by both Cr^{2+} and Mn^{2+}. For the MO_2^{2-} layer, the occupancies of Cr^{2+} and Mn^{2+} are 0.79 (1) and 0.21 (1) respectively, whereas those of Cr^{2+} and Mn^{2+} in the $M_2As_2^{2-}$layer are 0.12 (1) and 0.88 (1). The actual composition of this compound is refined to be $Sr_2Cr_{0.79(1)}Mn_{0.21(1)}O_2Mn_{1.76(2)}Cr_{0.24(2)}As_2$ ($Sr_2Cr_{1.03(3)}Mn_{1.97(3)}As_2O_2$) and the free refinement of the occupancies of the two sites reflects the input stoichiometry within the uncertainty. While there is no complete chemical ordering of the transition metals in this compound under the applied reaction conditions. it is found that Cr^{2+} has a strong preference to occupy the site in the oxide layers but Mn^{2+} prefers the site in the arsenide layers, which is chemically sensible because Cr^{2+} is more oxophilic than Mn^{2+}. The detailed comparison between the refined results of PND and PXRD on the sample of $Sr_2Cr_{0.79}Mn_{0.21}O_2Mn_{1.76}Cr_{0.24}As_2$ is listed in Table 4.4.

	$Sr_2Cr_{0.79}Mn_{0.21}O_2Mn_{1.76}Cr_{0.24}As_2$ (XX183)	
Lattice parameters		
Diffractometer	WISH (ISIS)	I11 (MAC)
Wavelength (Å)	white beam	0.82525
Temperature (K)	300	298
a (Å)	4.091742(14)	4.086911(9)
c (Å)	19.0947(10)	19.05860(5)
V (Å^3)	247.513(3)	318.333(2)
R_{wp}	3.13	7.13
χ^2	0.04[a]	2.64
Sr–O (Å)	2.6205(5)	2.6173(3)
Sr–As (Å)	3.3083(5)	3.3017(3)
Cr/Mn (1)-As (Å)	3.2419(6)	3.2321(4)
Cr/Mn (2)-As (Å)	2.5558(4)	2.5543(3)
Cr/Mn (1)-O (Å)	2.04587(0)	2.04346(0)
As–Mn/Cr (2)–As (°) [×4]	111.052(11)	111.099(8)
As–Mn/Cr (2)–As (°) [×2]	106.35(3)	106.263(14)

Table 4.4: Results of refinement against ISIS PND (WISH diffractometer) and I11 PXRD (MAC detector) data for $Sr_2Cr_{0.79}Mn_{0.21}O_2Mn_{1.76}Cr_{0.24}As_2$ (XX183) at room temperature; [a] The very low value results from the way that the R_{exp} is calculated from the (.dat) file

4.2.3 Magnetic susceptibility measurements

The measurement of magnetisation versus field, *M* vs *H*, of $Sr_2Cr_{0.79}Mn_{0.21}O_2Mn_{1.76}Cr_{0.24}As_2$ is linear at 300 K (Figure 4.4(a)), confirming that no room-temperature ferromagnetic impurities are present in the sample. The temperature-dependent ZFC and FC magnetic susceptibility (χ) measurements of $Sr_2Cr_{0.79}Mn_{0.21}O_2Mn_{1.76}Cr_{0.24}As_2$ were measured in an applied field of 1000 Oe between 2 K and 330 K (Figure 4.4(b)). The sample is found to be paramagnetic at all measured temperatures and does not exhibit any signature of long-range magnetic ordering; however, neutron powder diffraction data (section 4.2.4) clearly shows that long-range antiferromagnetic ordering occurs below 450 K.

The field-cooled susceptibility curve is then fitted applying *eqn* 4.1:

$$\chi = \chi_0 + \frac{C}{(T-\theta)} \tag{4.1}$$

from which the temperature-independent susceptibility χ_0 is found to be 0.005870 (8) emu mol^{-1} and the extracted Curie constant is 0.1497(8) emuKmol^{-1}, corresponding to S=0.242(1) using spin-only approximation (see *eqn* 1.8). This S is equivalent to 3.46(1) % of all magnetic moments in one mole of $Sr_2Cr_{1.03(3)}Mn_{1.97(3)}As_2O_2$, with S=2 for Cr^{2+} and S=5/2 for Mn^{2+}. Therefore, the paramagnetism in $Sr_2Cr_{0.79}Mn_{0.21}O_2Mn_{1.76}Cr_{0.24}As_2$ arises from a very small number of spins and it is probably from an impurity phase.

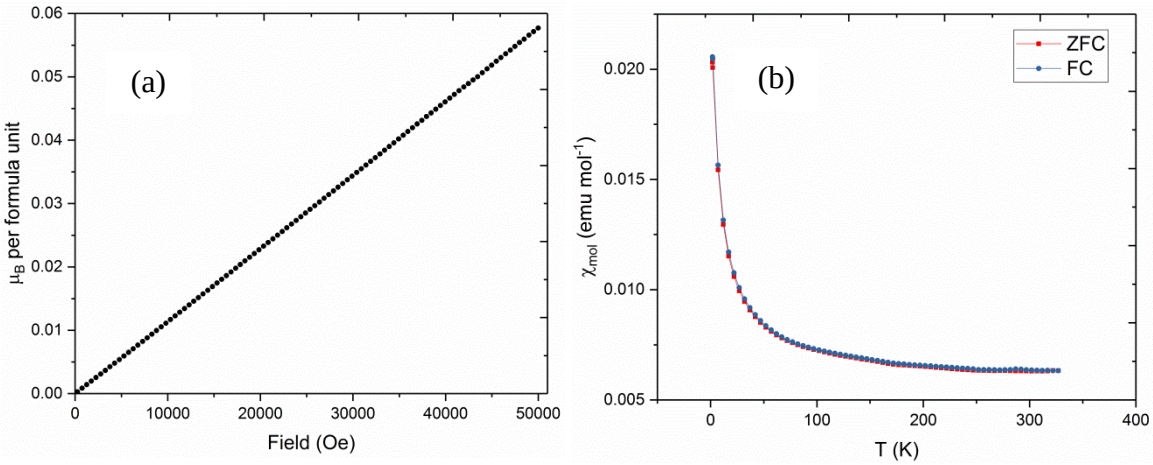

Figure 4.4: (a) Magnetic moment per mixed-metal ion of $Sr_2Cr_{0.79}Mn_{0.21}O_2Mn_{1.76}Cr_{0.24}As_2$ as a function of applied magnetic field, measured at 300 K; (b) The ZFC and FC magnetic susceptibility of $Sr_2Cr_{0.79}Mn_{0.21}O_2Mn_{1.76}Cr_{0.24}As_2$, measured at 1000 Oe between 2 K and 330 K

Furthermore, no divergence is observed between the ZFC and FC magnetic susceptibilities of $Sr_2Cr_{0.79}Mn_{0.21}O_2Mn_{1.76}Cr_{0.24}As_2$. The magnetisation isotherm measured at 5 K (Figure 4.5) also shows there is a straight line at low applied magnetic fields without any displacement from the origin (the loop is slightly open on the positive field side, so there could be a small glassy component to the magnetism).

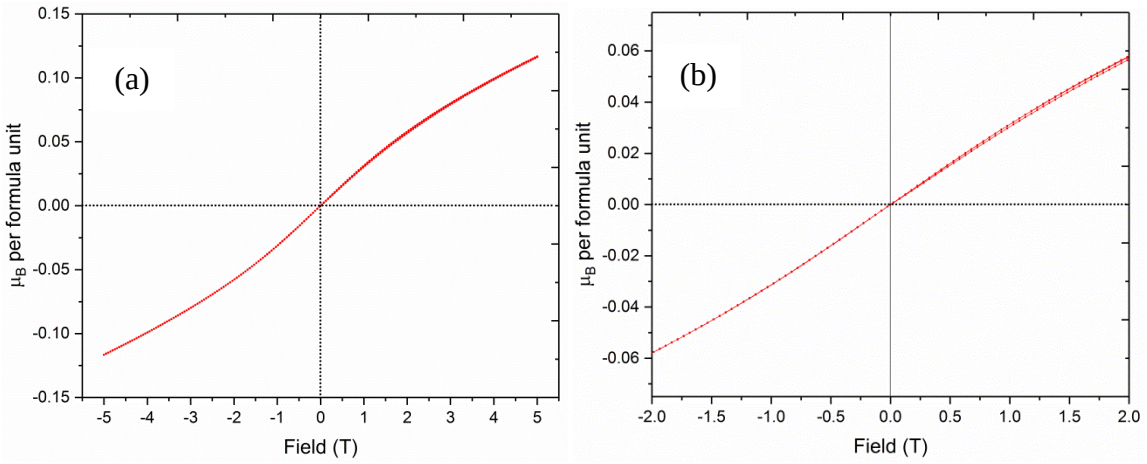

Figure 4.5: a) Magnetic moment per mixed-metal ion of $Sr_2Cr_{0.79}Mn_{0.21}O_2Mn_{1.76}Cr_{0.24}As_2$ as a function of applied magnetic field, measured at 5K in the range -5 ≤ H (T) ≤ +5; b) Zooming in the range of -2 T to 2 T

4.2.4 Variable temperature PND

In order to test whether this system also showed long range magnetic order like $Sr_2CrO_2Cr_2As_2$ and $Ba_2CrO_2Cr_2As_2$ which also show no obvious signature of long range magnetic order in the susceptibility measurements, variable-temperature neutron powder diffraction measurements were performed on a 3 g sample of $Sr_2Cr_{0.79}Mn_{0.21}O_2Mn_{1.76}Cr_{0.24}As_2$ (XX183) using the time-of-flight (ToF) WISH diffractometer at the ISIS Facility. The sample was placed into a 6 mm vanadium sample cylinder under an argon atmosphere in the glove box with an indium wire gasket to keep it air-tight. The sample was then measured in a low-temperature range of 7 K to 320 K in a helium cryostat and separately from room temperature to 450 K in a resistance furnace. The steel part of the sample holder was masked by cadmium metal (which strongly absorbs the neutron beam) below room temperature, while gadolinium foil was used for the same purpose above room temperature.

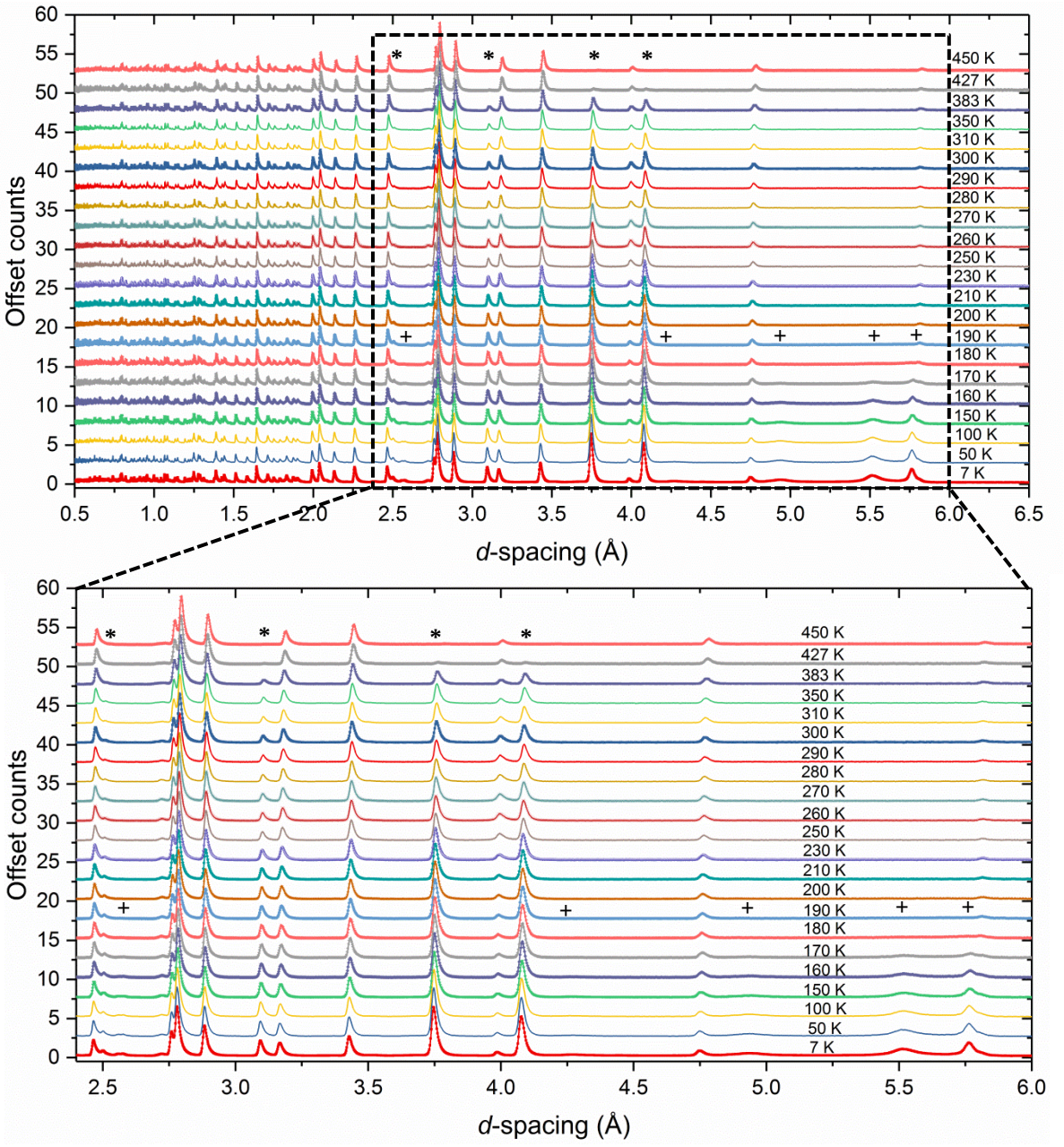

Figure 4.6: PND patterns obtained from banks 3 and 8 on the WISH, showing all magnetic Bragg reflections; The crosses (+) indicate the sets of magnetic reflections which are present from 7 K to 200 K, whereas for asterisks (*), the magnetic reflections are present until warming to 450 K

Data were collected from 7 K to 450 K, where several intense magnetic reflections are present and their intensities change continuously as a function of temperature. Figure 4.6 gives the diffraction patterns collected at these temperatures from the combination of banks 3 and 8 of the WISH instrument and clearly shows the appearance and growth of magnetic

Bragg reflections as the temperature cools. There are two sets of magnetic peaks marked with (*) and (+) present at 7 K. The intensities of the rather broad peaks with (+) have greatly diminished as the temperature increases and all of them are absent at around 200 K. The narrower peaks marked with (*) also decrease in intensity over the same range and they are completely absent in the PND pattern at 450 K. Similar to $Sr_2CrO_2Cr_2As_2$ and $Ba_2CrO_2Cr_2As_2$, the changes in intensities of two sets of magnetic peaks at different temperatures are due to the onset of ordering of the moments on the two mixed-transition-metal sublattices. In order to discuss the magnetic ordering in the oxide and arsenide layers separately, the PND data are divided into two main temperature ranges. Between 200 K and 450 K, magnetic reflections only appear due to ordering in the arsenide layers and the oxide-layer moments are magnetically disordered. Below 200 K, both sets of magnetic reflections are present in the PND pattern and their intensities grow consistently as the temperature cools.

Below 200 K, all magnetic Bragg reflections could be well indexed on a $\sqrt{2}a \times \sqrt{2}a \times c$ expansion of the unit cell, although for the ones on the Cr moments in the arsenide layer, a smaller magnetic unit cell can be used. The expanded cell was loaded into ISODISTORT[56] using the *P*1 space group and it was found that those intensities of the magnetic reflections could be well fitted using both $mX2^+(a)$ and $mM4^+(a)$ magnetic modes, in which the $mX2^+(a)$ mode represents nearest-neighbour antiferromagnetic coupling of the magnetic moments in the oxide layers with their moments directed along the *c*-direction, corresponding to those magnetic peaks with crosses (+) shown in the above PND data. Similarly, the values refined in the $mM4^+(a)$ mode indicate antiferromagnetic coupling of moments in the arsenide layers, with their orientations also aligned along the *c*-direction, corresponding to those magnetic peaks with asterisks (*).

In order to refine both magnetic modes together, a new space group was then calculated from ISODISTORT with a magnetic space group *Pbam* (55.353). The combination of both $mX2^+(a)$ and $mM4^+(a)$ magnetic modes gave a new magnetic model (as shown in Figure 4.7) to fit all of those magnetic peaks well in the PND data below 200 K, where both oxide and arsenide sublattices were antiferromagnetically ordered with their moments oriented along the *c*-axis and the moments in adjacent arsenide layers related by the vector ***c***/2 were aligned parallel with each other. The Rietveld refinements of the PND patterns and their magnetic models at 7 K and 150 K are plotted in Figure 4.8.

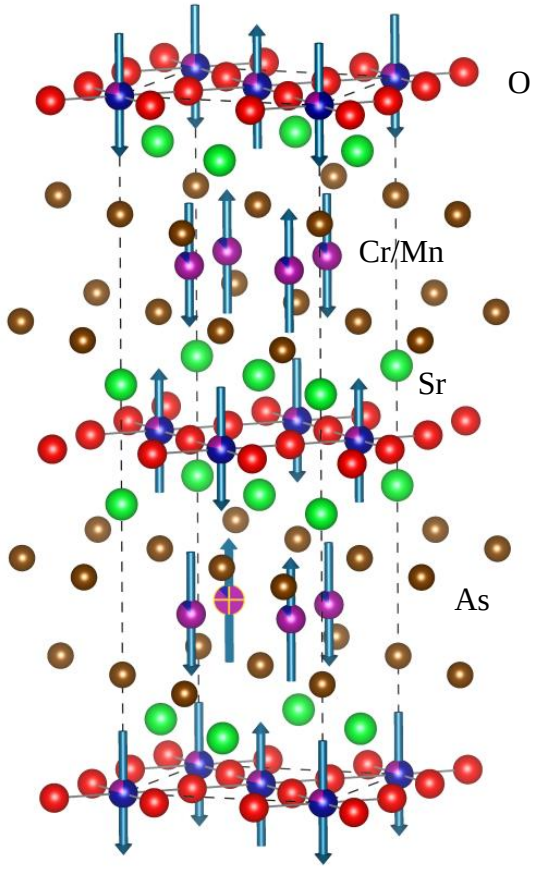

Figure 4.7: The magnetic model with combination of both $mX2^+(a)$ and $mM4^+(a)$ magnetic modes in the space group P*bam* (55.353); The blue (Cr^{2+}) and purple (Mn^{2+}) balls in the model represent the ratio of Cr^{2+} to Mn^{2+} occupying the mixed metal sites

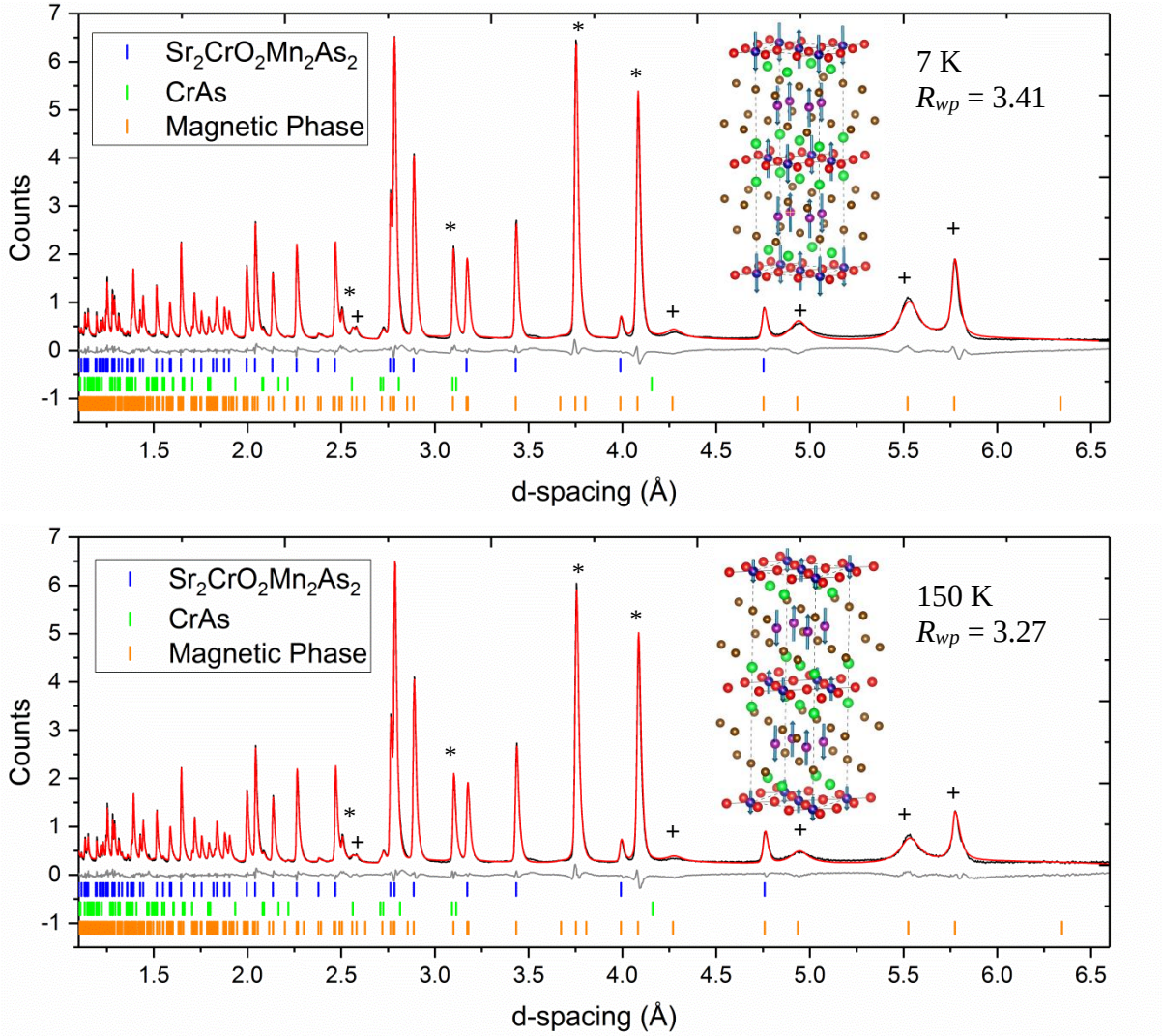

Figure 4.8: Rietveld refinements of $Sr_2Cr_{0.79}Mn_{0.21}O_2Mn_{1.76}Cr_{0.24}As_2$ (XX183) against PND patterns at 7 K and 150 K collected from bank 3 and 8 on WISH; The magnetic reflections with asterisks (*) and crosses (+) correspond to the magnetic moments observed in arsenide layer and oxide plane respectively

From 7 K to 200 K, the magnetic moments on the mixed-metal sites are antiferromagnetically ordered along the *c*-axis in both layers. However, the magnitude of moments drops much faster in the oxide layer than those in the arsenide layer in this temperature range. Above 200 K, the oxide-layer moments do not contribute to the magnetic scattering, and their magnetic moments are not ordered. Figure 4.9 shows the Rietveld refinement against the PND data (bank 3 and 8) and the magnetic model at 200 K. An impurity peak at the *d*-spacing of about 5.7 Å was also observed (see the arrow in Figure 4.9)

in the PND pattern at 200 K, which was from an unidentified nuclear impurity phase and appears at all temperatures. The position of this nuclear peak was close to those magnetic reflections generated from the ordered moments in the oxide planes and they were partially overlapped at the low-temperature diffraction patterns, making it difficult to obtain accurate results of the refinements on those magnetic peaks. Therefore, both intensity and position of this peak were first refined at 200 K and the result was then fixed to give one extra peak in the low-temperature (below 200 K) Rietveld refinements, which ensured the intensity of the overlapped magnetic peak to be refined more accurately.

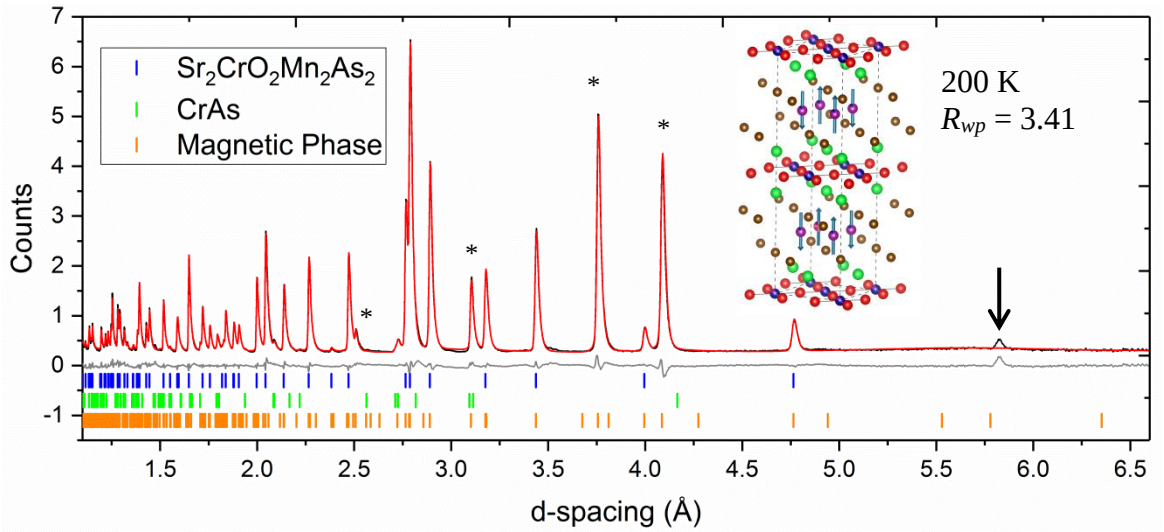

Figure 4.9: Rietveld refinements of $Sr_2Cr_{0.79}Mn_{0.21}O_2Mn_{1.76}Cr_{0.24}As_2$ (XX183) against PND patterns collected from bank 3 and 8 at 200 K on WISH; The magnetic reflections with asterisks (*) represents the magnetic moments observed in arsenide layer

Between 200 K and 450 K, only the arsenide-layer moments are magnetically ordered with the intensities of magnetic peaks (*) diminishing on warming to 450 K, as shown in Figure 4.6. However, in this temperature range several additional magnetic peaks were also observed in the diffraction pattern, overlapping with the corresponding nuclear reflections underneath. The intensities of these magnetic peaks grew quickly on warming to reach their maxima at 270 K and then diminished in intensity until completely absent at 383 K. The distinct change in the intensities of these extra magnetic peaks at different temperatures

indicates the fact that the orientations of some magnetic spins in arsenide layers are different in this temperature range. Figure 4.10 shows the intensity change of one of these extra magnetic reflections (marked with "#"), in comparison with a normal magnetic peak as discussed before (marked with "*") which drops consistently as the temperature goes up.

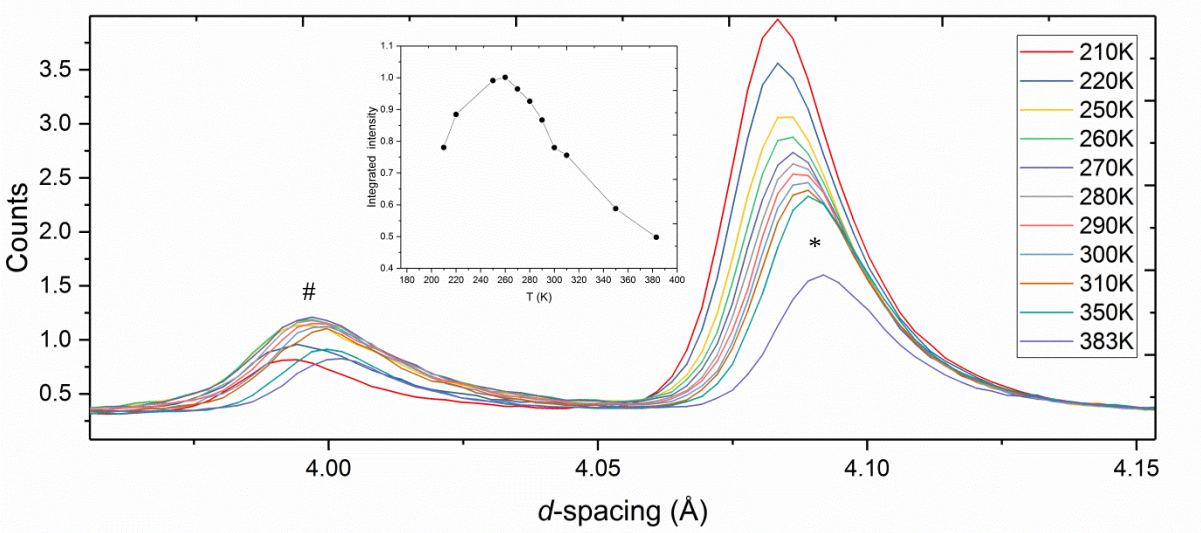

Figure 4.10: WISH PND data of $Sr_2Cr_{0.79}Mn_{0.21}O_2Mn_{1.76}Cr_{0.24}As_2$ (XX183) in the range 210 K to 383 K (combination of banks 3 and 8); The magnetic peak marked with (#) is one of these extra reflections observed from 210 to 383 K and the magnetic peak marked with (*) corresponds the antiferromagnetic ordering in the arsenide layer with the moment directed along *c*-axis; The inset shows the integrated intensity of the extra magnetic reflection "#" against temperature

These extra magnetic Bragg reflections could be indexed on the nuclear unit cell (but the resultant magnetic models below are still represented with a $\sqrt{2}a \times \sqrt{2}a \times c$ expansion of the unit cell; This is also applied for other compounds described in this chapter, for a good comparison of magnetic moments in both oxide and arsenide layers). With the help of ISODISTORT, it was found that the intensities of these peaks could be well fitted using a single magnetic mode, $mGM2^-(a)$, which corresponded to the magnetic moments coupled antiferromagnetically in the arsenide layers, with their moments directed along the *c*-axis. This result is similar to that refined by mode $mM4^+(a)$ (which is in accordance with the appearance of those normal magnetic peaks marked with "*" in the PND patterns), except that the magnetic spins in adjacent layers related by the vector $\boldsymbol{c}/2$ are aligned parallel in the

mode $mM4^+(a)$ rather than antiparallel in $mGM2^-(a)$. Therefore, in summary, two different magnetic structures are obtained for the mixed-metal ions in the arsenide layer in the temperature range of 200 K to 383 K. The magnetic model with antiparallel moments first occurs in the arsenide layer at 210 K and completely disappears on warming to 383 K, leaving the magnetic model with parallel moments remaining until the transition temperature (450 K). Figure 4.11 shows the appearance of two magnetic ordering schemes in $Sr_2Cr_{0.79}Mn_{0.21}O_2Mn_{1.76}Cr_{0.24}As_2$ at 270 K. The presence of this competing magnetic structure seems to be related to the magnetic ordering in the oxide layer since the disappearance of this extra phase on cooling occurs at the same temperature where the oxide ion moments start to order. Moreover, the magnitude of the intensity of magnetic peaks with the mode $mGM2^-(a)$ is much smaller than those with the $mM4^+(a)$ mode, which suggests that the antiparallel ordering scheme only represents a very small fraction of the two magnetic structures between 210 K and 383 K if one assumes these two magnetic structures have the same magnitude of magnetic moments. Figure 4.12 shows the fraction of the magnetic structure with antiparallel ordering in the temperature range of 210 K to 383 K. The fraction of the antiparallel scheme increases to a maximum of 17 % as the temperature is increased to 270 K, and then the fraction drops fast on warming up until the antiparallel ordering is completely absent at 383 K.

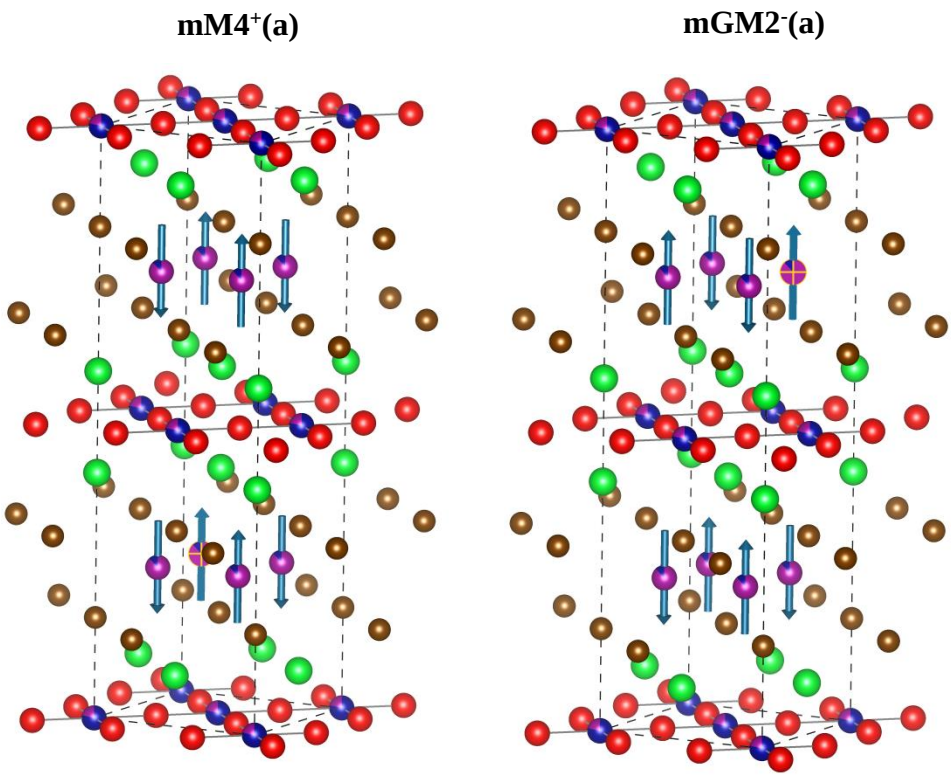

Figure 4.11: The ordering of magnetic moments in the arsenide layer of $Sr_2Cr_{0.79}Mn_{0.21}O_2Mn_{1.76}Cr_{0.24}As_2$ (XX183) at 270 K; Mode mM4$^+$(a) displays the moments in adjacent arsenide layers are coupled parallel with each other, comparing to the antiparallel ordering in mGM2$^-$(a)

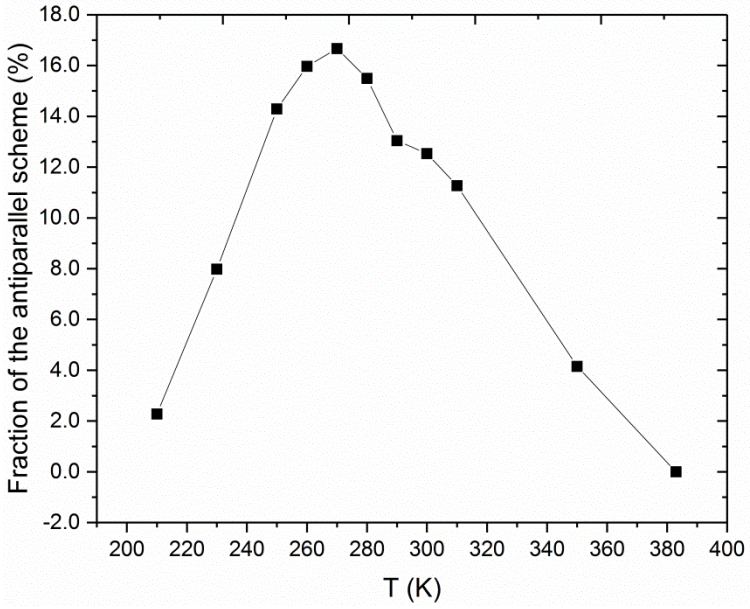

Figure 4.12: Fraction of the magnetic structure with antiparallel ordering in the temperature range of 210 K to 383 K in $Sr_2Cr_{0.79}Mn_{0.21}O_2Mn_{1.76}Cr_{0.24}As_2$

Figure 4.13 summarises the changes in the magnetic structures for the sample of $Sr_2Cr_{0.79}Mn_{0.21}O_2Mn_{1.76}Cr_{0.24}As_2$ (XX183) with temperature and Figure 4.14 shows the changes in the magnitudes of the refined moments and their components in both magnetic sublattices as a function of temperature. Moments in the arsenide layers reach a maximum value of 3.776(4) μB/M^{2+} at 7 K whilst those in the oxide planes reach 3.60(2) μB/M^{2+}, both of which are bigger than those in $Sr_2CrO_2Cr_2As_2$ (2.703(7) μB/Cr^{2+} in the arsenide layer and 3.352(8) μB/Cr^{2+} in the oxide layer) due to the substitution of Mn^{2+} (d^5) in both layers. Moreover, it is also worth noting that the magnitude of ordered M(2) moments in $Sr_2Cr_{0.79}Mn_{0.21}O_2Mn_{1.76}Cr_{0.24}As_2$ (3.776(4) μB/M^{2+}) at 7 K is also bigger than that (3.4(1) μB/Mn^{2+}) reported in $Sr_2MnO_2Mn_2As_2$ at 4 K.[38] The Mn/Cr disorder in this arsenide layer evidently does not lead to a reduced ordered moment.

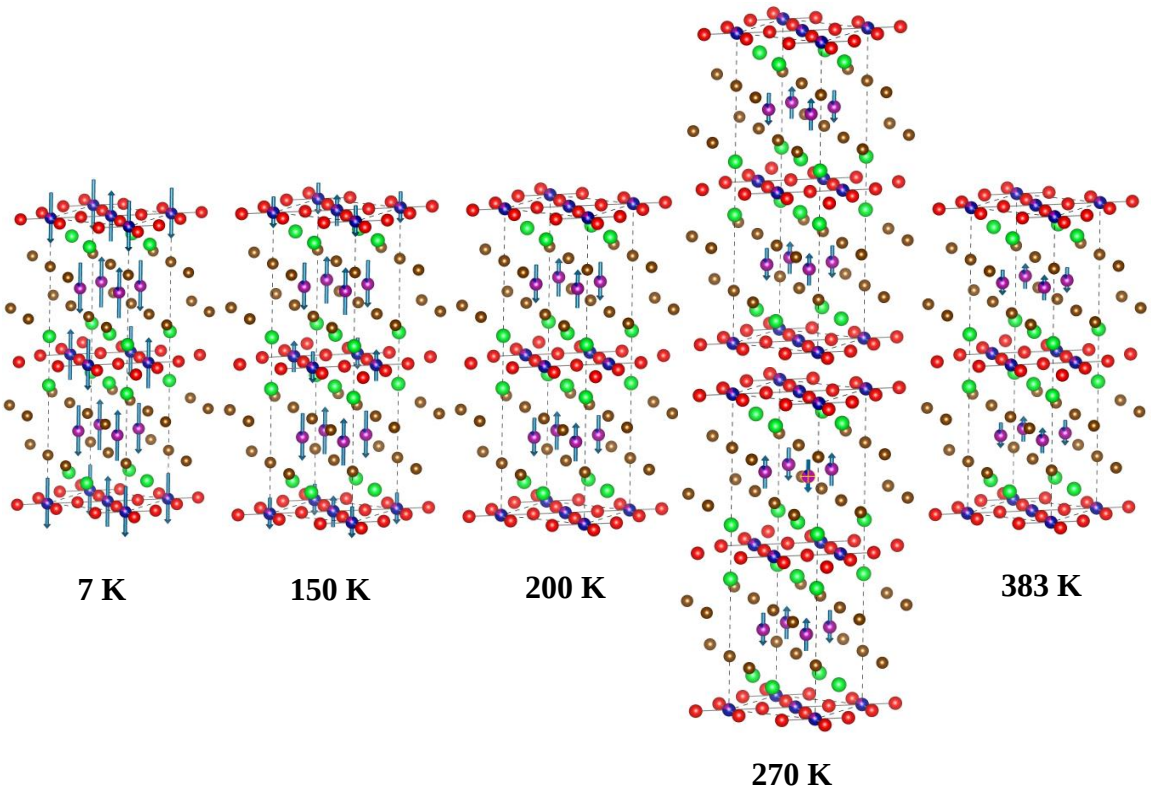

Figure 4.13: Magnetic unit cell of $Sr_2Cr_{0.79}Mn_{0.21}O_2Mn_{1.76}Cr_{0.24}As_2$ over the temperature range 7 K – 383 K, showing the magnitude and direction of magnetic moments for the two sublattices

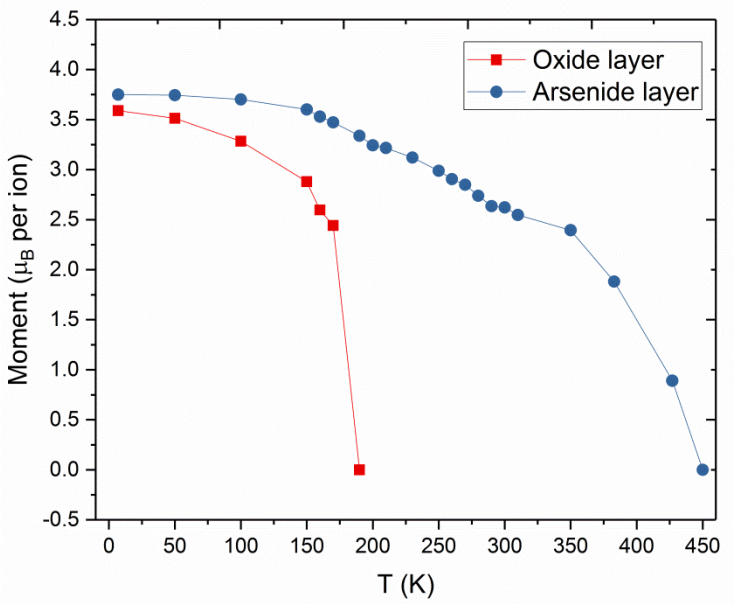

Figure 4.14: Magnitude of the long range ordered moments in the two sublattices of $Sr_2Cr_{0.79}Mn_{0.21}O_2Mn_{1.76}Cr_{0.24}As_2$ as a function of temperature

4.3 Synthesis and characterisation of $Sr_2Cr_{0.93}Mn_{0.07}O_2Mn_{0.92}Cr_{1.08}As_2$

A sample (XX182) with the composition of $Sr_2Cr_2MnAs_2O_2$ was synthesised using SrO (see section 2.1.3.1), Cr (Alfa, 99.95 %), Mn (Aldrich, 99.99 %) and As (Alfa, 99 %) as starting materials in the molar ratio 2: 2: 1: 1 in the glove box. A pellet of the starting materials was then placed in an Al_2O_3 crucible which was sealed inside a pre-dried evacuated silica tube. The reaction was first heated to 800 °C for 24 hours, after which the major phase in the product was found to be SrO, suggesting that the reaction was not complete at this temperature. Thus the mixture was then reground and sintered at a higher temperature of 1200 °C for another 4 hours followed by quenching the product in an ice bath.

4.3.1 Powder X-ray diffraction

The structure and composition of $Sr_2Cr_2MnAs_2O_2$ (XX182) were probed using high-resolution synchrotron powder X-ray diffraction (MAC detector on the I11 beamline). A refinement against the data is plotted in Figure 4.15, showing that the sample contains several small impurity peaks, which could not be indexed with any known impurity phase in the database. Similar to $Sr_2Cr_{0.79}Mn_{0.21}O_2Mn_{1.76}Cr_{0.24}As_2$ (XX183), the refinement result extracted from PXRD data showed that the oxide and arsenide layers of $Sr_2Cr_2MnAs_2O_2$ were fully occupied by Mn and Cr ions, although they cannot be distinguished except by PND experiments since PXRD cannot distinguish Cr and Mn atoms. The refined values against PXRD data of compound $Sr_2Cr_2MnAs_2O_2$ (XX182) are shown in Table 4.5, Table 4.6 and Table 4.7.

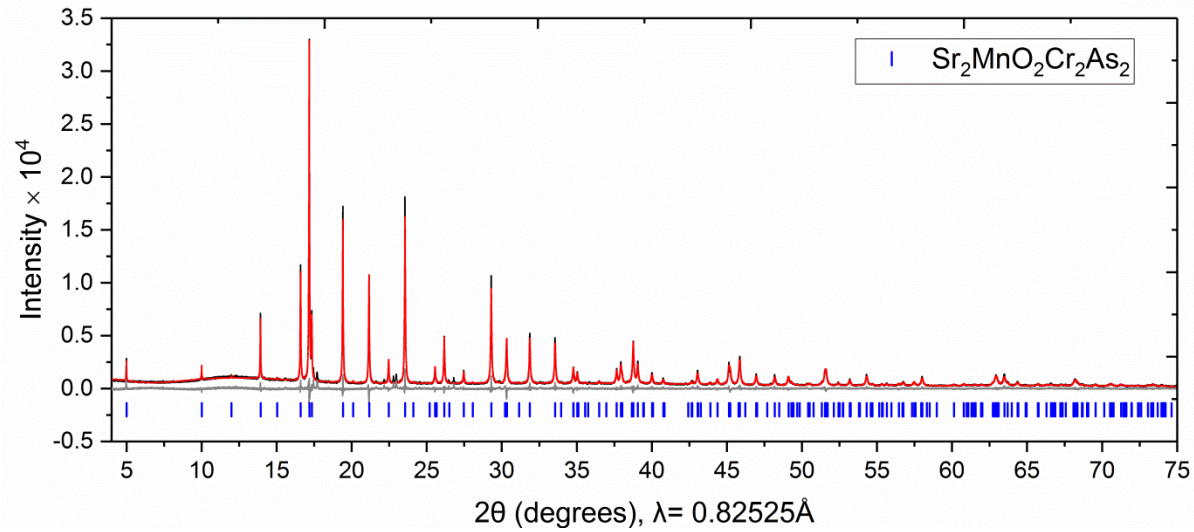

Figure 4.15: Rietveld refinement of $Sr_2Cr_2MnAs_2O_2$ (XX182) against synchrotron PXRD data measured at room temperature using MAC detector on the I11 beamline

	$Sr_2Cr_2MnAs_2O_2$
Diffractometer	I11 (MAC detector)
Temperature (K)	298
Space group	*I4/mmm*
a (Å)	4.04258(2)
c (Å)	18.92183(11)
V (Å^3)	309.229(3)
Phase density (g cm^{-3})	5.54191(5)
R_{wp}	7.75
χ^2	2.63

Table 4.5: Lattice Parameters of $Sr_2Cr_2MnAs_2O_2$ from Rietveld Refinement against PXRD data

I11 PXRD of $Sr_2Cr_2MnAs_2O_2$ at room temperature							
Atom	Site	*x*	*y*	*z*	U_{11} (Å^2)	U_{22} (Å^2)	U_{33} (Å^2)
Sr	4*e*	0	0	0.41288(3)	0.0015(2)	= U_{11}	0.0109(4)
Cr/Mn	2*a*	0	0	0	0.0029(4)	= U_{11}	0.0156(8)
Cr/Mn	4*d*	0	0.5	0.25	0.0021(3)	= U_{11}	0.0102(5)
As	4*e*	0	0	0.16968(2)	0.0037(2)	= U_{11}	0.0068(3)
O	4*c*	0	0.5	0	0.0018(8)[a] [U_{iso} (Å^2)]		

Table 4.6: Structure parameters for $Sr_2Cr_2MnAs_2O_2$ from the Rietveld Refinement against PXRD data; [a] O atoms were refined with the isotropic thermal displacement parameters

	I11 PXRD of $Sr_2Cr_2MnAs_2O_2$ at room temperature
Sr–O (Å)	2.6083(4)
Sr–As (Å)	3.2576(4)
M(1)-As (Å)	3.2107(4)
M(2)-As (Å)	2.5289(3)
M(1)-O (Å)	2.02129(0)
As–*M*(2)–As (°) [×4]	111.172(8)
As–*M*(2)–As (°) [×2]	106.121(14)

Table 4.7: Selected atomic distances and bond angles for $Sr_2Cr_2MnAs_2O_2$ from the Rietveld Refinement against PXRD data

4.3.2 Room temperature PND

Time of flight PND measurement was performed on a 3 g sample of $Sr_2Cr_2MnAs_2O_2$ (XX182) at room temperature on the WISH diffractometer at ISIS. A Rietveld refinement of $Sr_2Cr_2MnAs_2O_2$ against room temperature PND data collected from bank 3 and 8 is shown in Figure 4.16, where several impurity peaks are observed in the diffraction pattern, corresponding to those unindexed peaks seen at same *d*-spacings in the PXRD data. Furthermore, the appearance of magnetic reflections is also found in the room-temperature PND pattern, which will be discussed in detail in section 4.3.4. The refinement results of PND data are listed in Table 4.8, showing fair agreement with those derived from the Rietveld refinement against PXRD data. It was found by PND that Cr^{2+} and Mn^{2+} are partially ordered on both *M*(1) and *M*(2) sites in the oxide and arsenide layers. In the oxide layer, the fractional occupancies of Cr^{2+} and Mn^{2+} are refined to be 0.93(1) and 0.07 (1) respectively, whereas those of Cr^{2+} and Mn^{2+} in the $M_2As_2^{2-}$layer are 0.46(6) and 0.54(6). Thus the resultant freely-refined composition of this compound is determined to be $Sr_2Cr_{0.93(1)}Mn_{0.07(1)}O_2Mn_{0.92(2)}Cr_{1.08(2)}As_2$ ($Sr_2Cr_{2.01(3)}Mn_{0.99(3)}As_2O_2$), equal to the composition used in the synthesis within the uncertainty. Similar to the disordered ordering of Cr^{2+} and Mn^{2+} in $Sr_2Cr_{0.79}Mn_{0.21}O_2Mn_{1.76}Cr_{0.24}As_2$ (XX183) in section 4.2.2, the more oxophilic Cr^{2+} has a strong preference to occupy the *M*(1) sites in the oxide layers and Mn^{2+} prefers to occupy the *M*(2) sites in the arsenide layers.

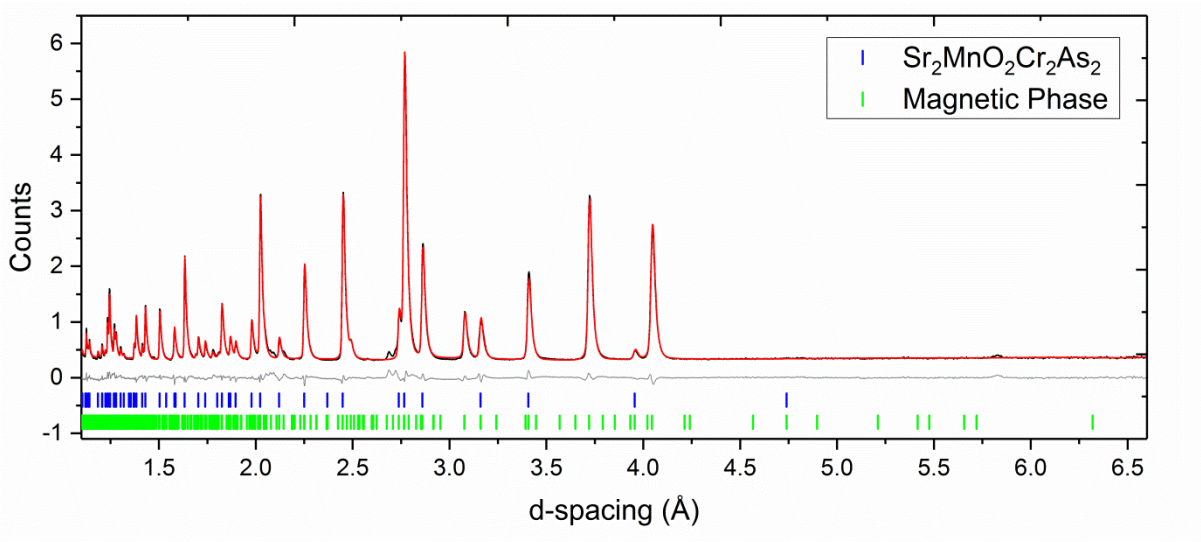

Figure 4.16: Rietveld refinement against the PND pattern of $Sr_2Cr_{0.93}Mn_{0.07}O_2Mn_{0.92}Cr_{1.08}As_2$ (XX182), measured at RT using WISH diffractometer on ISIS, R_{wp} = 3.43

	$Sr_2Cr_{0.93}Mn_{0.07}O_2Mn_{0.92}Cr_{1.08}As_2$ (XX182)	
Lattice parameters		
Diffractometer	WISH (ISIS)	I11 (MAC)
Wavelength (Å)	white beam	0.82525
Temperature (K)	293	298
a (Å)	4.044730(15)	4.04258(2)
c (Å)	18.95691(11)	18.92183(11)
V (Å^3)	310.132(3)	309.229(3)
R_{wp}	3.43	7.75
χ^2	0.03[a]	2.63
Sr–O (Å)	2.6125(4)	2.6083(4)
Sr–As (Å)	3.2625(4)	3.2576(4)
Cr/Mn (1)-As (Å)	3.2234(6)	3.2107(4)
Cr/Mn (2)-As (Å)	2.5274(4)	2.5289(3)
Cr/Mn (1)-O (Å)	2.02237(0)	2.02129(0)
As–Mn/Cr (2)–As (°) [×4]	111.082(11)	111.172(8)
As–Mn/Cr (2)–As (°) [×2]	106.30(3)	106.121(14)

Table 4.8: Results of refinement against PND (WISH diffractometer) and PXRD (MAC detector) data for $Sr_2Cr_{0.93}Mn_{0.07}O_2Mn_{0.92}Cr_{1.08}As_2$ (XX182) at room temperature; [a] The very low value results from the way that the R_{exp} is calculated from the (.dat) file

4.3.3 Magnetic susceptibility measurements

The *M* vs *H* isotherm of $Sr_2Cr_{0.93}Mn_{0.07}O_2Mn_{0.92}Cr_{1.08}As_2$ is linear at 300 K, suggesting the absence of room-temperature ferromagnetic impurities in the sample. The temperature-dependent ZFC and FC magnetic susceptibility (χ) measurements of $Sr_2Cr_{0.93}Mn_{0.07}O_2Mn_{0.92}Cr_{1.08}As_2$ were measured in an applied field of 1000 Oe between 2 K and 330 K (Figure 4.17). No divergence is observed between ZFC and FC magnetic susceptibilities of the sample. It appears that the sample has two broad cusps at 85 K and 200 K. The one at 85 K may correspond to the distinct antiferromagnetic ordering transition and the other one at 200 K is similar to the ferromagnetic impurity (Cr_4As_3) reported in $Sr_2CrO_2Cr_2As_2$ by previous Part II student Michael Jones.[81] Further characterisation was made using neutron powder diffraction.

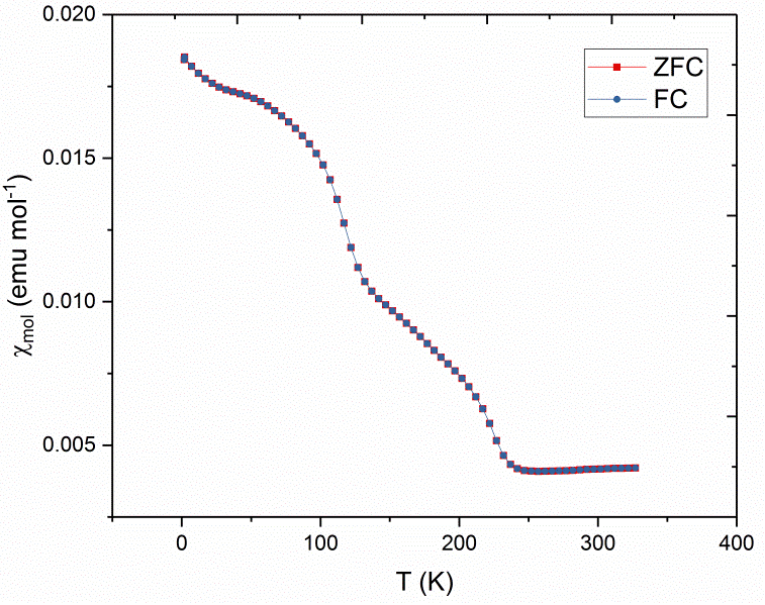

Figure 4.17: The ZFC and FC magnetic susceptibilities of $Sr_2Cr_{0.93}Mn_{0.07}O_2Mn_{0.92}Cr_{1.08}As_2$ (XX182) measured at 1000 Oe between 2 K and 330 K

4.3.4 Variable temperature PND

4.3.4.1 POLARIS

The magnetic ordering of $Sr_2Cr_{0.93}Mn_{0.07}O_2Mn_{0.92}Cr_{1.08}As_2$ was first probed using PND at room temperature on the POLARIS diffractometer at ISIS. Approximately 1 g of the sample was loaded into a vanadium can and sealed with indium wire under an inert argon atmosphere. The sample was then measured at POLARIS and the data was collected with five separate banks at room temperature. The diffraction pattern clearly showed the appearance of several magnetic peaks (marked with "+") at the *d*-spacings from 2.5 Å to 4.0 Å, which could be well indexed to the nuclear unit cell. ISODISTORT was applied to help the deduction of the magnetic models by using a magnetic subgroup *P*1(1.1), where refinement of all possible magnetic symmetry modes was attempted initially. It was found that the intensities of these magnetic peaks could be well fitted using $mM4^+(a)$ and $mM5^+(a)$ magnetic modes, both of which represented the checkerboard-type antiferromagnetically ordered magnetic moments in the arsenide layers. For $mM4^+(a)$, all the moments were refined to be aligned along the *c*-axis, while for the mM5+(a) model they lie within the *ab*-plane of arsenide layer. Both magnetic modes with their orientations of moments are shown in Figure 4.18, in which the blue (Cr^{2+}) and purple (Mn^{2+}) balls give the ratio of Cr^{2+} to Mn^{2+} in both sublattices of $Sr_2Cr_{0.93}Mn_{0.07}O_2Mn_{0.92}Cr_{1.08}As_2$.

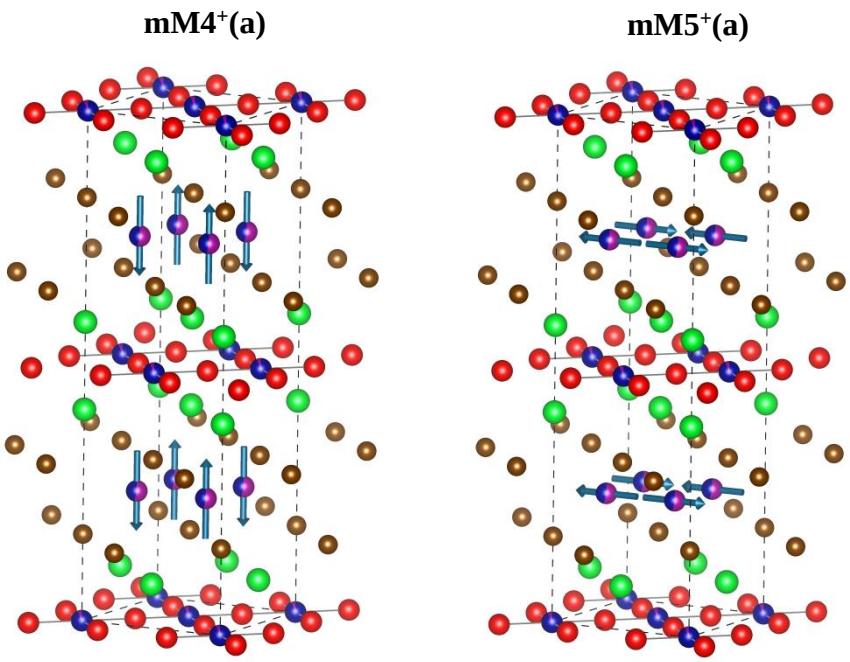

Figure 4.18: The magnetic modes mM4$^+$(a) and mM5$^+$(a) used in the refinement of magnetic model of $Sr_2Cr_{0.93}Mn_{0.07}O_2Mn_{0.92}Cr_{1.08}As_2$; The fractional occupancies of Cr^{2+} and Mn^{2+} in the oxide layer are refined to be 0.934(3) and 0.066(3) respectively, whereas those in the arsenide layer are 0.462(2) and 0.538(2)

The combination of both mM4$^+$(a) and mM5$^+$(a) magnetic modes showed that the moments in the arsenide layer were tilted with an arrangement of antiferromagnetic ordering (Figure 4.19). The resultant Rietveld refinement against the PND data collected from bank 3 on POLARIS is plotted in Figure 4.20 with $R_{wp} = 5.95$. The magnetic reflections in the diffraction pattern are comparable to those observed in the arsenide layer of Mn-rich sample, $Sr_2Cr_{0.79}Mn_{0.21}O_2Mn_{1.76}Cr_{0.24}As_2$ (XX183), in section 4.3.2, where two different magnetic structures are displayed in the temperature range between 200 K and 383 K. In order to see if this behaviour is also present in this Cr rich compound, the WISH diffractometer was then used at a wider range of temperatures.

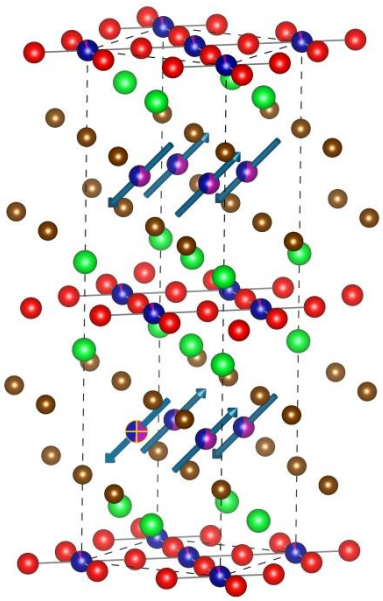

Figure 4.19: The magnetic model with the combination of both $mM4^+(a)$ and $mM5^+(a)$ magnetic modes in the arsenide layer

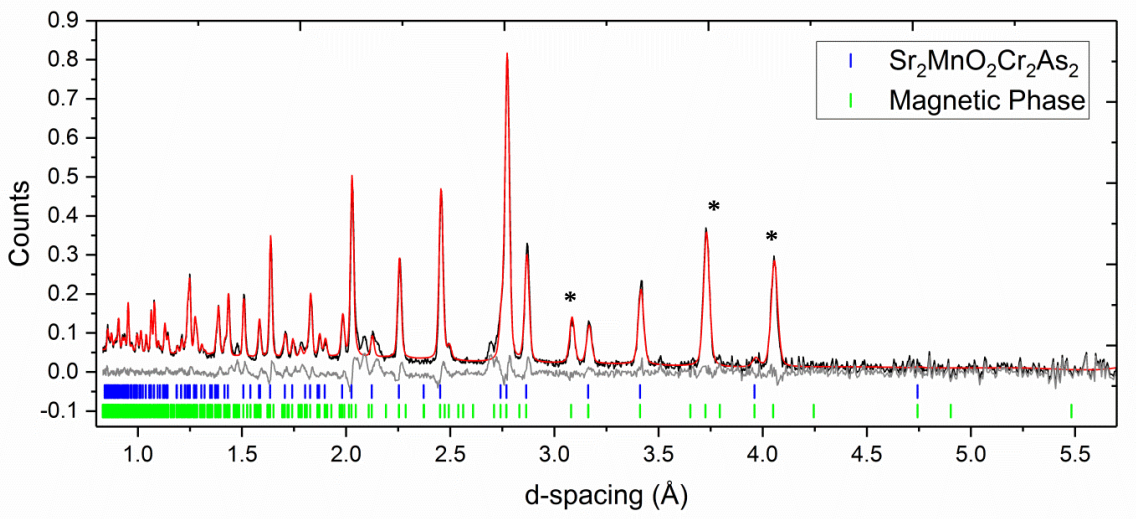

Figure 4.20: Rietveld refinement of $Sr_2Cr_{0.93}Mn_{0.07}O_2Mn_{0.92}Cr_{1.08}As_2$ (XX182) against PND data at room temperature from bank 3 on POLARIS

4.3.4.2 WISH

Approximately 3 g of the sample of $Sr_2Cr_{0.93}Mn_{0.07}O_2Mn_{0.92}Cr_{1.08}As_2$ (XX182) was measured on the WISH diffractometer to further investigate its magnetic ordering at variable temperatures. Data was collected from a minimum temperature of 7 K to a maximum temperature of 590 K, at which point all magnetic reflections had disappeared in the PND

pattern. Figure 4.21 displays the variable temperature data collected at these temperatures from banks 3 and 8 and clearly shows the appearance and growth of several magnetic Bragg reflections as the temperature cools. The changes in the intensity of two sets of magnetic peaks result from the ordering of the moments on the two mixed-metal sublattices occurring at different temperatures. The magnetic peaks marked with "*" and "+" present in the diffraction pattern at 7 K and persist on warming to 170 K. At 180K the peaks marked "+" have greatly diminished in intensity and are completely absent at around 230 K. However, the peaks marked "*" increase in intensity over the same temperature range until 180 K, after which these magnetic peaks start to diminish in intensity and are completely absent in the pattern at 590 K. This pattern of behaviour is broadly similar to that shown by the related phases described above and in Chapter 3. However, the unusual change in intensity of "*" peaks indicates the appearance of the spin-reorientation behaviour in this sample.

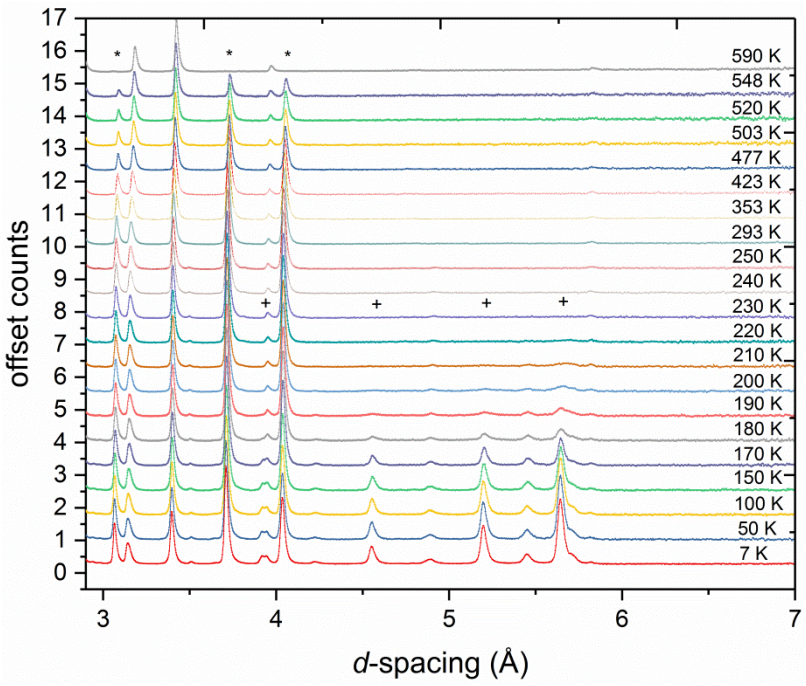

Figure 4.21: PND data obtained from banks 3 and 8 on the WISH, showing all magnetic Bragg reflections; The asterisks (*) and crosses (+) indicate the two sets of magnetic reflections which are present from 7 K to 590 K

Between 230 K and 590 K, the magnetic scattering marked with "*" was successfully modelled by just introducing long-range ordering of the magnetic moments in the arsenide layers. All these magnetic reflections could be indexed on the nuclear unit cell using both $mM4^+(a)$ and $mM5^+(a)$ magnetic modes as described for the room temperature data above. However, the refinement against variable temperature data on WISH between 230 K and 590 K also showed a reorientation of magnetic spins in the arsenide layers, with the tilted magnetic moments reorienting on warming to lie along the *c*-axis in this temperature range (similar to the case in the all-Cr compound).[78] By 423 K the reorientation transition was complete and the arsenide-layer moments were aligned antiferromagnetically along the *c*-axis in the magnetic unit cell until the transition temperature (590 K). Moreover, different to its Mn-rich analogue, only one magnetic structure was observed in the arsenide layers of this Cr-rich sample, in which the antiferromagnetically ordered spins in adjacent arsenide layers related by the vector *c*/2 are aligned parallel in the magnetic unit cell. Figure 4.22 shows the refinement and the magnetic models for $Sr_2Cr_{0.93}Mn_{0.07}O_2Mn_{0.92}Cr_{1.08}As_2$ at 230 K and 423 K with their magnetic reflections labelled by "*".

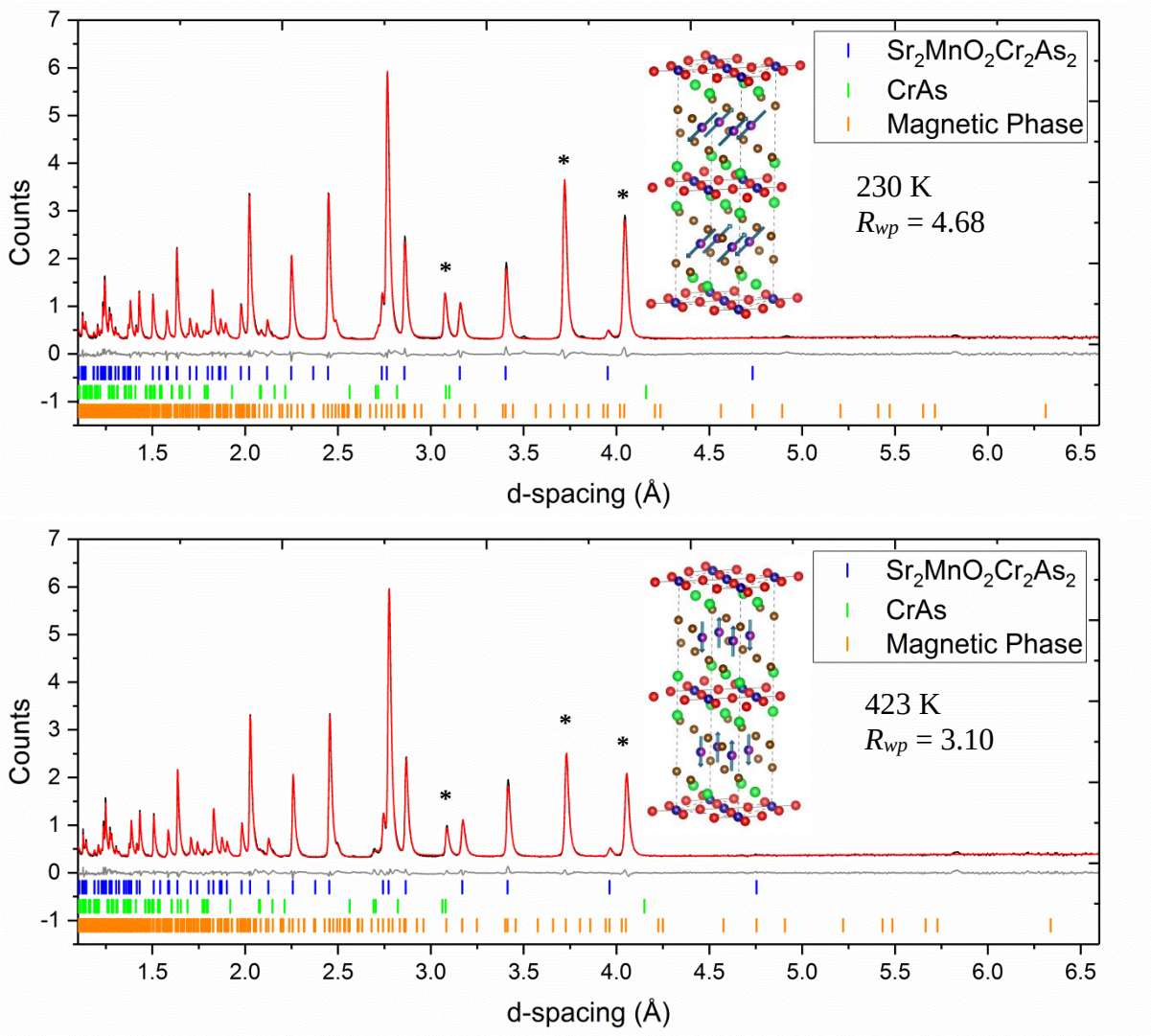

Figure 4.22: Rietveld refinement of $Sr_2Cr_{0.93}Mn_{0.07}O_2Mn_{0.92}Cr_{1.08}As_2$ against PND data at 230 K and 423 K collected from bank 3 and 8 on WISH

Below 230 K, several additional magnetic peaks (labelled with "+" in Figure 4.21) started to appear in the diffraction pattern when the sample was cooled down, which corresponded to long-range magnetic ordering of the magnetic moments in the oxide layer. In contrast to those in the arsenide layers, the magnetic reflections appeared in the oxide layers were indexed on a $\sqrt{2}a \times \sqrt{2}a \times 2c$ expansion of the unit cell. After attempts to refine different magnetic models against the PND data, it was found that the intensities of these magnetic reflections could be well fitted using two magnetic modes, $mX2^+(a)$ and mP4(a,b), both of which have the magnetic moments in the oxide layers antiferromagnetically aligned with

their nearest neighbour spins. For $mX2^+(a)$, the magnetic spins in adjacent layers related by the vector *c* were aligned parallel while they are antiparallel in the mode mP4(a,b). Therefore, similar to the phenomenon observed for the arsenide-layer moments of the Mn-rich sample ($Sr_2Cr_{0.79}Mn_{0.21}O_2Mn_{1.76}Cr_{0.24}As_2$), two different magnetic models were also obtained for oxide-layer moments below 230 K. The intensity arising from the mP4(a,b) mode is much bigger than that from the $mX2^+(a)$ mode at low temperatures, suggesting that the antiparallel ordering scheme dominates if one assumes these two magnetic structures have the same magnitude of magnetic moments. Figure 4.23 shows the two magnetic ordering schemes in the oxide layer at 7 K.

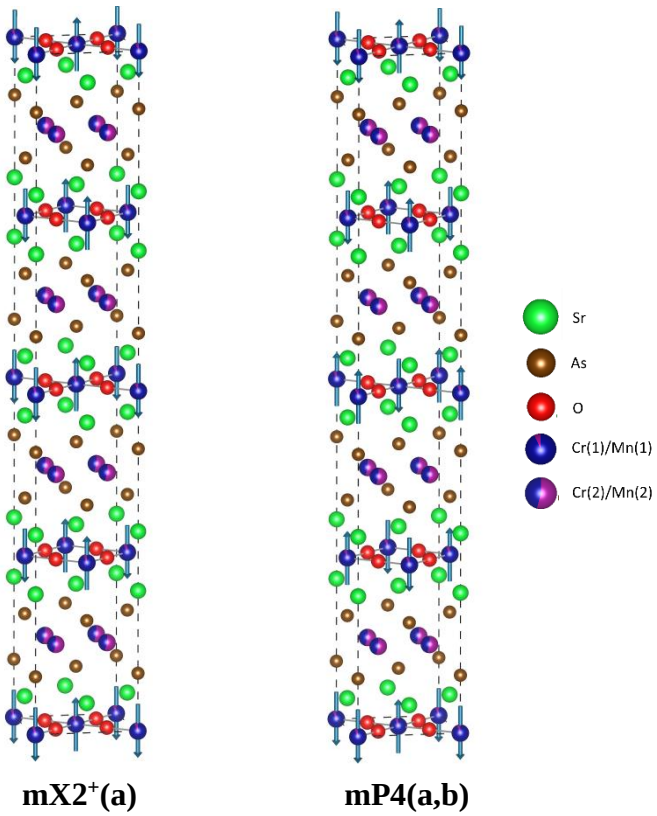

Figure 4.23: The magnetic modes $mX2^+(a)$ and mP4(a,b) used in the refinement of magnetic model of $Sr_2Cr_{0.93}Mn_{0.07}O_2Mn_{0.92}Cr_{1.08}As_2$; $mX2^+(a)$ displays the moments in adjacent oxide layers are coupled parallel with each other, comparing to the antiparallel ordering in mP4(a,b)

Figure 4.24 shows the fraction of the magnetic structure with parallel ordering in the temperature range of 7 K to 230 K. The fraction of parallel scheme increases to 50 % as the temperature is heated to 230 K.

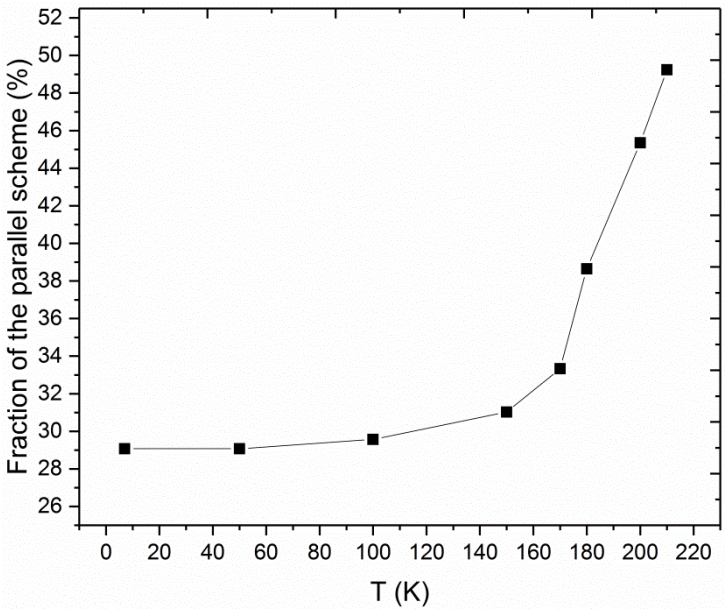

Figure 4.24: Fraction of the magnetic structure with parallel in the temperature range of 7 K to 230 K in $Sr_2Cr_{0.93}Mn_{0.07}O_2Mn_{0.92}Cr_{1.08}As_2$

For the arsenide layer in the temperature range below 230 K, the related magnetic reflections were indexed on a $\sqrt{2}a \times \sqrt{2}a \times c$ expansion of the unit cell, and the magnitude of refined magnetic moments was found to grow as the temperature decreases. Figure 4.25 shows the refinement of the PND data collected at 7 K and 150 K, with magnetic structures for the moments in both oxide and arsenide layers. A spin-reorientation was observed in the arsenide layers, where the magnetic moments gradually tilted towards the *ab*-plane as the sample was cooled to 7 K. The angle relative to *c*-axis as a function of temperature is plotted in Figure 4.26.

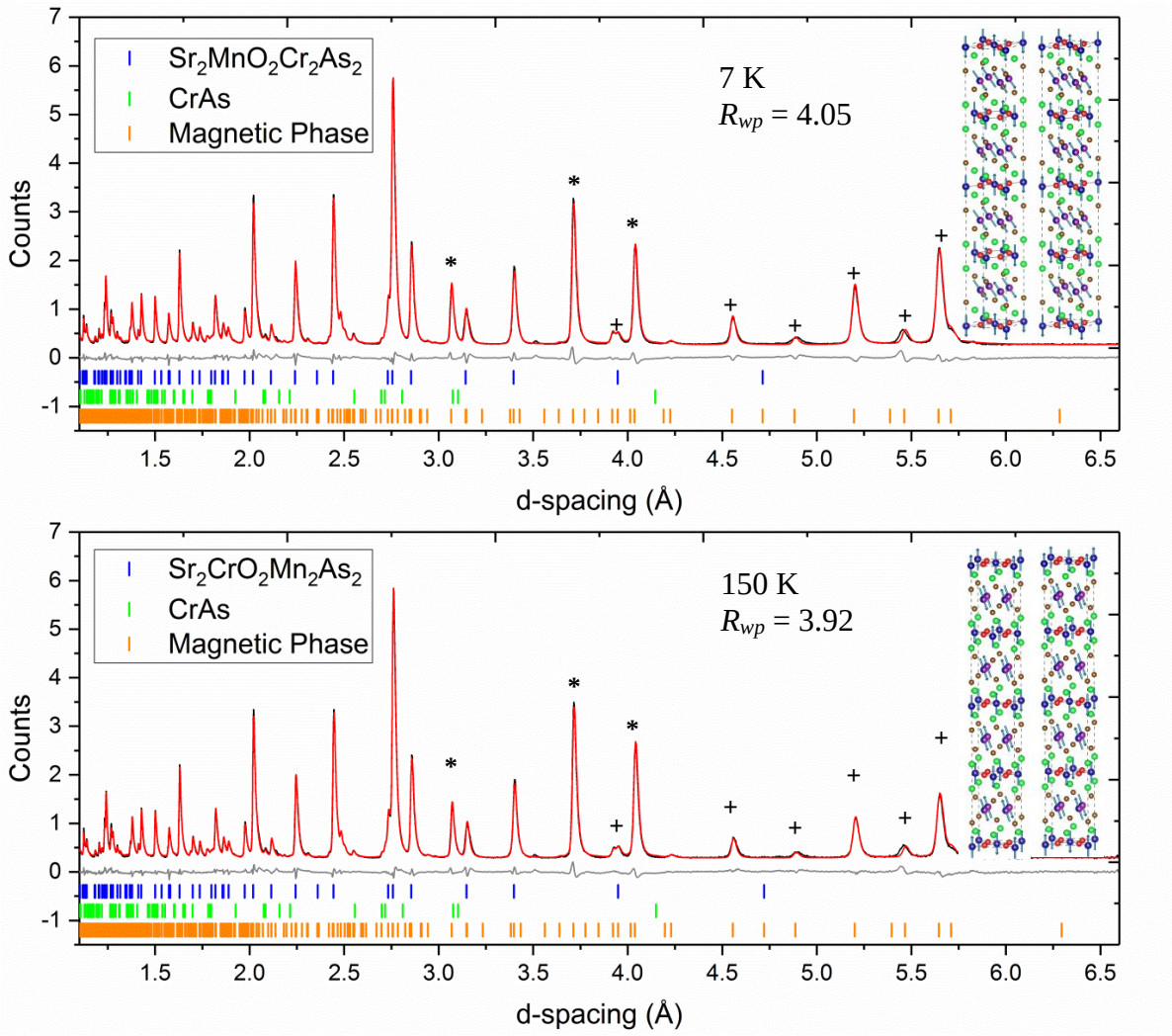

Figure 4.25: Rietveld refinements and resultant magnetic structures of $Sr_2Cr_{0.93}Mn_{0.07}O_2Mn_{0.92}Cr_{1.08}As_2$ (XX182) against PND patterns collected from bank 3 and 8 at 7 K and 150 K on WISH; The magnetic reflections with asterisks (+) and crosses(*) represent the magnetic moments observed in oxide and arsenide layers respectively

If the refinement results of PND data on both oxide and arsenide layers are combined together, then the changes in the magnetic model against the whole-temperature range can be plotted in Figure 4.27, where a gradual spin reorientation of moments in the arsenide layer is displayed between 7 K to 423 K, with the tilted magnetic moments rotating to lie in the *c*-axis at 423 K.

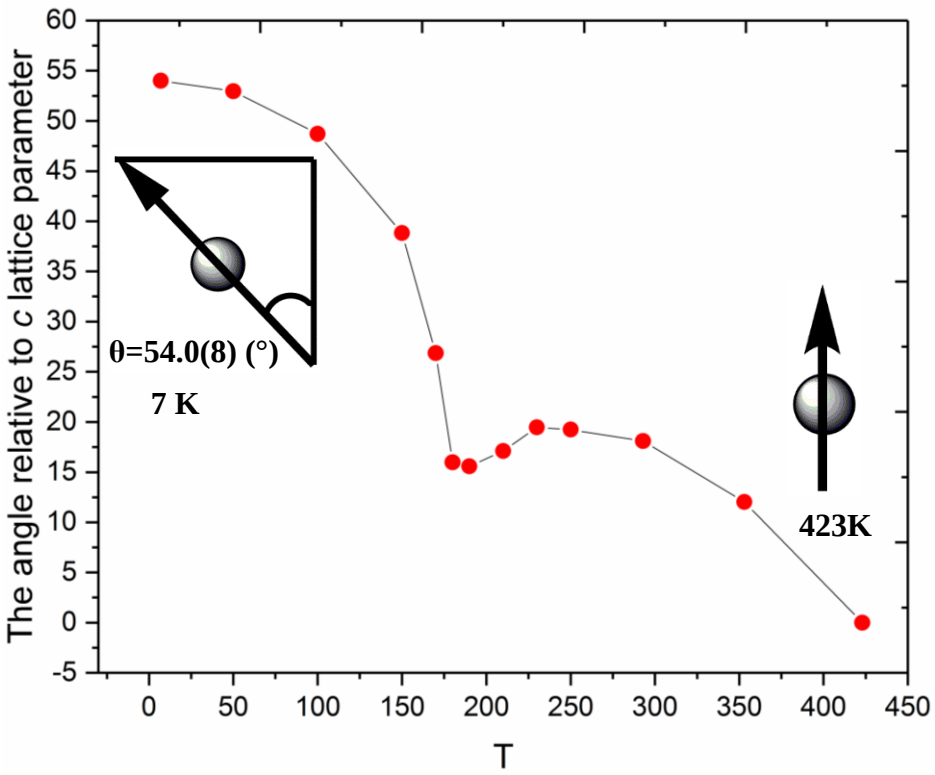

Figure 4.26: The angle relative to *c* lattice parameter at different temperatures, refined using WISH PND data

Moreover, in the oxide layer, two different magnetic structures are obtained to account for the corresponding magnetic reflections below 230 K, and the refined antiferromagnetically ordered moments are always aligned along the *c*-axis. The changes in the magnitudes of the refined magnetic moments and the arsenide-layer components in the directions along both *c*-axis and *ab*-plane are shown in Figure 4.28. Similar to the Mn-rich sample of $Sr_2Cr_{0.79}Mn_{0.21}O_2Mn_{1.76}Cr_{0.24}As_2$ (Figure 4.14), the magnetic moments in both layers of $Sr_2Cr_{0.93}Mn_{0.07}O_2Mn_{0.92}Cr_{1.08}As_2$ increase in magnitude as the sample is cooled down to 7 K, at which point they reach their maxima with a value of 2.71(2) $\mu B/M^{2+}$ for the moments in the oxide layer and 3.10(1) $\mu B/M^{2+}$ for the moments in the arsenide layer. It is found that the moments in oxide and arsenide layers are smaller than the corresponding moments in both layers in $Sr_2Cr_{0.79}Mn_{0.21}O_2Mn_{1.76}Cr_{0.24}As_2$ at 7 K (3.60(2) $\mu B/M^{2+}$ for oxide layer and 3.776(4) $\mu B/M^{2+}$ for arsenide layer), which is because less Cr^{2+} ions are substituted by Mn^{2+}

in both layers of $Sr_2Cr_{0.93}Mn_{0.07}O_2Mn_{0.92}Cr_{1.08}As_2$ and that the average moment per metal ion has decreased, comparing to that in the Mn-rich compound $Sr_2Cr_{0.79}Mn_{0.21}O_2Mn_{1.76}Cr_{0.24}As_2$. More details about the magnitude of ordered moments in these Cr and Mn $Sr_2Mn_3As_2O_2$-structure-type compounds will be discussed in section 4.5.

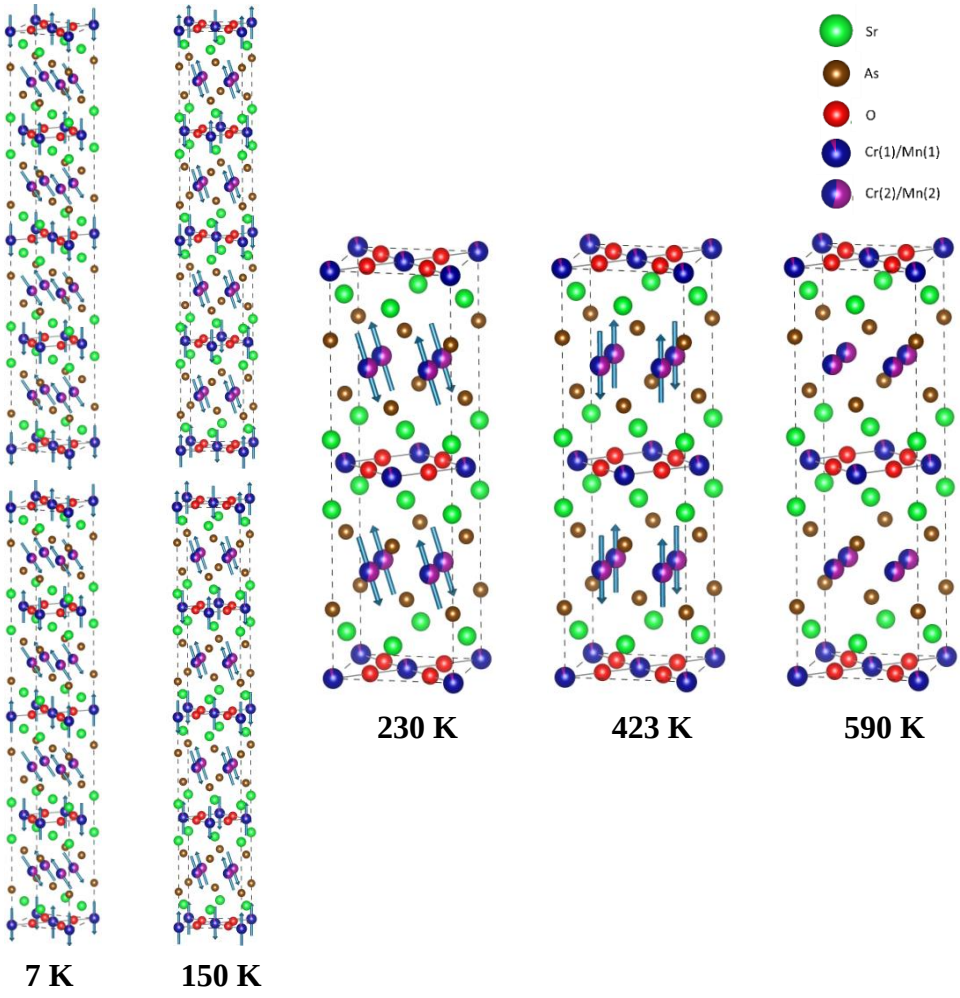

Figure 4.27: Magnetic structures of $Sr_2Cr_{0.93}Mn_{0.07}O_2Mn_{0.92}Cr_{1.08}As_2$ over the temperature range 7 K – 590 K, showing the magnitude and direction of magnetic moments in the two sublattices

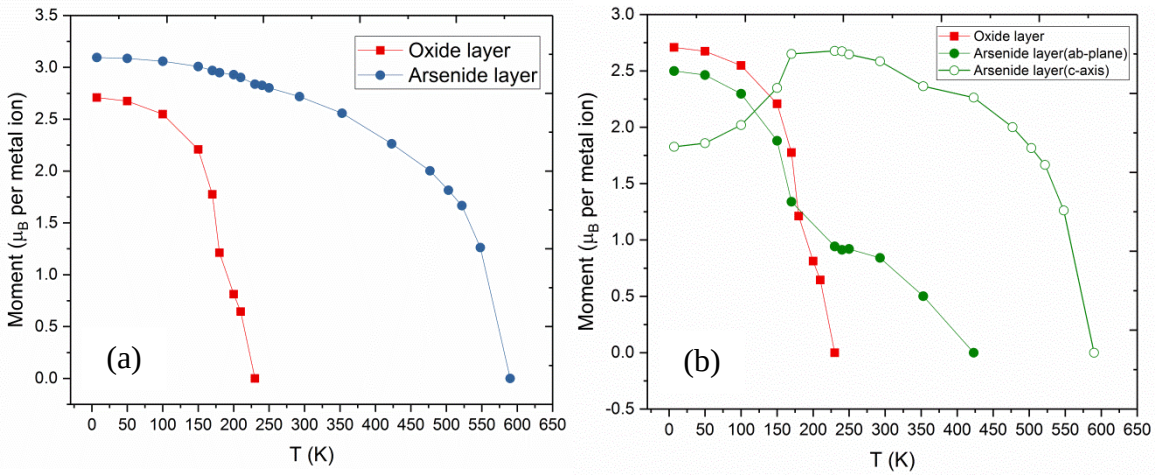

Figure 4.28: (a) Magnitudes of the long range ordered moments in the two sublattices of $Sr_2Cr_{0.93}Mn_{0.07}O_2Mn_{0.92}Cr_{1.08}As_2$ as functions of temperature; (b) Magnitudes and directions of moments in the arsenide layer

4.4 Synthesis and characterisation of $Ba_2CrO_2Cr_{1.02}Mn_{0.98}As_2$

Similar to the synthesis of its Sr analogues, the sample with the intended composition of $Ba_2Cr_2MnAs_2O_2$ was prepared by grinding together BaO (Aldrich, 99.99 %), Cr (Alfa, 99.95 %), Mn (Aldrich, 99.99 %) and As (Alfa, 99 %) in the molar ratio 2: 2: 1: 2 in the glove box. The mixture was then pressed into a pellet and loaded in an Al_2O_3 crucible which was sealed inside an evacuated silica tube. The tube was heated in a furnace to 800 °C for 24 hours at a slow rate of 2 °C/min. The product was then reground and repressed into a pellet and sintered at 1200 °C for 3 hours (10 °C/min) followed by quenching the solid in an ice bath. The synthesis of Mn-rich analogue $Ba_2CrMn_2As_2O_2$ was also tried in this work, but unfortunately this was not successful.

4.4.1 Powder X-ray diffraction

The structure and composition of $Ba_2Cr_2MnAs_2O_2$ (XX114B) were investigated using high-resolution synchrotron powder X-ray diffraction (MAC detector on the I11 beamline) at room temperature. X-rays show that both sites are fully occupied and neutrons were then used to work out the distribution. Rietveld refinement against the collected PXRD pattern is plotted in Figure 4.29 and the refined parameters are presented in Tables 4.9, 4.10 and 4.11.

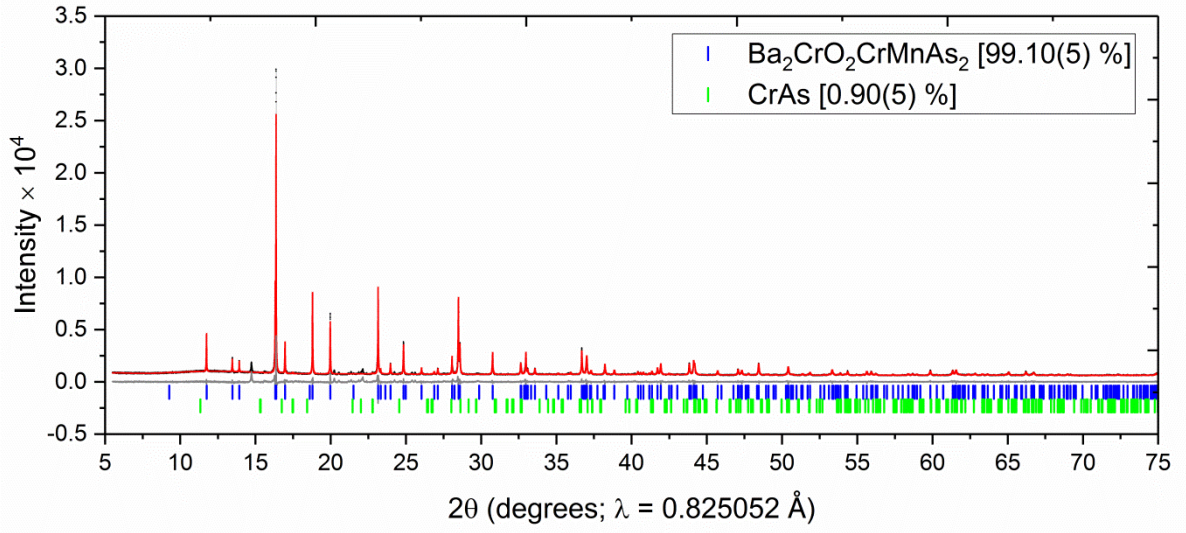

Figure 4.29: Rietveld refinement of $Ba_2Cr_2MnAs_2O_2$ (XX114B) against synchrotron PXRD data measured at room temperature using MAC detector on the I11 beamline

	$Ba_2Cr_2MnAs_2O_2$
Diffractometer	I11 (MAC detector)
Temperature (K)	298
Space group	*I4/mmm*
a (Å)	4.11105(2)
c (Å)	20.4148(1)
V (Å^3)	345.025(3)
Phase density (g cm^{-3})	5.962(4)
R_{wp}	11.90
χ^2	2.82

Table 4.9: Lattice Parameters of $Ba_2Cr_2MnAs_2O_2$ from Rietveld Refinement

I11 PXRD of $Ba_2Cr_2MnAs_2O_2$ at room temperature							
Atom	Site	*x*	*y*	*z*	U_{11} (Å^2)	U_{22} (Å^2)	U_{33} (Å^2)
Ba	4*e*	0	0	0.41122(3)	0.0072(2)	= U_{11}	0.0041(3)
Cr/Mn	2*a*	0	0	0	0.01(1)	= U_{11}	0.02(2)
Cr/Mn	4*d*	0	0.5	0.25	0.0114 (7)	= U_{11}	0.0013(8)
As	4*e*	0	0	0.17672(5)	0.0087(4)	= U_{11}	0.0050(7)
O	4*c*	0	0.5	0		0.009(2)[a] [U_{iso} (Å^2)]	

Table 4.10: Structure parameters for $Ba_2Cr_2MnAs_2O_2$ from the Rietveld Refinement of powder X-ray diffraction data; [a] O atoms were refined with the isotropic thermal displacement parameters

	I11 PXRD of $Ba_2Cr_2MnAs_2O_2$ at room temperature
Ba–O (Å)	2.7405(5)
Ba–As (Å)	3.4166(7)
M(1)-As (Å)	3.6077(11)
M(2)-As (Å)	2.5423(7)
M(1)-O (Å)	2.05552(0)
As–*M*(2)–As (°) [×4]	110.259(19)
As–*M*(2)–As (°) [×2]	107.91(4)

Table 4.11: Selected atomic distances and bond angles for $Ba_2Cr_2MnAs_2O_2$ from the Rietveld Refinement of powder X-ray diffraction data

4.4.2 Room temperature PND

Room temperature TOF PND was performed on a 2 g sample of $Ba_2Cr_2MnAs_2O_2$ (XX114B) using the WISH diffractometer at ISIS. A structural model was applied where the M^{2+} cation sites in both oxide and arsenide layers have a mixed occupancy of Cr and Mn. A plot of Rietveld refinement against room temperature PND data is shown in Figure 4.30, which gives a good agreement between the observed and calculated data (the observed magnetic reflections will be discussed in detail in section 4.4.3). CrAs was found to be present in the

product at less than 1 wt %. Additionally, several other small impurity peaks were also observed in the diffraction pattern (estimated to be less than 1 wt %, compared to CrAs), which cannot be indexed with any known phase in the database.

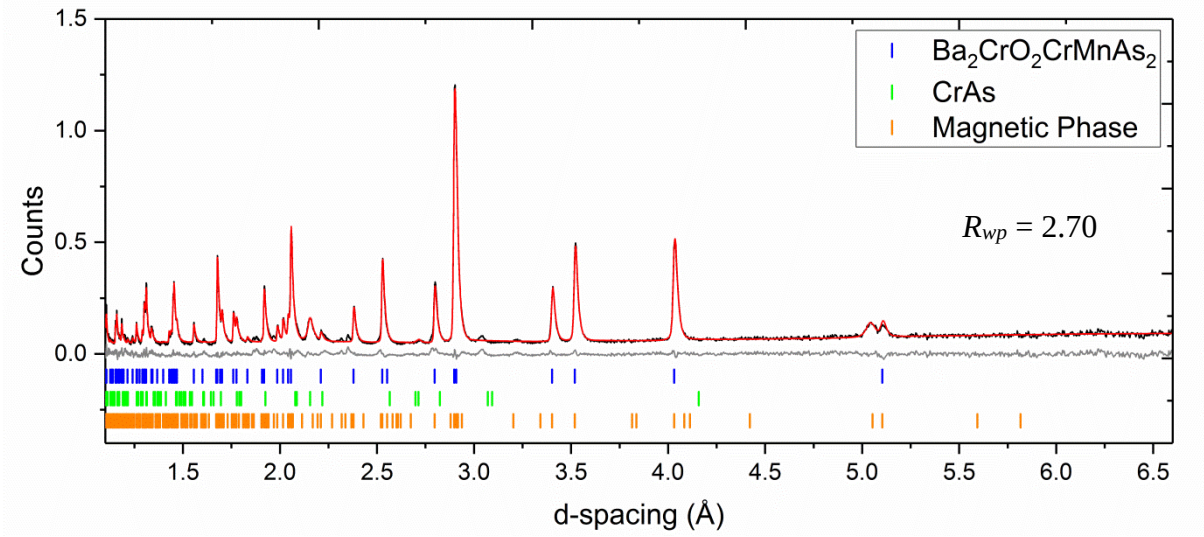

Figure 4.30: Rietveld refinement against the PND pattern of $Ba_2Cr_2MnAs_2O_2$ (XX114B) at room temperature collected from bank 3 and 8 on WISH

The refinement results showed that the oxide layer was fully occupied by Cr^{2+} and the arsenide layer was occupied by mixed M^{2+} cations with the fractional occupancies of Cr^{2+} and Mn^{2+} refined to be 0.510(2) and 0.490 (2) respectively. Therefore, the freely-refined composition of this compound is determined to be $Ba_2CrO_2Cr_{1.020(4)}Mn_{0.980(4)}As_2$ which is a chemically sensible result as Cr^{2+} is more oxophilic than Mn^{2+}, and corresponds to the composition used in the synthesis within the uncertainty. This is also consistent with the refinement results in other mixed-metal Sr analogues and confirms the preferred chemical ordering of Cr^{2+} and Mn^{2+} in the oxide and arsenide layers in these compounds. The detailed comparison between the refined results of PND and PXRD on the sample of $Ba_2CrO_2Cr_{1.02}Mn_{0.98}As_2$ is listed in Table 4.12.

	$Ba_2CrO_2Cr_{1.02}Mn_{0.98}As_2$ (XX114B)	
Lattice parameters		
Diffractometer	WISH (ISIS)	I11 (MAC)
Wavelength (Å)	white beam	0.825052
Temperature (K)	293	298
a (Å)	4.11251(3)	4.11105(2)
c (Å)	20.4162(2)	20.4148(1)
V (Å^3)	345.294(5)	345.025(3)
R_{wp}	2.70	11.90
χ^2	/	2.82
Ba–O (Å)	2.7449(11)	2.7405(5)
Ba–As (Å)	3.4208(11)	3.4166(7)
Cr (1)-As (Å)	3.6198(11)	3.6077(11)
Mn/Cr (2)-As (Å)	2.5360(6)	2.5423(7)
Cr (1)-O (Å)	2.05625(0)	2.05552(0)
As–Mn/Cr (2)–As (°) [×4]	110.033(19)	110.259(19)
As–Mn/Cr (2)–As (°) [×2]	108.35(4)	107.91(4)

Table 4.12: Results of refinement against PND (WISH diffractometer) and PXRD (MAC detector) data for $Ba_2CrO_2Cr_{1.02}Mn_{0.98}As_2$ (XX114B) at room temperature

4.4.3 Magnetic susceptibility measurements

The measurement of magnetisation versus field, *M* vs *H*, of $Ba_2CrO_2Cr_{1.02}Mn_{0.98}As_2$ (XX114B) is linear at 300 K, confirming that no room-temperature ferromagnetic impurities are present in the sample. The magnetic properties of $Ba_2CrO_2Cr_{1.02}Mn_{0.98}As_2$ (XX114B) were characterised by temperature-dependent zero-field-cooled (ZFC) and field-cooled (FC) magnetic susceptibility (χ) measurements in an applied field of 1000 Oe between 2 K and 330 K. Figure 4.31(a) shows a significant divergence between the ZFC and FC susceptibility curves below 230 K, indicating the appearance of ferromagnetic behaviour at low temperatures. This signature is similar to the ferromagnetic impurity (Cr_4As_3) that reported in the susceptibility measurements in the first paper published on $Sr_2CrO_2Cr_2As_2$[77] (previous Part II student Michael Jones also found this impurity to varying extents in his samples of

$Sr_2CrO_2Cr_2As_2$). This was also confirmed by the magnetisation isotherm measured at 5 K (Figure 4.31(b)), where a ferromagnetic-like hysteresis loop was present at the low field. This behaviour is probably not intrinsic to the main phase.

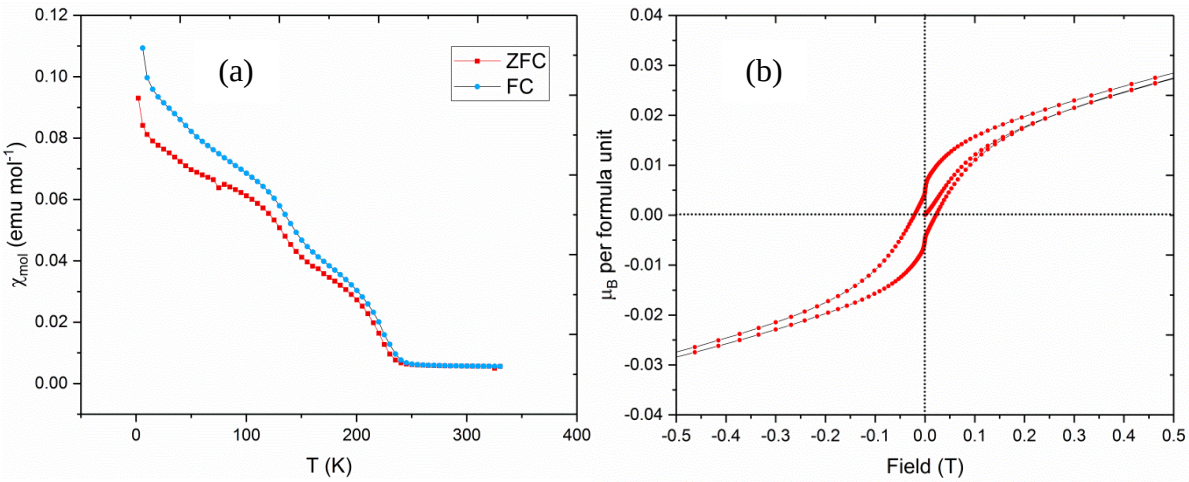

Figure 4.31: (a) The ZFC and FC magnetic susceptibilities of $Ba_2CrO_2Cr_{1.02}Mn_{0.98}As_2$, measured at 1000 Oe between 2 K and 330 K; (b) Magnetic moment per mixed-metal ion of $Ba_2CrO_2Cr_{1.02}Mn_{0.98}As_2$ as a function of applied magnetic field, measured at 5 K in the range $-5 \leq H\ (T) \leq +5$

4.4.4 Variable temperature PND

ToF PND was performed to fully characterise the magnetic ordering of $Ba_2CrO_2Cr_{1.02}Mn_{0.98}As_2$. The measurements were made on a 2 g sample of $Ba_2CrO_2Cr_{1.02}Mn_{0.98}As_2$ (XX114B) using the WISH diffractometer from a minimum temperature of 5 K to a maximum temperature of 448 K. Figure 4.32 shows all the peaks collected from banks 3 and 8 on WISH in this temperature range, where the appearance and growth of several additional magnetic peaks are observed as the temperature is decreased. The magnetic peaks marked with "*" and "+" correspond to the related magnetic ordering in the arsenide and oxide layers respectively, both of which are present in the diffraction pattern at 5 K and gradually diminish in intensity on warming up. This resembles the behaviour of the compounds considered above. However in contrast, in this case these two

sets of magnetic peaks become absent on warming to around 215 K, while several new peaks marked with "-" start to appear at 200 K, which may indicate the generation of an additional magnetic structure in the arsenide layer, analogous to those observed in its Sr analogue $Sr_2Cr_{0.79}Mn_{0.21}O_2Mn_{1.76}Cr_{0.24}As_2$.

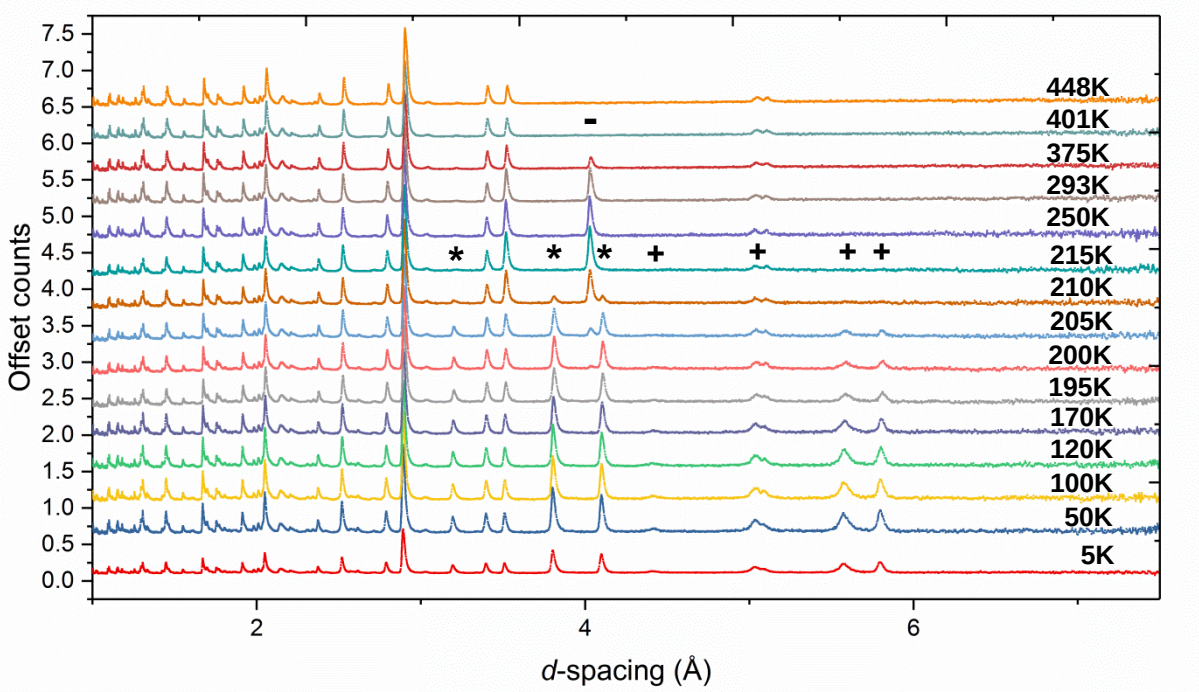

Figure 4.32: PND patterns obtained from banks 3 and 8 on the WISH, showing all magnetic Bragg reflections; The crosses (+) and asterisks (*) indicate the sets of magnetic reflections which are present from 5 K to 250 K, whereas for minus signs (-), the magnetic reflections are present until warming to 401 K

Below 215 K, all magnetic Bragg reflections with "*" and "+" could be well indexed to a $\sqrt{2}a \times \sqrt{2}a \times c$ magnetic unit cell. Using ISODISTORT[56] and initially assuming the a $P1$ space group it was found that the intensities of all magnetic reflections could be well fitted by refining two magnetic modes $mX2^+(a)$ and $mM4^+(a)$ together. The $mX2^+(a)$ mode has nearest-neighbour magnetic moments coupled antiferromagnetically in the oxide layers with their moments directed along the *c*-direction, which corresponds to the magnetic peaks with crosses (+) shown in Figure 4.32. The $mM4^+(a)$ mode represents the checker-board-type antiferromagnetic moments in the arsenide layers, with their orientations also aligned along

the *c*-direction, corresponding to those magnetic peaks with asterisks (*) observed in the variable temperature PND patterns. Like the case for $Sr_2Cr_{0.79}Mn_{0.21}O_2Mn_{1.76}Cr_{0.24}As_2$, a magnetic space group P*bam* (55.353) was deduced from ISODISTORT[56] to allow the refinement of both $mX2^+(a)$ and $mM4^+(a)$ magnetic modes, yielding a magnetic model (Figure 4.33) to fit all magnetic peaks well in the PND data, where the magnetic moments in both oxide and arsenide layers are antiferromagnetically ordered and oriented along the *c*-axis in the temperature range below 215 K. The Rietveld plots of the PND patterns and their magnetic models at 5 K and 120 K are shown in Figure 4.34.

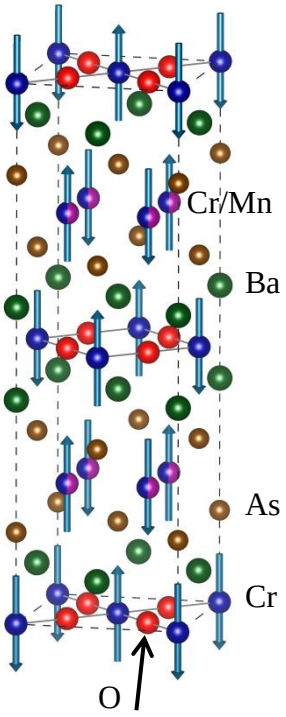

Figure 4.33: The magnetic model with combination of both $mX2^+(a)$ and $mM4^+(a)$ magnetic modes in the space group P*bam* (55.353); The blue (Cr^{2+}) and purple (Mn^{2+}) balls in the model represent the ratio of Cr^{2+} to Mn^{2+} occupying the mixed-metal sites in the arsenide layer

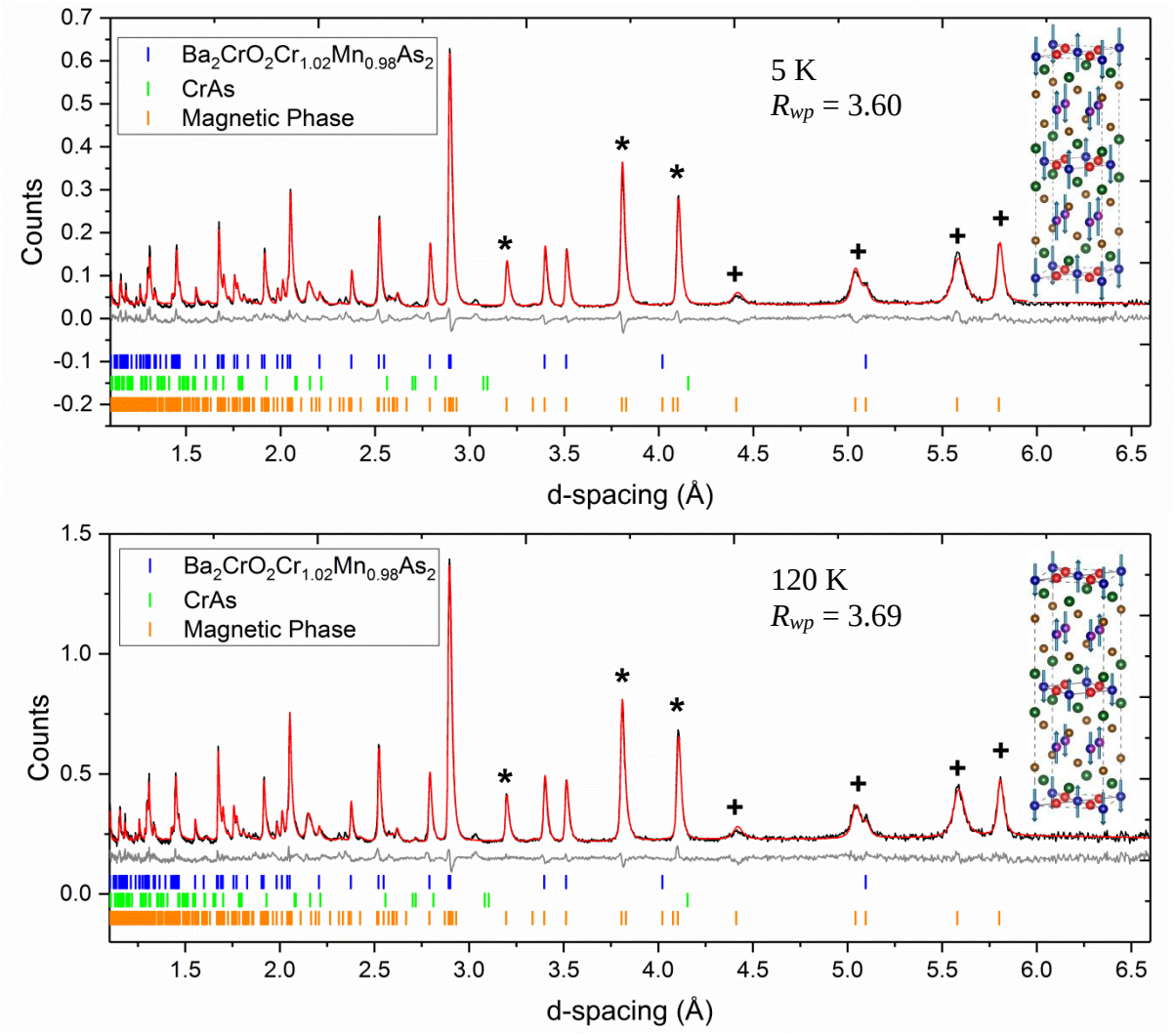

Figure 4.34: Rietveld refinements of $Ba_2CrO_2Cr_{1.02}Mn_{0.98}As_2$ against PND patterns at 5 K and 120 K collected from bank 3 and 8 on WISH; The magnetic reflections with asterisks (*) and crosses (+) correspond to the magnetic moments observed in arsenide layer and oxide plane respectively

At 200 K, the magnetic spins were ordered in both oxide and arsenide layers, with the orientation of their moments aligned along *c*-axis (this is the same magnetic structure as described for $Ba_2CrO_2Cr_2As_2$ in chapter 3). However, several additional magnetic peaks were also observed to appear in the PND pattern on warming to 200 K, some of which were overlapped with the nuclear reflections at the same *d*-spacings (e.g. the magnetic reflection at the *d*-spacing of 3.52 Å in Figure 4.35).

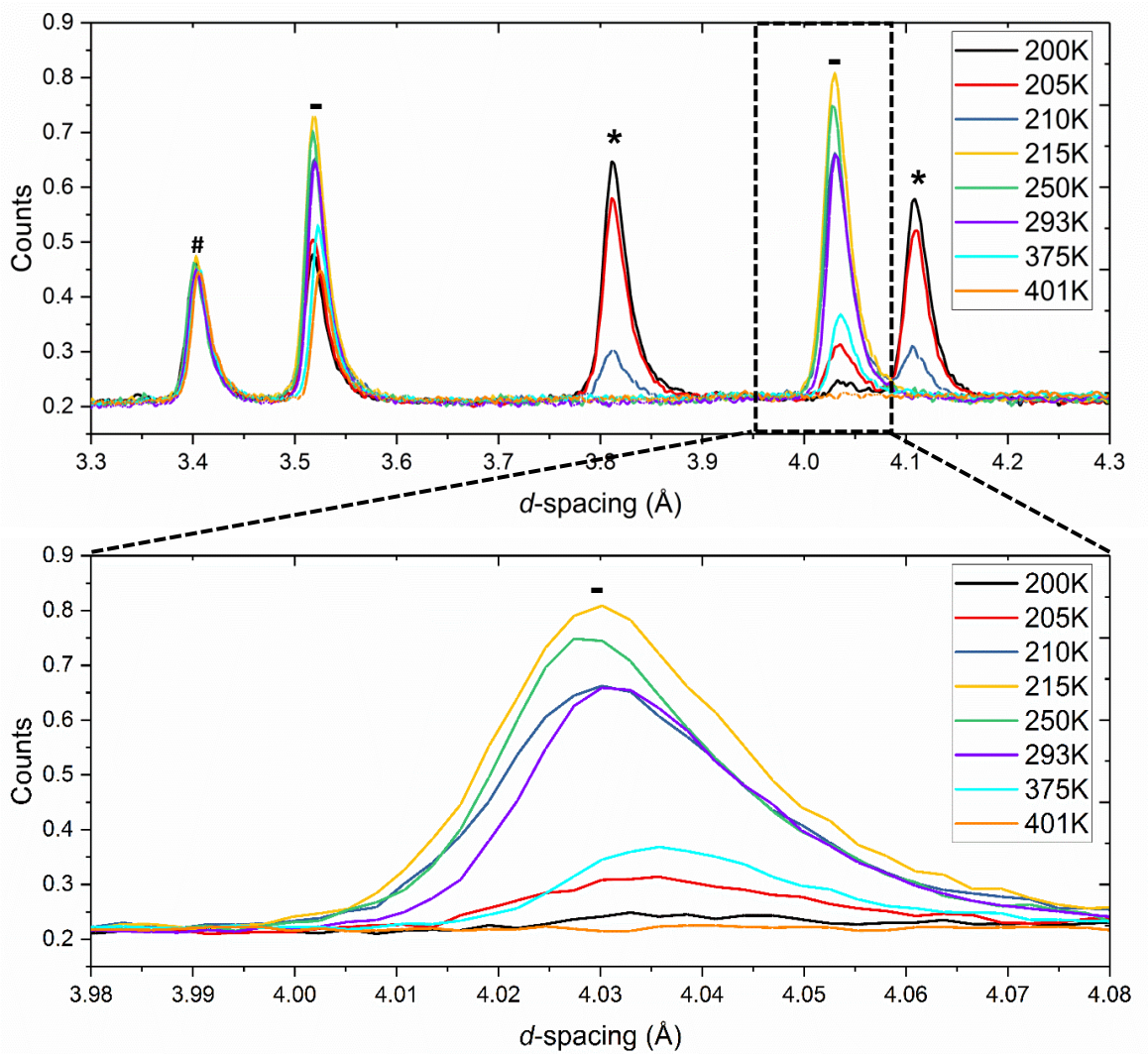

Figure 4.35: WISH PND data of $Ba_2CrO_2Cr_{1.02}Mn_{0.98}As_2$ in the temperature range 205 K to 401 K (a combination of banks 3 and 8); The magnetic peaks marked with (-) are extra reflections observed from 200 K, those marked with (*) are magnetic peaks observed at low temperatures in the arsenide layer and those labelled with (#) are nuclear peaks which does not change in intensity as the temperature is increased

The intensities of these extra magnetic peaks grew quickly to reach their maximum intensity at 215 K, and then diminished in intensity until completely absent at 401 K. Figure 4.35 shows the intensity change of the extra magnetic reflections (marked with "-") between 200 K and 401 K, in comparison with the nuclear reflections and those "normal" magnetic peaks generated from arsenide layer that completely disappear on warming to 215 K (marked with "*"). It is found that the appearance of these extra magnetic peaks in the diffraction pattern is probably related to the magnetic transition of the moments in the oxide layers in

$Ba_2CrO_2Cr_{1.02}Mn_{0.98}As_2$, since those oxide-layer magnetic peaks simultaneously disappear at the temperature (215 K) where the intensities of the extra magnetic peaks reach their maxima. Moreover, these extra "-" magnetic peaks were not found in the all-Cr analogue $Ba_2CrO_2Cr_2As_2$ (chapter 3).

These extra magnetic Bragg reflections could be indexed on a nuclear unit cell ($a \times a \times c$). The intensities of these peaks were well fitted if the value of a single magnetic mode $mGM2^-$(a) was refined in TOPAS, giving a magnetic structure with the antiferromagnetically coupled spins all directed along the *c*-axis in the arsenide layer. This is similar to the mode $mM4^+$(a) used in the magnetic structure at low temperatures, which is in accordance with the appearance of those normal magnetic peaks "*" in the arsenide layers, except that the magnetic spins in adjacent arsenide layers related by the vector ***c***/2 are aligned antiparallel in the mode $mGM2^-$(a) rather than parallel in $mM4^+$(a) (see Figure 4.36).

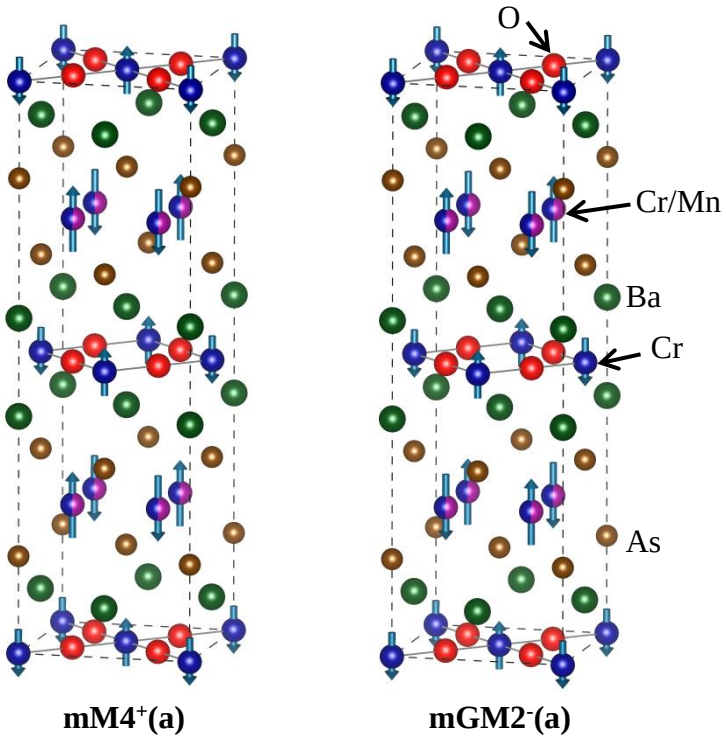

Figure 4.36: The ordering of magnetic moments in the arsenide layer of $Ba_2CrO_2Cr_{1.02}Mn_{0.98}As_2$ at 200 K, where the oxide-layer Cr moments are also ordered; Magnetic mode $mM4^+$(a) represents the moments in adjacent arsenide layers are coupled parallel with each other, comparing with the antiparallel ordering in $mGM2^-$(a)

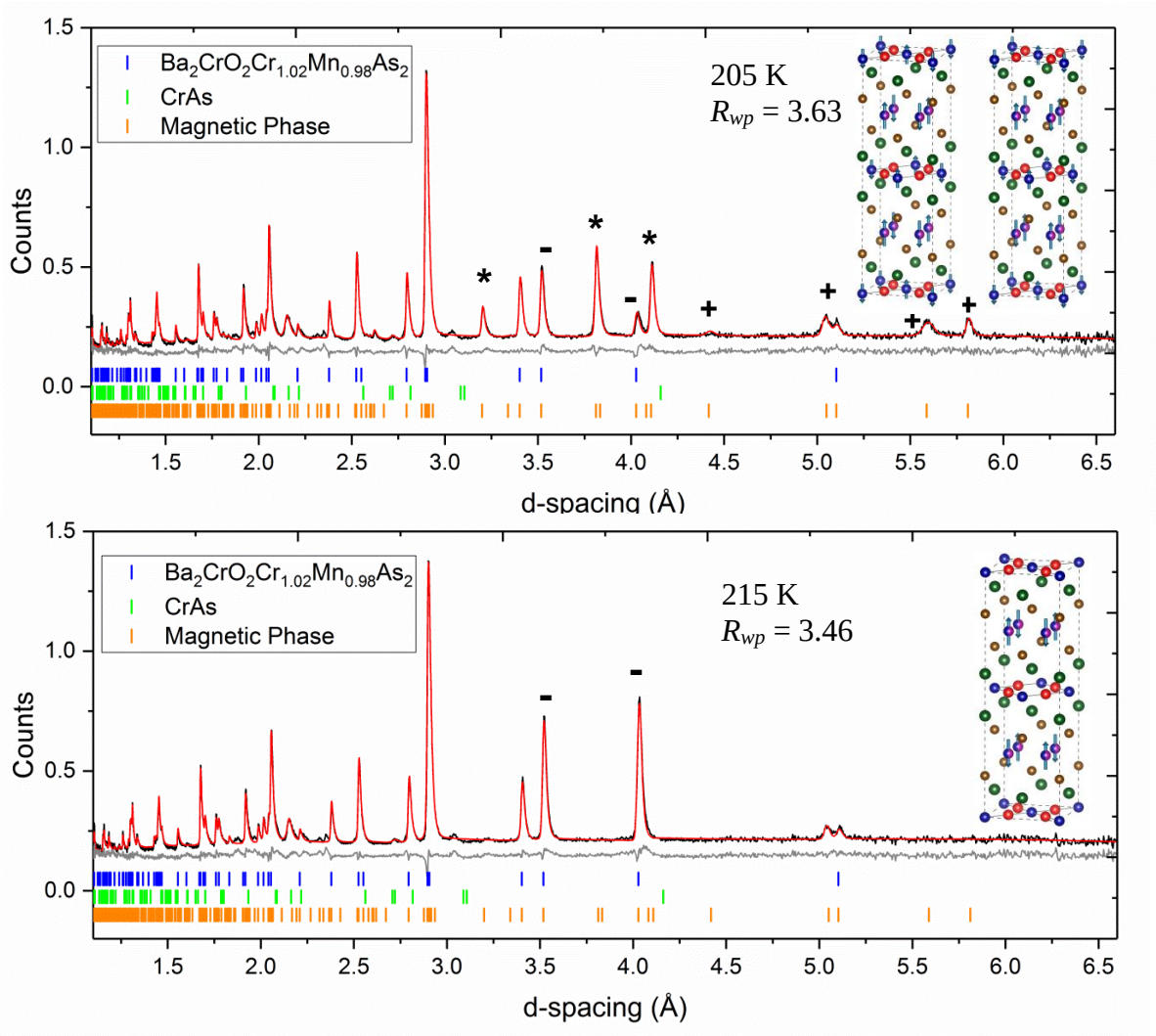

Figure 4.37: Rietveld refinements of $Ba_2CrO_2Cr_{1.02}Mn_{0.98}As_2$ against PND patterns at 205 K and 215 K collected from bank 3 and 8 on WISH; The magnetic reflections labelled with crosses (+) represent the magnetic ordering in the oxide layer; The asterisks (*) correspond to the parallel arrangement of magnetic spins in adjacent arsenide layers; The minus signs (-) show the magnetic peaks with the antiparallel scheme of spins in the arsenide layers

Therefore, two similar but different magnetic structures were found to exist with the magnetic ordering of mixed Cr^{2+} and Mn^{2+} ions in the arsenide layer between 200 K and 215 K. The magnetic structure with parallel moments were ordered in the arsenide layer at low temperatures and were completely absent at 215 K, leaving the magnetic structure with the antiparallel scheme remaining until its transition temperature (401 K). Plots of Rietveld refinement for $Ba_2CrO_2Cr_{1.02}Mn_{0.98}As_2$ against PND data at 205 K and 215 K are displayed

in Figure 4.37, which gives a good fit between the observed data and calculated results by applying the corresponding magnetic structures.

Figure 4.38 summarises the changes in the magnetic model for $Ba_2CrO_2Cr_{1.02}Mn_{0.98}As_2$ with temperature and Figure 4.39 shows the changes in the magnitudes of the refined moments in both magnetic sublattices as a function of temperature. The magnetic moments of both layers gradually grow in magnitude as the sample is decreased to 5 K, at which point the moments in both layers reach their maxima. Those in the arsenide layers reach a value of 2.971(5) μB/M^{2+} at 5 K, which is smaller than the saturated spin-only ordered magnetic moment (4.5 μB) generated from a mixture of Cr^{2+} and Mn^{2+} ions in a ratio of almost one to one. While the oxide layer is fully occupied by Cr^{2+} ions, and their moments can go up to 3.56(3) μB/Cr^{2+} at 5 K, below the value that expected for Cr^{2+} (4 μB). The difference between the measured magnitude of moments and their calculated values is probably because the ordered moments are partially reduced by the effects of covalency in both sublattices. The comparison between $Ba_2CrO_2Cr_{1.02}Mn_{0.98}As_2$ and its all-Cr analogue is discussed in section 4.5.

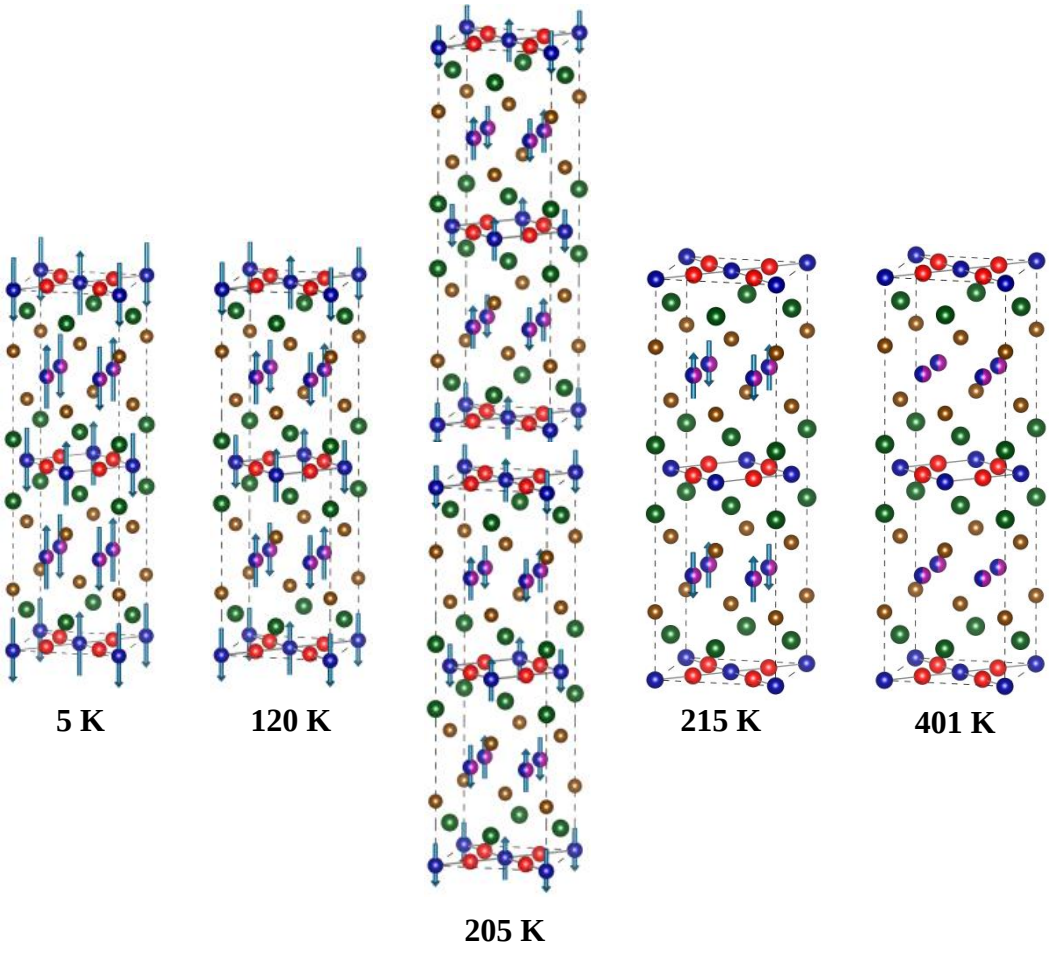

Figure 4.38: Magnetic structures of $Ba_2CrO_2Cr_{1.02}Mn_{0.98}As_2$ over the temperature range 5 K – 448 K, showing the magnitude and direction of magnetic moments for the two sublattices

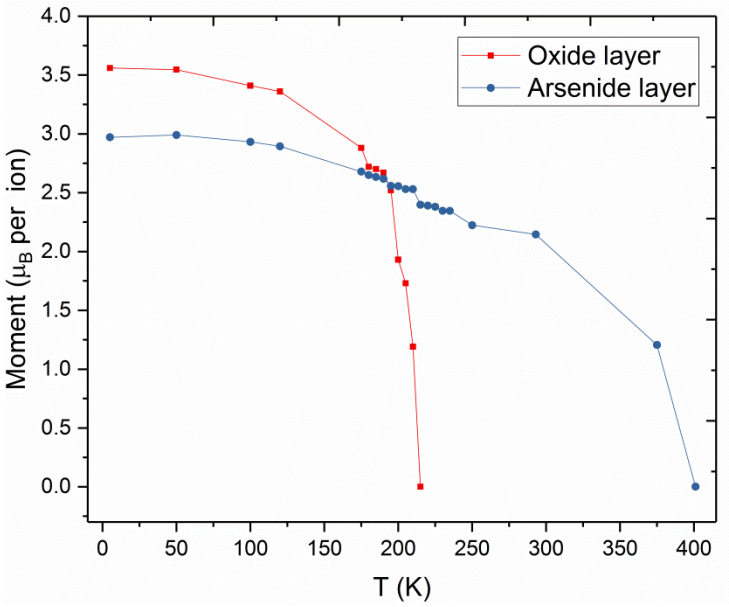

Figure 4.39: Magnitude of the long range ordered moments in the two sublattices of $Ba_2CrO_2Cr_{1.02}Mn_{0.98}As_2$ as a function of temperature

4.5 Discussion

4.5.1 Crystal structures

As the Cr^{2+} ions are partially substituted by Mn^{2+} in $Sr_2CrO_2Cr_2As_2$, both lattice parameters *a* (hence the *M*(1)–O and *M*(2)–*M*(2) distances) and *c* significantly increase (Table 4.13) because of the larger ionic radius of the d^5 Mn^{2+} ion (0.83 Å) compared with the d^4 Cr^{2+} ion (0.73 Å).[90] It is also observed that the expansion of both lattice parameters will be greater if more Cr^{2+} is substituted by Mn^{2+} in the arsenide layers. For the Ba analogues, it was found that only the Cr-rich compound could be synthesized as a single-phase sample; $BaCrMn_2As_2O_2$ was not successfully synthesized. In $Ba_2CrO_2Mn_{0.98}Cr_{1.02}As_2$, the oxide layer is fully occupied with Cr^{2+} and the arsenide layer is occupied by both Cr^{2+} and Mn^{2+} in a ratio of almost 1:1. From $Ba_2CrO_2Cr_2As_2$ to $Ba_2CrO_2Mn_{0.98}Cr_{1.02}As_2$, the lattice parameter *a* increases by 1.42 % on substituting Mn^{2+} for Cr^{2+} in the arsenide layer (Table 4.14). However, the lattice parameter *c* in $Ba_2CrO_2Mn_{0.98}Cr_{1.02}As_2$ is 0.72 % smaller than that in $Ba_2CrO_2Cr_2As_2$, which corresponds to the phenomenon that the lattice parameter *c* is much longer in the full-Cr compound $Ba_2CrO_2Cr_2As_2$ than in the full-Mn compound $Ba_2MnO_2Mn_2As_2$ (chapter 3.3.1). Some of the refinement parameters are plotted against the Cr-content in the arsenide layers of these Sr compounds (Figure 4.40).

Furthermore, for Sr mixed-metal compounds, the larger ratio of Mn^{2+} to Cr^{2+} cations in the the arsenide layer can lead to the longer *M*(1)–As distance (e.g. from 3.2107(4) Å in $Sr_2Cr_{0.93}Mn_{0.07}O_2Mn_{0.92}Cr_{1.08}As_2$ to 3.2321(4) Å in $Sr_2Cr_{0.79}Mn_{0.21}O_2Mn_{1.76}Cr_{0.24}As_2$), which makes the already highly distended $M(1)O_4As_2$ environment in $Sr_2CrO_2Cr_2As_2$ (*M*(1)–As distance of 3.2063(6) Å) even more distended. For $Ba_2CrO_2Mn_{0.98}Cr_{1.02}As_2$, the substitution of Mn^{2+} for Cr^{2+} in the arsenide layers results in a decrease of *M*(1)–As distance,

from 3.6630(8) Å in $Ba_2CrO_2Cr_2As_2$ to 3.6198(11) Å in $Ba_2CrO_2Mn_{0.98}Cr_{1.02}As$, both of which are bigger than that in the full-Mn compound $Ba_2MnO_2Mn_2As_2$ (3.458(4) Å). Moreover, in both Sr and Ba based compounds the bond distance ratio of *M*(1)–As to *M*(1)–O is much bigger in all-Cr cases compared to the others with the same structure type, which is due to the single occupancy of d_z^2 orbital (σ-antibonding with respect to the axial ligands) in the d^4 Cr^{2+} of $Sr_2CrO_2Cr_2As_2$ (see Figure 4.41), leading to increased antibonding electron density along the apical Cr–As axis and hence the lengthened apical bond (by comparison, in $Sr_2MnO_2Mn_2As_2$, the *σ*-antibonding d_z^2 and $d_{x^2-y^2}$ orbitals are both occupied, resulting in smaller ratios of the apical bond to basal ones).

Compound	$Sr_2CrO_2Cr_2As_2$	$Sr_2MnO_2Mn_2As_2$	$Sr_2Cr_{0.79}Mn_{0.21}O_2$ $Mn_{1.76}Cr_{0.24}As_2$	$Sr_2Cr_{0.93}Mn_{0.07}O_2$ $Mn_{0.92}Cr_{1.08}As_2$
T (K)	298	300	298	298
a (Å)	4.00806(3)	4.1500(4)	4.086911(9)	4.04258(2)
c (Å)	18.8216(2)	18.867(2)	19.05860(5)	18.92183(11)
c/*a*	4.6959(1)	4.546(1)	4.66333(2)	4.68063(3)
V (Å^3)	302.347(4)	324.95(6)	318.333(2)	309.229(3)
M(1)–As (Å)	3.2063(6)	3.189(7)	3.2321(4)	3.2107(4)
M(1)–O (Å) = *a* / 2	2.00403(1)	2.075(1)	2.04346(0)	2.02129(0)
M(1) Bond Distance Ratio	1.5999(3)	1.537(3)	1.5817(2)	1.5884(2)
M(2)–As (Å)	2.5083(15)	2.577(6)	2.5543(3)	2.5289(3)
As–*M*(2)–As (deg) [2]	106.12(9)	107.3(4)	106.263(14)	106.121(14)
As–*M*(2)–As (deg) [4]	111.17(5)	110.59(18)	111.099(8)	111.172(8)

Table 4.13: Lattice parameters and selected bond distances for compounds $Sr_2M_3As_2O_2$ (*M*= Mn or Cr) with the substitution of Mn^{2+} for Cr^{2+} in both oxide and arsenide layers

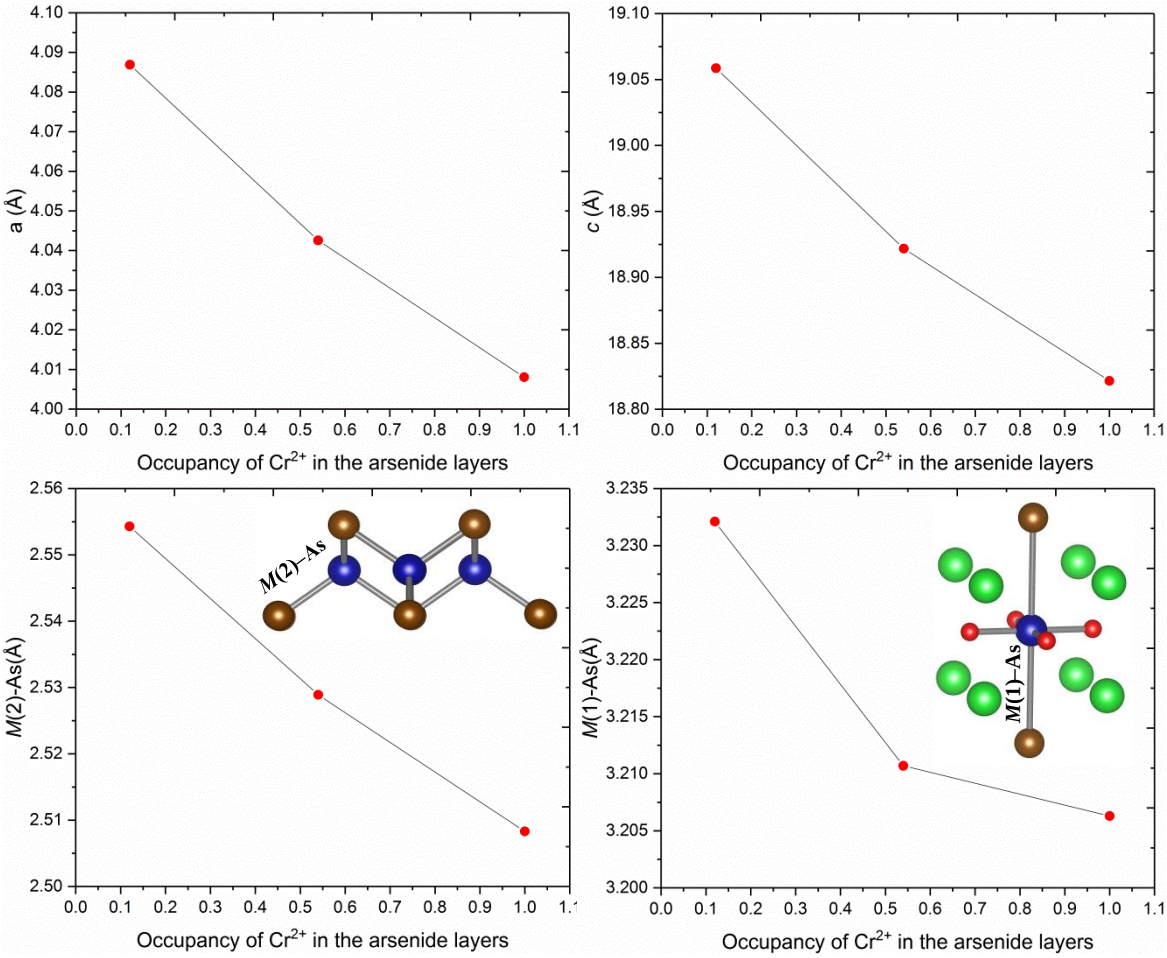

Figure 4.40: Various parameters in $Sr_2MO_2M_2As_2$ compounds as functions of occupancy of Cr^{2+} in the arsenide layers

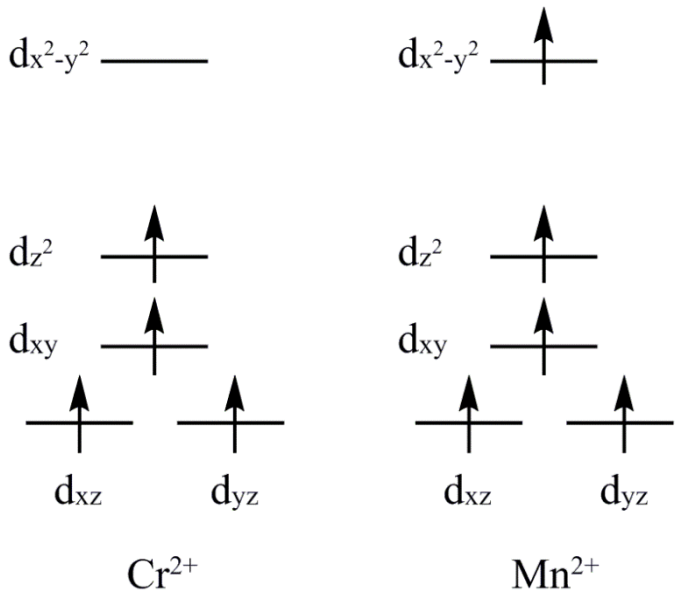

Figure 4.41: The ligand fields for Cr^{2+} and Mn^{2+} ions in $Sr_2MO_2M_2As_2$

Compound	$Ba_2CrO_2Cr_2As_2$	$Ba_2MnO_2Mn_2As_2$	$Ba_2CrO_2Mn_{0.98}Cr_{1.02}As_2$
T (K)	298	298	298
a (Å)	4.05506(2)	4.248(5)	4.11251(3)
c (Å)	20.5637(1)	19.77(3)	20.4162(2)
c/*a*	5.07112(3)	4.653(9)	4.96441(8)
V (Å^3)	338.140(4)	356.8(8)	345.293(5)
M(1)–As (Å)	3.6630(8)	3.458(4)	3.6198(11)
M(1)–O (Å) = *a* / 2	2.02753(1)	2.124(1)	2.05625(0)
M(1) Bond Distance Ratio	1.8066(4)	1.628(2)	1.76039(5)
M(2)–As (Å)	2.5090(5)	2.593(1)	2.5360(6)
As–*M*(2)–As (deg) [2]	107.82(3)	109.16(7)	108.35(4)
As–*M*(2)–As (deg) [4]	110.302(16)	110.09(13)	110.033(19)

Table 4.14: Lattice parameters and selected bond distances for compounds $Ba_2M_3As_2O_2$ (*M*= Mn or Cr) with the substitution of Mn^{2+} for Cr^{2+} in the arsenide layer

4.5.2 Magnetic ordering

The transition temperatures and magnitude of moments at base temperatures for the magnetic ordering of $Sr_2Cr_{0.79}Mn_{0.21}O_2Mn_{1.76}Cr_{0.24}As_2$, $Sr_2Cr_{0.93}Mn_{0.07}O_2Mn_{0.92}Cr_{1.08}As_2$ and $Ba_2CrO_2Mn_{0.98}Cr_{1.02}As_2$ are listed in Table 4.15 and Table 4.16, in comparison with those collected in the reported Sr and Ba analogues where both oxide and arsenide layers are fully ordered with Cr and Mn (unfortunately, there is no available information about the magnetic ordering of $Ba_2MnO_2Mn_2As_2$ in the literature).

Compound	$Sr_2CrO_2Cr_2As_2$	$Sr_2MnO_2Mn_2As_2$	$Sr_2Cr_{0.79}Mn_{0.21}O_2$ $Mn_{1.76}Cr_{0.24}As_2$	$Sr_2Cr_{0.93}Mn_{0.07}O_2$ $Mn_{0.92}Cr_{1.08}As_2$
T_N (oxide)	330	75	200	230
T_N (arsenide)	600	340	450	590
Moments in the arsenide layers	2.703(7) [1.5 K]	3.4(1) [4 K]	3.776(4) [7 K]	3.10(1) [7 K]
Moments in the oxide layers	3.352(8) [1.5 K]	/	3.60(2) [7 K]	2.71(2) [7 K]
M(1)–O (Å)	2.00403(1)	2.075(1)	2.04346(0)	2.02129(0)
M(2)–M(2) (Å)	2.83413(2)	2.9345(3)	2.889882(6)	2.85854(1)

Table 4.15: Refined magnetic parameters of $Sr_2CrO_2Cr_2As_2$, $Sr_2MnO_2Mn_2As_2$, $Sr_2Cr_{0.79}Mn_{0.21}O_2Mn_{1.76}Cr_{0.24}As_2$ and $Sr_2Cr_{0.93}Mn_{0.07}O_2Mn_{0.92}Cr_{1.08}As_2$, measured from PND

Compound	$Ba_2CrO_2Cr_2As_2$	$Ba_2CrO_2Mn_{0.98}Cr_{1.02}As_2$
T_N (oxide) (K)	248	298
T_N (arsenide) (K)	470	401
Moments in the arsenides	2.971(5) [5 K]	2.298(8) [5.5 K]
Moments in the oxide layers	3.56(3) [5 K]	3.30(1) [5.5 K]
M(1)–O (Å)	2.02753(1)	2.05625(0)
M(2)–M(2) (Å)	2.86736(2)	2.90798(2)

Table 4.16: Refined magnetic parameters of $Ba_2CrO_2Cr_2As_2$ and $Ba_2CrO_2Mn_{0.98}Cr_{1.02}As_2$, measured from PND

Similar to the Sr and Ba compounds with full-Cr and full-Mn occupancies ($Sr_2CrO_2Cr_2As_2$, $Sr_2MnO_2Mn_2As_2$ and $Ba_2CrO_2Cr_2As_2$), the M(2) moments in the arsenide layers of all Sr and Ba mixed-metal compounds order at a much higher temperature than the M(1) moments in the oxide layer. Furthermore, in those Sr and Ba compounds, the Néel temperatures (T_N) corresponding to the oxide and arsenide layers decrease dramatically as more Cr^{2+} ions are substituted by Mn^{2+} in both layers. This can be explained by the shorter Cr(1)–O and Cr(2)–Cr(2) distances within oxide and arsenide layers, compared with those in the more Mn-rich analogues, combined with the less-contracted 3*d* orbitals of Cr^{2+}, which facilitate stronger

intraplanar exchange interactions through direct Cr(2)–Cr(2) exchange, and Cr(2)–As-Cr(2) and Cr(1)–O–Cr(1) superexchange. For Ba compounds, the longer Cr(1)–O and Cr(2)–Cr(2) distances result in both sublattices undergoing long range magnetic ordering at significantly lower temperatures than those in the Sr analogues. The change of Néel temperatures of both layers in Sr compound against the occupancy of Cr^{2+} is shown in Figure 4.42.

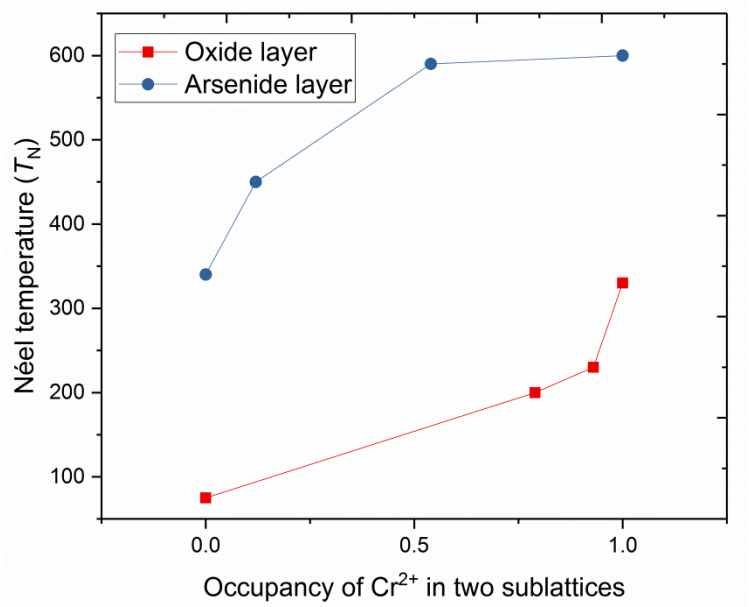

Figure 4.42: The Néel temperatures (T_N) in the two sublattices of $Sr_2MO_2M_2As_2$ as functions of occupancy of Cr^{2+}

For the Ba mixed-metal sample $Ba_2CrO_2Mn_{0.98}Cr_{1.02}As_2$, the magnitude of moments in the oxide layers (3.30(1) μB/Cr^{2+}) is similar to that measured in $Ba_2CrO_2Cr_2As_2$ (3.56(3) μB/Cr^{2+}). By contrast, the arsenide-layer moments in $Ba_2CrO_2Mn_{0.98}Cr_{1.02}As_2$ (2.298(8) μB/M^{2+}) is much smaller than the value of 2.971(5) μB/Cr^{2+} in $Ba_2CrO_2Cr_2As_2$. This is presumably because $Ba_2CrO_2Mn_{0.98}Cr_{1.02}As_2$ with more of a mixture of Mn and Cr ions in the arsenide layers has a lower ordered moment owing to the disorder. However, in the cases of Sr-analogues, it seems that the disorder effect is less than the effect of increasing the moment by incorporating Mn. For $Sr_2Cr_{0.79}Mn_{0.21}O_2Mn_{1.76}Cr_{0.24}As_2$, the moments in the arsenide layers reach a value of 3.776(4) μB/M^{2+} at 7 K whilst those in the oxide planes reach

3.60(2) μB/M^{2+}, both of which are bigger than those in $Sr_2CrO_2Cr_2As_2$ (2.703(7) μB/Cr^{2+} in the arsenide layer and 3.352(8) μB/Cr^{2+} in the oxide layer). The superexchange interaction between the d^4 Cr^{2+} and d^5 Mn^{2+} usually results in FM alignment (displayed in Figure 4.43). But for the mixed-metal compounds described in this work, the strong antiferromagnetic ordering in the oxide layers which are richer in Cr is observed. This is probably due to the individual superexchange through Cr^{2+}(d^4) to Cr^{2+}(d^4) and Mn^{2+}(d^5) to Mn^{2+}(d^5), the sigma superexchange via the middle lobe of d_{z^2} and the π-type superexchange interactions involving the d_{xz}, d_{yz} and d_{xy} orbitals (Figure 4.44), which are large enough that the overall interaction is always antiferromagnetic in practice.

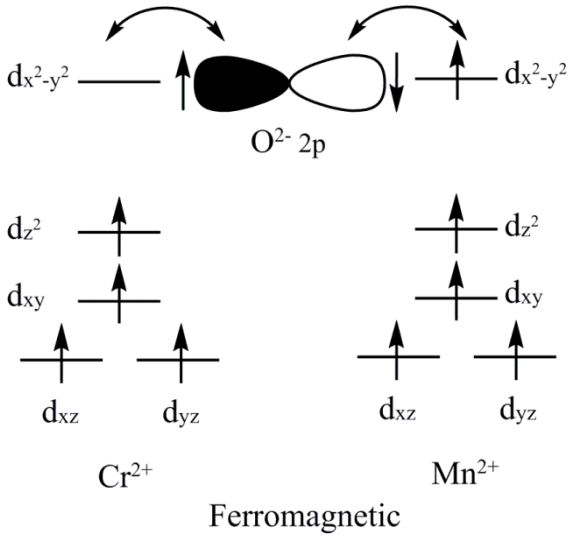

Figure 4.43: The superexchange between the Cr^{2+} and Mn^{2+}, mediated by O-2*p*

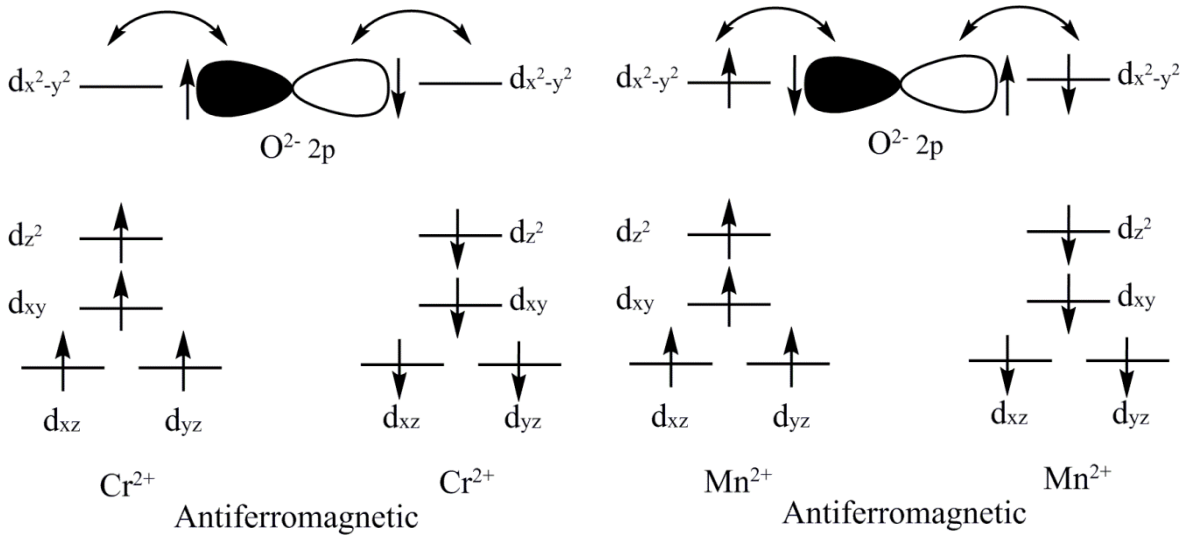

(a)

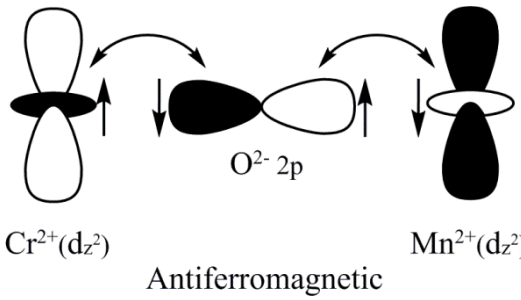

(b)

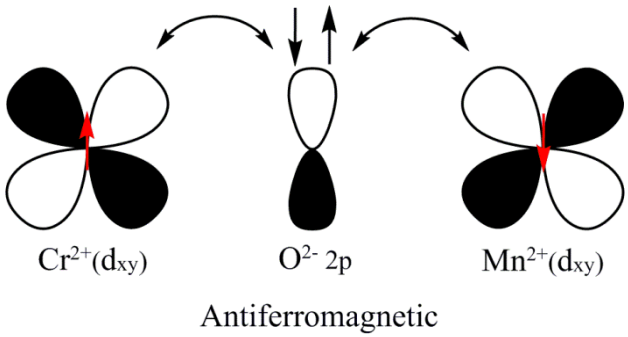

(c)

Figure 4.44: Schematic of antiferromagnetic super-exchange interactions between Cr^{2+} and Mn^{2+}: a) σ-type superexchange between $d_{x^2-y^2}$; b) σ-type superexchange between d_{z^2} ; c) π-type superexchange between d_{xy}

The preferred orientation (along the *c*-axis) of the magnetic moments of oxide-layer Cr^{2+} can be rationalised on the basis of considerations of spin-orbit coupling in terms of HOMO(highest occupied orbital) – LUMO(lowest unoccupied orbital) interaction between *d*-orbitals as described in chapter 3. This result is in a good agreement with the spin orientations observed for oxide-layer Cr^{2+} moments in $Sr_2CrO_2Cr_2As_2$, $Ba_2CrO_2Cr_2As_2$ and $Ba_2CrO_2Mn_{0.98}Cr_{1.02}As_2$. This method is much weaker when it is used to explain the orientation of Mn^{2+} magnetic moments and the Mn^{2+} (d^5) case has much less preference, thus presumably the Cr preference drives the spin orientations in these Cr/Mn mixed compounds since there is very little Mn in the oxide layers.

Similar to the oxide layer, the arsenide-layer magnetic coupling is also antiferromagnetic even though there is a mixture of Mn and Cr in the arsenide layers. This strong antiferromagnetic behavior is probably due to the *M*-*M* direct exchange interactions via the *e* non-bonding orbitals (both ions have the e^2 configuration) across the shared tetrahedral edges. The Mn^{2+} (d^5) and Cr^{2+} (d^4) moments in the arsenide layers have been reported to order antiferromagnetically in LaMnAsO, LaCrAsO, $BaMn_2As_2$ and $BaCr_2As_2$, with their moments directed along the *c*-axis.[91-93] This is also the experimentally-observed orientation of the moments corresponding to the Mn(2) (d^5) or Cr(2) (d^4) ions in $Sr_2MnO_2Mn_2Pn_2$, $Ba_2CrO_2Cr_2As_2$ (at all temperatures) and $Sr_2CrO_2Cr_2As_2$ (at temperatures above the ordering temperature of the Cr(1) moments). In addition, the spin orientations of mixed-metal (Cr and Mn) moments in the arsenide layers are also found to align along the *c*-axis in $Sr_2Cr_{0.79}Mn_{0.21}O_2Mn_{1.76}Cr_{0.24}As_2$ (at all temperatures), $Sr_2Cr_{0.93}Mn_{0.07}O_2Mn_{0.92}Cr_{1.08}As$ (above the temperature where the spin-reorientation of *M*(2) is complete) and $Ba_2CrO_2Mn_{0.98}Cr_{1.02}As_2$ (at all temperatures). Therefore, for all three compounds reported in this chapter, the preferred moment directions on both sublattices are found to be the alignment along the *c*-axis.

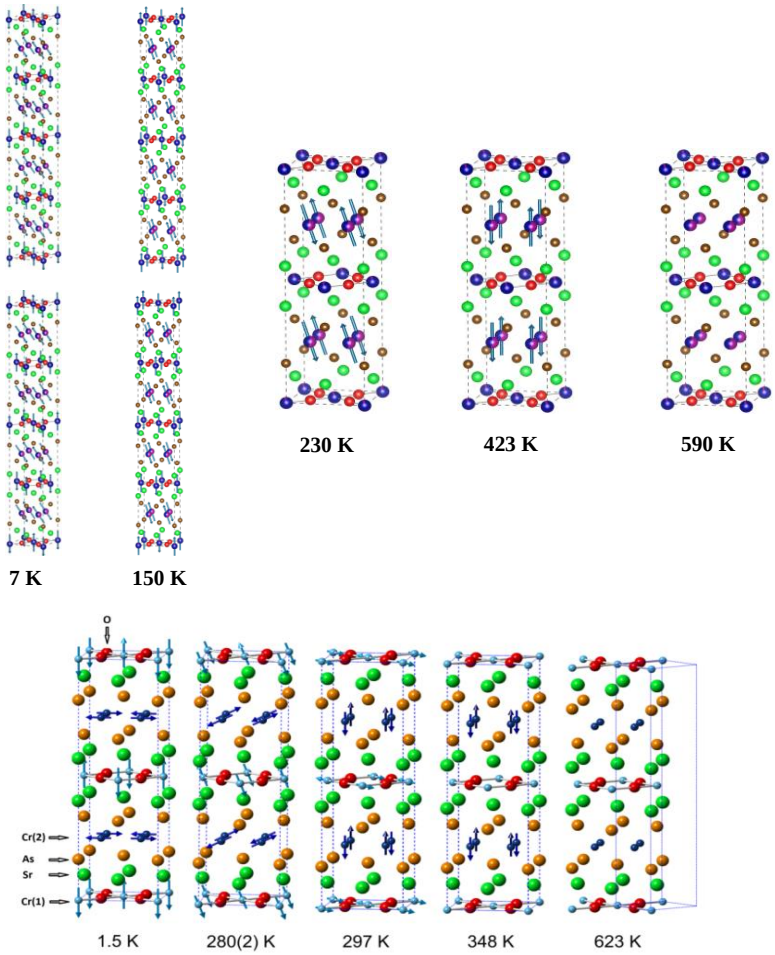

Figure 4.45: Top: Magnetic unit cell of $Sr_2Cr_{0.93}Mn_{0.07}O_2Mn_{0.92}Cr_{1.08}$ over the temperature range 7 K – 590 K, showing the magnitude and direction of magnetic moments for the two sublattices; Bottom: analogous diagrams showing the evolution in $Sr_2CrO_2Cr_2As_2$

Similar to $Sr_2CrO_2Cr_2As_2$, a spin-reorientation of the moments is also found in the arsenide layer of the Cr-rich compound $Sr_2Cr_{0.93}Mn_{0.07}O_2Mn_{0.92}Cr_{1.08}$ (the arsenide layer is occupied by both Mn and Cr in a ratio of nearly 1:1), where the *M*(2) moments rotate from the *c*-axis to lie within the *ab*-plane in a two times bigger magnetic unit cell with a $\sqrt{2}a \times \sqrt{2}a \times 2c$ expansion. This is probably due to the slight incommensurability of the magnetic structure with the crystal structure that makes the coupling interaction between the *M*(1) and *M*(2) sublattices possible (see discussion below). However, the magnetic moments in the oxide layers of $Sr_2Cr_{0.93}Mn_{0.07}O_2Mn_{0.92}Cr_{1.08}$ are observed to orient along the *c*-axis at all temperatures, which is different to the spin-reorientation of oxide-layer Cr(1) moments

reported in $Sr_2CrO_2Cr_2As_2$. Figure 4.45 compares the magnetic structures observed in $Sr_2Cr_{0.93}Mn_{0.07}O_2Mn_{0.92}Cr_{1.08}$ and $Sr_2CrO_2Cr_2As_2$ at different temperatures. The spin-reorientation transition is not found in the Mn-rich sample of $Sr_2Cr_{0.79}Mn_{0.21}O_2Mn_{1.76}Cr_{0.24}As_2$, which is consistent with the magnetic behaviour reported in the full-Mn compound $Sr_2MnO_2Mn_2As_2$. Furthermore, in their Ba analogues ($Ba_2CrO_2Cr_2As_2$ and $Ba_2CrO_2Mn_{0.98}Cr_{1.02}As_2$), it is found the magnetic moments always align along the *c*-axis at all measured temperatures without any observation of spin-reorientation.

Another interesting behaviour observed in all compounds described in this chapter is the appearance of an extra magnetic structure representing the different magnetic ordering scheme in oxide or arsenide layer. For $Sr_2Cr_{0.79}Mn_{0.21}O_2Mn_{1.76}Cr_{0.24}As_2$, two similar magnetic structures are present between 210 K and 383 K, except that the magnetic spins in adjacent arsenide layers related by the vector $\boldsymbol{c}/2$ are aligned parallel in one structure compared with antiparallel in the other one. In the temperature range where the magnetic spins are ordered in the arsenide layer, the moments in the adjacent arsenide layers in $Sr_2CrO_2Cr_2As_2$ are reported to be parallel but those in $Sr_2MnO_2Mn_2As_2$ are antiparallel. Therefore, the two magnetic structures displayed in the arsenide layers of Mn-rich compound $Sr_2Cr_{0.79}Mn_{0.21}O_2Mn_{1.76}Cr_{0.24}As_2$ amount to a combination of $Sr_2CrO_2Cr_2As_2$-like scheme with parallel ordering and $Sr_2MnO_2Mn_2As_2$-like scheme with antiparallel ordering. Figure 4.46 shows the magnetic structures of $Sr_2Cr_{0.79}Mn_{0.21}O_2Mn_{1.76}Cr_{0.24}As_2$, $Sr_2CrO_2Cr_2As_2$ and $Sr_2MnO_2Mn_2As_2$ at 270 K.

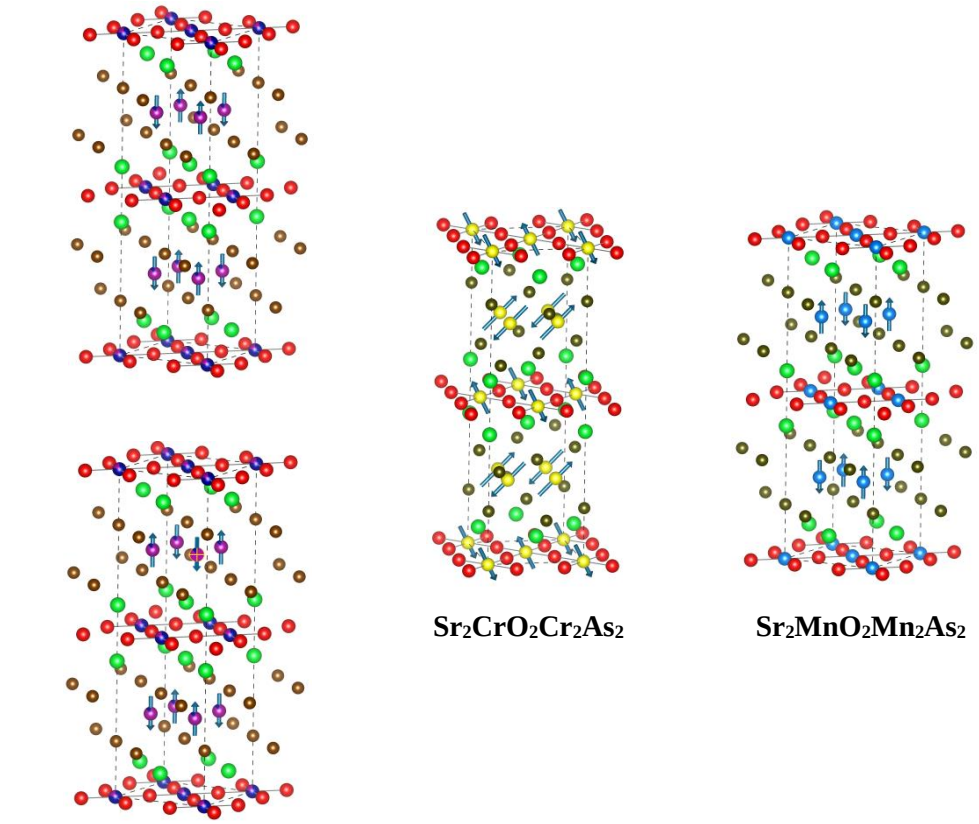

Figure 4.46: Magnetic structures of $Sr_2Cr_{0.79}Mn_{0.21}O_2Mn_{1.76}Cr_{0.24}As_2$, $Sr_2CrO_2Cr_2As_2$ and $Sr_2MnO_2Mn_2As_2$ at 270 K

The appearance of two magnetic structures in the arsenide layers of $Ba_2CrO_2Mn_{0.98}Cr_{1.02}As_2$ is similar to those in $Sr_2Cr_{0.79}Mn_{0.21}O_2Mn_{1.76}Cr_{0.24}As_2$. Two magnetic structures with parallel and antiparallel ordering between adjacent arsenide layers are observed in the narrow temperature range of 200 K to 215 K. It has been found in $Ba_2CrO_2Cr_2As_2$ (chapter 3) that the moments align parallel with each other in the adjacent arsenide layers at all temperatures. The magnetic ordering of $Ba_2MnO_2Mn_2As_2$ is not reported yet.

For $Sr_2Cr_{0.93}Mn_{0.07}O_2Mn_{0.92}Cr_{1.08}$, two magnetic structures are obtained below 230 K, where the magnetic spins in adjacent oxide layers related by the vector ***c*** are aligned either parallel or antiparallel. In the full-Cr compound $Sr_2CrO_2Cr_2As_2$, those magnetic moments in the

oxide layer related by the vector *c* are found to order parallel at base temperature (Figure 4.45). However, previous research of $Sr_2MnO_2Mn_2As_2$ indicates that the magnetic moments in the oxide layer actually do not give a long range magnetic ordering at low temperatures. For its Sb analogue $Sr_2MnO_2Mn_2Sb_2$, the ordered oxide-layer magnetic moments are aligned within the *ab*-plane rather than along the *c*-axis. Figure 4.47 compares the magnetic structures of $Sr_2Cr_{0.93}Mn_{0.07}O_2Mn_{0.92}Cr_{1.08}$, $Sr_2CrO_2Cr_2As_2$, $Sr_2MnO_2Mn_2As_2$ and $Sr_2MnO_2Mn_2Sb_2$ at low temperature.

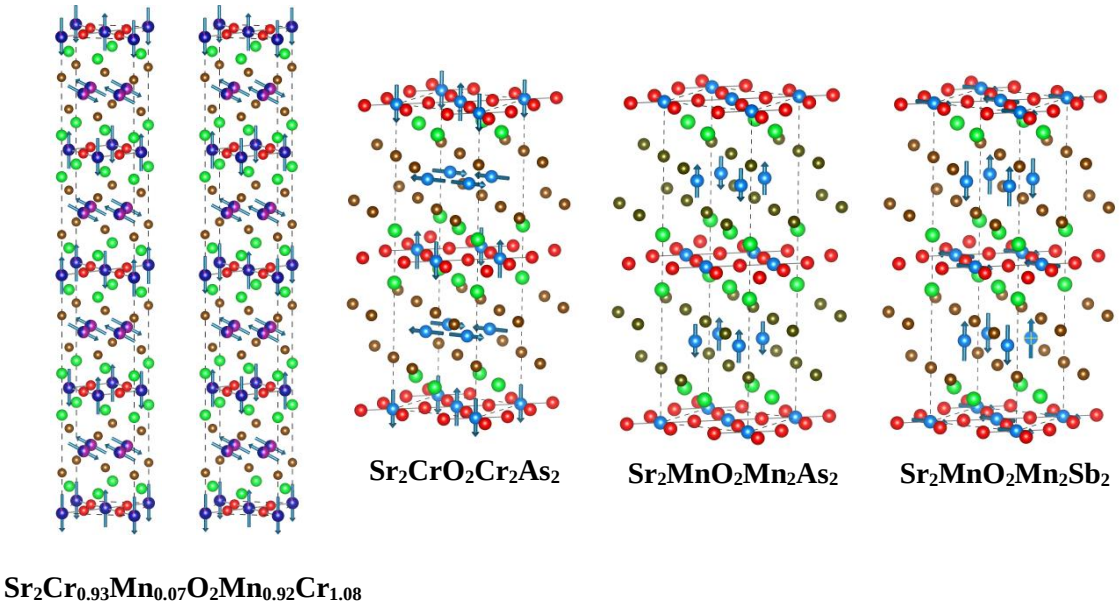

Figure 4.47: Magnetic structures of $Sr_2Cr_{0.93}Mn_{0.07}O_2Mn_{0.92}Cr_{1.08}$, $Sr_2CrO_2Cr_2As_2$, $Sr_2MnO_2Mn_2As_2$ and $Sr_2MnO_2Mn_2Sb_2$ at low temperature

The good quality of diffraction data collected at the high *d*-spacing range on the WISH diffractometer allowed the observation of one additional magnetic reflection at about 16.5 Å to 17 Å in both $Sr_2Cr_{0.79}Mn_{0.21}O_2Mn_{1.76}Cr_{0.24}As_2$ and $Sr_2Cr_{0.93}Mn_{0.07}O_2Mn_{0.92}Cr_{1.08}As_2$ that was not present in the Ba analogues. But for $Sr_2Cr_{0.93}Mn_{0.07}O_2Mn_{0.92}Cr_{1.08}As_2$, this extra reflection emerges at the temperature (423 K) of the spin reorientation transition in the arsenide layer, similar to the behaviour of the long *d*-spacing magnetic peak found in

$Sr_2CrO_2Cr_2As_2$, where the extra scattering emerges at the temperature of the spin reorientation transition in the main $Sr_2CrO_2Cr_2As_2$ phase. Moreover, the additional magnetic scattering in $Sr_2CrO_2Cr_2As_2$ and both mixed-metal compounds shifts markedly to longer *d*-spacings on further cooling, as shown in Figure 4.48 (a much larger shift and in the opposite sense than can be explained by thermal effects). The plots of peak positions against temperatures are displayed in Figure 4.49. This unusual phenomenon observed in all these Sr compounds might indicate a slight incommensurability of the magnetic structure with the crystal structure which is proposed for the all-Cr compound. Moreover, the refinement results show that there is another peak at about 5.5 Å in $Sr_2Cr_{0.93}Mn_{0.07}O_2Mn_{0.92}Cr_{1.08}As_2$ (Figure 4.25) that is not in the right position compared with other well fitted peaks, which is probably also a sign of the incommensurability. It is presumably this which enables the arsenide and oxide layer moments to communicate and for the spin-reorientation to occur even though they order with different propagation vectors and should not couple. The detailed magnetic behaviour of these compounds is listed in Table 4.18. A further analysis of the magnetic properties is probably required using single crystal neutron diffraction to disentangle the complex magnetism in these phases. The microstructure of these mixed-metal samples will also be investigated since it has been found that there are some stacking defects in all-Cr phase and it is plausible that these could be relevant to the magnetic behaviour.

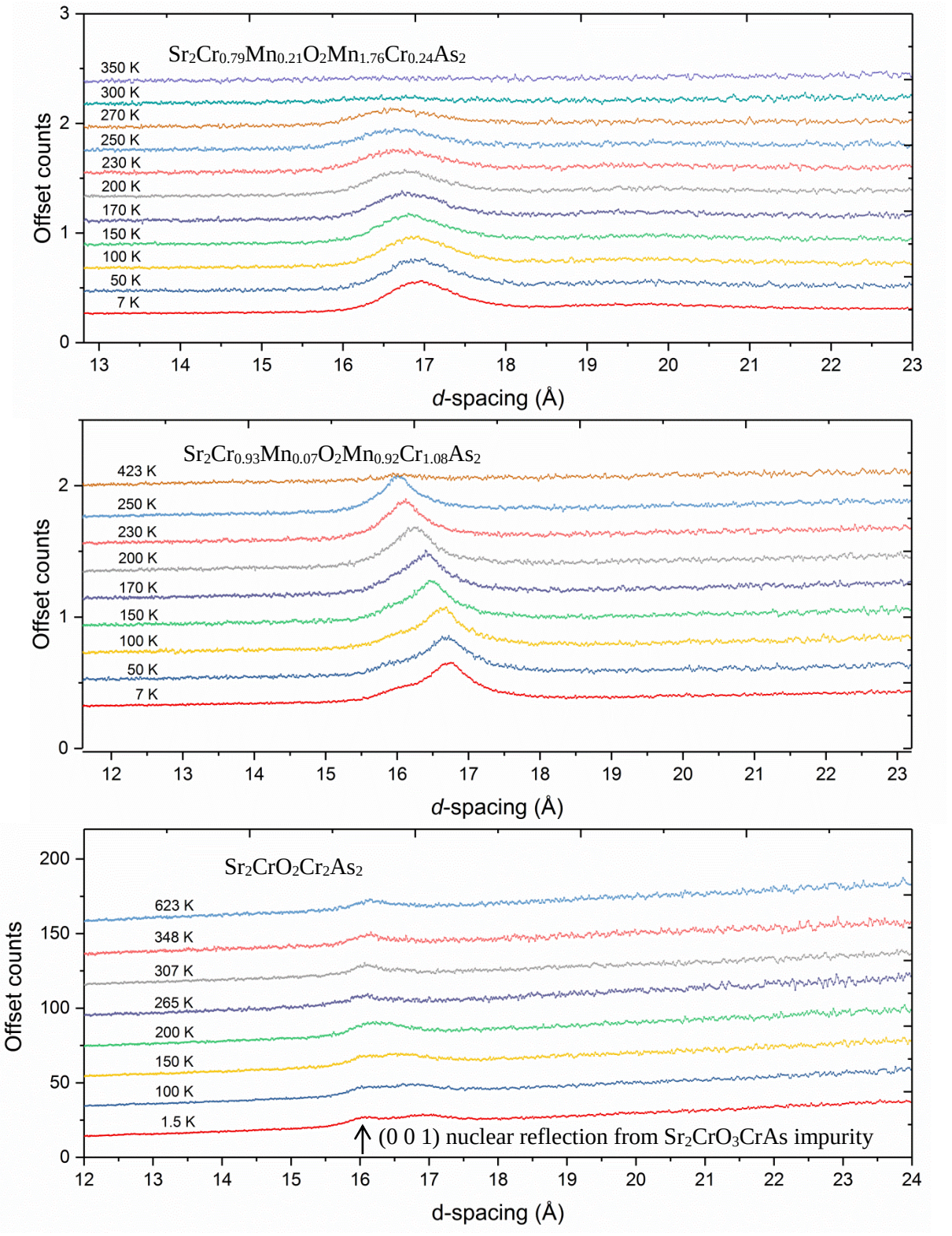

Figure 4.48: The extra magnetic scattering for $Sr_2Cr_{0.79}Mn_{0.21}O_2Mn_{1.76}Cr_{0.24}As_2$, $Sr_2Cr_{0.93}Mn_{0.07}O_2Mn_{0.92}Cr_{1.08}As_2$ and $Sr_2CrO_2Cr_2As_2$ at long *d*-spacing range collected from bank 1 and 10 on WISH

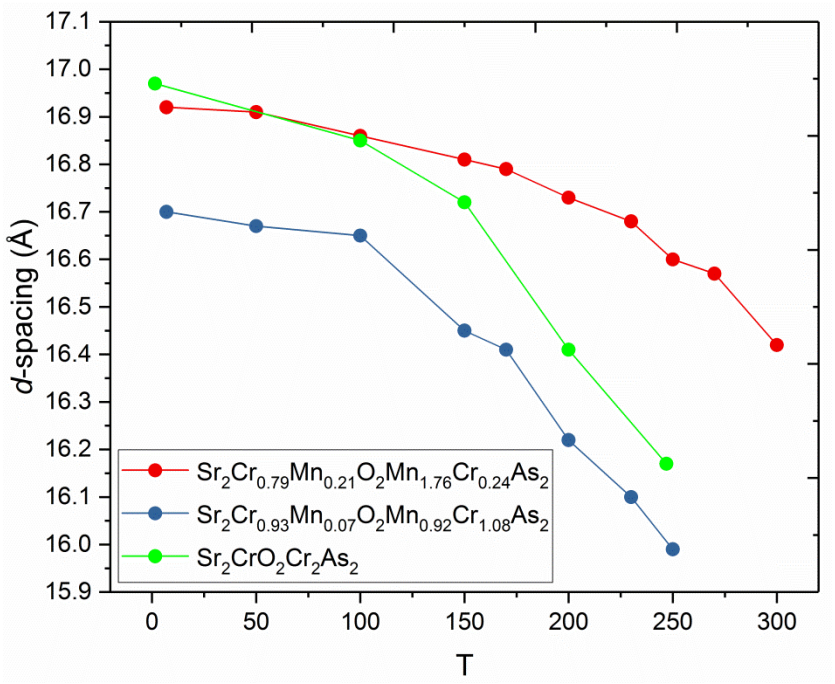

Figure 4.49: The positions of this extra magnetic peak for $Sr_2Cr_{0.79}Mn_{0.21}O_2Mn_{1.76}Cr_{0.24}As_2$, $Sr_2Cr_{0.93}Mn_{0.07}O_2Mn_{0.92}Cr_{1.08}As_2$ and $Sr_2CrO_2Cr_2As_2$ against measured temperatures from bank 1 and 10 on WISH

Compound		$Sr_2CrO_2Cr_2As_2$	$Sr_2Cr_{0.93}Mn_{0.07}O_2Mn_{0.92}Cr_{1.08}As_2$	$Sr_2Cr_{0.79}Mn_{0.21}O_2Mn_{1.76}Cr_{0.24}As_2$
T_N (oxide) (K)		330	230	200
T_N (arsenide) (K)		600	590	450
Spin reorientation	T	Below 297 K	Below 423 K	/
	Sublattice	Oxide and arsenide layers	Arsenide layer	
	Change of direction of spins as the temperature is decreased	Oxide layer: from ab-plane to *c*-axis Arsenide layer: from *c*-axis to ab-plane	From *c*-axis to ab-plane	
Mixed magnetic structures		/	7 K to 230 K	210 K to 383 K
			Main phase: antiparallel	Main phase: parallel

Table 4.18: The magnetic behaviour of $Sr_2CrO_2Cr_2As_2$, $Sr_2Cr_{0.79}Mn_{0.21}O_2Mn_{1.76}Cr_{0.24}As_2$ and $Sr_2Cr_{0.93}Mn_{0.07}O_2Mn_{0.92}Cr_{1.08}As_2$

Chapter 5

Synthesis and characterisation of Sr_2MnO_3CuSe, Sr_2MnO_3CuS and $Sr_2MnO_3Cu_{0.94}S$

5.1 Introduction

The synthesis and characterisation of the first layered oxychalcogenide, A_2MO_3CuCh (where *A* is an alkaline earth metal, *M* is a 3*d* transition metal and *Ch* is S or Se) were reported for Sr_2CuGaO_3S by Zhu et al. in 1997.[94] The solid possesses both square-pyramidal MO_5 polyhedral layers and anti-fluorite chalcogenides Cu_2Ch_2 layers, which are stabilized by Sr^{2+} layers connecting these two types of structural blocks together. After this, several other Sr_2CuGaO_3S-type layered oxychalcogenides with 1st-row transition metals (like Sr_2MnO_3CuS[95], Sr_2CrO_3CuS[96], Sr_2FeO_3CuS, Sr_2FeO_3CuSe[97], Ca_2FeO_3CuS and Ca_2FeO_3CuSe[98]) were also reported. The magnetic susceptibilities of Sr_2MnO_3CuS, Sr_2CrO_3CuS, Ca_2FeO_3CuS and Ca_2FeO_3CuSe exhibited antiferromagnetic transitions with reported Néel temperatures T_N of about 120, 60, 110 and 125 K. This family of compounds have interesting magnetic properties but few of them have been characterised by using neutron powder diffraction to fully understand their magnetic ordering.

Several other novel compounds with the Sr_2CuGaO_3S-type structure have also been investigated in the context of the Fe-based superconductors within the group by Dr A J

Corkett.[99] Sr_2ScO_3FeAs was reported to be paramagnetic down to 2 K without long-range Fe order after the magnetic susceptibility measurements. The low-temperature neutron powder diffraction also exhibited no additional magnetic Bragg reflections for this compound. By replacing Sc with Cr in the oxide layer, another novel solid Sr_2CrO_3FeAs was also reported. SQUID magnetometry measurements revealed a broad maximum at about 40 K, indicating antiferromagnetic order of Cr^{3+} moments in the oxide layer. Variable temperature PND measurements confirmed antiferromagnetic ordering of Cr moments with them orientated in the *ab*-plane (Figure 5.1) in a chequerboard arrangement, which was also reported by Tegel *et al*.[100]

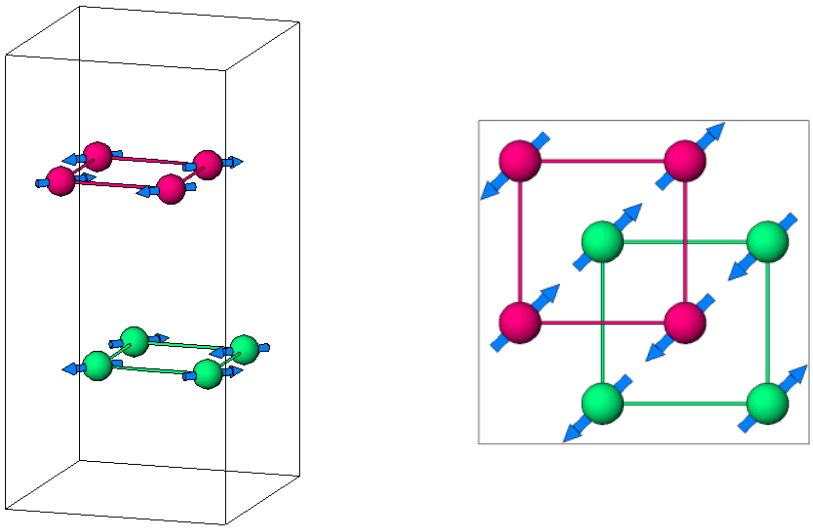

Figure 5.1: The magnetic ordering of the antiferromagnetic Cr^{3+} moments in the oxide layers of Sr_2CrO_3FeAs; The graph was taken from Dr A J Corkett's thesis[99]

An improved synthetic route to a pure sample of the superconducting phase Sr_2VO_3FeAs was also optimised by Corkett. It was found that this sample showed reproducible magnetic properties with a superconducting transition temperature at about 25 K. Furthermore, the substitution of Sr^{2+} by Ca^{2+} on the structure revealed an increase in T_c, which is maximised at 29.5 K in $Sr_{1.95}Ca_{0.05}VO_3FeAs$.[101] Moreover, Johrendt's group also investigated this compound using polarized neutrons, indicating the appearance of weak antiferromagnetic

ordering in the V sublattice of Sr_2VO_3FeAs at ≈ 45 K with the magnetic moments aligned along the *c*-axis.[102]

This chapter reports the synthesis and characterisation of Sr_2MnO_3CuSe, Sr_2MnO_3CuS and $Sr_2MnO_3Cu_{0.94}S$. They all show antiferromagnetic long range ordering with ordering temperatures between 80 K and 120 K with additional glassy behaviour evident in the SQUID magnetometry measurements. Low-temperature PND has revealed long-range antiferromagnetic ordering, with the magnetic moments of Mn^{3+} directed along the *c*-axis. $Sr_2MnO_3Cu_{1-\delta}S$ has been found to have a Cu-deficiency of up to 0.06 %, but with a different magnetic unit cell compared with the parent compound Sr_2MnO_3CuS from which it is derived, showing the importance of small compositional changes on the physical properties.

5.2 Synthesis and characterisation of Sr_2MnO_3CuSe

A single-phase sample of Sr_2MnO_3CuSe was successfully synthesised by grinding together SrO, Mn (Aldrich, 99.99 %), CuO (Alfa, 99.995 %) and Se (Alfa, 99.999 %) in the molar ratio 2: 1: 1: 1 under argon. SrO was made by thermal decomposition of Sr_2CO_3 (Alfa, 99.994 %) at 1100 °C (as detailed in section 2.1.3.1). A pellet of the ground mixtures was sealed in an evacuated silica tube as previously described in section 2.1.1. The sample was then heated slowly to 900 °C for 60 hours and followed by quenching into ice-water.

5.2.1 Powder X-ray diffraction

The structure of Sr_2MnO_3CuSe (XX211C) was probed using powder X-ray diffraction (Mythen detector on the I11 beamline). Refinement against the data is plotted in Figure 5.2, showing that the sample crystallises in the space group *P*4/*nmm* with the Sr_2CuGaO_3S structure type. Its structure features anti-PbO-type CuSe layers separated by two oxide layers

that resemble a portion of the K_2NiF_4 structure,[103] with the Mn^{3+} cation in a square pyramidal geometry (Figure 5.3). The refined values are listed in Table 5.2 and 5.3 with the results of room temperature PND data.

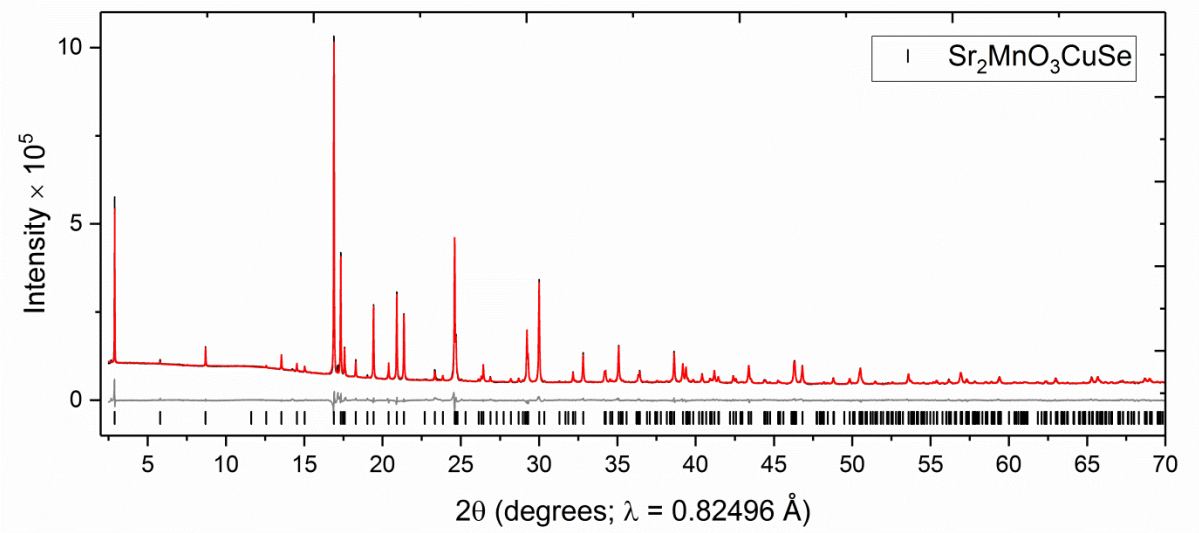

Figure 5.2: Rietveld refinement against the PXRD pattern of the sample of Sr_2MnO_3CuSe (XX211C), measured at RT using the Mythen detector on the I11 beamline

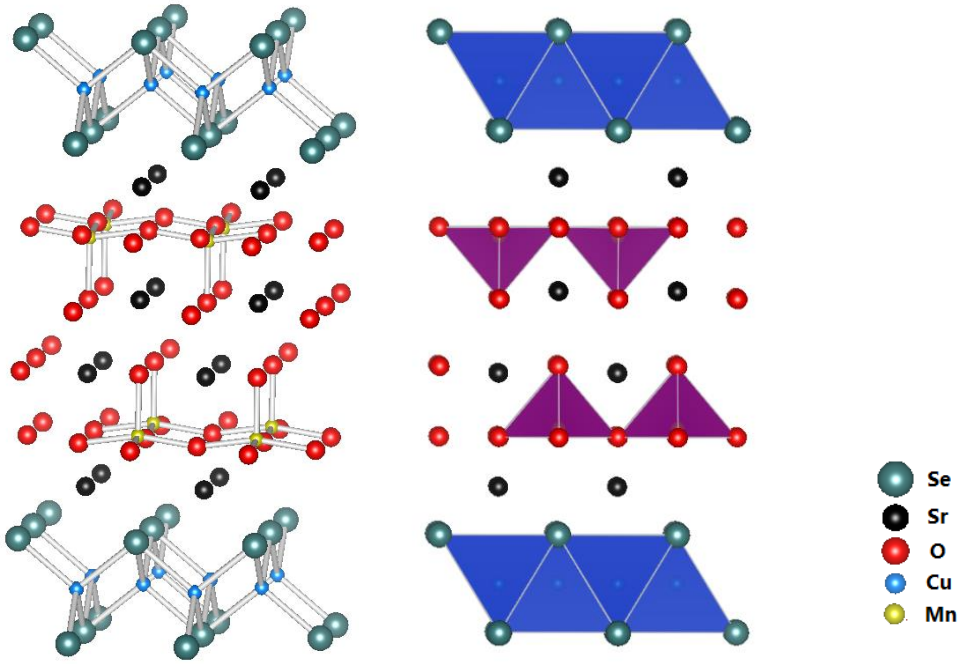

Figure 5.3: Crystal structure of Sr_2MnO_3CuSe, showing alternate stacking of the Cu_2Se_2 and square-pyramidal MnO_3 layers

Compound	Sr_2MnO_3CuSe	Sr_2MnO_3CuS	Sr_2FeO_3CuS	Sr_2CrO_3CuS
a (Å)	3.87050(3)	3.86560(3)	3.8951(11)	3.9000(6)
c (Å)	16.3055(1)	15.8984(2)	15.613(5)	15.333(3)
c/*a*	4.21276(4)	4.164(2)	4.008(1)	3.932(1)
M–O(1) (Å) [×4]	1.9568(6)	1.9511(5)	1.984(2)	1.966(1)
M–O(2) (Å) [×1]	2.011(6)	2.035(4)	1.907(15)	1.845(10)
M–S(Se) (Å) [×1]	3.4599(15)	3.361(5)	3.386(12)	3.200(6)
Cu–S(Se) (Å) [×4]	2.5013(6)	2.422(2)	2.456(6)	2.448(3)

Table 5.1: Comparison of selected structural parameters for Sr_2MnO_3CuSe (synchrotron PXRD data, this thesis), Sr_2CrO_3CuS (PND data, obtained from ref. 2), Sr_2MnO_3CuS(D2B PND data, this thesis) and Sr_2FeO_3CuS (PND data, obtained from ref. 3)

Selected structural parameters are also compared for Sr_2MnO_3CuSe, Sr_2CrO_3CuS, Sr_2MnO_3CuS and Sr_2FeO_3CuS in Table 5.1. [96, 104] In the structure of Sr_2MO_3CuX, the M^{3+} is square pyramidally coordinated by oxide. The M-*X* bond is long and weak in the structure of Sr_2MO_3CuX compared with those seen in other related materials (e.g. MnSe). In Sr_2MnO_3CuS the four Mn−O(1) distances of 1.9511(5) Å and Mn−O(2) distance of 2.035(4) Å produce a BVS for Mn^{3+} of 3.10. If the S is included (Mn-S distance of 3.361(5) Å) the BVS value will increase slightly to 3.15. This suggests that the Mn coordination geometry could be described as a square pyramidal MnO_5 or a highly distended octahedral environment MnO_5S, where the distention is forced by the intervening Sr^{2+} cations. Moreover, the lattice parameter *a* dramatically increases as the sizes of the transition metals and chalcogenide anions increase (The trivalent Mn^{3+}, Fe^{3+} and Cr^{3+} cations in the octahedral coordination geometry have ionic radii of 0.58 Å, 0.58 Å and 0.615 Å respectively).[105] But surprisingly, the lattice parameter *c* increases inversely. The lattice parameter *c* in Sr_2MnO_3CuS is 2.2 % larger than that in Sr_2FeO_3CuS which is again 1.8 % larger than the one in Sr_2CrO_3CuS. This corresponds to the fact that the Mn–O(2) distance is 5.9 % longer than the corresponding Fe–O(2) distance in Sr_2FeO_3CuS and Fe–O(2) distance is 1.8 % larger than Cr–O(2) distance in Sr_2CrO_3CuS. The very different M–O(2) distances between

Cr, Mn an Fe compounds are due to their different d-orbital occupancies, which is discussed in Chapter 6.3.2.

5.2.2 Magnetic susceptibility measurements

The ZFC and FC magnetic susceptibilities (Figure 5.4) of Sr_2MnO_3CuSe (XX211C) were measured in an applied field of 1000 Oe between 5 K and 300 K. A broad maximum is observed at around 100 K, analogous to that seen in Sr_2MnO_3CuS (120 K), indicative of the low-dimensional antiferromagnetic ordering of Mn^{3+} moments in pyramidal MnO_5 layers.[95]

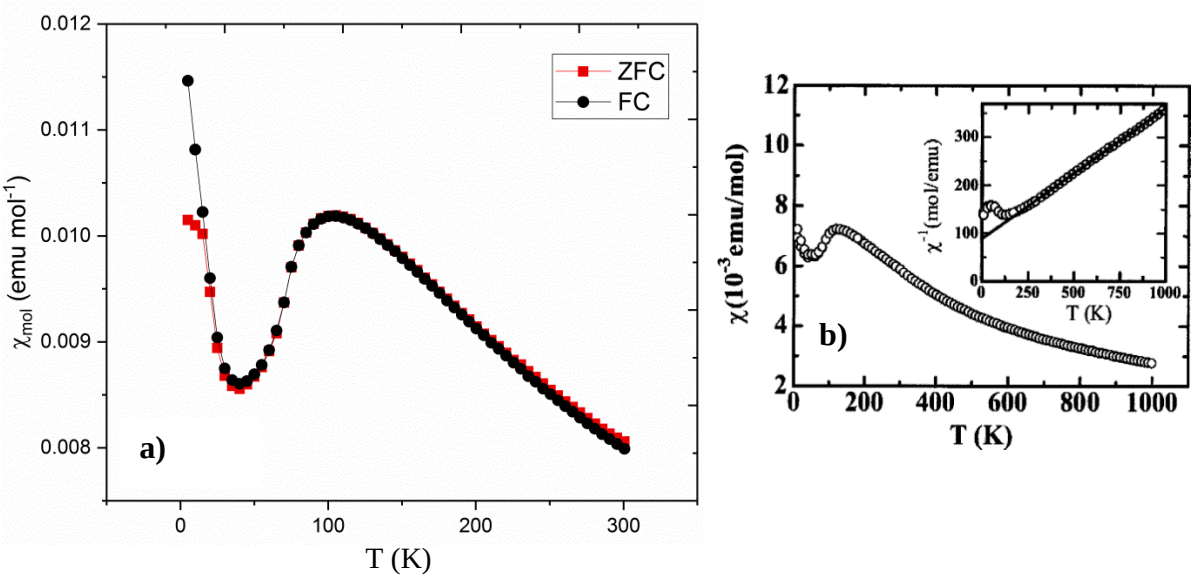

Figure 5.4: a) The ZFC and FC magnetic susceptibilities of Sr_2MnO_3CuSe (XX211C), using a measuring field of 1000 Oe between 5 K and 300 K; b) Reported magnetic susceptibility as a function of the temperature in Sr_2MnO_3CuS;[95] The inset shows the inverse magnetic susceptibility and the theoretical line fitted (200 K–1000 K) by Curie–Weiss law

The magnetic susceptibility of Sr_2MnO_3CuSe (XX211C) was also measured using a 3 T/4 T subtraction (Appendix D) to ensure the effects of any ferromagnetic impurities in the sample were eliminated. Fitting the data from the linear region of 150 K-300 K to the Curie-Weiss law (see Appendix D) gives a Weiss temperature of θ = -414 K and an effective moment of 6.17 μB per Mn atom. The obtained Weiss temperature is about four times bigger than the

Néel temperature and the calculated μeff from the Curie–Weiss formula is much larger than the value expected from the spin-only formula for high-sp in Mn^{3+} (S=2 and the magnetic moment = 4.9 μB). Thus we conclude that Sr_2MnO_3CuSe doesn't obey the Curie-Weiss law in the measured temperature range, which is not large enough to give a reliable estimate of both Curie and Weiss constants.

It is also found there is a small divergence between ZFC and FC of Sr_2MnO_3CuSe (XX211C) below approximately 40 K. The magnetisation isotherm measured at 5 K (Figure 5.5) shows a hysteresis at the low field with a slight displacement from the origin, suggesting a little spin-glass component to the magnetism arising from some disorder and frustration of the magnetic interactions.

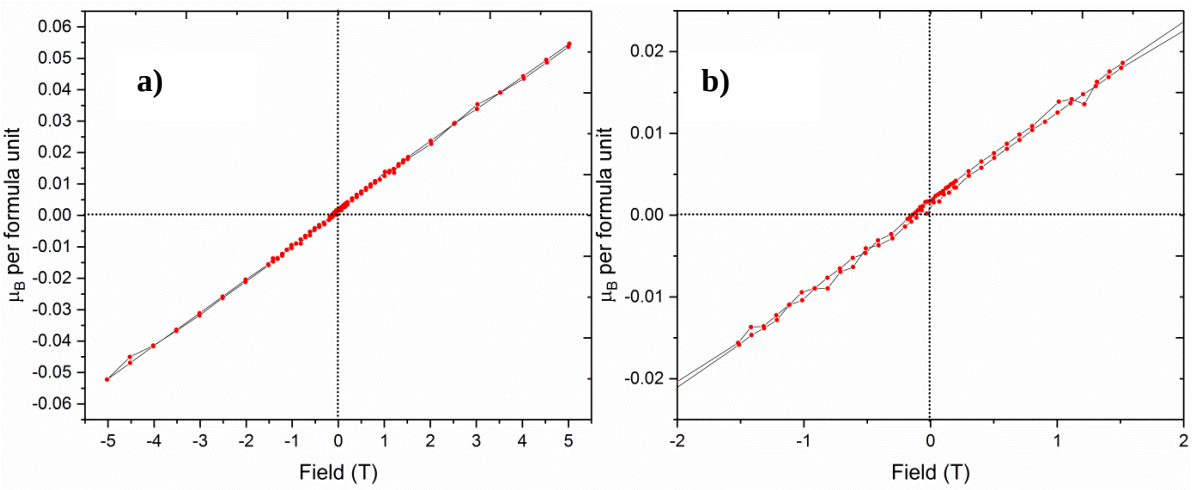

Figure 5.5: a) Magnetic moment per Mn ion of Sr_2MnO_3CuSe as a function of applied magnetic field, measured at 5 K in the range -5 ≤ H (T) ≤ +5; b) Zooming in the range of -2 T

5.2.3 Room temperature PND

This compound (XX211C) was measured at room temperature on the D2B diffractometer to investigate the exact occupancy of Cu sites. A Rietveld refinement of Sr_2MnO_3CuSe (XX211C) against room temperature PND data is shown in Figure 5.6, which gives a good fit between the observed and calculated result. The composition of this compound is refined to be Sr_2MnO_3CuSe with fully occupied Cu [0.995(7)] in the selenide layers, which shows the agreement with the occupancy of Cu [0.9999(11)] derived from PXRD (Mythen) refinement of Sr_2MnO_3CuSe (XX211C). The X-ray and neutron data are both consistent and there is no evidence for any Cu deficiency in this sample. The structural parameters and selected atomic distances from PND data are presented in Tables 5.2 and Table 5.3.

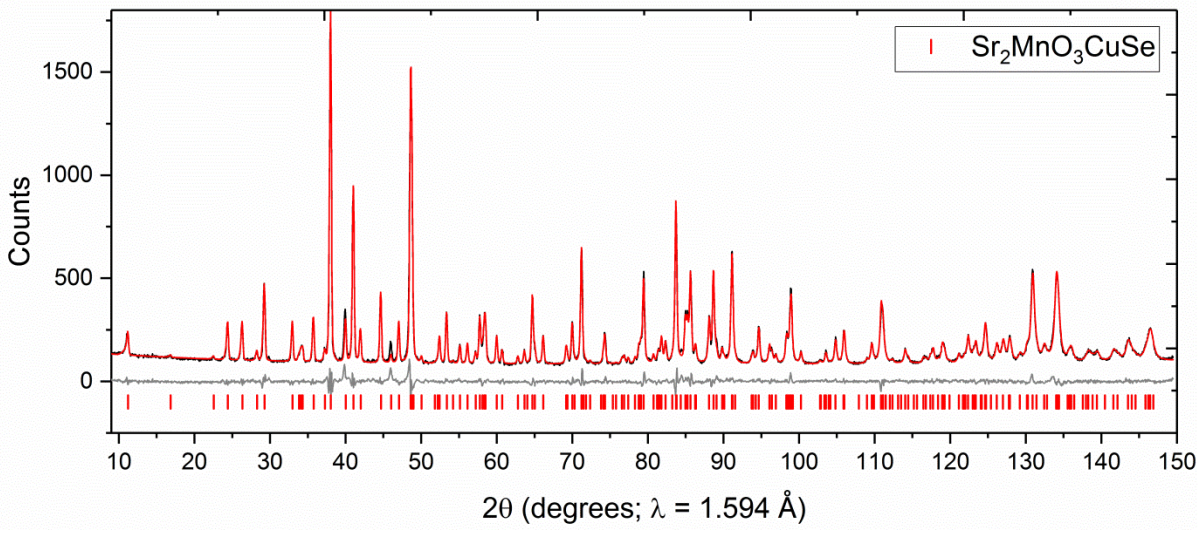

Figure 5.6: Rietveld refinement against the PND pattern of Sr_2MnO_3CuSe (XX211C), measured at RT using the D2B diffractometer on ILL

Parameter	Sr_2MnO_3CuSe	Sr_2MnO_3CuSe
Diffractometer	ILL (D2B)	I11 (Mythen)
Wavelength (Å)	1.594	0.82496(10)
Temperature (K)	298	298
Space group	*P*4/*nmm*	*P*4/*nmm*
a (Å)	3.87187(4)	3.87050(3)
c (Å)	16.3079(2)	16.3055(1)
V (Å^3)	244.477(6)	244.270(4)
Cu occupancy	0.995(11)	0.9999(11)
R_{wp}	5.23	2.17
χ^2	2.05	5.56
Mn–O(1) (Å) [×4]	1.9570(6)	1.9568(6)
Mn–O(2) (Å) [×1]	1.993(4)	2.011(6)
Mn–Se (Å) [×1]	3.475(4)	3.4599(15)
Cu–Se (Å) [×4]	2.5044(12)	2.5013(6)

Table 5.2: Lattice parameters and selected atomic distances from Rietveld refinement against the PND and PXRD patterns of the sample of Sr_2MnO_3CuSe (XX211C) at room temperature

D2B PND of Sr_2MnO_3CuSe at room temperature					
Atom	Site	*x*	*y*	*z*	U_{iso} (Å^2)
Sr(1)	2*c*	0.75	0.75	0.1916(1)	0.0027(8)
Sr(2)	2*c*	0.75	0.75	0.4179(1)	0.0110(6)
Mn	2*c*	0.25	0.25	0.3105(2)	0.0023(4)
Cu	2*a*	0.25	0.75	0	0.0057(4)
Se	2*c*	0.25	0.25	0.0974(1)	0.0042(4)
O(1)	4*f*	0.25	0.75	0.29293(9)	0.0035(4)
O(2)	2*c*	0.25	0.25	0.4327(1)	0.0053(5)

I11 PXRD of Sr_2MnO_3CuSe at room temperature							
Atom	Site	*x*	*y*	*z*	U_{11} (Å^2)	U_{22} (Å^2)	U_{33} (Å^2)
Sr(1)	2*c*	0.75	0.75	0.19157(8)	0.0040(4)	= U_{11}	0.0061(6)
Sr(2)	2*c*	0.75	0.75	0.41782(6)	0.0046(4)	= U_{11}	0.0120(7)
Mn	2*c*	0.25	0.25	0.3084(8)	0.0000(6)	= U_{11}	0.0081(9)
Cu	2*a*	0.25	0.75	0	0.0088(5)	= U_{11}	0.0198(8)
Se	2*c*	0.25	0.25	0.09658(6)	0.0058(4)	= U_{11}	0.0058(7)
O(1)	4*f*	0.25	0.75	0.2914(1)		0.01159(5)^a [U_{iso} (Å^2)]	
O(2)	2*c*	0.25	0.25	0.4310(2)		0.01203(8)^a [U_{iso} (Å^2)]	

Table 5.3: Structure parameters for Sr_2MnO_3CuSe from the Rietveld refinement of D2B PND and I11 PXRD data at room temperature; ^{a} O atoms were refined with the isotropic thermal displacement parameters

5.2.4 Variable temperature PND

In order to fully characterise the magnetic behaviour of Sr_2MnO_3CuSe, complementary neutron powder diffraction measurements were performed on a 2 g sample of Sr_2MnO_3CuSe (XX211C) using the WISH (ISIS) and fixed-wavelength D2B (ILL) diffractometers. Data were collected at 1.5, 50, 100, 140 K on WISH and 4, 75, 100 and 298 K on D2B. The data collected on both diffractometers shows that several magnetic reflections are present and the intensities of these reflections are found to decrease as the temperature is increased until 100 K where almost no intensity is seen at the positions of the magnetic reflection. This corresponds to the transition temperature (100 K) measured from ZFC and FC magnetic susceptibilities. Figure 5.7 shows the evolution of Bragg intensities of the magnetic reflections as a function of temperature from banks 3 and 8 on WISH diffractometer.

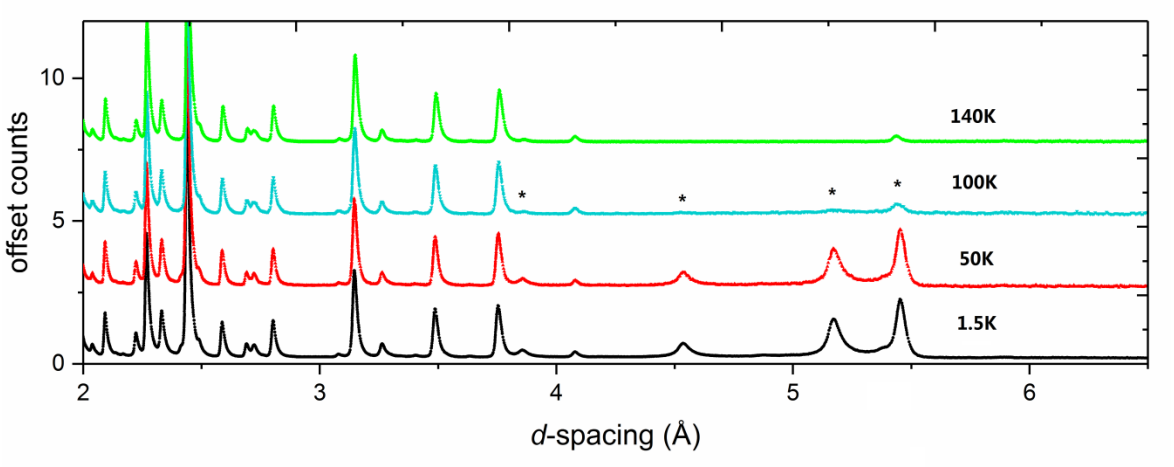

Figure 5.7: WISH PND data of Sr_2MnO_3CuSe (XX211C) in the range of 1.5 K to 140 K from banks 3 and 8; The asterisks (*) indicate the sets of magnetic reflections which are present until warming to 100 K

The magnetic reflections in the sample of Sr_2MnO_3CuSe (XX211C) were indexed on a $\sqrt{2}a \times \sqrt{2}a \times c$ expansion of the unit cell according to a magnetic propagation vector q = (1/2, 1/2, 0) based on the original tetragonal unit cell. The magnetic model was tested by adding a magnetic phase into the TOPAS Rietveld refinement initially assuming the *P*1 space group with the aid of ISODISTORT.[56] The magnitude of the Mn^{3+} magnetic moments could then be well accounted for through the symmetry mode mM4(a,b) giving a magnetic space group P_Cba2 (32.141). During the refinement of low-temperature WISH and D2B data, it was found the fit between the observed and calculated data could be significantly improved by applying a Stephens-type anisotropic broadening function[106] appropriate to the tetragonal system in the refinement. Figure 5.8 shows that the magnetic peak (100) is narrower and magnetic peak (102) is broader than other calculated peaks at 4 K on D2B diffractometer if the anisotropic broadening terms are not refined.

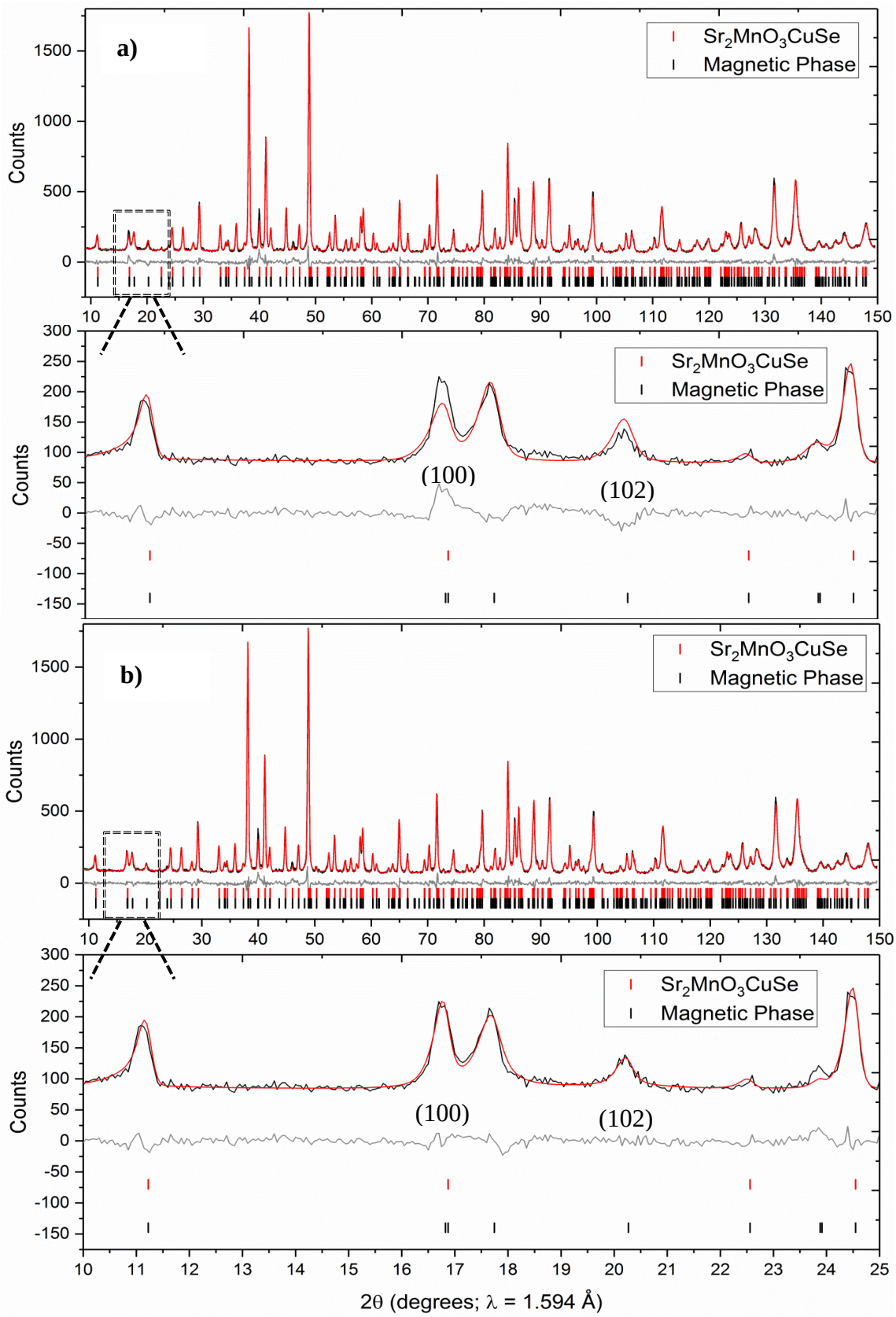

Figure 5.8: Comparison of the Rietveld refinement of Sr_2MnO_3CuSe (XX211C) measured at 4 K on D2B; a) Refinement without applying anisotropic broadening terms, giving a narrow magnetic peak (100) and a broad magnetic peak (102): $\chi^2 = 1.71$, $R_{wp} = 6.42$; b) Anisotropic broadening terms included: $\chi^2 = 1.66$, $R_{wp} = 6.20$

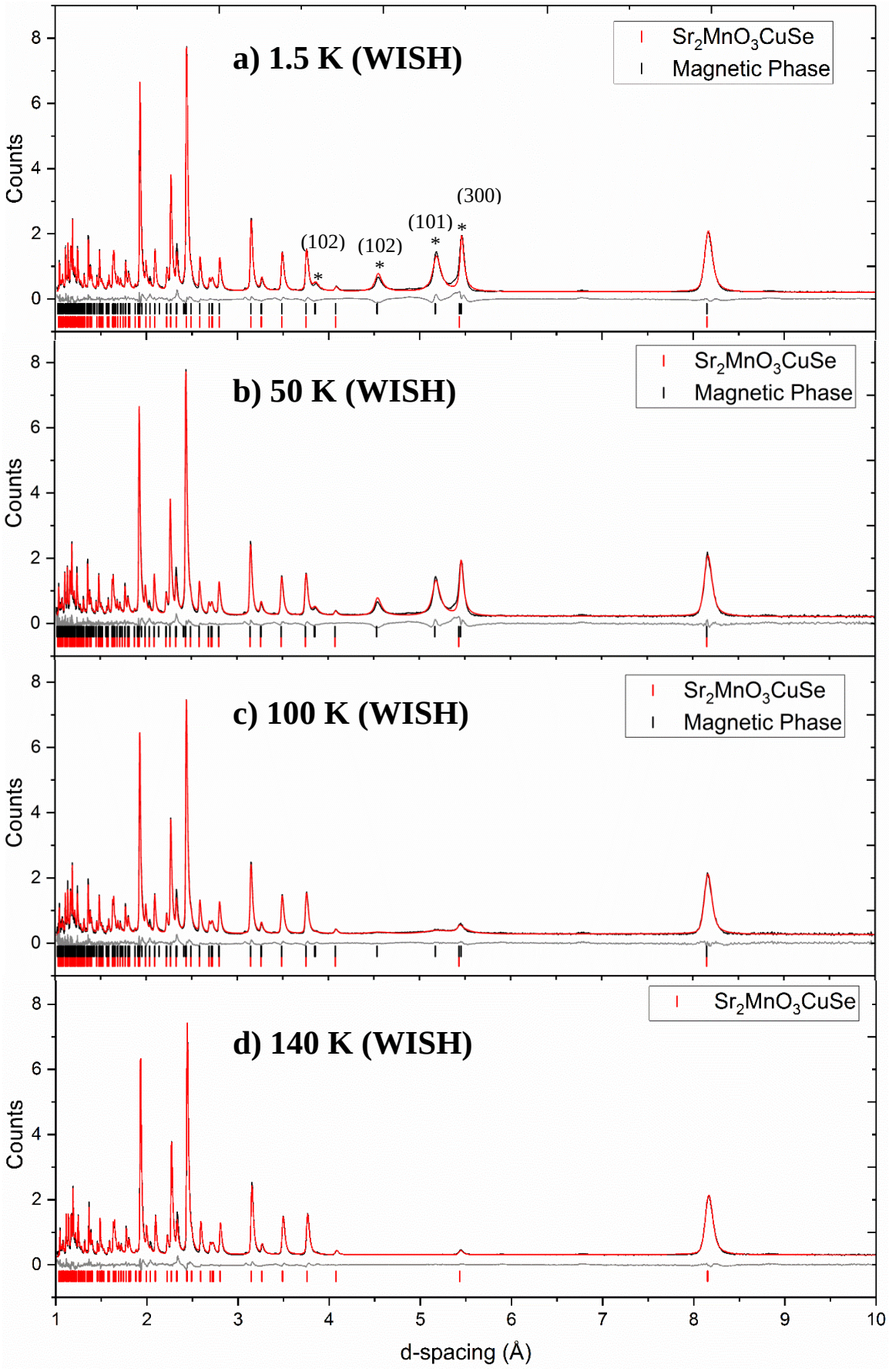
a) 1.5 K (WISH)
b) 50 K (WISH)
c) 100 K (WISH)
d) 140 K (WISH)
Sr2MnO3CuSe
Magnetic Phase
(102)
(102)
(101)
(300)
Counts
d-spacing (Å)

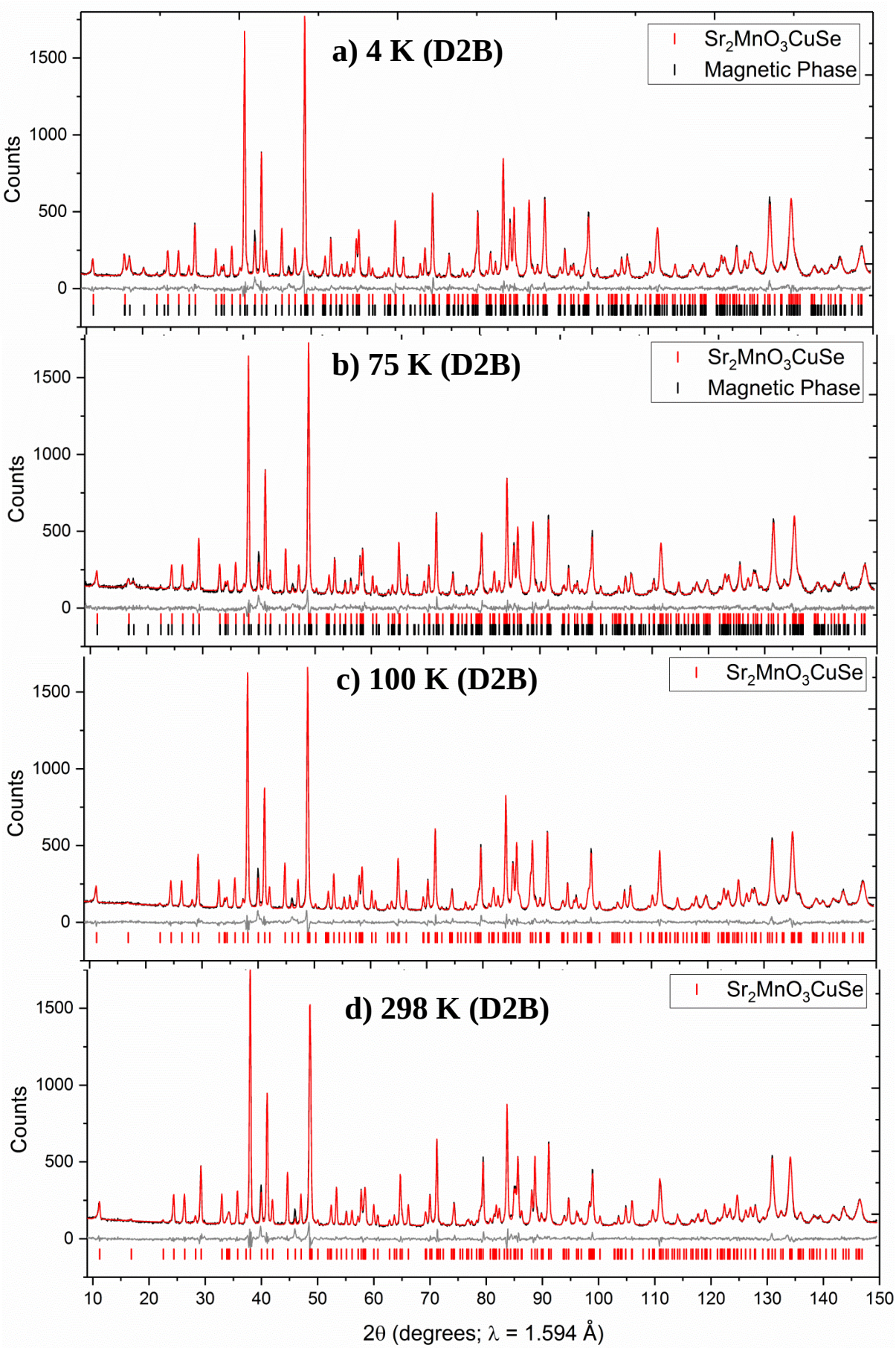

Figure 5.9: Rietveld fit for Sr_2MnO_3CuSe (XX211C) measured by both WISH and D2B diffractometers at 1.5, 4, 50, 75, 100, 140 and 298 K

Since the variable temperature data were collected on both WISH and D2B diffractometers, to make their refined magnetic moments comparable, a magnetic model was first refined against the temperatures at 1.5 K and 4 K. The results showed both refined magnetic moments have reasonable values and are, as expected equal within the uncertainties at two base temperatures, 3.76(6) μB/Mn^{3+} at 4 K (D2B) and 3.76(2) μB/Mn^{3+} at 1.5 K(WISH). For subsequent refinements the absorption parameters for the WISH data banks were then fixed to the 1.5 K values. The resultant Rietveld plots for all temperatures collected from both WISH and D2B diffractometers are shown in Figure 5.9. It was observed that all the magnetic peaks in both WISH and D2B diffraction patterns could be well fitted by applying a single magnetic mode mM4(a,b). These refinement results indicate a long-range magnetic ordering of the moments of Mn^{3+} in the MnO_5 layers below the Neél temperature (100 K). Nearest-neighbour moments were coupled antiferromagnetically in a checkerboard fashion with the moments directed along the *c*-direction perpendicular to the planes. Figure 5.10 shows the magnetic model of Sr_2MnO_3CuSe (XX211C) below 100 K.

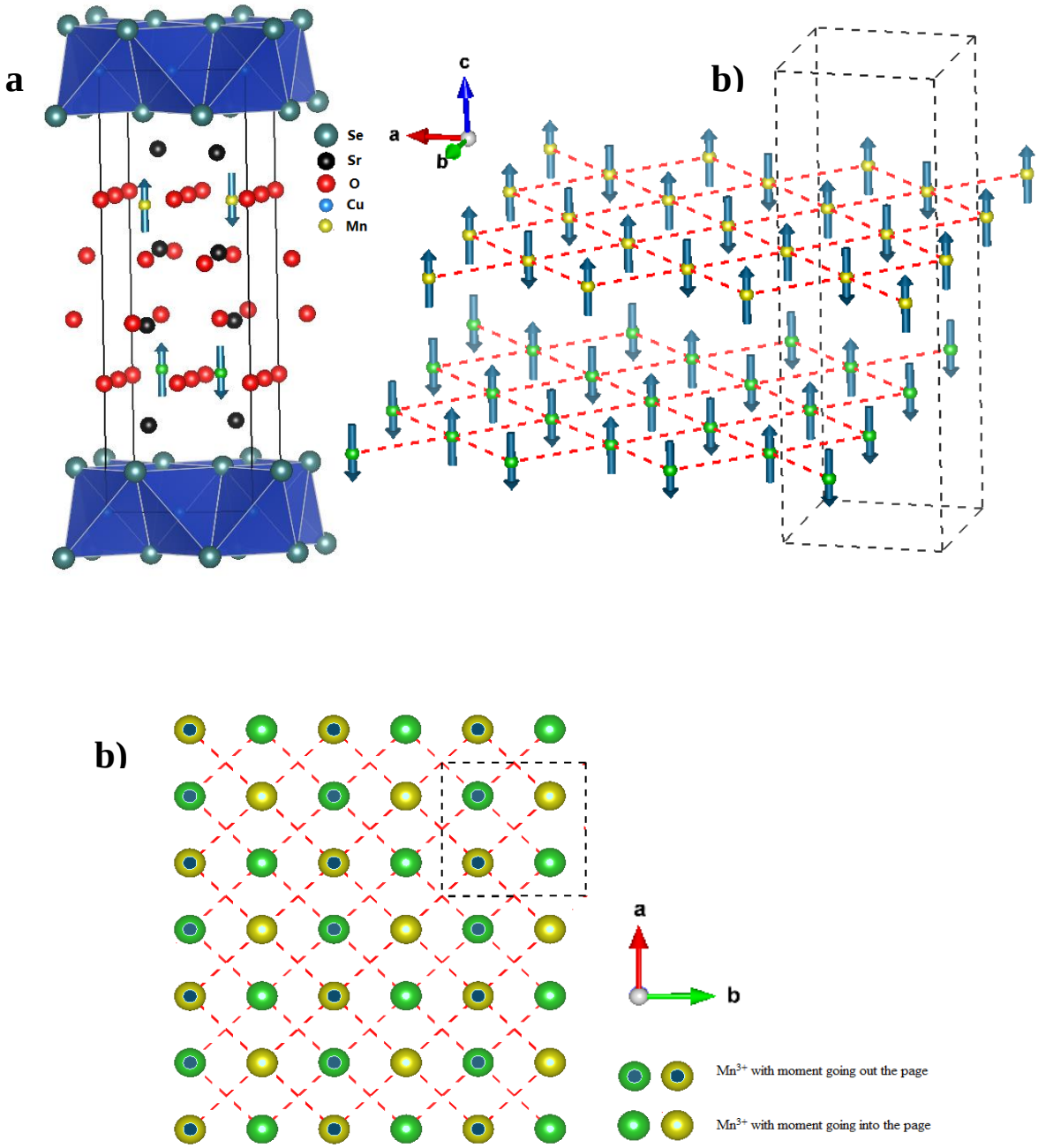

Figure 5.10: a) The ordering of Mn^{3+} magnetic moments in a magnetic unit cell of Sr_2MnO_3CuSe; b) The checkerboard-type antiferromagnetic ordering of Mn^{3+} in the two oxide layers with their magnetic moments parallel to c axis (the green and yellow balls represent the two oxide layers)

For Sr_2MnO_3CuSe, the magnetic moments of the Mn^{3+} ions grow in magnitude as the sample is cooled down from 100 K to 1.5 K, at which point the moments reach their maxima of 3.76 (2) μB/Mn^{3+}. This is lower than the expected saturated spin-only ordered magnetic moment of a Mn^{3+} of 4 μB and probably due to the covalency of the Mn–O bonds in both layers, decreasing the density of unpaired electrons by delocalisation. The function of magnitudes of the magnetic moments collected on both diffractometers against measured temperatures is shown in Figure 5.11.

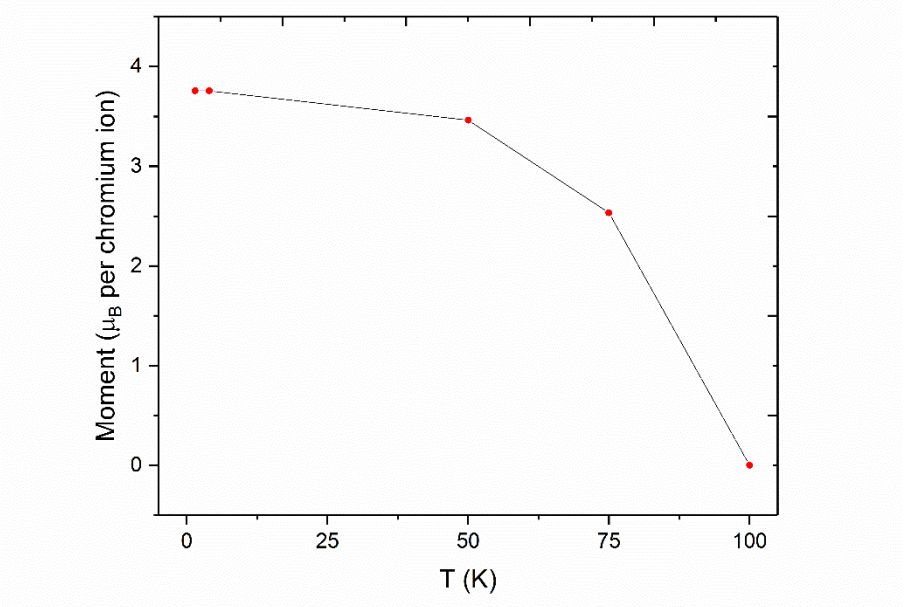

Figure 5.11: Magnitudes of the Mn^{3+} moments in Sr_2MnO_3CuSe as a function of temperature

Table 5.4 gives the refined results of Mn^{3+} magnetic moments and selected structural parameters of Sr_2MnO_3CuSe (XX211C) at all measured temperatures on both WISH and D2B diffractometers, from which the lattice parameter *a* and volume of Sr_2MnO_3CuSe increases as the temperature goes up owing to the thermal expansion. However, the refinements on both diffractometers show that the lattice parameter *c* is increased as the temperature is cooled down to the base temperature, during which the magnetic moments of Mn^{3+} are ordered in the oxide layers. After the magnetic transition (on warming) at around

100 K, the change of the lattice parameter *c* will go back to obey the thermal expansion. The example of changes of refined parameters as a function of temperature measured on D2B can be seen in Figure 5.12, where the lattice parameter *c* is 0.0018 (5) Å longer at 4 K than at 100 K. The further investigation on the lattice parameters of Sr_2MnO_3CuSe (XX211C) at different temperatures was also performed using variable temperature PXRD, which is shown in Appendix E.

Instrument	WISH			
Temperature (K)	1.5	50	100	140
$\mu B/Mn^{3+}$	3.76(2)	3.38(2)	/	/
R_{wp}	5.57	6.64	6.33	5.20
χ^2	0.05	0.06	0.06	0.05
a (Å)	3.85521(2)	3.85531(3)	3.85773(3)	3.86097(2)
c (Å)	16.3040(2)	16.3039(3)	16.3023(2)	16.3025(28)
V (Å^3)	242.320(4)	242.334(5)	242.612(5)	243.027(95)
Instrument	D2B			
Temperature (K)	4	75	100	298
$\mu B/Mn^{3+}$	3.76(6)	2.53(9)	/	/
R_{wp}	6.20	5.24	5.01	5.23
χ^2	1.66	10.85	1.94	2.05
a (Å)	3.85266(4)	3.85453(4)	3.85744(4)	3.87187(4)
c (Å)	16.2972(3)	16.2971(3)	16.2954(2)	16.3079(2)
V (Å^3)	241.900(7)	242.131(7)	242.473(6)	244.477(6)

Table 5.4: Results of refinement against PND data at variable temperatures measured on the WISH and D2B diffractometers

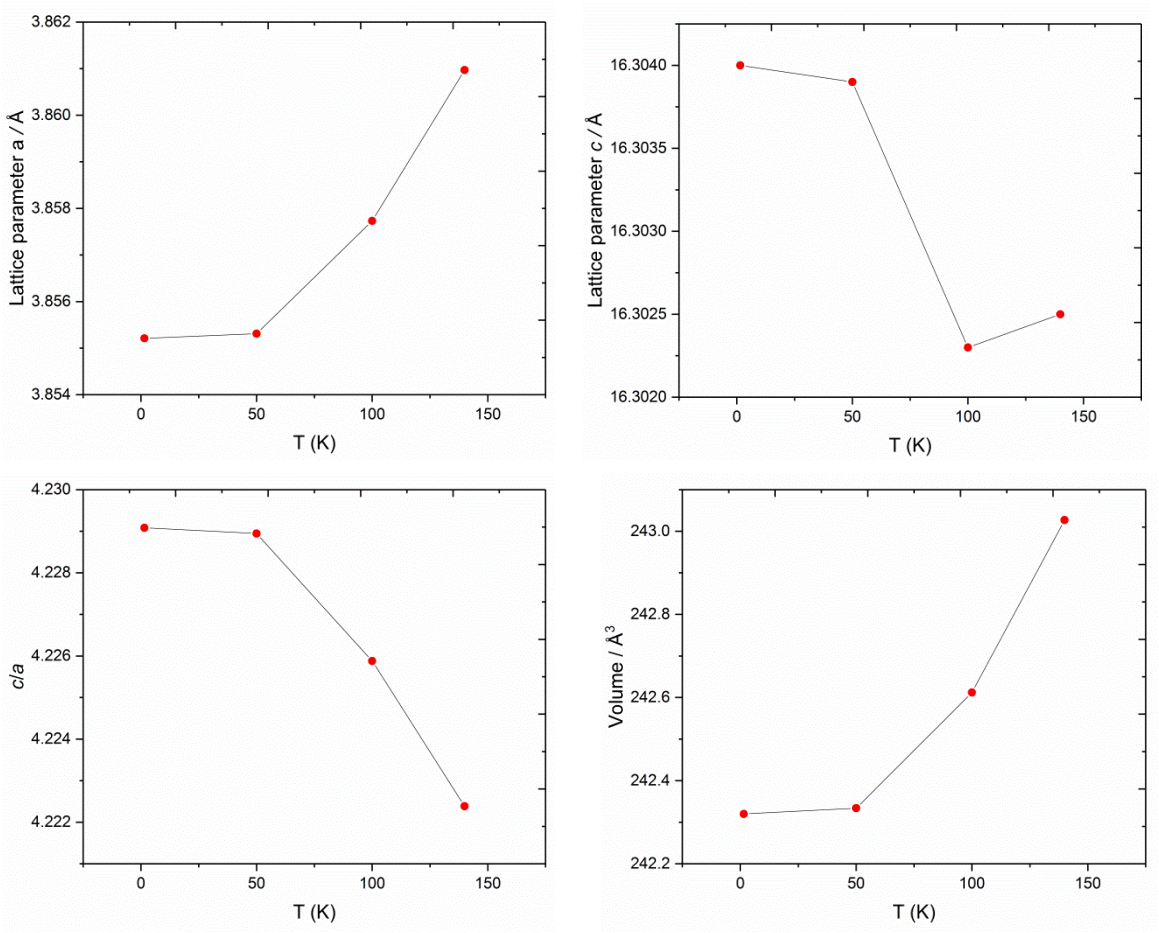

Figure 5.12: The change of lattice parameters *a* and *c*, *c*/*a* ratio and unit cell volume of Sr_2MnO_3CuSe (XX211C) on warming from 1.5 K, measured by WISH diffractometer

5.3 Synthesis and characterisation of Sr_2MnO_3CuS

The synthesis of Sr_2MnO_3CuS, the isostructural sulfide analogue of Sr_2MnO_3CuSe, was first reported in 2000 by Zhu.[45] However, no neutron characterisation of the long-range magnetic ordering has been reported in the literature. The variable-temperature PND on Sr_2MnO_3CuSe shows checkerboard-type antiferromagnetic ordering in the MnO_5 layers, suggesting that one may find similar magnetic properties in Sr_2MnO_3CuS. A pure sample of Sr_2MnO_3CuS was synthesized by Jack Blandy (a previous DPhil and post-doctoral researcher in our group), which allowed the variable-temperature PND studies reported here to be performed. The sample of Sr_2MnO_3CuS (JNB448) was synthesized from SrS, $SrCuO_2$, MnO_2 (Alfa,

99.997 %) and Mn (Aldrich, 99 %) in the ratio of 2 : 2 : 1 : 1. Precursor SrS was prepared by hydrogen reduction of $SrSO_4$ at 900 °C for 24h, while $SrCuO_2$ was prepared by reacting $SrCO_3$ with CuO at 920 °C. The solids were mixed and ground in an argon-filled glove box and the sample was put in an alumina crucible and sealed in a silica tube. The sample was then heated to 800 °C for 12 hours at a slow rate of 2 °C/min. The detailed analysis of the magnetic properties of Sr_2MnO_3CuS and the comparison with other related compounds are discussed in this chapter.

5.3.1 Powder X-ray diffraction

High-resolution synchrotron powder X-ray diffraction was measured at room-temperature on the sample of Sr_2MnO_3CuS (JNB448) synthesised by the method described above. A refinement against data collected on the MAC detector of the instrument I11 at the Diamond Light Source is shown in Figure 5.13. Although elemental Cu is present in the diffraction pattern as 0.55 (1) weight %, the Cu site in the compound was refined to be fully occupied [0.998(1)], which indicates several other unindexed peaks in the PXRD data are probably due to the impurity phase with the composition of other elements (Sr, Mn, O and S). The refinement results are compared with those from Sr_2MnO_3CuSe in Table 5.5 and Table 5.6. The substitution of Se^{2-} (1.98 Å) with the smaller S^{2-} (1.84 Å) at the (0.25, 0.25, *z*) crystallographic site in the CuSe layer gives rise to the contraction of the lattice parameter *a* by 0.88 % and lattice parameter *c* by 2.04 %.[105] By contrast, the Cu-*Ch* bond length shrinks by 3.53 %. The structure of the tetrahedral Cu*Ch* layer is therefore more compressed along the *c* axis in Sr_2MnO_3CuS (α S-Cu-S = 105.84(5) ° and β S-Cu-S = 111.32(3) °) than Sr_2MnO_3CuSe (α Se-Cu-Se = 101.40(3) ° and β Se-Cu-Se = 113.653(16) °).

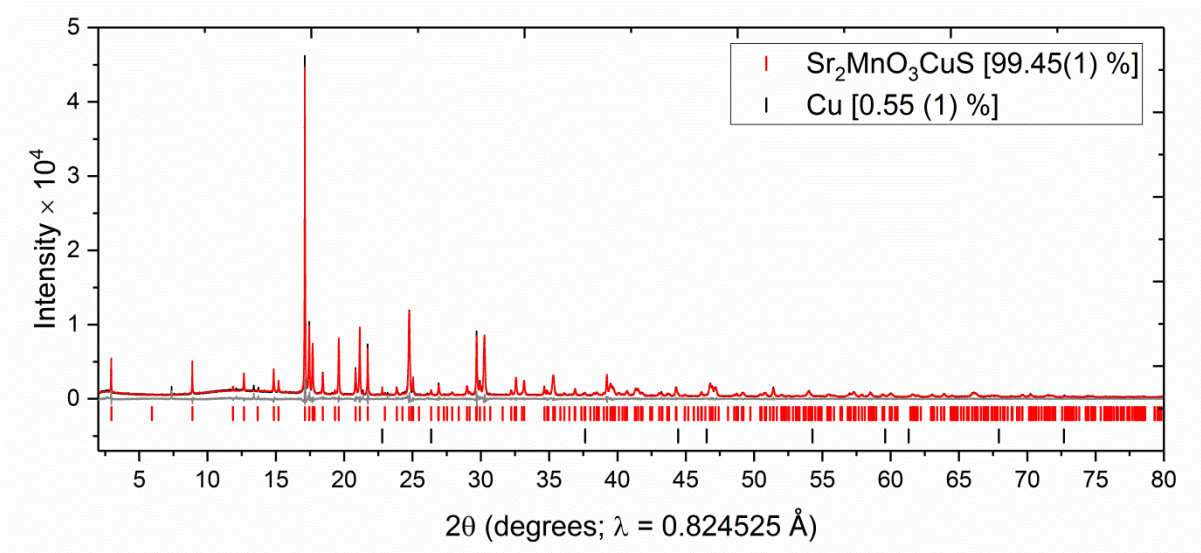

Figure 5.13: Rietveld refinement against the PXRD pattern of the sample of Sr_2MnO_3CuS (JNB448), measured at RT using the MAC detector on the I11 beamline

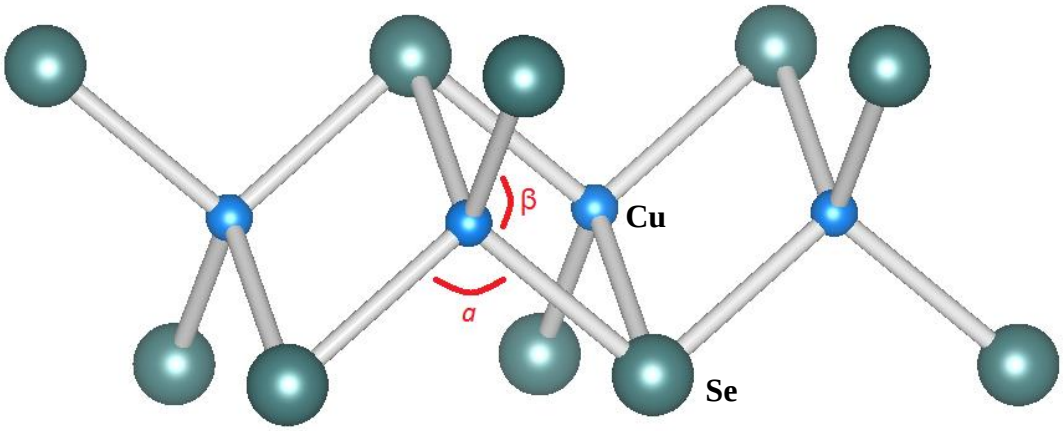

Figure 5.14: α and β S(Se)-Cu- S(Se) angles in the CuS(Se) layer

	Sr_2MnO_3CuS	Sr_2MnO_3CuSe
Diffractometer	I11 (MAC detector)	I11 (Mythen detector)
Wavelength (Å)	0.8245(2)	0.82496(10)
Temperature (K)	298	298
Space group	*P4/nmm*	*P4/nmm*
a (Å)	3.84551(2)	3.87050(3)
c (Å)	15.95988(9)	16.3055(1)
V (Å^3)	236.014(2)	244.270(4)
Phase density (g cm^{-3})	5.25977(5)	5.7196(1)
R_{wp}	7.50	2.17
χ^2	2.56	5.56
Cu–Cu (Å) [×1]	2.71918(0)	2.73681(3)
Cu–S(Se) (Å) [×4]	2.4101(8)	2.5013(6)
β S(Se)-Cu- S(Se) (°) [×4]	111.32(3)	113.653(16)
α S(Se)-Cu- S(Se) (°) [×2]	105.84(5)	101.40(3)

Table 5.5: Refined parameters, selected atomic distances and bond angles (see Figure 5.14) from Rietveld refinement against the PXRD data for Sr_2MnO_3CuS and Sr_2MnO_3CuSe

I11 PXRD of Sr_2MnO_3CuS at room temperature							
Atom	Site	*x*	*y*	*z*	U_{11} (Å^2)	U_{22} (Å^2)	U_{33} (Å^2)
Sr(1)	2c	0.75	0.75	0.18313(3)	0.0045(2)	= U_{11}	0.0031(3)
Sr(2)	2*c*	0.75	0.75	0.41530(3)	0.0091(2)	= U_{11}	0.0085(4)
Mn	2c	0.25	0.25	0.30227(5)	0.0038(3)	= U_{11}	0.0070(4)
Cu	2*a*	0.25	0.75	0	0.0170(3)	= U_{11}	0.0186(5)
S	2*c*	0.25	0.25	0.09105(8)	0.0090(5)	= U_{11}	0.0014(7)
O(1)	4f	0.25	0.75	0.2837(1)		0.0038(5) [a] [U_{iso} (Å^2)]	
O(2)	2c	0.25	0.25	0.4292(2)		0.0105(8) [a] [U_{iso} (Å^2)]	

Table 5.6: Structure parameters for Sr_2MnO_3CuS (JNB448) from the Rietveld Refinement of PXRD data; [a] O atoms were refined with the isotropic thermal displacement parameters

5.3.2 Room temperature PND

A Rietveld refinement of Sr_2MnO_3CuS (JNB448) against room temperature PND data is shown in Figure 5.15, which gives a good fit between the observed result and calculated model. Cu is found in the refinement as an impurity phase and present at a level of 1.05 (8) weight %. The composition of this compound is refined to be Sr_2MnO_3CuS with fully occupied Cu [0.99 (1)] in the S^{2-} layers, which shows the agreement with the occupancy of Cu [0.998(1)] derived from PXRD (MAC) refinement of Sr_2MnO_3CuS. The refined structural parameters are given in Table 5.7, Table 5.8 and Table 5.9, showing good agreement with those derived from the I11 PXRD data.

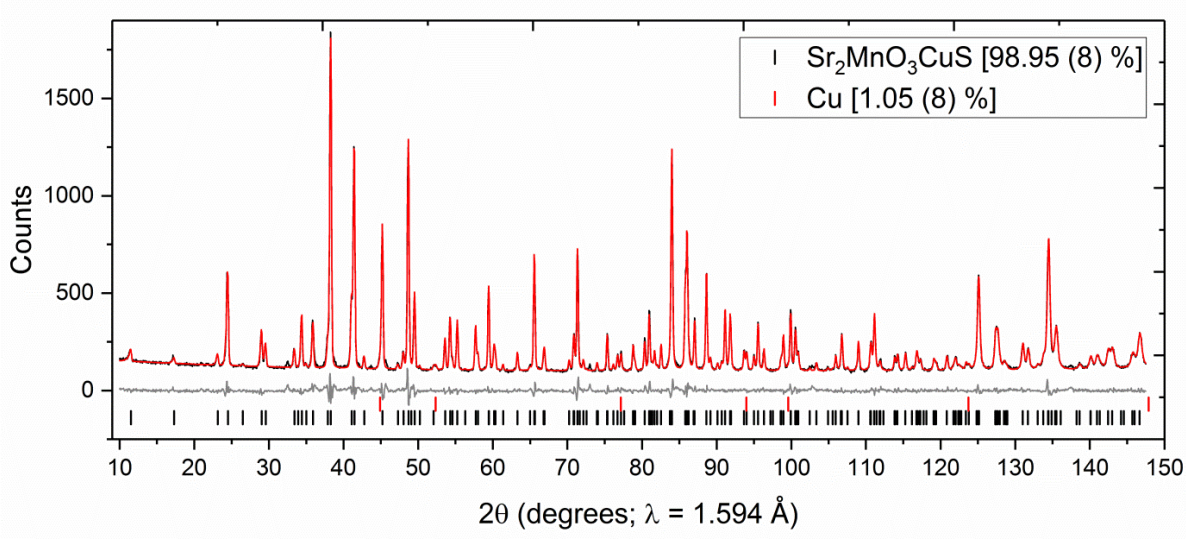

Figure 5.15: Rietveld refinement of Sr_2MnO_3CuS (JNB448) collected at RT on the D2B diffractometer

	Sr_2MnO_3CuS (JNB448)
Diffractometer	ILL (D2B)
Wavelength (Å)	1.594
Temperature (K)	298
Space group	*P4/nmm*
a (Å)	3.86560(3)
c (Å)	15.8984(2)
V (Å^3)	237.568(4)
Phase density (g cm^{-3})	5.22535(9)
R_{wp}	4.74
χ^2	1.95

Table 5.7: Lattice Parameters for Sr_2MnO_3CuS from PND Rietveld Refinement

D2B PND of Sr_2MnO_3CuS at room temperature					
Atom	Site	*x*	*y*	*z*	U_{iso} (Å^2)
Sr(1)	2*c*	0.75	0.75	0.18351(9)	0.0022(6)
Sr(2)	2*c*	0.75	0.75	0.4136(1)	0.0114(5)
Mn	2*c*	0.25	0.25	0.3032(2)	0.0044(4)
Cu	2*a*	0.25	0.75	0	0.0106(4)
S	2*c*	0.25	0.25	0.0918(3)	0.0053(6)
O(1)	4*f*	0.25	0.75	0.28645(8)	0.0063(3)
O(2)	2*c*	0.25	0.25	0.4312(1)	0.0103(5)

Table 5.8: Structure parameters for Sr_2MnO_3CuS from the Rietveld Refinement of PND data

	D2B PND of Sr_2MnO_3CuS at room temperature
Mn–O(1) (Å) [×4]	1.9511(5)
Mn–O(2) (Å) [×1]	2.035(4)
Mn–S (Å) [×1]	3.361(5)
Cu–Cu (Å) [×1]	2.73338(3)
Cu–S (Å) [×4]	2.422(2)
β S-Cu- S (°) [×4]	111.29(7)
α S-Cu- S (°) [×2]	105.89(13)

Table 5.9: Selected atomic distances and bond angles for Sr_2MnO_3CuS from the Rietveld Refinement of PND data

5.3.3 Magnetic susceptibility measurements

The measurement of magnetisation versus field, $M(H)$, of Sr_2MnO_3CuS (JNB448) is linear at 300 K (Figure 5.16a), confirming that no room-temperature ferromagnetic impurities are present in the sample JNB448. The temperature-dependent ZFC and FC magnetic susceptibilities (χ) measured in an applied field of 1000 Oe between 2 K and 330 K are shown in Figure 5.16b. The broad maximum at around 95 K indicates the low-dimensional antiferromagnetic ordering of Mn^{3+} which was also identified by Kamihara et al. in their previous publication.[95] There is a small divergence between ZFC and FC data below T_g (approximately 70 K), suggesting the appearance of spin glass behaviour.

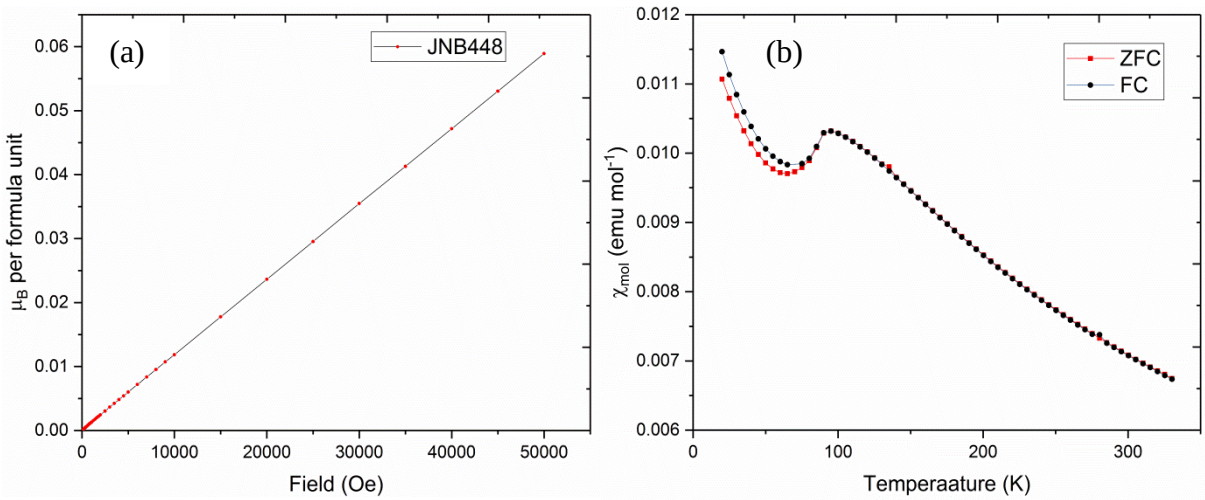

Figure 5.16: (a) Magnetic moment per Mn ion of Sr_2MnO_3CuS as a function of applied magnetic field, measured at 300 K; (b) The ZFC and FC magnetic susceptibilities of Sr_2MnO_3CuS, measured at 1000 Oe between 2 K and 330 K

Attempts to draw a Curie-Weiss plot with linear regression of $1/\chi$ between 130 K and 330 K (Figure 5.17a) leads to unreasonably large values. The extracted Weiss constant, θ = -308 K is comparable to the higher end of the temperature range used for the measurement, and μ_{eff} = 5.87 μ_B is significantly larger than the expected values, which suggests the sample doesn't obey the Curie-Weiss law in the measured temperature range. The reported Weiss

temperature and effective magnetic moment were determined to be θ = -327 K and 3.82 μ_B in the temperature range of 200 K-1000 K showing that the larger temperature range gives more reasonable values, as expected.[95] The magnetisation isotherm of Sr_2MnO_3CuS at 5 K (Figure 5.17b) shows there is a hysteresis present within the sample and the loop is displaced from the origin, consistent with the presence of a spin glass component to the magnetism.

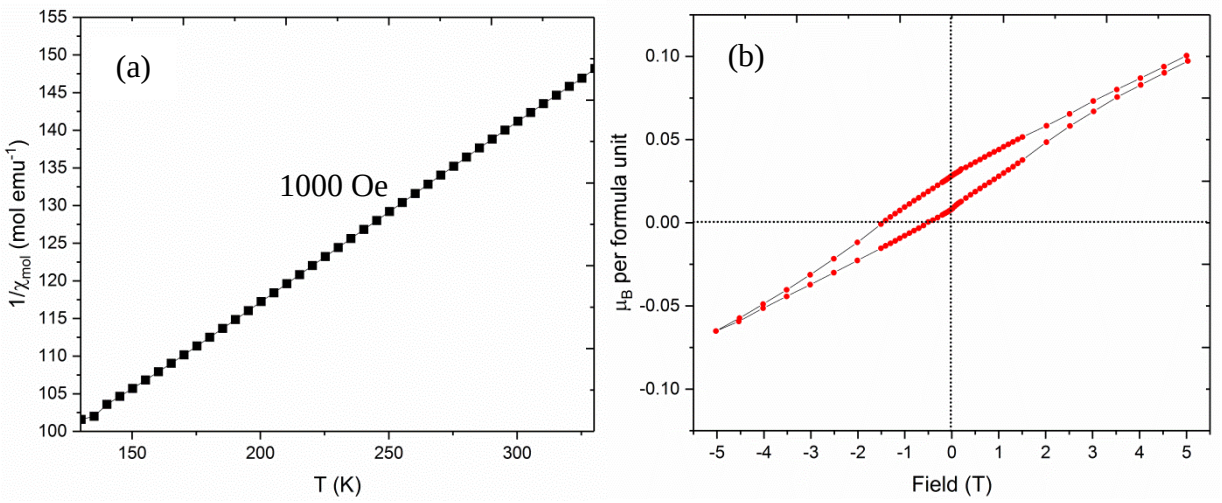

Figure 5.17: (a) The inverse magnetic susceptibilities (zfc) of Sr_2MnO_3CuS with line of best fit (130 K-330 K), measured in an applied field of 1000 Oe; (b) M vs H isotherm of Sr_2MnO_3CuS measured at 5 K in the range -5 ≤ H (T) ≤ +5

5.3.4 Variable temperature PND

Having observed the appearance of broad antiferromagnetic ordering of Sr_2MnO_3CuS at 95 K in the magnetic susceptibility measurements, which is also found in isostructural Sr_2MnO_3CuSe (T_N = 100 K), it was expected that low-temperature neutron powder diffraction would further identify the exact magnetic ordering of Mn^{3+} moments in the sample. PND measurement was performed on Sr_2MnO_3CuS at 4 K on D2B (λ = 1.594 Å). In comparison with the PND data at 298 K, several additional Bragg reflections are present in the diffraction pattern at 5 K (Figure 5.18). The appearance of additional magnetic Bragg peaks at high *d*-spacing are consistent with the antiferromagnetic ordering of Mn^{3+} in the

oxide layers. However, MnO is also found in the sample as an impurity phase (although the peaks of its nuclear structure can't be refined in the PND data due to the fairly small amount). This is antiferromagnetic at 4 K and gives a single intense magnetic Bragg reflection (001) in the diffraction pattern.[107]

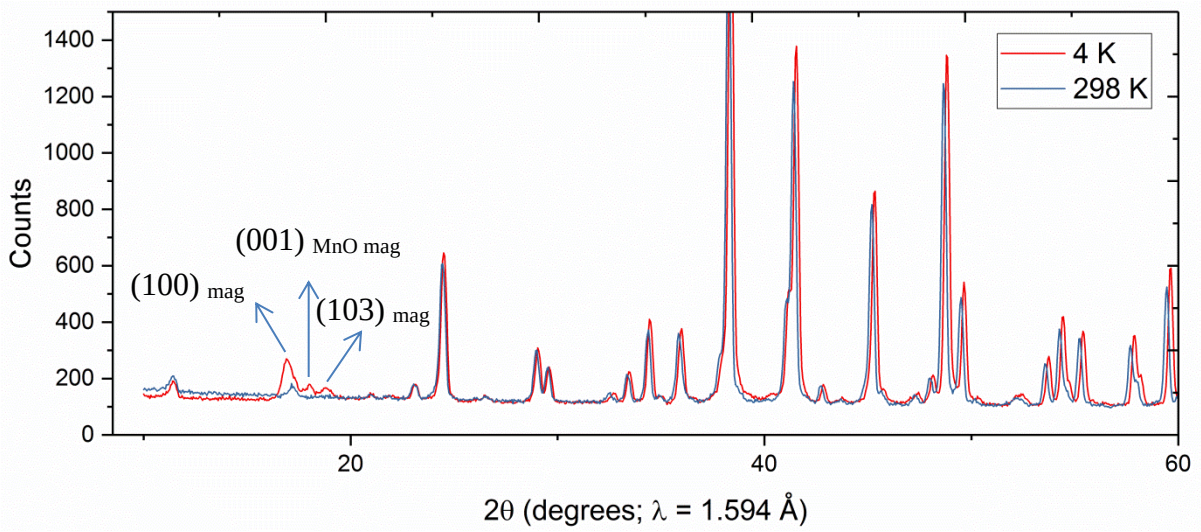

Figure 5.18: Comparison of PND data of Sr_2MnO_3CuS collected on the D2B diffractometer at 4 K and 298 K

As described above in Sr_2MnO_3CuSe, the magnetic Bragg reflections were first modelled using a $\sqrt{2}a \times \sqrt{2}a \times c$ expanded unit cell in which the moments are antiferromagnetically aligned along the *c* axis with each MnO plane. However, using a similar model for this S analogue did not reproduce the corresponding magnetic peaks in the Rietveld refinement. Instead, these magnetic reflections of Sr_2MnO_3CuS were indexed to a magnetic cell that is a $\sqrt{2}a \times \sqrt{2}a \times 2c$ expansion of the structural unit cell. The web-based software ISODISTORT [56] was used to aid the deduction of the magnetic models prior to Rietveld refinement, starting with the magnetic space group *P*1(1.1), where all possible magnetic symmetry modes were tried to fit the intensity of the magnetic Bragg reflections. It was observed that the magnetic peaks in the diffraction pattern could be well fitted by applying

a single magnetic mode mA4(a,b), leading to the magnetic space group I_cba2 (45.239).[56] As in the previous refinements of Sr_2MnO_3CuSe, for Sr_2MnO_3CuS, the magnetic peak (100) is narrower and magnetic peak (103) is broader than other calculated peaks (Figure 5.19), which was improved by applying anisotropic broadening terms in the refinement. The improved Rietveld plot at 4 K is shown in Figure 5.20 with $R_{wp} = 4.79$.

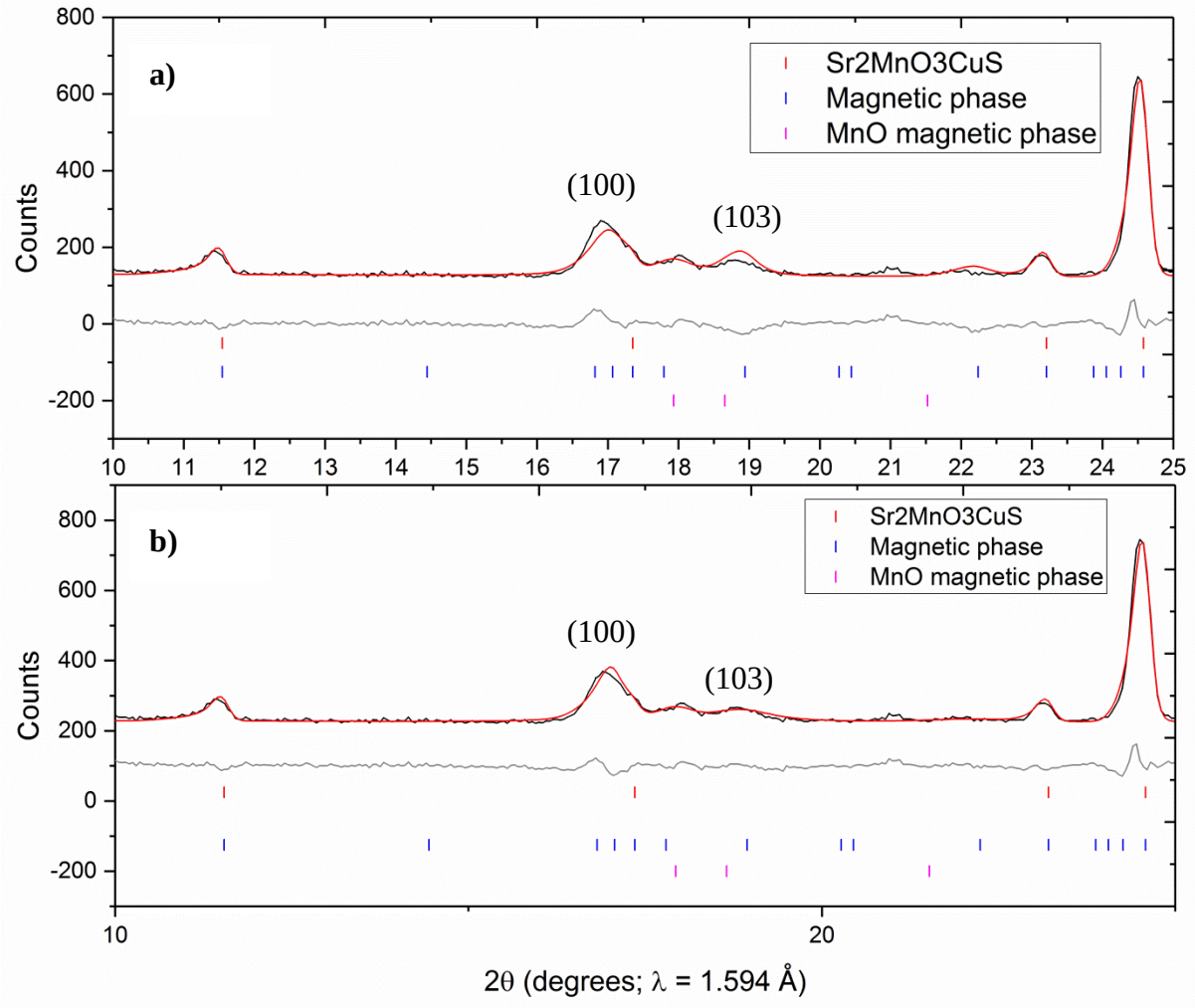

Figure 5.19: Comparison of the Rietveld refinement of Sr_2MnO_3CuS (JNB448) measured at 4 K on D2B; a) Refinement without applying anisotropic broadening terms, giving a narrow magnetic peak (100) and a broad magnetic peak (103): $\chi^2 = 2.58$, $R_{wp} = 4.93$; b) Anisotropic broadening terms included: $\chi^2 = 2.51$, $R_{wp} = 4.79$

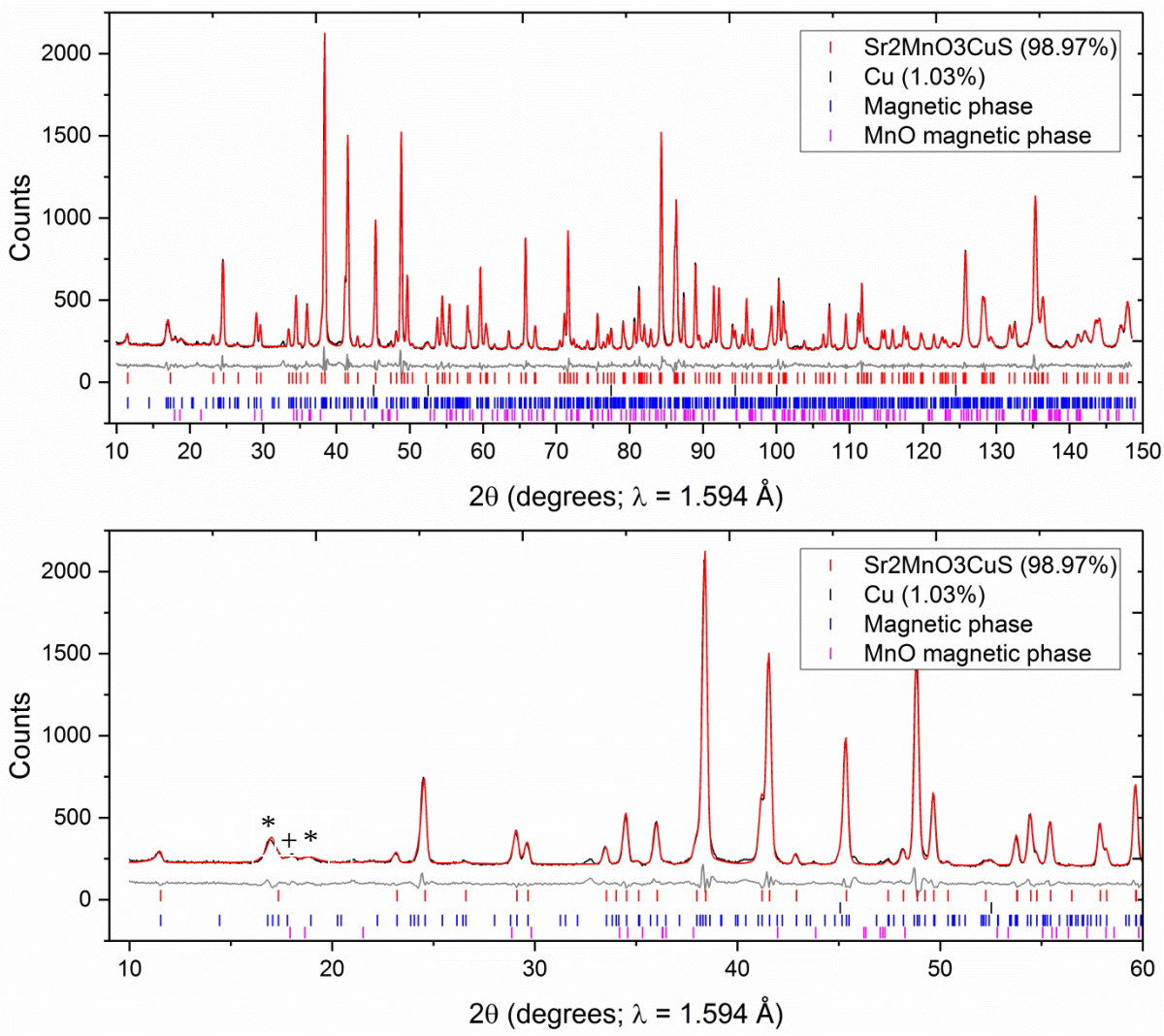

Figure 5.20: Rietveld refinement of Sr_2MnO_3CuS (JNB448) collected at 4 K (R_{wp} = 4.79, χ^2 = 2.51); The asterisks(*) and crosses (+) indicate the magnetic reflections for Sr_2MnO_3CuS and MnO respectively

Similar to its Se analogue, the magnetic mode mA4(a,b) of Sr_2MnO_3CuS corresponds to a long-range antiferromagnetic ordering of the spins in the Mn planes(Figure 5.21a). The neighbouring moments were coupled antiferromagnetically in a checkerboard fashion with their moments directed along the *c*-direction. By contrast, the $\sqrt{2}a \times \sqrt{2}a \times 2c$ expansion gives a doubled volume of the cell along the *c*-direction (*i.e.* four times bigger than that of the nuclear cell), where there is an antiferromagnetic alignment of Mn^{3+} between the adjacent alternating Mn planes, together with AFM ordering within the planes (Figure 5.21b).

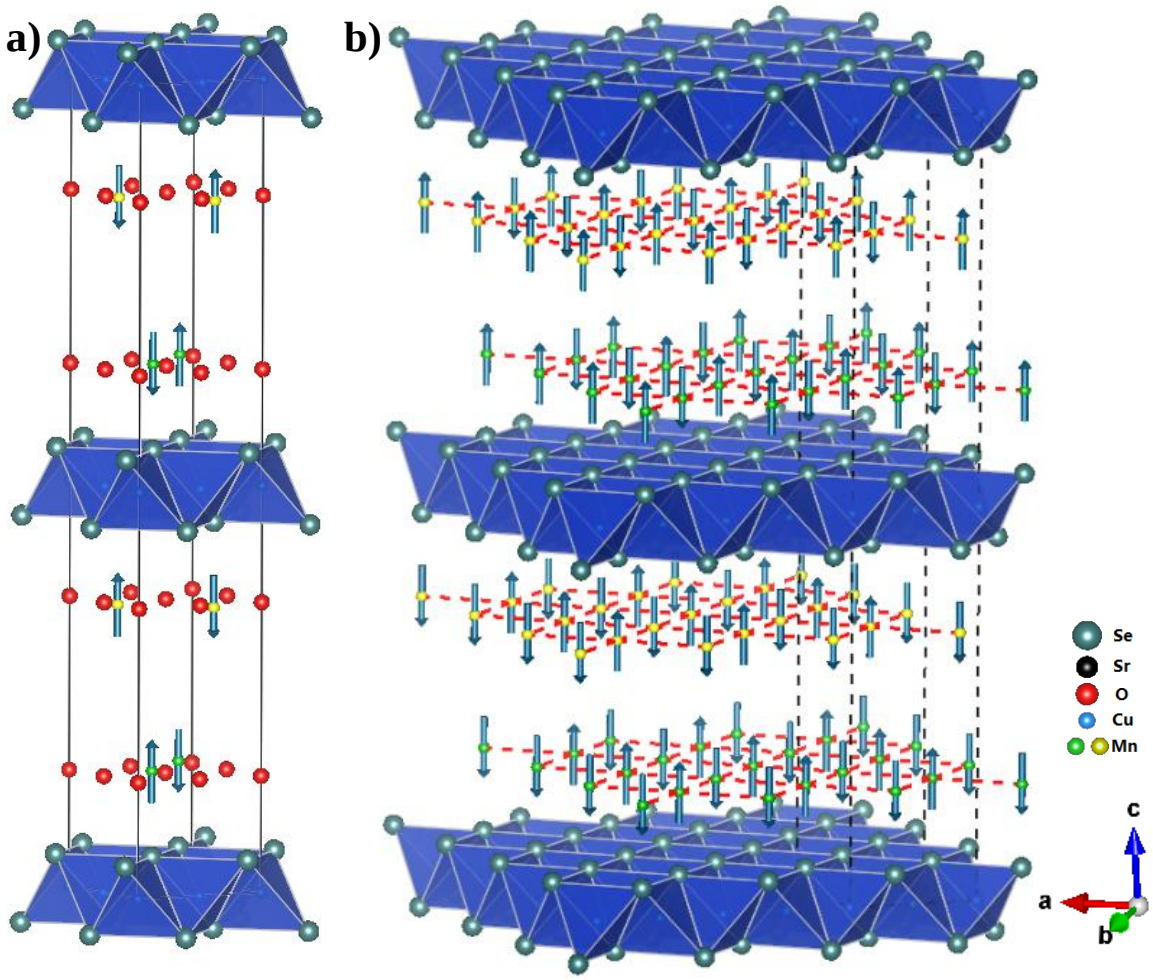

Figure 5.21: (a) The ordering of Mn^{3+} magnetic moments in a magnetic unit cell of Sr_2MnO_3CuS; (b) The checkerboard-type antiferromagnetic ordering of Mn^{3+} in the $\sqrt{2}a \times \sqrt{2}a \times 2c$ expansion of the nuclear cell with their magnetic moments parallel to c axis

A further significant difference between Sr_2MnO_3CuSe and Sr_2MnO_3CuS is that the refined ordered magnetic moment of Mn^{3+} at 4 K in Sr_2MnO_3CuS is 2.89(6) μB/Mn^{3+} which is 23.1(2) % smaller than that seen in its Se analogue (3.76 (2) μB/Mn^{3+}). It was also found that there was a prominent glassy component to the magnetism in Sr_2MnO_3CuS, suggesting some disorder and frustration in the sulphide compound that means the full moment expected for Mn^{3+} does not develop. A possible reason for this is discussed below. The measured ordering temperatures for the Mn^{3+} moments of the oxide layers are 95 K in Sr_2MnO_3CuS

and 100 K in Sr_2MnO_3CuSe, with only a difference of 5 K, which is due to their similar Mn-O(1) distances, leading to the similar intraplanar exchange interactions in both compounds.

5.4 Synthesis and characterisation of $Sr_2MnO_3Cu_{0.94}S$

Refinements of the structure of Sr_2MnO_3CuS using both PXRD (Mythen on I11) and PND (D2B on ILL) confirm that Cu site is fully occupied and the phase is stoichiometric with the uncertainties. It was found in preliminary chemical investigations in our group that this compound could be made Cu deficient in an analogous way to $Sr_2MnO_2Cu_{1.5}S_2$ and $Sr_2CoO_2Cu_{2-\delta}S_2$, which were reported by Smura *et al.* [27, 108] The oxidation of parent compound Sr_2MnO_3CuS by I_2 was performed within the group by Dr Jack Blandy. In this work, synchrotron PXRD (Mythen detector) and PND (D2B) were used to probe both the Cu deficiency and its effect on magnetic properties of this sample.

5.4.1 Deintercalation of Sr_2MnO_3CuS

The parent material Sr_2MnO_3CuS was synthesised using the method in section 5.3. SrS, $SrCuO_2$, MnO_2 (Alfa, 99.997 %) and Mn (Aldrich, 99 %) were ground together in the ratio of 2 : 2 : 1 : 1 and heated to 800 °C for 12 hours, before cooling the sample in the furnace. 0.1 molar equivalent (Mn:I_2 ratio is 1:10) of I_2 (99.99%, Alfa Aesar) was dissolved in approximately 50 cm^3 of MeCN. All the procedures were carried out in the absence of air and moisture (MeCN was pre-dried by using a commercial molecular sieve and the cooled iodine was dried under dynamic vacuum for about 20 minutes). The I_2/MeCN mixture was then cooled in an ice-water bath, after which the solution was transferred into a pre-cooled Schlenk flask containing the reactant Sr_2MnO_3CuS (parent material JNB448, described in section 5.3). The reaction was then left stirring for 2 days and the product was filtered and

washed three times in clean MeCN before it was dried for 20 minutes under dynamic vacuum and the powder was unloaded in the glovebox. The synthesis of this deintercalated sample was made by Dr Jack Blandy.

5.4.2 Powder X-ray diffraction

High-resolution synchrotron powder X-ray diffraction was measured by using MAC detector at room-temperature on the daughter sample (JNB449, obtained from exactly the same batch of parent material JNB448, Sr_2MnO_3CuS, described in section 5.3). Comparing the superimposition of the synchrotron PXRD data of the deintercalated and parent sample indicates the shifts in the Bragg peaks of two samples in different directions, which means they indeed have different compositions (Figure 5.22). Table 5.10 gives the refined values of the lattice parameters which differ significantly compared with the uncertainties.

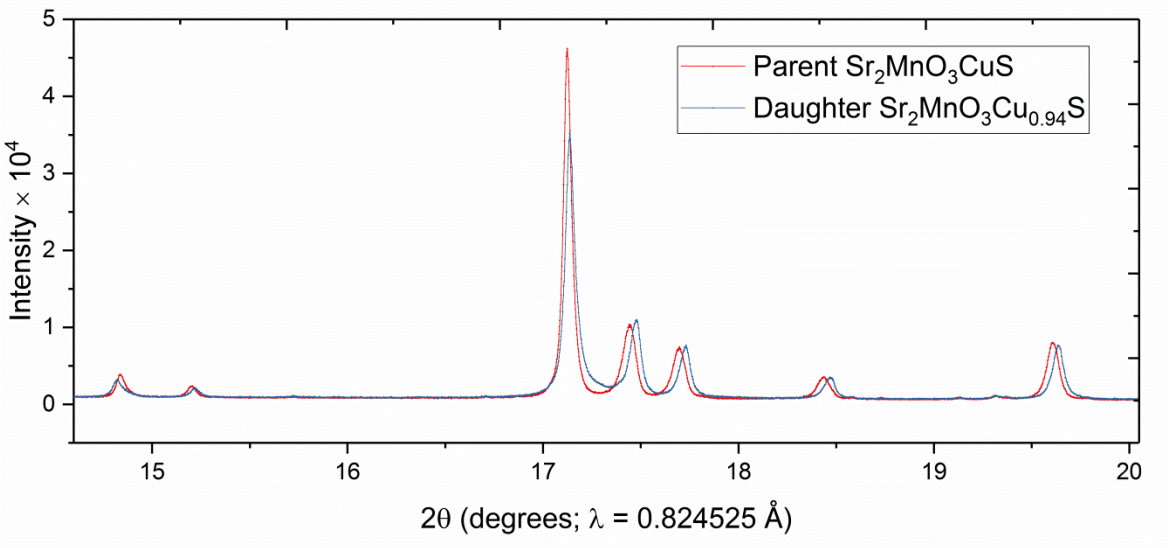

Figure 5.22: The shifts of Bragg reflections in Sr_2MnO_3CuS and $Sr_2MnO_3Cu_{0.94}S$

A Rietveld refinement of daughter sample against the data is shown in Figure 5.23, from which the compound composition is refined to be $Sr_2MnO_3Cu_{0.94}S$ with the Cu occupancy of 0.940(1). To avoid the over-correlation between the refinement of Cu occupancy values

and anisotropic thermal displacement parameters (ADPs used in the synchrotron PXRD data), the Cu occupancy of the parent compound was fixed with "1" and the ADPs were left to refine. These ADP values were then copied to the refinement of the daughter compound which had freely refined Cu occupancy with fixed ADPs. The refined parameters with those from parent Sr_2MnO_3CuS are shown in Table 5.10 and Table 5.11.

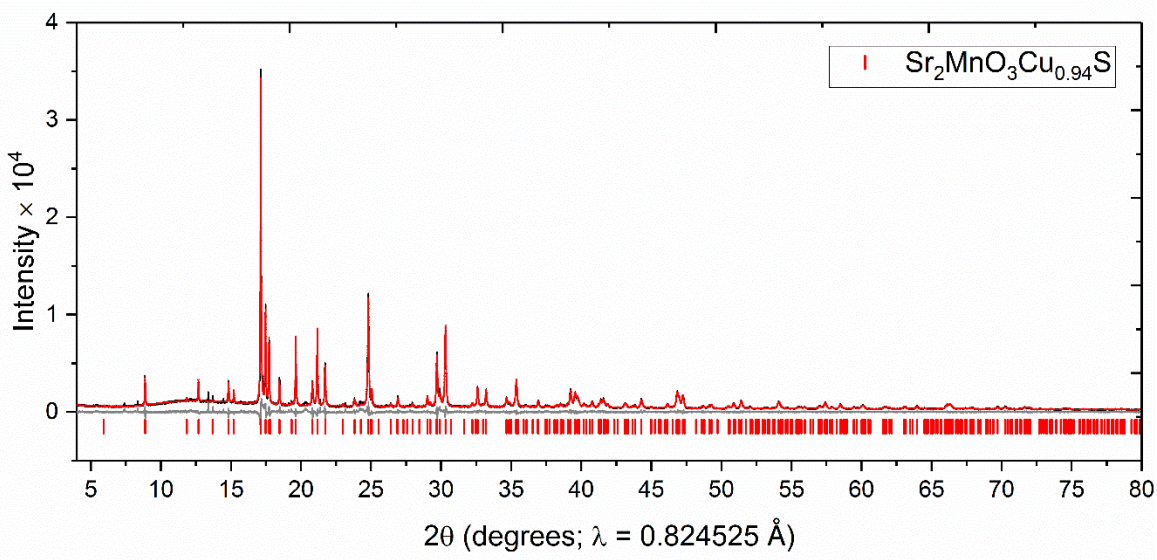

Figure 5.23: Rietveld refinement against the PXRD pattern of the deintercalated sample (JNB449) of Sr_2MnO_3CuS, measured at RT using the Mythen detector on the I11

	$Sr_2MnO_3Cu_{0.94}S$	Sr_2MnO_3CuS
Diffractometer	I11 (MAC detector)	I11 (MAC detector)
Wavelength (Å)	0.8245(2)	0.8245(2)
Temperature (K)	298	298
a (Å)	3.83856(4)	3.84551(2)
c (Å)	15.9714(2)	15.95988(9)
V (Å^3)	235.330(5)	236.014(2)
Phase density (g cm^{-3})	5.221(1)	5.25977(5)
R_{wp}	8.05	7.50
χ^2	2.75	2.56
Cu occupancy	0.940(15)	0.998(1)

Table 5.10: Lattice Parameters of refinement against I11 PXRD (MAC detector) data for $Sr_2MnO_3Cu_{0.94}S$ and Sr_2MnO_3CuS at room temperature

I11 PXRD of $Sr_2MnO_3Cu_{0.94}S$ at room temperature							
Atom	Site	*x*	*y*	*z*	U_{11} (Å^2)	U_{22} (Å^2)	U_{33} (Å^2)
Sr(1)	2*c*	0.75	0.75	0.18333(4)	0.0052(3)	= U_{11}	0.0017(4)
Sr(2)	2*c*	0.75	0.75	0.41607(4)	0.0059(3)	= U_{11}	0.0133(5)
Mn	2*c*	0.25	0.25	0.30271(7)	0.0026(3)	= U_{11}	0.0053(5)
Cu	2*a*	0.25	0.75	0	0.0170(3)	= U_{11}	0.0186(5)
S	2*c*	0.25	0.25	0.09105(8)	0.0090(6)	= U_{11}	0.0000(8)
O(1)	4*f*	0.25	0.75	0.2847(1)		0.0033(6) [a] [U_{iso} (Å^2)]	
O(2)	2*c*	0.25	0.25	0.4269(2)		0.0086(9) [a] [U_{iso} (Å^2)]	

I11 PXRD of Sr_2MnO_3CuS at room temperature							
Atom	Site	*x*	*y*	*z*	U_{11} (Å^2)	U_{22} (Å^2)	U_{33} (Å^2)
Sr(1)	2*c*	0.75	0.75	0.18313(3)	0.0045(2)	= U_{11}	0.0031(3)
Sr(2)	2*c*	0.75	0.75	0.41530(3)	0.0091(2)	= U_{11}	0.0085(4)
Mn	2*c*	0.25	0.25	0.30227(5)	0.0038(3)	= U_{11}	0.0070(4)
Cu	2*a*	0.25	0.75	0	0.0170(3)	= U_{11}	0.0186(5)
S	2*c*	0.25	0.25	0.09105(8)	0.0090(5)	= U_{11}	0.0014(7)
O(1)	4*f*	0.25	0.75	0.2837(1)		0.0038(5) [a] [U_{iso} (Å^2)]	
O(2)	2*c*	0.25	0.25	0.4292(2)		0.0105(8) [a] [U_{iso} (Å^2)]	

Table 5.11: Structure parameters for $Sr_2MnO_3Cu_{0.94}S$ and Sr_2MnO_3CuS from the Rietveld Refinement of PXRD data; [a] O atoms were refined with the isotropic thermal displacement parameters

5.4.3 Room temperature PND

The sample of $Sr_2MnO_3Cu_{0.94}S$ (JNB449) was also measured at room temperature on the D2B diffractometer to confirm the Cu occupancy. A Rietveld refinement of the compound against room temperature PND data is shown in Figure 5.24, which gives a good fit between the observed and calculated data. The occupancy of Cu atoms was refined to be 0.938(6) in the sulfide layers, which showed excellent agreement with the occupancy of Cu [0.940(15)] derived from PXRD (MAC) refinement of the same sample $Sr_2MnO_3Cu_{0.94}S$ (JNB449). The

structural parameters from PND data are presented in Tables 5.12 and Table 5.13. The refined bond distances are shown in Table 5.14 to compare with Sr_2MnO_3CuS.

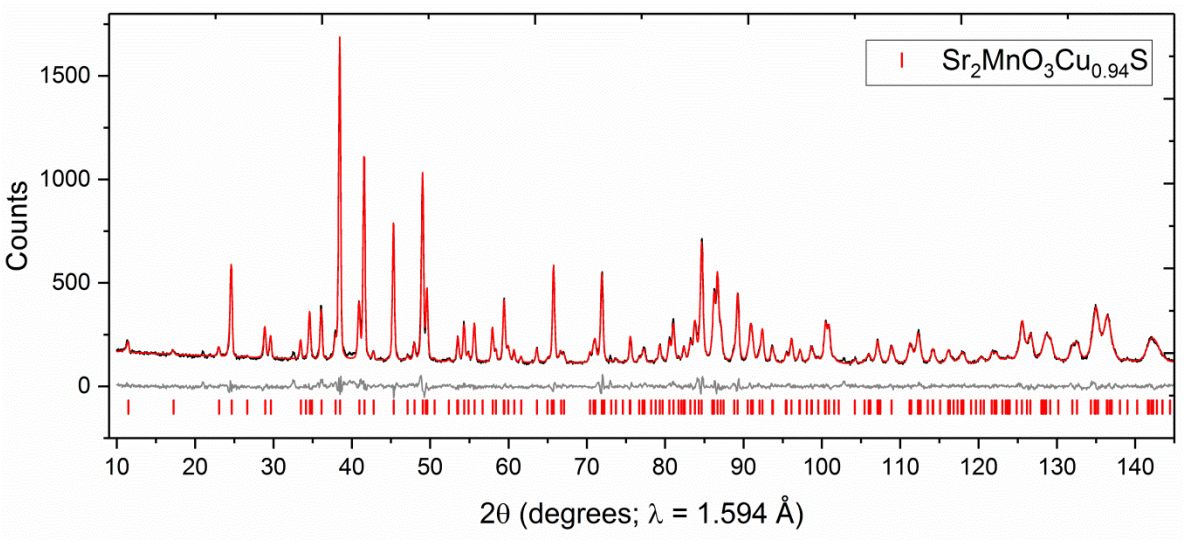

Figure 5.24: Rietveld refinement against the PND pattern of $Sr_2MnO_3Cu_{0.94}S$ (JNB449), measured at RT using the D2B diffractometer on ILL

Parameter	$Sr_2MnO_3Cu_{0.94}S$ (JNB449)
Diffractometer	D2B (ILL)
Wavelength (Å)	1.594
Temperature (K)	298
Space group	*P4/nmm*
a (Å)	3.83917(7)
c (Å)	15.9467(4)
V (Å^3)	235.04(1)
Phase density (g cm^{-3})	5.226(6)
R_{wp}	4.36
χ^2	1.85

Table 5.12: Lattice parameters from Rietveld refinement against the PND pattern of $Sr_2MnO_3Cu_{0.94}S$ (JNB449), measured at RT using D2B at ILL

D2B PND of $Sr_2MnO_3Cu_{0.94}S$ at room temperature					
Atom	Site	*x*	*y*	*z*	U_{iso} (Å^2)
Sr(1)	2c	0.75	0.75	0.1824(1)	0.0003(8)
Sr(2)	2*c*	0.75	0.75	0.4153(1)	0.0098(5)
Mn	2c	0.25	0.25	0.3042(3)	0.0030(5)
Cu	2*a*	0.25	0.75	0	0.0060(5)
S	2*c*	0.25	0.25	0.0922(3)	0.0054(9)
O(1)	4f	0.25	0.75	0.28668(9)	0.0038(4)
O(2)	2c	0.25	0.25	0.4302(2)	0.0072(8)

Table 5.13: Structure parameters for $Sr_2MnO_3Cu_{0.94}S$ from the Rietveld refinement of D2B PND data

	$Sr_2MnO_3Cu_{0.94}S$	Sr_2MnO_3CuS
Mn–O(1) (Å) [×4]	1.9398(8)	1.9511(5)
Mn–O(2) (Å) [×1]	2.009(6)	2.035(4)
Cu–Cu (Å) [×1]	2.71470(5)	2.73338(3)
Cu–S (Å) [×4]	2.418(3)	2.422(2)
β S-Cu- S (°) [×4]	111.70(10)	111.29(7)
α S-Cu- S (°) [×2]	105.10(18)	105.89(13)

Table 5.14: Selected atomic distances and bond angles for $Sr_2MnO_3Cu_{0.94}S$ and Sr_2MnO_3CuS from the Rietveld Refinement of PND data

5.4.4 Magnetic susceptibility measurements

A measurement of magnetisation versus field, *M*(*H*), of $Sr_2MnO_3Cu_{0.94}S$ (JNB449), was measured to be linear at 300 K, confirming the absence of room-temperature ferromagnetic impurities in the daughter compound. The result of measurement is shown in Figure 5.25 together with those derived from the parent sample.

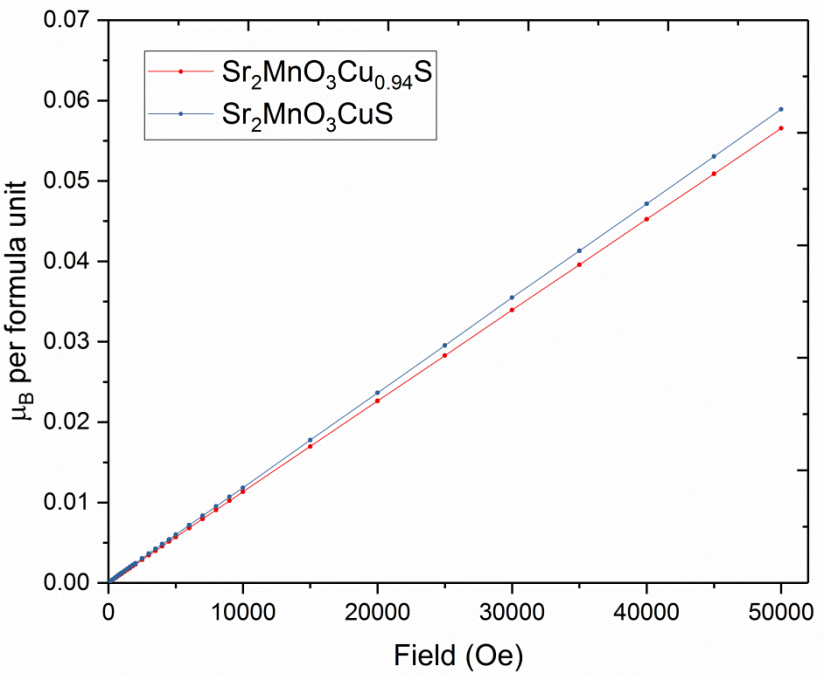

Figure 5.25: Magnetic moment per Mn ion of $Sr_2MnO_3Cu_{0.94}S$ and Sr_2MnO_3CuS as a function of applied magnetic field, measured at 300 K

The temperature-dependent ZFC and FC magnetic susceptibilities (χ) measured in an applied field of 1000 Oe between 2 K and 330 K are shown in Figure 5.26. Similar to the parent sample, a broad maximum was observed in $Sr_2MnO_3Cu_{0.94}S$, but with the maximum at a higher temperature of about 130 K, consistent again with the appearance of low-dimensional antiferromagnetic ordering. The divergence between ZFC and FC data was also shown below T_g (approximately 80 K), giving the evidence of spin-glass behaviour. The sample of $Sr_2MnO_3Cu_{0.94}S$ doesn't obey the Curie-Weiss law in the measured temperature range. The magnetisation isotherm at 5 K (Figure 5.27) displays a hysteresis loop which is slightly displaced from the origin, indicative of a spin-glass-like component to the magnetism, as in the parent, stoichiometric compound.

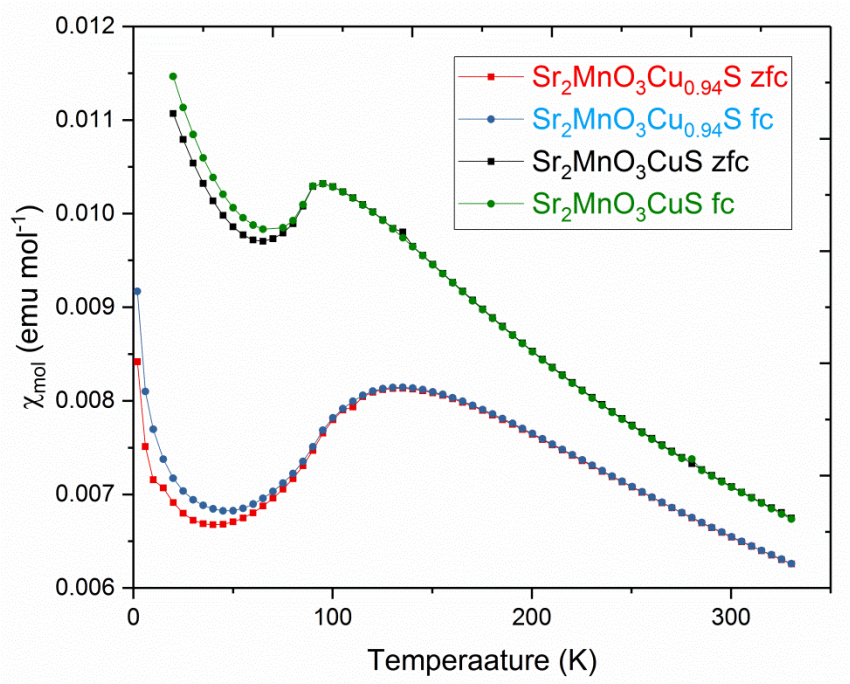

Figure 5.26: The ZFC and FC magnetic susceptibilities of $Sr_2MnO_3Cu_{0.94}S$ and Sr_2MnO_3CuS, measured at 1000 Oe between 2 K and 330 K

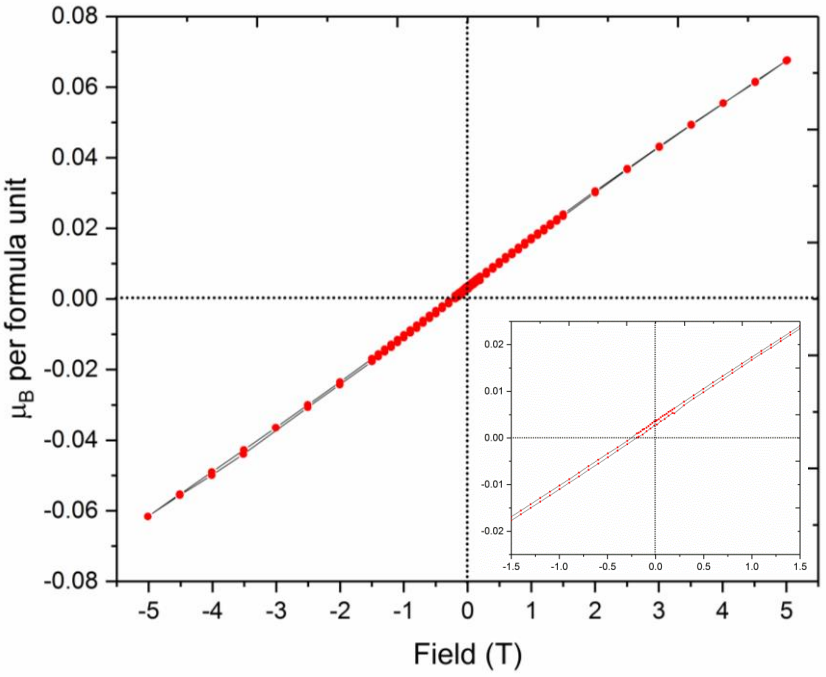

Figure 5.27: M vs H isotherm of $Sr_2MnO_3Cu_{0.94}S$ measured at 5K in the range $-5 \leq H\ (T) \leq +5$. The inset indicates the slight offset from the origin

5.4.5 Variable temperature PND

A PND measurement was performed to investigate the magnetic ordering of $Sr_2MnO_3Cu_{0.94}S$ suggested by the susceptibility measurements. The measurement was made at 5 K with $\lambda = 1.594$ Å using the D2B diffractometer. Comparing to the PND pattern at toom temperature, several strong additional Bragg reflections are present at low angles at 5 K (Figure 5.28), corresponding to the AFM ordering of Mn ions. Furthermore, the magnetic impurity phase MnO observed in the parent sample is not found in the diffraction pattern of this daughter sample (they were made in the same batch originally), which was probably eliminated in the process of deintercalation.

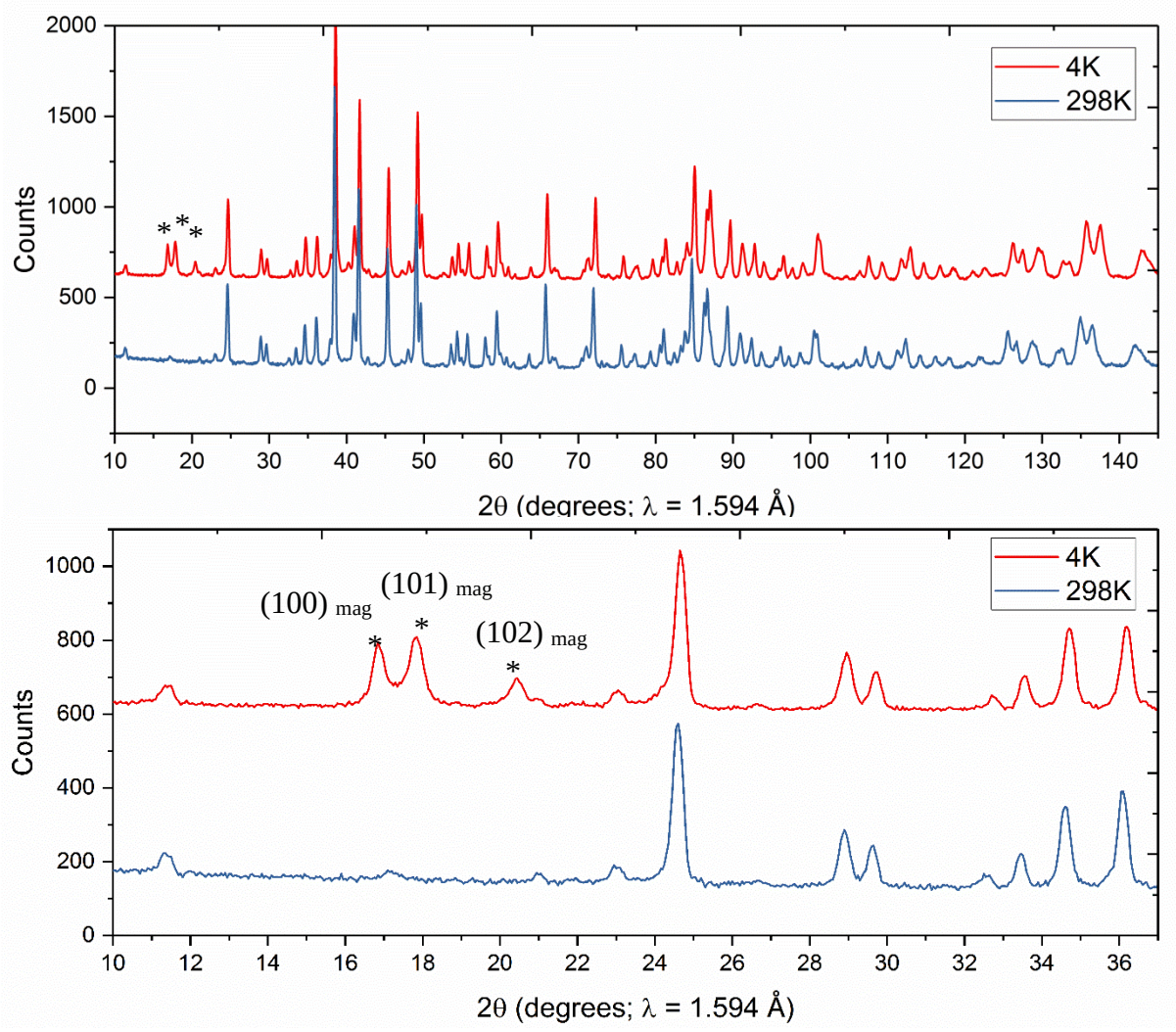

Figure 5.28: Comparison of PND data of $Sr_2MnO_3Cu_{0.94}S$ (JNB449) collected on the D2B diffractometer at 4 K and 298 K

These magnetic reflections were then indexed into a magnetic cell with $\sqrt{2}a \times \sqrt{2}a \times c$ expansion of the structural unit cell, which is different to that observed in parent compound ($\sqrt{2}a \times \sqrt{2}a \times 2c$ expansion), but similar to that seen in the Se analogue Sr_2MnO_3CuSe. ISODISTORT [56] was also used to find the best magnetic model for its Rietveld refinement. Based on the magnetic cell with the $\sqrt{2}a \times \sqrt{2}a \times c$ expansion directed along *a*, *b* and *c* axes all magnetic reflections at 5 K could be well refined by using a single magnetic mode mM4(a,b) with a highest-symmetry magnetic space group P_Cba2 (32.141) on the Mn sites,[56] same as the that refined for Sr_2MnO_3CuSe.

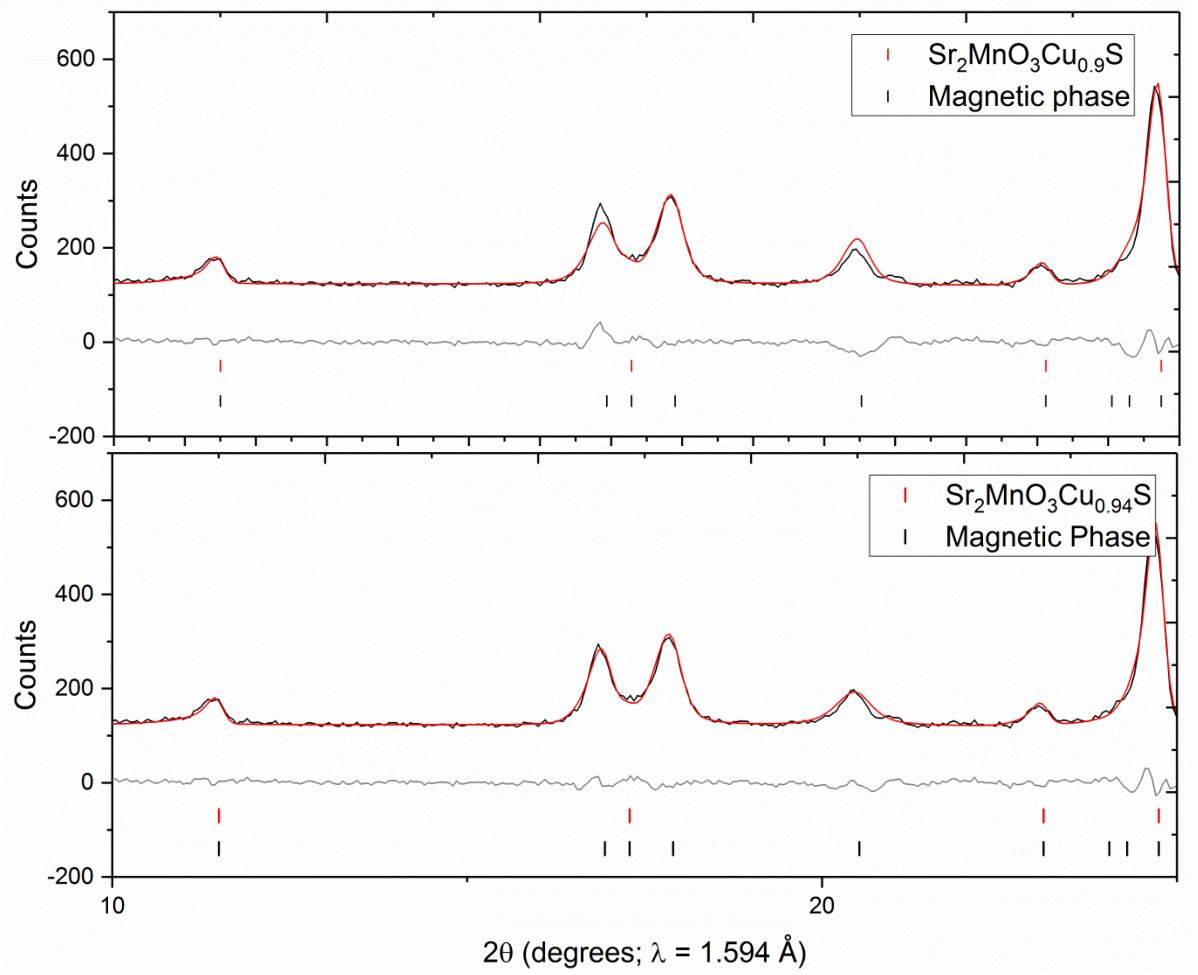

Figure 5.29: Comparison of the Rietveld refinement of $Sr_2MnO_3Cu_{0.94}S$ (JNB449) measured at 4 K on D2B; a) Refinement without applying anisotropic broadening terms, giving a narrow magnetic peak (100) and a broad magnetic peak (102): $\chi^2 = 2.52$, $R_{wp} = 5.11$; b) Anisotropic broadening terms included: $\chi^2 = 2.45$, $R_{wp} = 4.96$

As seen in the previous refinements of Sr_2MnO_3CuSe and Sr_2MnO_3CuS, the magnetic peak (100) is narrower and magnetic peak (102) is broader than other calculated peaks (Figure 5.29), which could be then improved by applying the anisotropic broadening terms in the TOPAS. The improved Rietveld plot at 4 K is shown in the Rietveld refinement in Figure 5.30 with R_{wp} = 4.96.

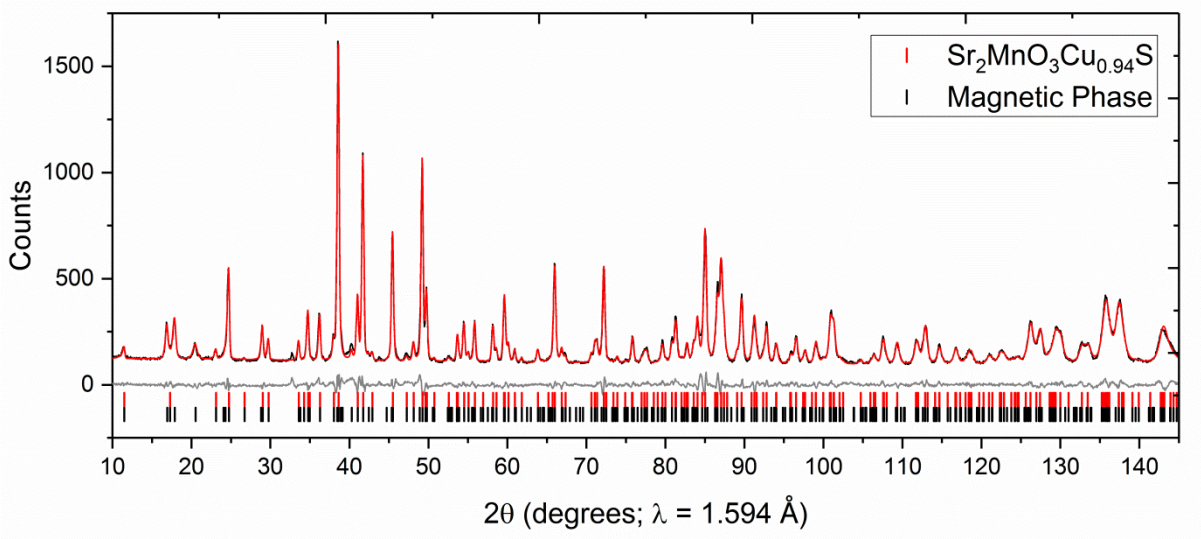

Figure 5.30: Rietveld refinement of $Sr_2MnO_3Cu_{0.94}S$ (JNB449) collected at 4 K (R_{wp} = 4.96, χ^2 = 2.45)

Similar to Sr_2MnO_3CuSe, the magnetic mode mM4(a,b) of $Sr_2MnO_3Cu_{0.94}S$ gives antiferromagnetically ordered Mn ions in the MnO layers with their magnetic moments aligned along *c*-axis in a checkerboard fashion (see Figure 5.31) as mentioned in both Sr_2MnO_3CuSe and Sr_2MnO_3CuS. The refined magnetic moment of $Sr_2MnO_3Cu_{0.94}S$ at 4 K is 3.60 (4) μB/Mn^{3+}, a value one might expect for a fully ordered Mn^{3+} system, which is significantly bigger than 2.89(6) μ_B in its parent compound Sr_2MnO_3CuS and similar to that of Sr_2MnO_3CuSe. It seems surprising that the magnetic moments vary in this way since the deficiency of Cu should introduce mixed-valence on Mn and one might expect that to reduce the ordered moment (A possible reason for this is discussed below).

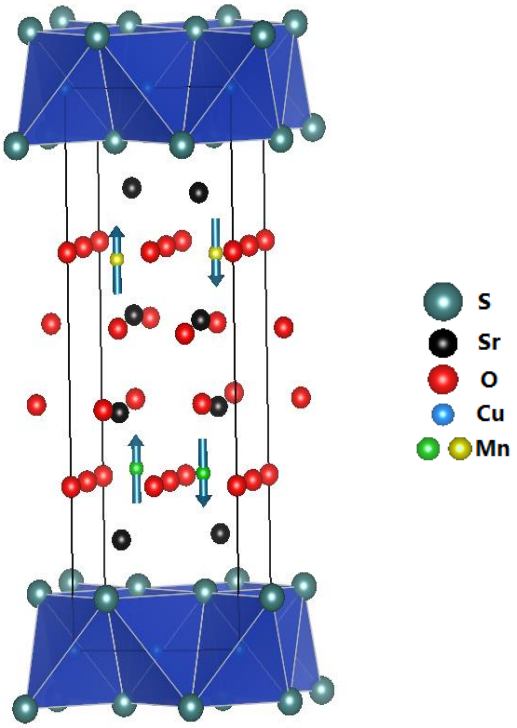

Figure 5.31: The ordering of Mn^{3+} magnetic moments in $Sr_2MnO_3Cu_{0.94}S$

5.5 Discussion

The successful synthesis of Sr_2MnO_3CuSe has been reported for the first time in this chapter. The magnetic transition temperature T_N has been estimated at around 100 K using the magnetic susceptibility measurements. PND has also been used to investigate the magnetic model of this compound at several low temperatures, indicating the antiferromagnetic ordering of Mn^{3+} directed along *c*-axis in the oxide layers. An ordered moment of 3.76(2) $\mu B/Mn^{3+}$ was found as expected for Mn^{3+}. The refined magnetic model is similar to that recently reported in Sr_2CrO_3FeAs, where the antiferromagnetically ordered Cr^{3+} were found in the oxide layers but with the magnetic moments aligned in the *ab*-plane.

Purer Sr_2MnO_3CuS has also been synthesised, although with a little elemental Cu as the impurity phase (about 0.5 wt%) in the sample. The sample has a similar Néel temperature

(95 K) and oxide-layer antiferromagnetic ordering to its selenium analogue, but with a doubling of the magnetic unit cell along the *c*-direction. The comparison with other compounds with the same structure but different transition metals is made in Chapter 6.

Suprisingly, Sr_2MnO_3CuS has a much lower ordered magnetic moment (2.83(6) $\mu B/Mn^{3+}$) than that for the selenide analogue (3.76(2) $\mu B/Mn^{3+}$). However, the oxidative deintercalation of just 6% of the Cu from Sr_2MnO_3CuS changed the crystal structure slightly and not only resulted in adoption of the same magnetic structure as found for the selenide analogue, but also led to a much larger ordered moment than in stoichiometric Sr_2MnO_3CuS with a value approaching that of Sr_2MnO_3CuSe. Table 5.15 shows the refinement parameters of Sr_2MnO_3CuS, $Sr_2MnO_3Cu_{0.94}S$ and another deintercalated sample $Sr_2MnO_3Cu_{0.97}S$ (synthesised by previous Part II student Louise Todd[109]). It is observed that the ordered magnetic moments of Mn ions increase as more Cu atoms are deintercalated from the crystal structure. It is interesting that Sr_2MnO_3CuSe and Sr_2MnO_3CuS have such different values for the long range ordered moment despite both being found to be stoichiometric with the uncertainties of the refinement. The reduced moment suggests a possible scenario that the Mn^{3+} ions in Sr_2MnO_3CuS were slightly reduced by electrons that transferred from the sulfide ions to the transition metal ions. This would introduce some Mn^{2+} ions and lead to moment reduction due to frustration.

This is supported by the observation that the deintercalation of small amount of Cu increases the ordered moment to the value similar to that found in Sr_2MnO_3CuSe which is consistent with Mn^{3+} ions. According to this, removal of Cu would result in oxidation of the small amount of Mn^{2+} to give only Mn^{3+}. The investigations with experiments on more samples and techniques (e.g. conductivity) are required to explore this further.

Compound	Sr_2MnO_3CuS	$Sr_2MnO_3Cu_{0.97}S$	$Sr_2MnO_3Cu_{0.94}S$
Diffractometer	D2B (ILL)	WISH (ISIS)	D2B (ILL)
T (K)	298	298	298
a (Å)	3.86537(4)	3.83547(4)	3.83916(2)
c (Å)	15.8975(2)	15.9649(2)	15.9467(1)
V (Å^3)	237.527(6)	234.857(6)	235.04(1)
R_{wp}	4.41	5.88	4.35
χ^2	1.82	0.02	1.85
Cu occupancy	0.995(7)	0.972(3)	0.938(7)
O(1) occupancy	1.000(7)	0.999(3)	1.000(7)
O(2) occupancy	0.980(8)	1.000(4)	1.000(9)
μB per Mn ion at base temperature	2.83(6)	3.46(2)	3.60(4)

Table 5.15: Structural and magnetic refinement results collected from Sr_2MnO_3CuS, $Sr_2MnO_3Cu_{0.97}S$ and $Sr_2MnO_3Cu_{0.94}S$

Chapter 6

Synthesis and characterisation of Sr_2FeO_3CuSe and Sr_2CrO_3CuSe

6.1 Introduction

The compounds with the compositions of A_2MO_3CuCh have been previously discussed in chapter 5, where *A* is an alkaline earth metal ion such as Ca^{2+} or Sr^{2+}, *M* is a trivalent first-row transition metal and *Ch* is S^{2-} or Se^{2-}. The Fe compound, Sr_2FeO_3CuSe, was first synthesised and reported by Berthebaud *et al* in 2014.[97] Sr_2FeO_3CuSe has infinite FeO_3 layers with Fe^{3+} in square-pyramidal coordination with five oxide ions and the square pyramids sharing all four of their basal vertices. Fe^{3+} is also weakly coordinated by an axial Se^{2-} ion, giving a highly distorted octahedral environment. The anti-fluorite Cu_2Ch_2 layers contain Cu^{+} ions in a tetrahedral coordination by Se^{2-} ions. The iron and copper layers are separated by Sr^{2+} ions. Furthermore, Berthebaud also reported the synthesis and characterisation of another two analogues Sr_2FeO_3CuS and Ca_2FeO_3CuS, both of which crystallise in the space group *P*4/*nmm* with the Sr_2CuGaO_3S structure type. However, in the original paper, Fe_3O_4 was found to be an impurity phase in Sr_2FeO_3CuSe and Ca_2FeO_3CuS, showing characteristic features in the magnetic measurements. The presence of Fe_3O_4 in their sample, with two magnetic transitions at 50 and 120 K,[97] made it difficult to tell the real magnetic behaviour of samples of Sr_2FeO_3CuSe and Ca_2FeO_3CuS in the same temperature range. Small Fe and O deficiencies of Sr_2FeO_3CuSe were also observed in

Berthebaud's work, which needs to be further confirmed by using neutron powder diffraction data.

In this chapter, the synthesis of a phase-pure sample of Sr_2FeO_3CuSe was achieved without the presence of any impurity phases and unindexed peaks. The composition, structure and magnetic behaviour of this compound were investigated using powder X-ray diffraction, neutron powder diffraction and magnetic susceptibility measurements. An interesting spin-reorientation of the Fe^{3+} magnetic moments was also found by analysing the variable-temperature PND data, which is discussed in detail in section 6.2.3.

A novel compound with the composition of Sr_2CrO_3CuSe was also synthesised by using a similar synthesis route. After many attempts at optimizing the reaction conditions and purifying the samples, it was found that a completely phase-pure sample of Sr_2CrO_3CuSe could not be achieved. SrSe was always present as an impurity phase and there were several other unindexed peaks in the product. Both room-temperature PXRD and PND measurements were used to study the structure and composition of this sample. The magnetic susceptibility measurements and low-temperature PND were also performed to probe its magnetic behaviour.

6.2 Synthesis and characterisation of Sr_2FeO_3CuSe

A sample with the composition of Sr_2FeO_3CuSe was prepared by grinding together SrO, Fe (Alfa, 99.998 %), CuO (Alfa, 99.995 %) and Se (Alfa, 99.999 %) in the molar ratio 2: 1: 1: 1 in the glove box. SrO was made by thermal decomposition of Sr_2CO_3 (Alfa, 99.994 %) at 1100 °C (as detailed in section 2.1.3.1). A pellet of the ground mixture was placed in an Al_2O_3 crucible which was then sealed inside an evacuated silica tube as described in section 2.1.1. By trying different reaction conditions for this sample, it was found that the presence

of impurity phases of Fe_3O_4 and $Cu_{1.8}Se$ in the previously reported sample of Sr_2FeO_3CuSe is likely due to the relatively low synthesis temperature (850 °C).[97] Thus, in this work, a higher temperature (900 °C) was used to anneal the sample with a ramp rate of 2 °C min^{-1} for 60 hours. After this, the sample was reground and heated to 900 °C for another 24 hours in order to obtain a phase-pure sample of Sr_2FeO_3CuSe.

6.2.1 Powder X-ray diffraction

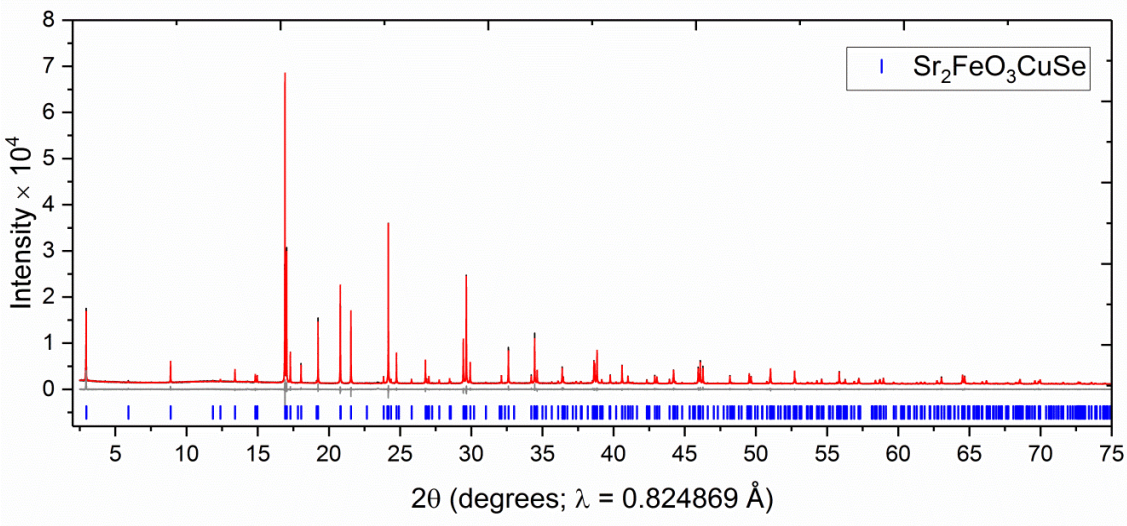

Figure 6.1: Rietveld refinement of high resolution powder x-ray diffraction data for Sr_2FeO_3CuSe (XX210) using the MAC detector of the instrument I11 at the Diamond Light Source

The structure of Sr_2FeO_3CuSe (XX210) was probed at room temperature by using high-resolution synchrotron powder X-ray diffraction (MAC detector on the I11 beamline). Rietveld refinement against the collected data is plotted in Figure 6.1, confirming that Sr_2FeO_3CuSe was synthesised phase pure. The compound is isotypic to its Mn-analogues (discussed in chapter 5) in the space group *P*4/*nmm*, with the Sr_2CuGaO_3S structure type. The perovskite-related double layers of the square-pyramidal FeO_5 are separated by anti-fluorite chalcogenide Cu_2Se_2 layers. The two structural blocks are separated by intervening

Sr^{2+} cations in the electropositive metal sites. Structural parameters, selected atomic distances and bond angles from X-ray data are presented in Tables 6.1, 6.2 and 6.3.

	Sr_2FeO_3CuSe
Diffractometer	I11 (MAC detector)
Temperature (K)	298
Space group	*P4/nmm*
a (Å)	3.937591(6)
c (Å)	15.97075(3)
V (Å^3)	247.620(1)
Phase density (g cm^{-3})	5.654(1)
R_{wp}	7.36
χ^2	2.22

Table 6.1: Lattice Parameters for Sr_2FeO_3CuSe from Rietveld Refinement

I11 PXRD of Sr_2FeO_3CuSe at room temperature							
Atom	Site	*x*	*y*	*z*	U_{11} (Å^2)	U_{22} (Å^2)	U_{33} (Å^2)
Sr(1)	2*c*	0.75	0.75	0.19216(4)	0.0041(1)	= U_{11}	0.0046(2)
Sr(2)	2*c*	0.75	0.75	0.41370(3)	0.0042(2)	= U_{11}	0.0047(3)
Fe	2*c*	0.25	0.25	0.31367(5)	0.0015(3)	= U_{11}	0.0064(4)
Cu	2*a*	0.25	0.75	0	0.0136(3)	= U_{11}	0.0145(4)
Se	2*c*	0.25	0.25	0.09732(3)	0.0055(2)	= U_{11}	0.0037(3)
O(1)	4*f*	0.25	0.75	0.2914(1)		0.0000(6) [a] [U_{iso} (Å^2)]	
O(2)	2*c*	0.25	0.25	0.4310(2)		0.0000(9) [a] [U_{iso} (Å^2)]	

Table 6.2: Structure parameters for Sr_2FeO_3CuSe from the Rietveld Refinement of powder X-ray diffraction data; [a] O atoms were refined with the isotropic thermal displacement parameters

	I11 PXRD of Sr_2FeO_3CuSe at room temperature
Fe–O(1) (Å) [×4]	2.0009(4)
Fe–O(2) (Å) [×1]	1.874(3)
Fe–Se (Å) [×1]	3.4553(10)
Cu–Se (Å) [×4]	2.5083(3)
Se-Cu-Se (°) [×4]	112.575(10)
Se-Cu-Se (°) [×2]	103.427(18)

Table 6.3: Selected atomic distances and bond angles for Sr_2FeO_3CuSe from the Rietveld Refinement of powder X-ray diffraction data

6.2.2 Room temperature PND

The Fe and O sites in Sr_2FeO_3CuSe were reported to be deficient in the previous work by Berthebaud,[97] where a deficiency of approximately 10 % on the iron sites and a 5 % oxygen deficiency on both O(1) and O(2) sites give a calculated composition as $Sr_2CuFe_{0.9}O_{2.85}Se$. However, only laboratory X-ray powder diffraction was used in their paper to detect the deficiency of Sr_2FeO_3CuSe, which is not very sensitive to the light oxygen atoms in the structure. Thus the room temperature PND was performed on a 3 g sample of Sr_2FeO_3CuSe on D2B diffractometer at ILL to investigate the exact deficiencies of atoms. No significant deficiencies were observed in the sample (XX210) synthesised in this work after analysing the Rietveld refinement result for the data collected at room temperature on the D2B diffractometer. A plot of the refinement for Sr_2FeO_3CuSe (XX210) against room temperature PND data is shown in Figure 6.2, which shows a good fit between the observed data and calculated result (the magnetic ordering at room temperature will be discussed in section 6.2.3).

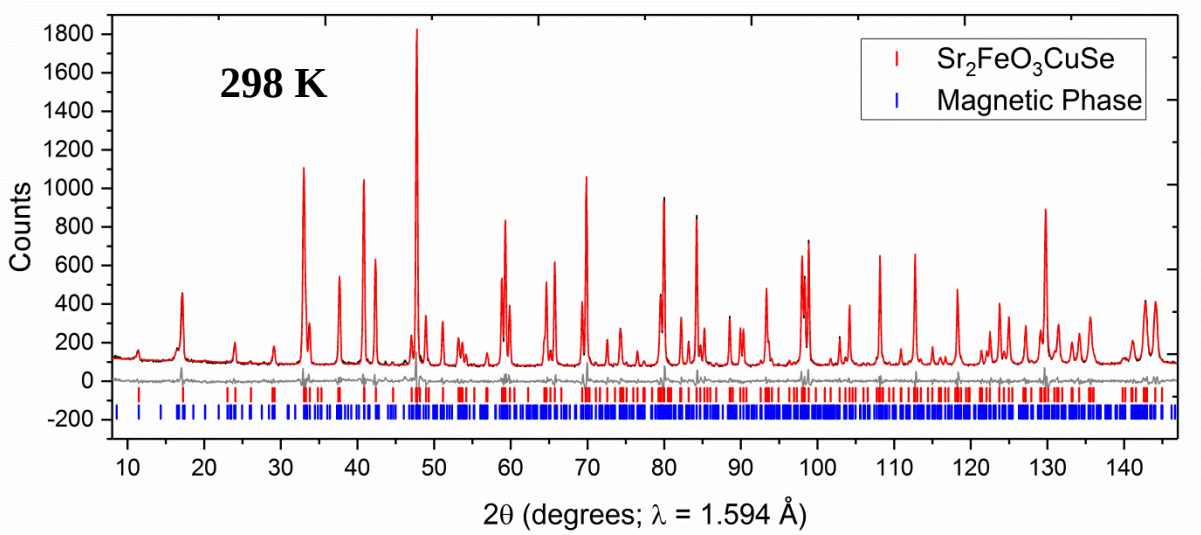

Figure 6.2: Rietveld refinement against the PND pattern of Sr_2FeO_3CuSe (XX210), measured at RT using the D2B diffractometer on ILL, χ^2 = 1.99, R_{wp} = 5.27

The calculated composition of the product is finally refined to be Sr_2FeO_3CuSe with fully occupied Cu, Fe, O(1) and O(2) atoms within the experimental uncertainty. For Cu and Fe sites, there is good agreement with the occupancy of those atoms derived from PXRD (MAC) refinement. But for both O(1) and O(2) atoms, the site occupancy is refined to a 10 to 15 % deficiency using X-ray diffraction, which doesn't correspond to the full occupancy determined from neutron diffraction and this is due to the low sensitivity of PXRD data for relatively light oxygen atoms. The detailed comparison between the refined results of PND and PXRD data is listed in Table 6.4. Freely refined occupancies of the proposed deficient sites are given.

	Sr_2FeO_3CuSe	Sr_2FeO_3CuSe
Lattice parameters		
Diffractometer	ILL (D2B)	I11 (MAC)
Wavelength (Å)	1.594	0.824869
Temperature (K)	298	298
a (Å)	3.93702(2)	3.937591(6)
c (Å)	15.9685(12)	15.97075(3)
V (Å^3)	247.513(3)	247.620(1)
R_{wp}	5.45	7.35
χ^2	2.05	2.22
Cu occupancy	0.999(9)	1.000(1)
Fe occupancy	1.000(7)	0.993(2)
O(1) occupancy	1.012(7)	0.916(4)
O(2) occupancy	0.994(12)	0.854(4)

Table 6.4: Results of refinement against ILL PND (D2B diffractometer) and I11 PXRD (MAC detector) data for Sr_2FeO_3CuSe (XX210) at room temperature

The appearance of both Fe and O deficiencies in Berthebaud's work is likely due to the artefact of the refinement against laboratory PXRD data (similar refinement results of deficiencies were also seen in the PXRD refinement of Sr_2FeO_3CuSe (XX210) in Table 6.4). Another reason for the observation of these deficiencies in their work is probably related to other impurity phases seen in the sample (e.g. Fe_3O_4 and $Cu_{1.8}Se$). Their magnetic susceptibility measurements showed a characteristic feature of Fe_3O_4 observed in the ZFC-FC data. Both Fe_3O_4 and $Cu_{1.8}Se$ impurity phases were successfully avoided in this work by increasing the reaction temperature from 850 to 900 °C and heating in the furnace for a longer time.

6.2.2 Magnetic susceptibility measurements

The measurement of magnetisation versus field, $M(H)$, of Sr_2FeO_3CuSe (XX210) is linear at 300 K (Figure 6.3a), confirming that no room-temperature ferromagnetic impurities are present in the sample XX210. The temperature-dependent ZFC and FC magnetic susceptibility (χ) measurements of Sr_2FeO_3CuSe (XX210) were measured in an applied field of 1000 Oe between 2 K and 330 K (Figure 6.3b). The graph shows evidence for paramagnetism from 2 K-100 K, but the size of this Curie-like term is small. Since the neutron powder diffraction data clearly show that long range magnetic ordering occurs below 400 K (see section 6.2.3), the rising susceptibility from 100 K to 300 K presumably leads to a peak in the susceptibility characteristic of magnetic ordering at higher temperatures.

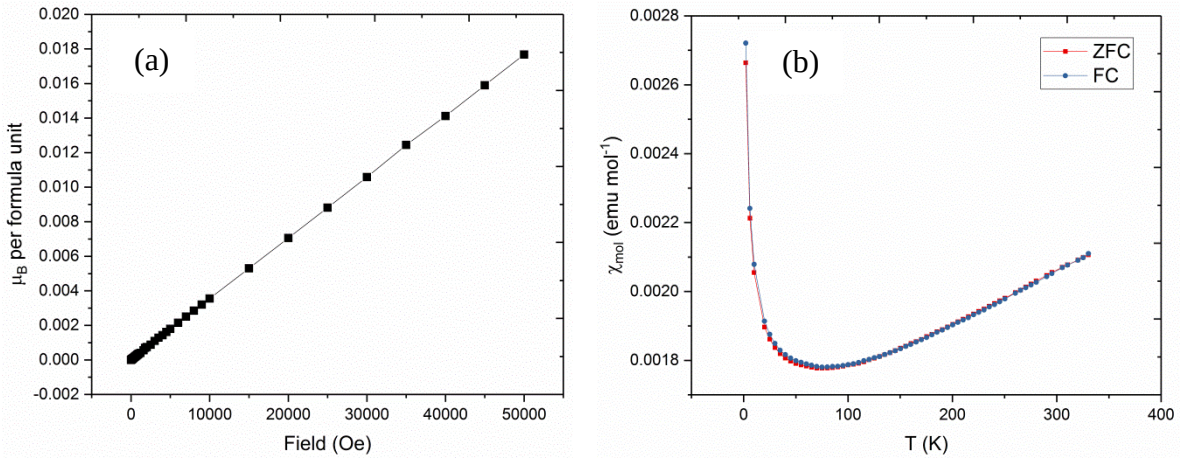

Figure 6.3: (a) Magnetic moment per Fe ion of Sr_2FeO_3CuSe as a function of applied magnetic field, measured at 300 K; (b) The ZFC and FC magnetic susceptibility of Sr_2FeO_3CuSe, measured at 1000 Oe between 2 K and 330 K

It is also found there is a small divergence between ZFC and FC of Sr_2FeO_3CuSe (XX210) below approximately 50 K. The magnetisation isotherm measured at 5 K (Figure 6.4) shows a hysteresis at the low field with a slight displacement from the origin, suggesting a little

spin-glass component to the magnetism arising from some disorder and frustration of the magnetic interactions.

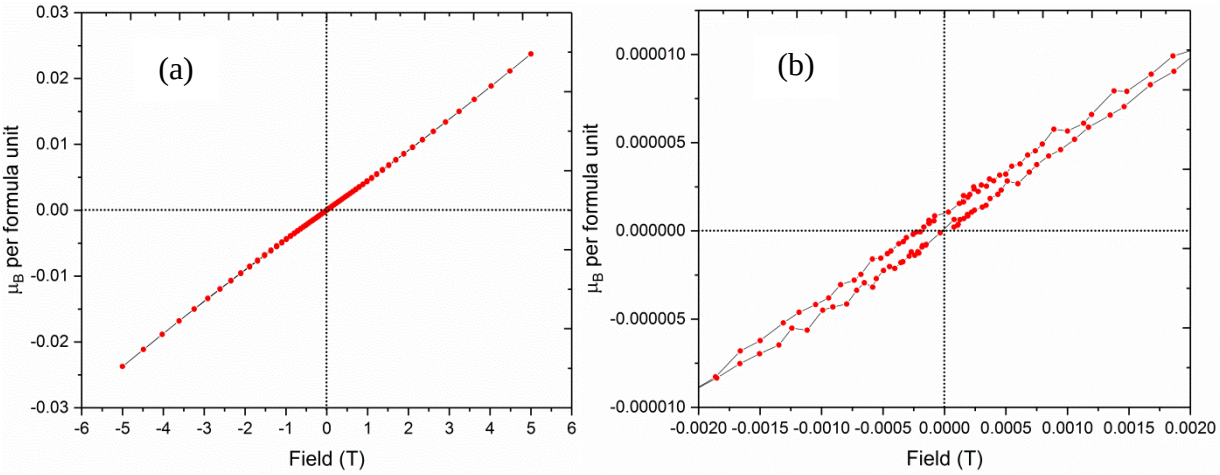

Figure 6.4: a) Magnetic moment per Fe ion of Sr_2FeO_3CuSe (XX210) as a function of applied magnetic field, measured at 5 K in the range -5 ≤ H (T) ≤ +5; b) Zooming in the range of -0.2 T to 0.2 T

6.2.3 Variable temperature PND

Although no obvious magnetic ordering transition was observed in the susceptibility measurement for Sr_2FeO_3CuSe, the increase of χ from 100 K to 300 K still suggests that it is possible having an antiferromagnetic transition at a higher temperature. Thus, in order to fully investigate its magnetic properties, variable-temperature neutron diffraction measurements were carried out on the sample of Sr_2FeO_3CuSe using the WISH diffractometer at ISIS and the D2B diffractometer at ILL. Preliminary measurements were performed using the WISH instrument at low temperatures, revealing antiferromagnetic ordering and a spin reorientation transition as the temperature changes. It was also found the magnetic transition temperature of this sample was higher than the room temperature. Therefore the measurements on D2B were used to confirm its magnetic ordering in the high-temperature range.

6.2.3.1 Low temperature magnetic structure

Low-temperature neutron powder diffraction measurements were performed on a 3 g sample of Sr_2FeO_3CuSe (XX210) using the time-of-flight (ToF) WISH diffractometer at the ISIS Facility. The sample was loaded into a 6 mm vanadium can under an argon atmosphere (with an indium wire gasket to keep it air-tight) and measured at low temperatures in a helium cryostat. The steel part of the sample holding stick was masked by Cadmium metal, which strongly absorbs the neutron beam. Data were collected at 1.5, 3, 20, 50, 100 and 150 K, where several intense magnetic reflections were present and their intensities changed continuously as a function of temperature. Figure 6.5 shows the data collected at these temperatures from banks 3 and 8 of the WISH instrument and clearly depicts the appearance and growth of the magnetic Bragg reflections as the temperature cools. Two sets of magnetic peaks marked with (*) and (+) are present at 1.5 K, which all persist on warming to 150 K. The intensities of peaks marked with (*) start to decrease at 50 K and then drop much faster from 100 K to 150 K. However, the peaks marked with (+) almost keep the same intensity over the temperature range of 1.5 K to 150 K. This distinct change in the intensities of two sets of magnetic peaks at different temperatures indicates the appearance of spin-reorientation on Fe^{3+} sites.

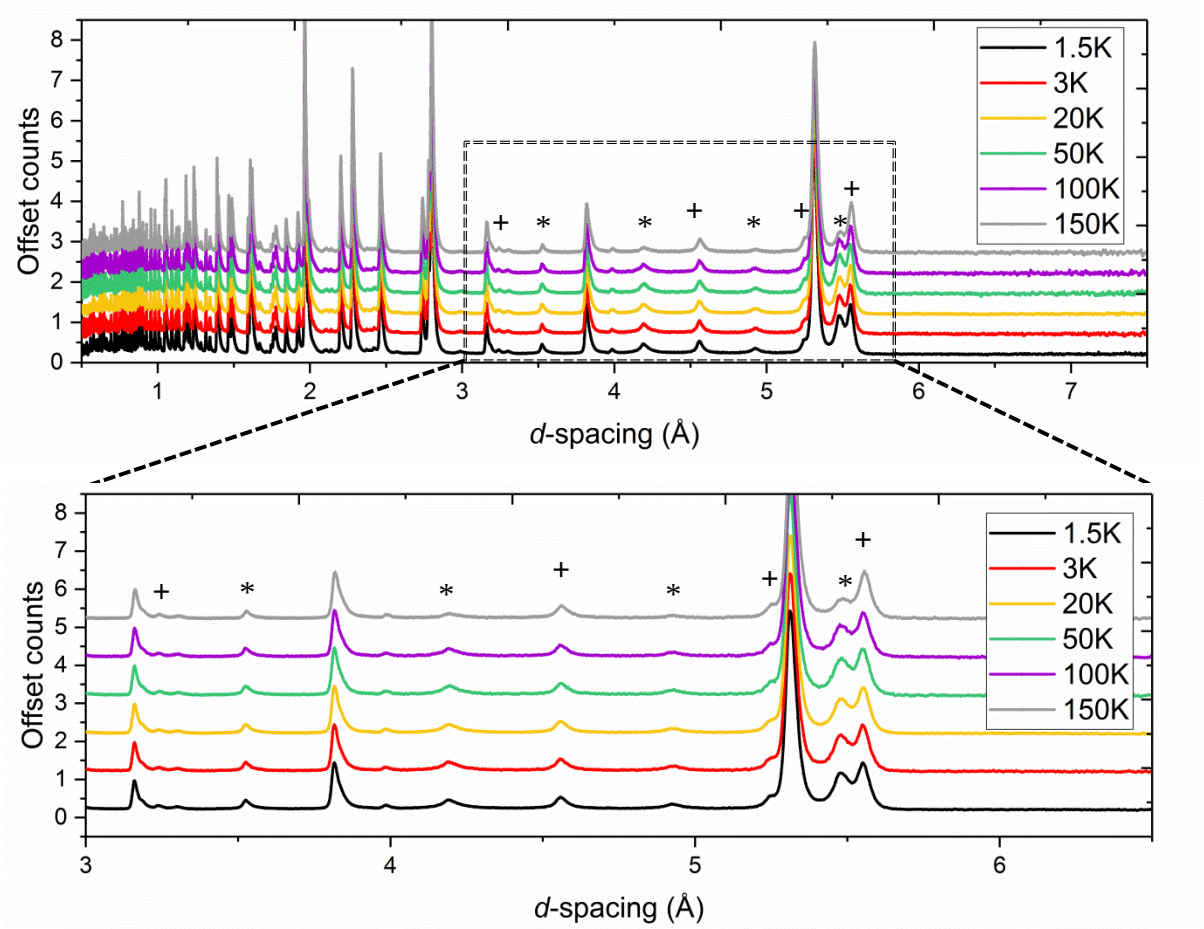

Figure 6.5: PND data obtained from banks 3 and 8 on the WISH, showing all magnetic Bragg reflections; The asterisks (*) and crosses (+) indicate the two sets of magnetic reflections which are present from 1.5 K to 150 K

At 1.5 K, all magnetic Bragg reflections could be indexed on a $\sqrt{2}a \times \sqrt{2}a \times 2c$ expansion of the unit cell. The expanded cell was loaded into ISODISTORT[56] using the *P*1 space group and the magnetic Fe sites were considered for calculation. It was found that the intensity of the magnetic peaks could be well fitted by applying both mM1(a) and mA4(a) magnetic modes. The mM1(a) mode represents that the nearest-neighbour magnetic moments are coupled antiferromagnetically with their moments directed within the *ab*-plane and this mode corresponds to the magnetic peaks with crosses (+) shown in the above PND data. For mA4(a) mode, the ordering of moments is similar to that observed for Sr_2MnO_3CuS in section 5.3.3.2. These magnetic moments were antiferromagnetically ordered but with the

moments aligned along the *c*-direction, corresponding to those magnetic peaks with asterisks (*) observed in the PND pattern. Both magnetic modes are shown in Figure 6.6.

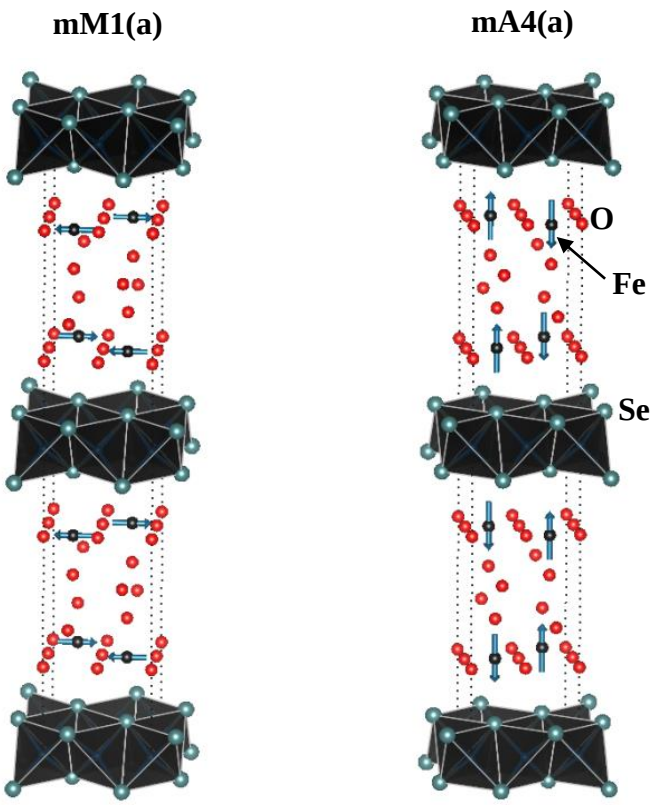

Figure 6.6: The magnetic modes mM1(a) and mA4(a) used in the refinement of magnetic model of Sr_2FeO_3CuSe

To allow the refinement of both magnetic modes, a new space group was then searched from ISODISTORT, giving a magnetic space group P*Cbca* (61.439). The combination of both mM1(a) and mA4(a) magnetic modes (Figure 6.7) shows that Fe^{3+} moments in the oxide layers are antiferromagnetically tilted and the refined magnetic model was found to fit all of those magnetic peaks well in the PND data. The Rietveld refinement at 1.5 K is plotted in Figure 6.8 with $\chi^2 = 0.04$, $R_{wp} = 4.48$.

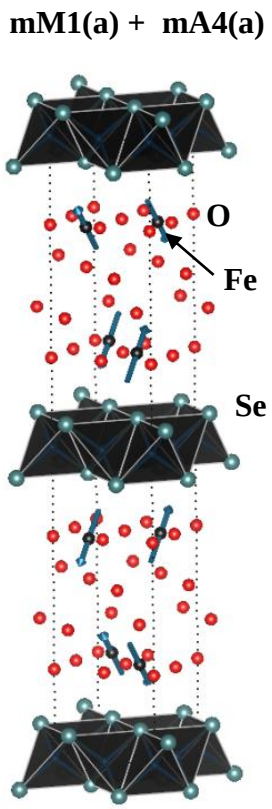

Figure 6.7: The combination of both mM1(a) and mA4(a) magnetic modes in the P_Cbca (61.439) magnetic space group

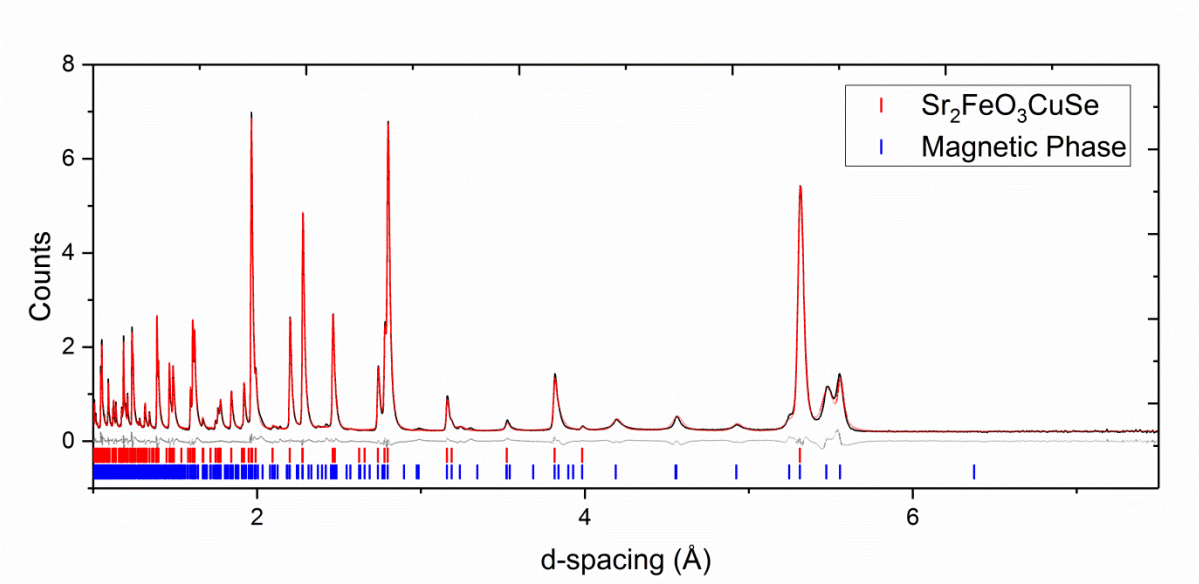

Figure 6.8: Rietveld refinement of Sr_2FeO_3CuSe (XX210) against PND data at 1.5 K collected from bank 3 and 8 on WISH; $\chi^2 = 0.04$, $R_{wp} = 4.48$

The same magnetic model was also used to refine the WISH PND data collected at other temperatures (3, 20, 50, 100 and 150 K), where all the magnetic peaks could be well fitted by applying both mM1(a) and mA4(a) magnetic modes. The resultant Rietveld plots for other temperatures collected from bank 3 and 8 on WISH diffractometer are shown in Figure 6.9, with their insets showing the magnetic ordering and relative magnitudes of the magnetic Fe^{3+} moments. Between 1.5 K and 50 K, the magnetic peaks in the PND data are well modelled when the Fe^{3+} spins are tilted between the *c*-axis and *ab*-plane, where their magnetic moments are antiferromagnetically ordered in each oxide plane. Above 50 K, the intensities of peaks marked with (*) appear to decrease (as seen above), corresponding to the decreased magnitude of the mA4(a) magnetic mode in Rietveld refinement. This suggests a subtle spin-reorientation in its magnetic structure where the tilted Fe^{3+} magnetic moments in the oxide planes gradually rotate to lie within the *ab*-plane. It is found the rotation is carried out more rapidly in the temperature range of 100 K to 150 K, after which the majority component of the Fe^{3+} magnetic moments in the oxide planes is now aligned within the *ab*-plane. After analysing the magnetic model from variable-temperature PND data from WISH, it seems that the spin-reorientation would be complete at a higher temperature, at which point the Fe^{3+} moments in each oxide plane would be completely directed with the *ab*-plane. Thus the D2B diffractometer was then used in a wider range of temperatures, including temperatures above room temperature, to investigate the magnetic ordering and spin-reorientation of Sr_2FeO_3CuSe.

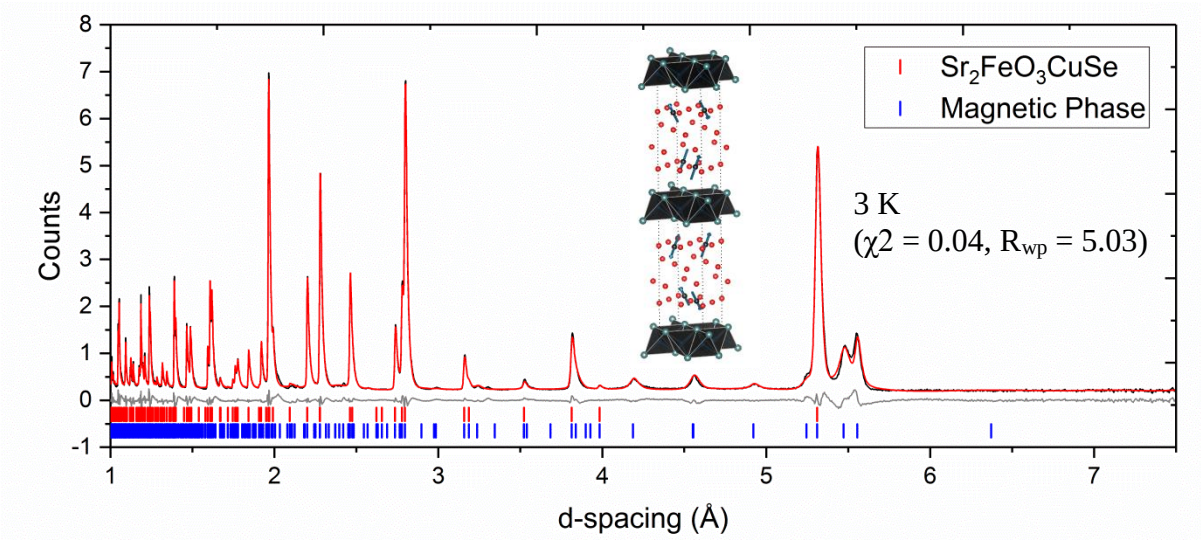
Sr2FeO3CuSe
Magnetic Phase
3 K
(χ2 = 0.04, Rwp = 5.03)
Counts
d-spacing (Å)

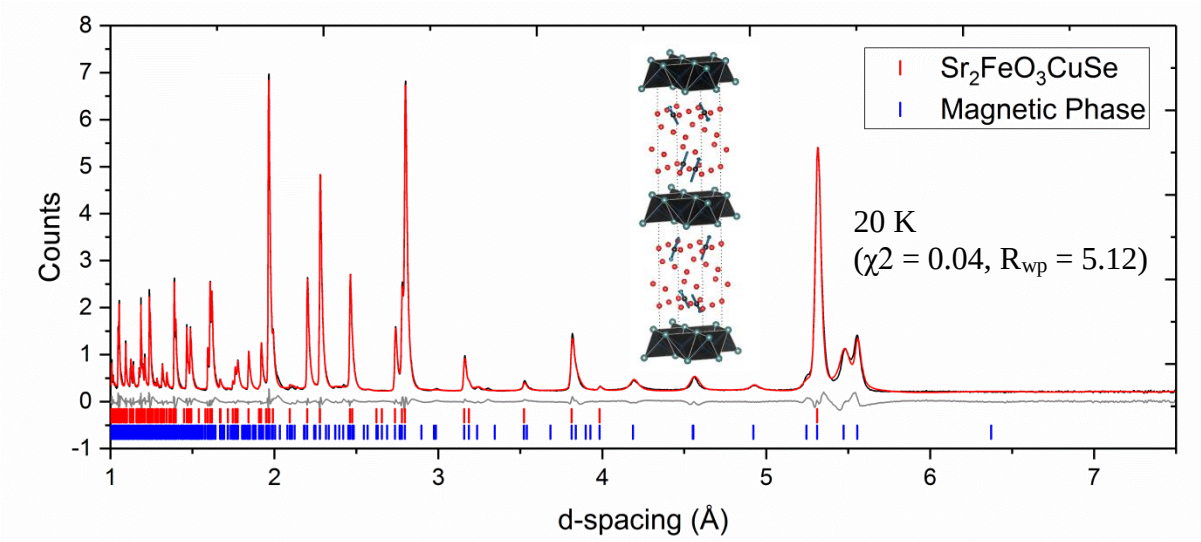
Sr2FeO3CuSe
Magnetic Phase
20 K
(χ2 = 0.04, Rwp = 5.12)
Counts
d-spacing (Å)

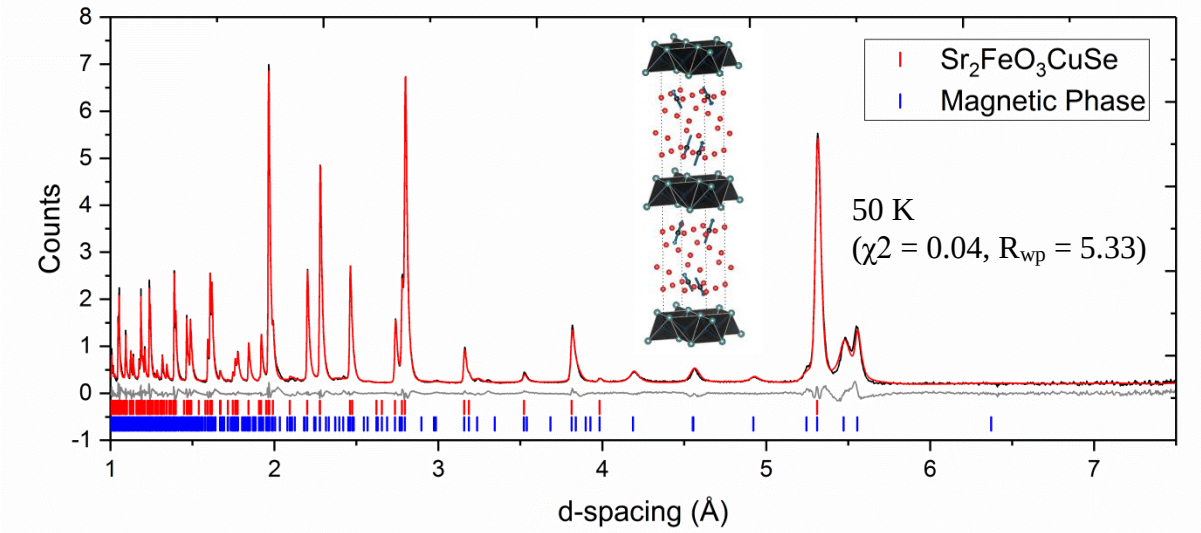
Sr2FeO3CuSe
Magnetic Phase
50 K
(χ2 = 0.04, Rwp = 5.33)
Counts
d-spacing (Å)

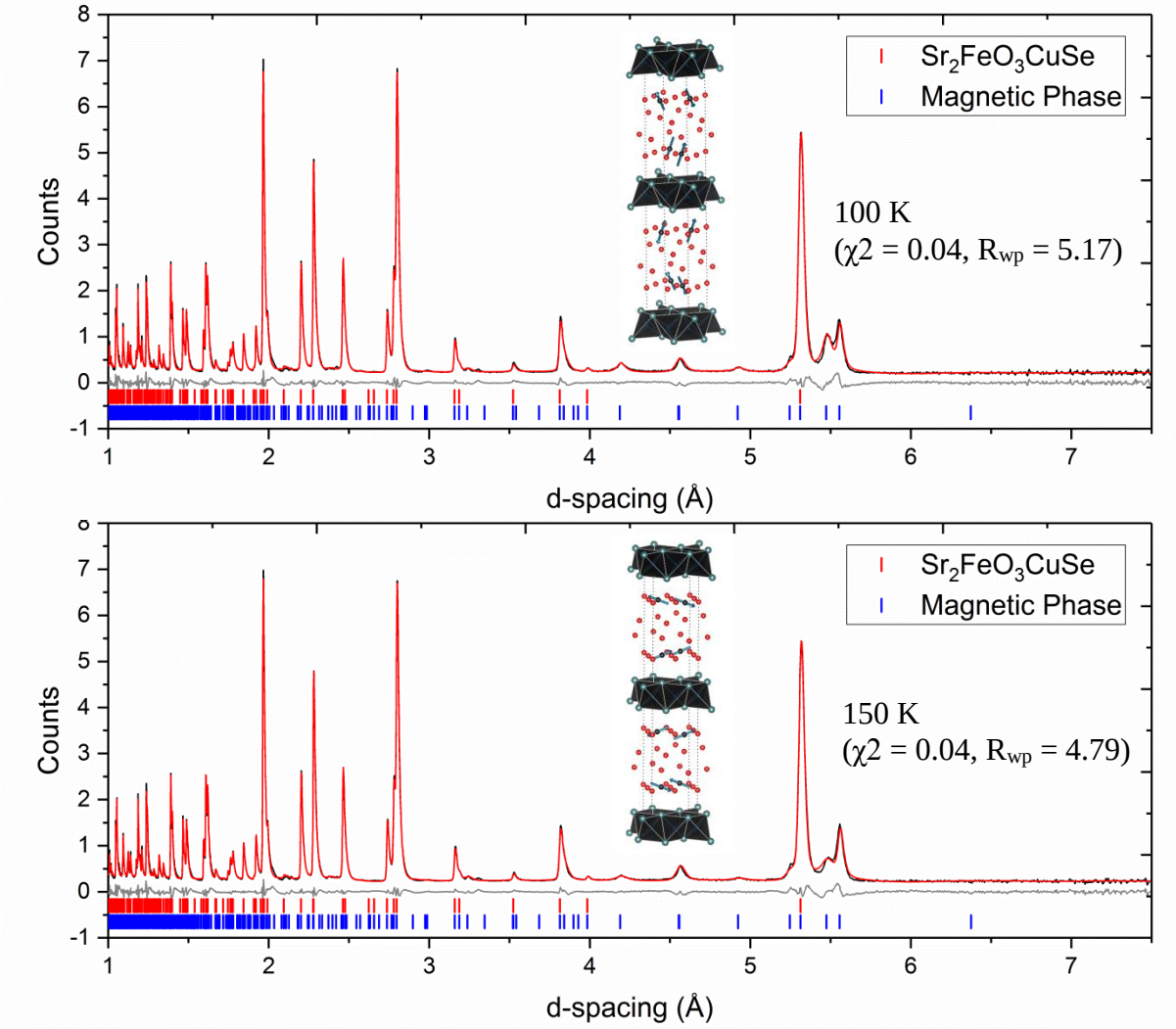

Figure 6.9: Rietveld refinements of PND data collected at 3, 20, 50, 100 and 150 K from bank 3 and 8 at WISH diffractometer, showing the change of the intensities of magnetic peaks as the sample is warmed up; The insets depict the magnetic ordering and relative magnitudes of Fe^{3+} moments.

6.2.3.2 High temperature magnetic structure

In order to identify the magnetic ordering of Fe^{3+} moments in the temperature range higher than 150 K, PND measurements were also performed on a 3 g sample of Sr_2FeO_3CuSe at several higher temperatures (230, 298 and 400 K) with $\lambda = 1.594$ Å using the D2B diffractometer. The magnetic Bragg reflections (Figure 6.10) decrease in intensity as a function of temperature and are almost absent in the pattern at 400 K. However, above 230

K, the magnetic peaks marked with asterisks (*) in Figure 6.6 do not appear in this temperature range, suggesting that the tilted Fe^{3+} magnetic moments are totally rotated into the *ab*-plane and the spin-reorientation is complete before 230 K.

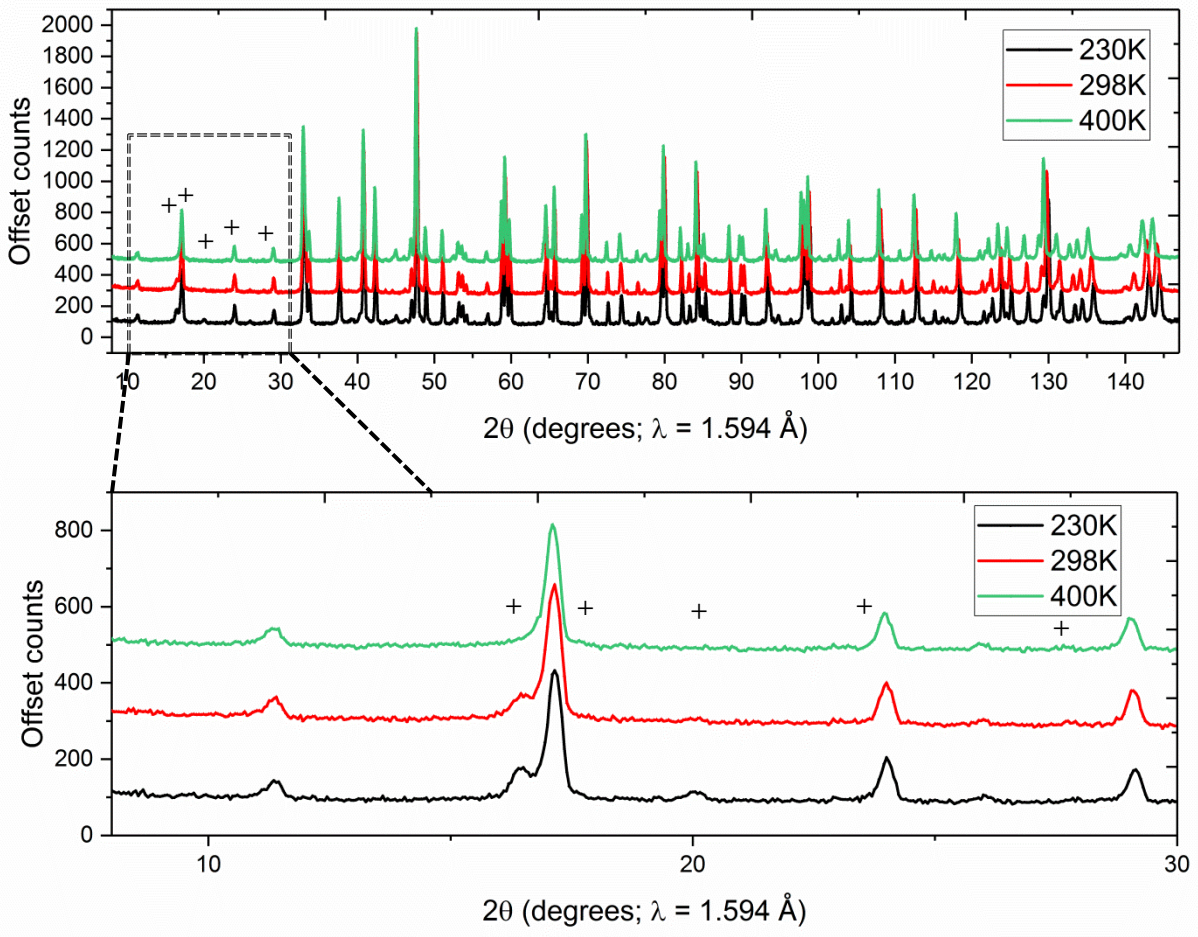

Figure 6.10: PND data obtained on the D2B diffractometer, showing that several magnetic Bragg reflections marked with crosses (+) are present until 400 K

As described above in the analysis of WISH PND data, all the variable-temperature data collected at D2B were successfully indexed using a $\sqrt{2}a \times \sqrt{2}a \times 2c$ expanded unit cell. It was found that those magnetic peaks in the D2B diffraction patterns could be well fitted by applying just the mM1(a) magnetic mode with a highest-symmetry magnetic space group $P_c2_12_12$ (18.23), where all the Fe^{3+} magnetic moments in the oxide planes are antiferromagnetically ordered within the *ab*-plane. During the refinement against D2B PND

data, the fit between the observed and calculated data could also be significantly improved by applying a Stephens-type anisotropic broadening function in the refinement.[106] Figure 6.11 shows an example that the magnetic peak (010) is narrower and magnetic peak (700) is broader than other calculated peaks at 230 K on D2B diffractometer if the anisotropic broadening terms are not refined. Therefore the anisotropic broadening function was also used in the refinement against the D2B PND data at several other temperatures. The resultant Rietveld plots for all temperatures collected from D2B are shown in Figure 6.12.

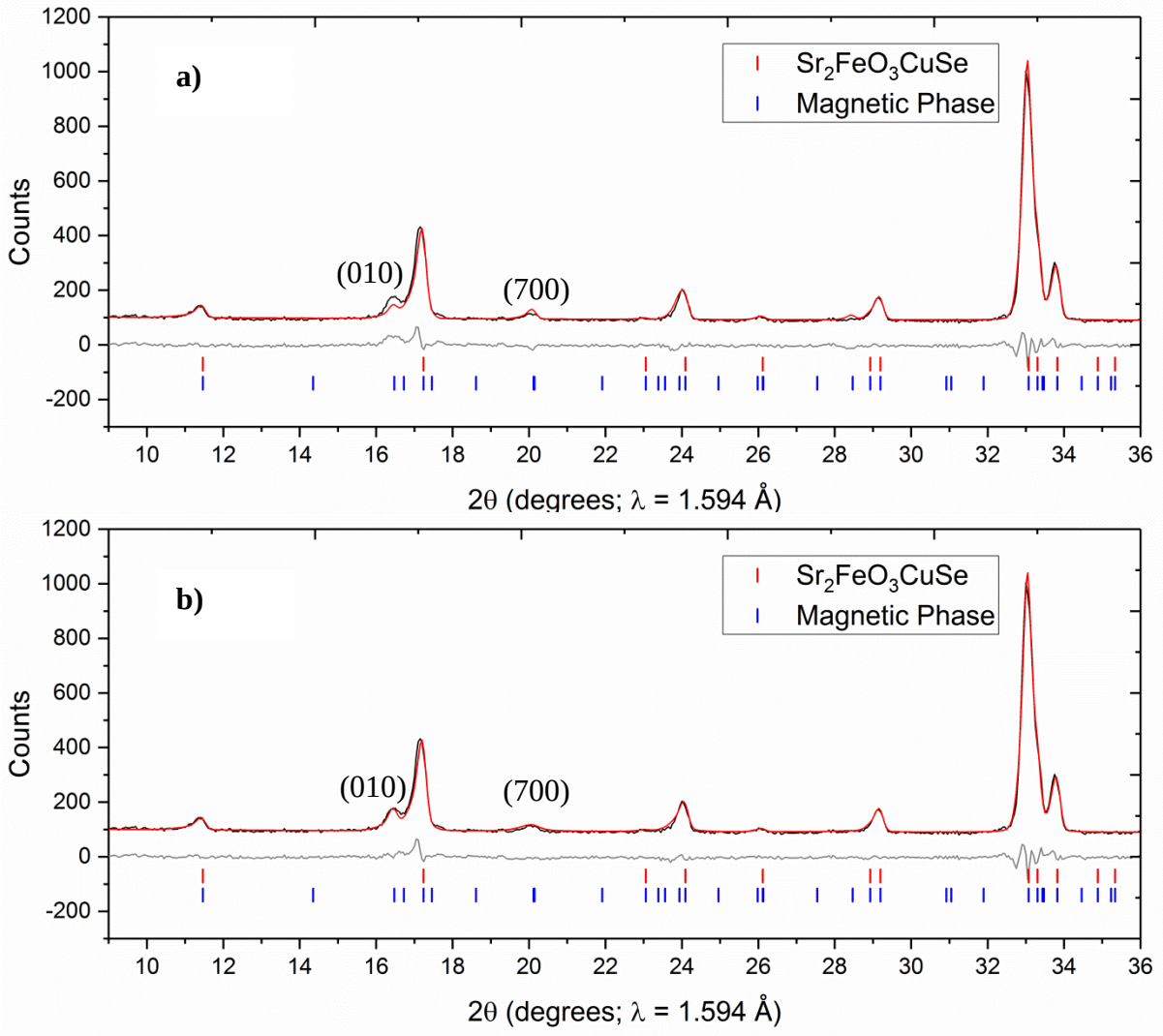

Figure 6.11: Comparison of the Rietveld refinement of Sr_2FeO_3CuSe (XX210) measured at 230 K on D2B; a) Refinement without applying anisotropic broadening terms, giving a narrow magnetic peak (010) and a broad magnetic peak (700): $\chi^2 = 2.48$, $R_{wp} = 6.53$. b) Anisotropic broadening terms included: $\chi^2 = 2.43$, $R_{wp} = 6.38$

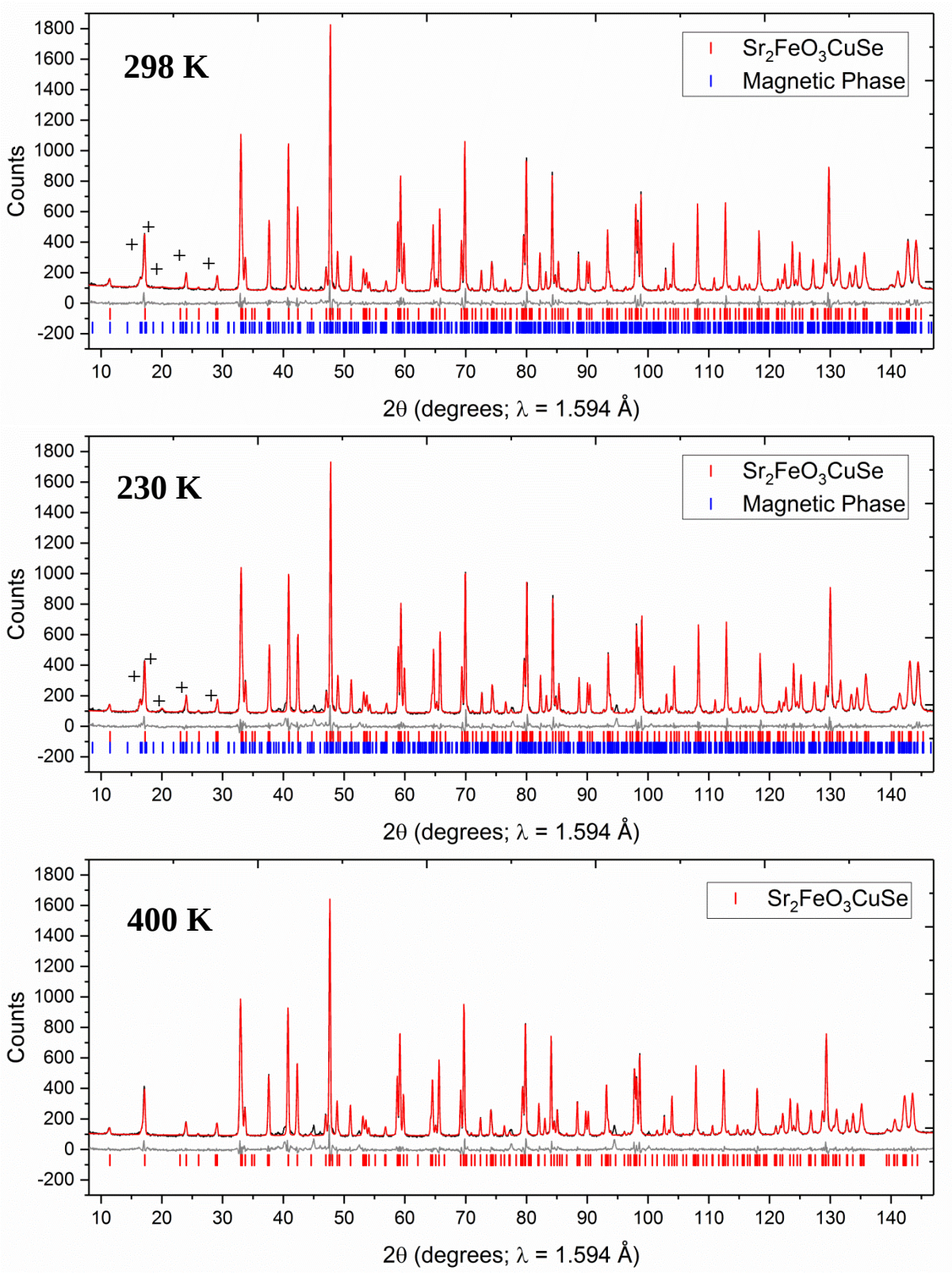

Figure 6.12: Rietveld fit for Sr2FeO3CuSe (XX210) measured by D2B diffractometer at 230 K (χ^2 = 2.43, R_{wp} = 6.38), 298 K (χ^2 = 1.99, R_{wp} = 5.27) and 400 K (χ^2 = 2.34, R_{wp} = 6.22)

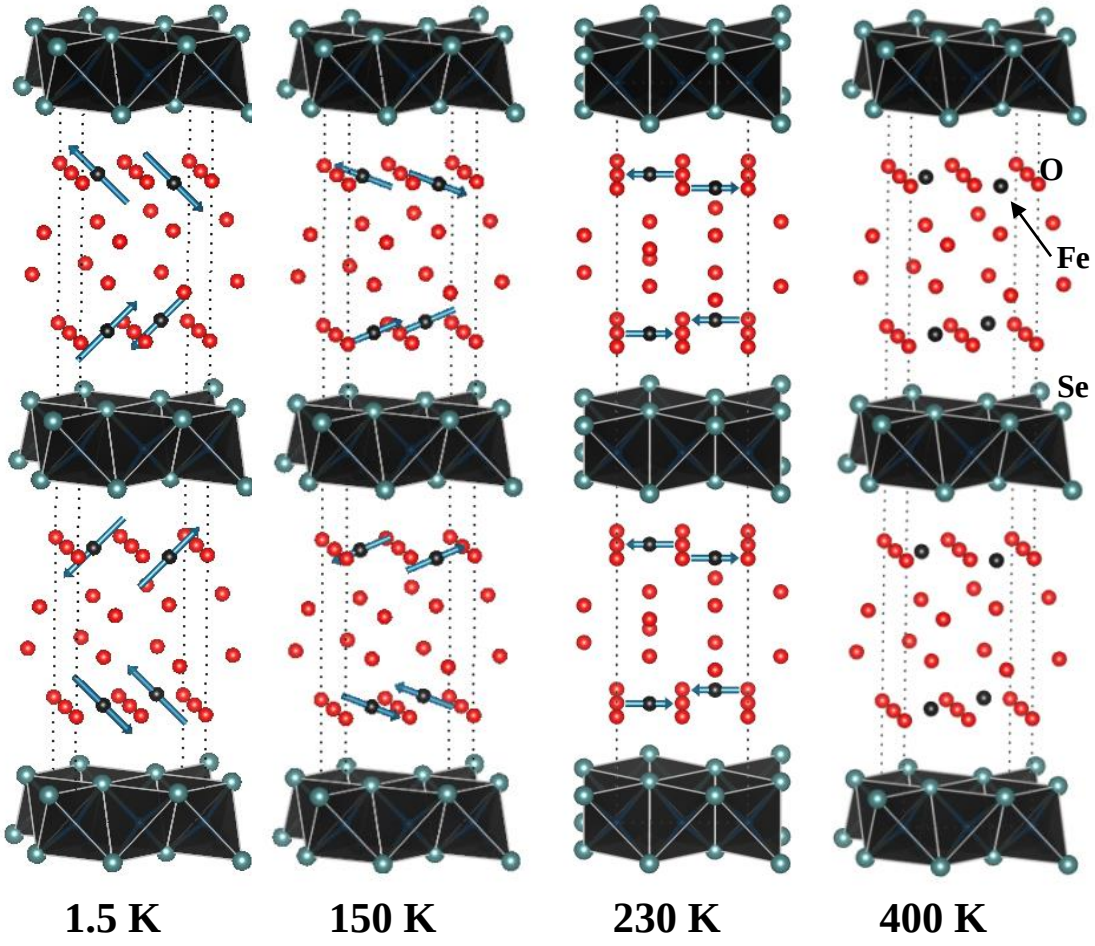

Figure 6.13: Magnetic models of Sr_2FeO_3CuSe over the temperature range 1.5 K to 623 K, showing the magnitude and direction of magnetic moments for Fe^{3+} in the oxide layers

The refinement results suggest that there is a long-range magnetic ordering of Fe^{3+} in the oxide layers below the Neél temperature (between 350 K and 400 K), with all magnetic moments coupled antiferromagnetically in a checkerboard fashion and directed within the *ab*-plane. Figure 6.13 summarises the magnetic models from 1.5 K to 400 K, indicating a spin reorientation transition between 1.5 K and 230 K with the tilted Fe^{3+} magnetic moments reorienting to lie in the *ab* plane by 230 K. The changes in the magnitudes of the refined magnetic moments and their components in the directions along both *c*-axis and *ab*-plane are shown in Figure 6.14, where the magnitude of the moments is shown as a function of temperature. The total magnetic moment of Fe^{3+} increases slowly in magnitude as the sample

is cooled down to 1.5 K, at which point the moment reach its maxima with a value of 4.07(8) μB/ Fe^{3+}. This is smaller than the saturated spin-only ordered magnetic moment of a d^5 Fe^{3+} ion of 5 μB because of the covalency of the Fe–Se and Fe–O bonds, decreasing the density of unpaired electrons on Fe by delocalisation.

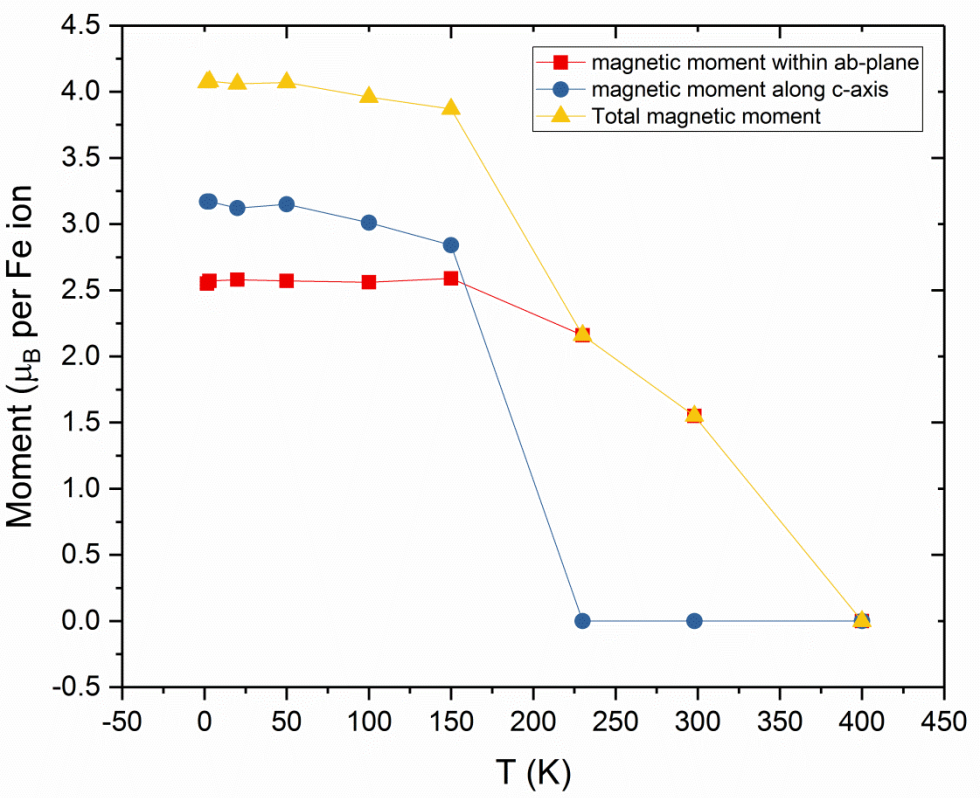

Figure 6.14: Magnitudes and directions of the Fe^{3+} magnetic moments as a function of temperature

6.3 Synthesis and characterisation of Sr_2CrO_3CuSe

The samples with the composition of Sr_2CrO_3CuSe were synthesised using SrO, Cr (Alfa, 99.95 %), CuO (Alfa, 99.995 %) and Se (Alfa, 99.999 %) as starting materials in the molar ratio 2: 1: 1: 1. SrO was made by thermal decomposition of Sr_2CO_3 (Alfa, 99.994 %) at 1100 °C (as detailed in section 2.1.3.1). A pellet was sealed inside an evacuated silica tube as previously described in section 2.1.1. Preparation of a phase-pure sample of Sr_2CrO_3CuSe

was difficult to achieve, with a large number of impurity phases such as SrSe and SrO and some other unidentified peaks. The reaction was first carried out by heating to 900 °C for 96 hours, after which the major phase in the product was found to be SrO, indicating that the reaction was not complete at this temperature. Thus the mixture was then reground and sintered at a higher temperature of 1050 °C for another 24 hours and it was found that Sr_2CrO_3CuSe phase was formed in the product (XX198C), with a small amount of SrSe and some other unidentified peaks. Further reheats of the product at 1050 °C and even at a higher temperature (1200 °C) did not improve the purity of the target phase but lead to the generation of more SrSe in the product.

6.3.1 Powder X-ray diffraction

The structure and composition of Sr_2CrO_3CuSe (XX198C) were probed using synchrotron powder X-ray diffraction (Mythen detector on the I11 beamline). A refinement against the data is plotted in Figure 6.15, showing that the sample contains the impurity SrSe and a large number of unindexed peaks of low intensity, which are probably related to the impurity phases with the elements of Cr, Cu and O but could not be indexed with any known impurity phase in the database. The site occupancies of both Cu and Cr were refined to be fully occupied within error and there was no evidence for O deficiency. The refined values of compound Sr_2CrO_3CuSe are shown in Table 6.5, Table 6.6 and Table 6.7.

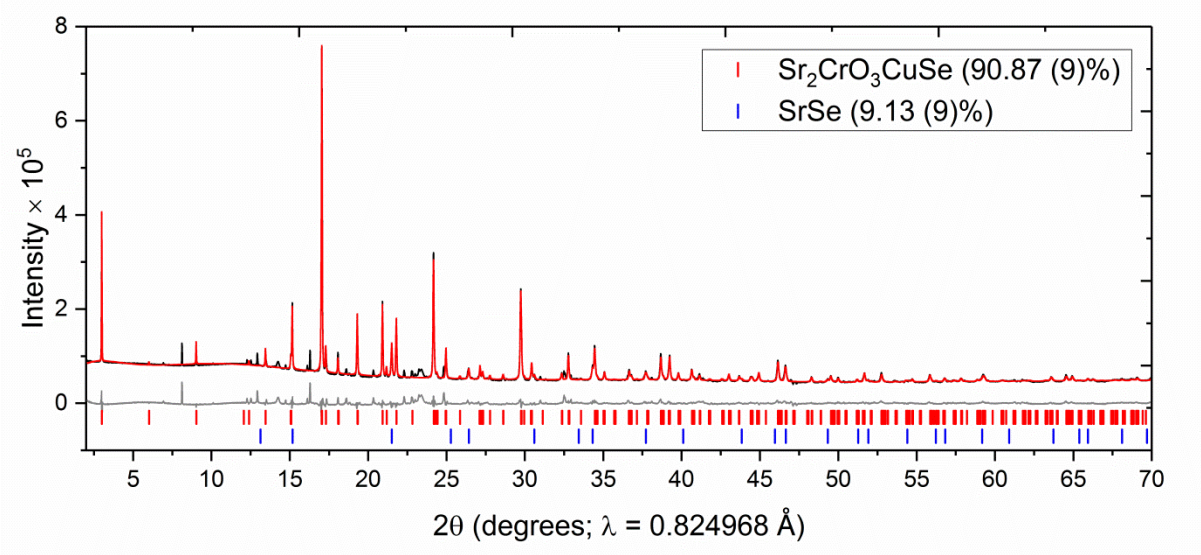

Figure 6.15: Rietveld refinement of Sr_2CrO_3CuSe (XX198C) against synchrotron PXRD data measured at room temperature using Mythen detector on the I11 beamline

Parameter	Sr_2CrO_3CuSe
Diffractometer	I11 (Mythen)
Wavelength (Å)	0.824968
Temperature (K)	298
Space group	*P*4/*nmm*
a (Å)	3.93848(6)
c (Å)	15.7103(3)
V (Å^3)	243.693(4)
Phase density (g cm^{-3})	5.6930(2)
R_{wp}	3.81
χ^2	9.17

Table 6.5: Refined parameters from Rietveld refinement against the PXRD pattern of the sample of Sr_2CrO_3CuSe (XX198C), measured at RT using the Mythen detector on the I11 beamline

I11 PXRD of Sr_2CrO_3CuSe at room temperature							
Atom	Site	*x*	*y*	*z*	U_{11} (Å^2)	U_{22} (Å^2)	U_{33} (Å^2)
Sr(1)	2c	0.75	0.75	0.1925(2)	0.0012(9)	= U_{11}	0.017(2)
Sr(2)	2*c*	0.75	0.75	0.4130(14)	0.004(1)	= U_{11}	0.002(2)
Cr	2c	0.25	0.25	0.3074(2)	0.000(14)	= U_{11}	0.003(2)
Cu	2*a*	0.25	0.75	0	0.010(1)	= U_{11}	0.000(2)
Se	2*c*	0.25	0.25	0.0976(15)	0.004(1)	= U_{11}	0.008(2)
O(1)	4f	0.25	0.75	0.2927(7)		0.000(3) [a] [U_{iso} (Å^2)]	
O(2)	2c	0.25	0.25	0.4347(9)		0.000(3) [a] [U_{iso} (Å^2)]	

Table 6.6: Atomic parameters for Sr_2CrO_3CuSe (XX198C) from the Rietveld refinement of powder X-ray diffraction data, measured at RT using the Mythen detector on the I11 beamline; [a] O atoms were refined with the isotropic thermal displacement parameters

	I11 PXRD of Sr_2CrO_3CuSe at room temperature
Cr–O(1) (Å) [×4]	1.9830(14)
Cr–O(2) (Å) [×1]	1.999(15)
Cr–Se (Å) [×1]	3.296(4)
Cu–Se (Å) [×4]	2.4965(15)
Se-Cu-Se (°) [×4]	112.18(5)
Se-Cu-Se (°) [×2]	104.17(9)

Table 6.7: Selected atomic distances and bond angles for Sr_2CrO_3CuSe from the Rietveld refinement of I11 PXRD data

6.3.2 Room temperature PND

Despite the presence of impurity phases the PND pattern was measured on a 2 g sample of Sr_2CrO_3CuSe (XX198C) at room temperature with $\lambda = 1.594$ Å on D2B diffractometer at ILL, Grenoble. A Rietveld refinement of Sr_2CrO_3CuSe (XX198C) against room temperature NDP data is shown in Figure 6.16. Unindexed peaks correspond to those seen in the PXRD data. Refined structural parameters are listed in Table 6.8 and Table 6.9, showing fair

agreement with those derived from the Rietveld refinement against PXRD data. The resultant fractional occupancies of Cu and Cr are refined to be 0.91(4) and 0.92(2) by PND, which is different from those fully occupied results obtained from the refinements of PXRD data. Given that there are still some impurity phases observed in the diffraction patterns, the sample is probably not fully stoichiometric.

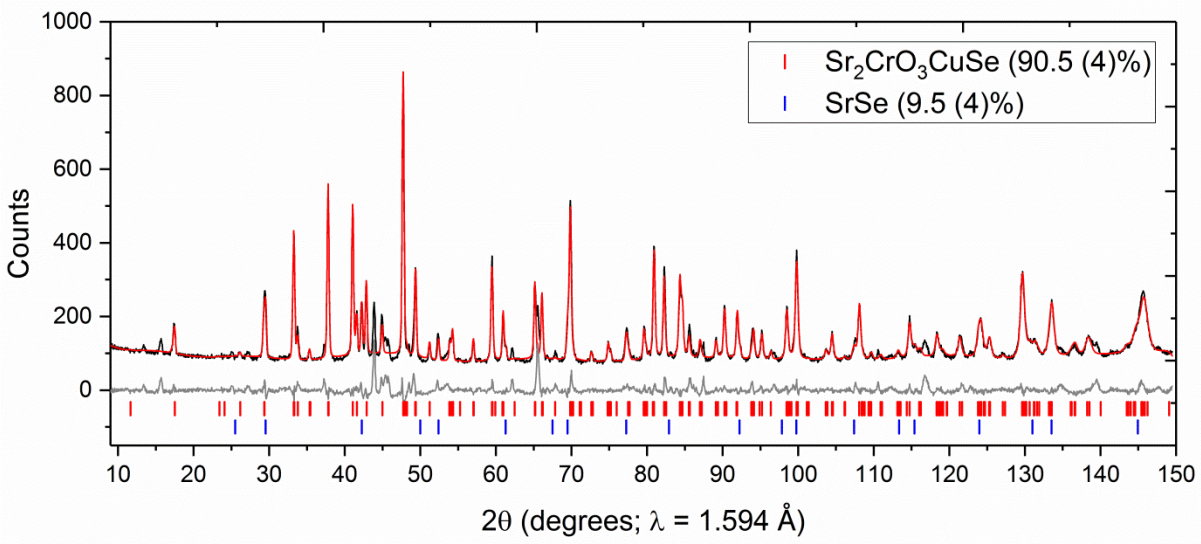

Figure 6.16: Rietveld refinement against the PND pattern of Sr_2CrO_3CuSe (XX198C), measured at RT using the D2B diffractometer on ILL, $\chi^2 = 2.87$, $R_{wp} = 8.25$

Parameter	Sr_2CrO_3CuSe
Diffractometer	D2B (ILL)
Wavelength (Å)	1.594
Temperature (K)	298
Space group	*P*4/*nmm*
a (Å)	3.93866(9)
c (Å)	15.7107(6)
V (Å^3)	243.72(14)
Phase density (g cm^{-3})	5.49(3)
R_{wp}	8.25
χ^2	2.87

Table 6.8: Lattice parameters from Rietveld refinement against the PND pattern of Sr_2CrO_3CuSe (XX198C), measured at RT using D2B at ILL

D2B PND of Sr_2CrO_3CuSe at room temperature					
Atom	Site	*x*	*y*	*z*	U_{iso} (Å^2)
Sr(1)	2*c*	0.75	0.75	0.1941(4)	0.001(1)
Sr(2)	2*c*	0.75	0.75	0.4138(4)	0.008(13)
Cr	2*c*	0.25	0.25	0.3141(7)	0.000(3)
Cu	2*a*	0.25	0.75	0	0.005(2)
Se	2*c*	0.25	0.25	0.0995(4)	0.009(2)
O(1)	4*f*	0.25	0.75	0.2944(3)	0.003(1)
O(2)	2*c*	0.25	0.25	0.4303(5)	0.006(2)

Table 6.9: Structure parameters for Sr_2CrO_3CuSe from the Rietveld refinement of D2B PND data

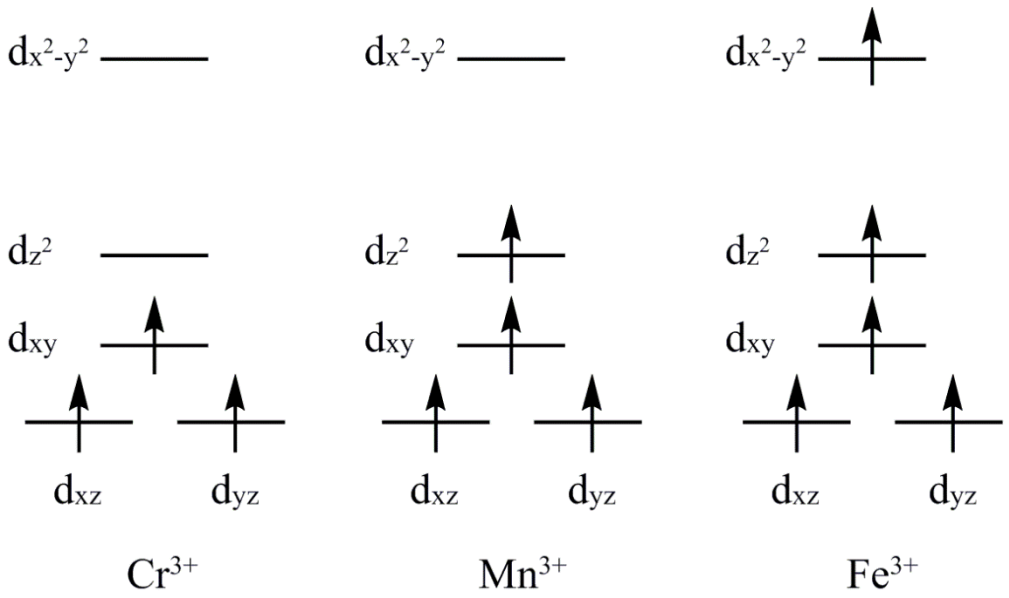

Figure 6.17: The ligand fields for Cr^{3+}, Mn^{3+} and Fe^{3+} ions in Sr_2MO_3CuSe

In order to compare Sr_2CrO_3CuSe with its Mn and Fe analogues, the lattice parameters, selected atomic distances and bond angles for these compounds under the distorted octahedral environment are shown in Table 6.10. The *a* lattice parameter of Sr_2CrO_3CuSe is similar to that of Sr_2FeO_3CuSe but is 1.7250(4) % longer than that of Sr_2MnO_3CuSe, related to a Cr-O(1) bond distance (1.9938(19) Å) that is almost same to the Fe-O(1) distance (1.9956(4) Å) but 1.88(4) % longer than the Mn-O(1) length (1.9571(6) Å). However, a

longer *c* lattice parameter is found in the case of Sr_2MnO_3CuSe, which is 3.800(5) % and 2.126(2) % longer than those in Sr_2CrO_3CuSe and Sr_2FeO_3CuSe respectively. It is also found that the axial Mn–O(2) distance of Sr_2MnO_3CuSe (1.993(4) Å) is longer than their equatorial Mn–O(1) distance (1.9571(6) Å) in the oxide layers, in contrast to the refined results observed in both Sr_2CrO_3CuSe and Sr_2FeO_3CuSe compounds, where the equatorial M–O(1) distances are much longer than those axial M–O(2) distances (the Mn-O(2) distance (1.993(4) Å) is 9.1(3) % longer than the corresponding distance in Sr_2CrO_3CuSe and 5.4(4) % longer than that of Sr_2FeO_3CuSe), which is a consequence of the single occupancy of d_z^2 orbital (σ-antibonding with respect to the axial ligands) in the d^4 Mn^{3+} of Sr_2MnO_3CuSe (see Figure 6.17), leading to increased antibonding electron density along the apical Mn–O axis and hence the lengthened apical bond (by comparison, in Sr_2CrO_3CuSe and Sr_2FeO_3CuSe, the σ-antibonding d_z^2 and $d_{x^2-y^2}$ orbitals are either both empty or both occupied, resulting in smaller ratios of the apical bond to basal ones). Moreover, the Cu-Se bond distances are found to be fairly similar in all three compounds but Sr_2MnO_3CuSe has a bigger axial Se-Cu-Se angle and a smaller equatorial Se-Cu-Se angle (These are a consequence of the smaller *a* parameter) compared with the Cr and Fe compounds. The transition metals (Cr, Mn and Fe) in the oxide layers are squeezed with the intervening Sr^{2+} cations to form a highly distended octahedral environment (MO_5Se) where the *M*–Se distance is quite long, indicating a weak interaction between *M* and Se. For Sr_2MnO_3CuSe, the Mn–Se distance is 3.1(2) % longer than the Cr–Se distance in Sr_2CrO_3CuSe and 0.4(2) % longer than the Fe–Se distance in Sr_2FeO_3CuSe, suggesting the axial M-Se is more distended in Sr_2MnO_3CuSe. Therefore, a more distended octahedral environment is found in the oxide layer of Sr_2MnO_3CuSe, which is shown in Figure 6.18, in comparison with its Cr and Fe analogues.

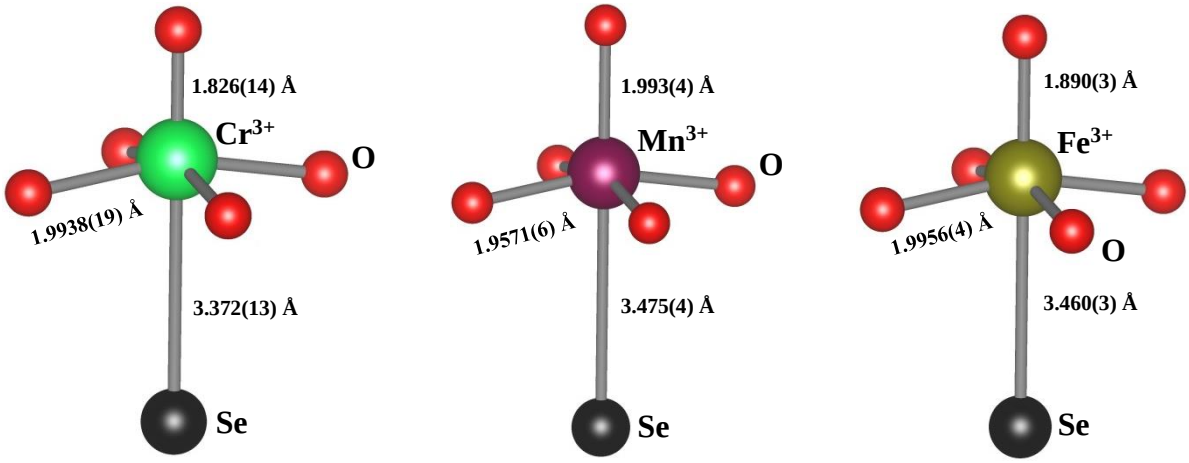

Figure 6.18: MO_5Se coordination environment with 1st row transition metals M (Cr, Mn and Fe); The bond lengths obtained at room temperature from D2B PND at ILL

Compound	Sr_2CrO_3CuSe	Sr_2MnO_3CuSe	Sr_2FeO_3CuSe
Diffractometer	D2B (ILL)	D2B (ILL)	D2B (ILL)
T (K)	298	298	298
a (Å)	3.93868(9)	3.87189(4)	3.93702(2)
c (Å)	15.7109(6)	16.3080(2)	15.9685(1)
V (Å^3)	243.72(1)	244.482(6)	247.513(3)
M–O(1) (Å) [×4]	1.9938(19)	1.9571(6)	1.9956(4)
M–O(2) (Å) [×1]	1.826(14)	1.993(4)	1.890(3)
M–Se (Å) [×1]	3.372(13)	3.475(4)	3.460(3)
Cu–Se (Å) [×4]	2.514(4)	2.5043(12)	2.5113(11)
Se-Cu-Se (°)$_{ax}$ [×4]	112.74(12)	113.73(4)	112.68(4)
Se-Cu-Se (°)$_{eq}$ [×2]	103.1(3)	101.26(7)	103.23(7)

Table 6.10: Lattice parameters, selected atomic distances and bond angles for the A_2MO_3CuCh-structure-type compounds with different 1st row transition metals (Cr, Mn and Fe)

6.3.3 Magnetic susceptibility measurements

A measurement of magnetisation (*M*) versus magnetic field (*H*) was measured (Figure 6.19a) to be linear at 300 K, suggesting the absence of room-temperature ferromagnetic impurities in the sample of Sr_2CrO_3CuSe (XX198C). The temperature-dependent ZFC and FC magnetic susceptibilities (χ) were then measured in an applied field of 1000 Oe between 2

K and 330 K as shown in Figure 6.19b. A broad maximum is observed at around 60 K, analogous to that seen in both Sr_2MnO_3CuSe (100 K) and Sr_2MnO_3CuS (95 K), indicative of the low-dimensional antiferromagnetic ordering of Cr^{3+} in the oxide layers of the sample as previously observed in other 1st-row transition metals with the A_2MO_3CuCh-type structure.

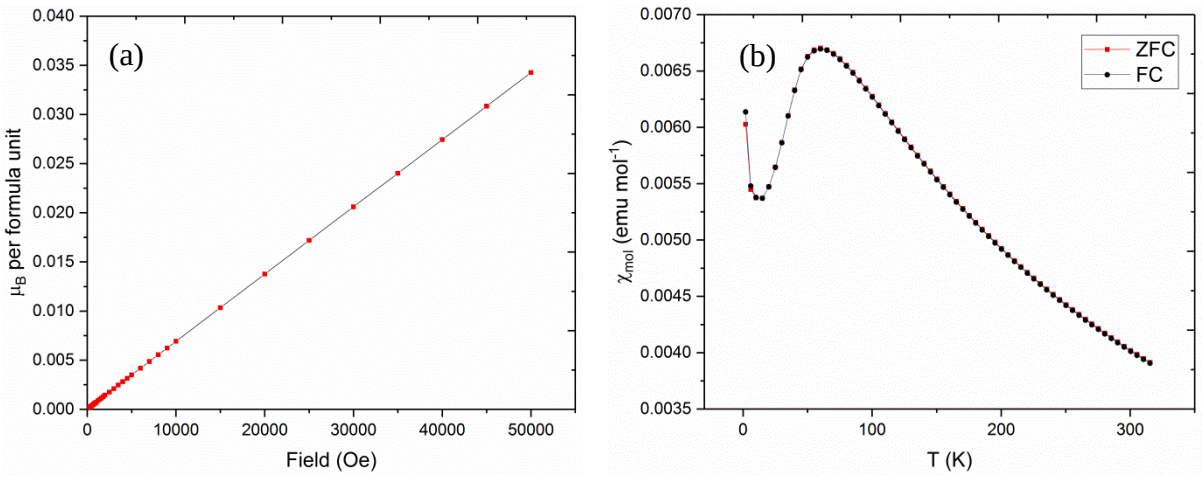

Figure 6.19: (a) *MvH* for Sr_2CrO_3CuSe (XX198C) at 300 K; (b) The zfc and fc magnetic susceptibilities of Sr_2CrO_3CuSe (XX198C), measured at 1000 Oe between 2 K and 330 K

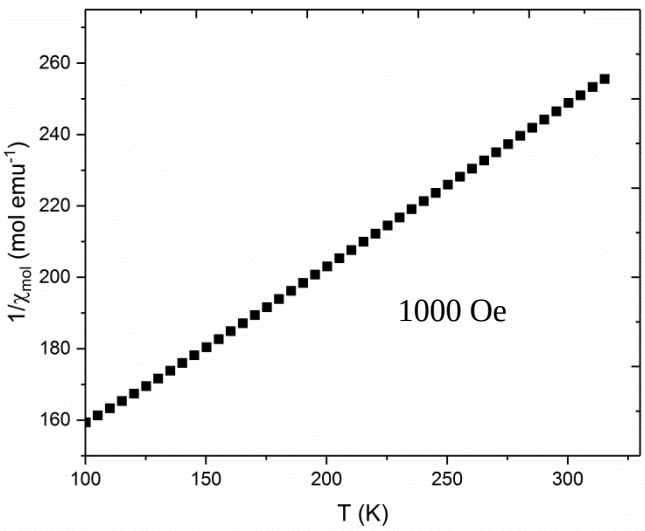

Figure 6.20: The inverse magnetic susceptibility (zfc) of Sr_2CrO_3CuSe with a line of best fit (100 K-330 K), measured in an applied field of 1000 Oe

A Curie-Weiss plot of 1/ χ against temperature is also shown in Figure 6.20. While the dependence seems linear, the extracted Weiss constant, θ = -250 K is comparable to the

range of temperatures considered, suggesting that the Curie-Weiss law may not be valid in this regime. The value of μ_{eff} = 4.21 μ_B is significantly larger than expected for Cr^{3+} using the spin-only formula, although a second order orbital enhancement cannot be ruled out.

There was no divergence between zfc and fc data of Sr_2CrO_3CuSe and the performed hysteresis measurement at 5 K also suggested that the spin glass behaviour was not observed, where the isotherm is symmetric and a straight line intersects with the origin in the low applied field from -0.2 T to 0.2 T (Figure 6.21).

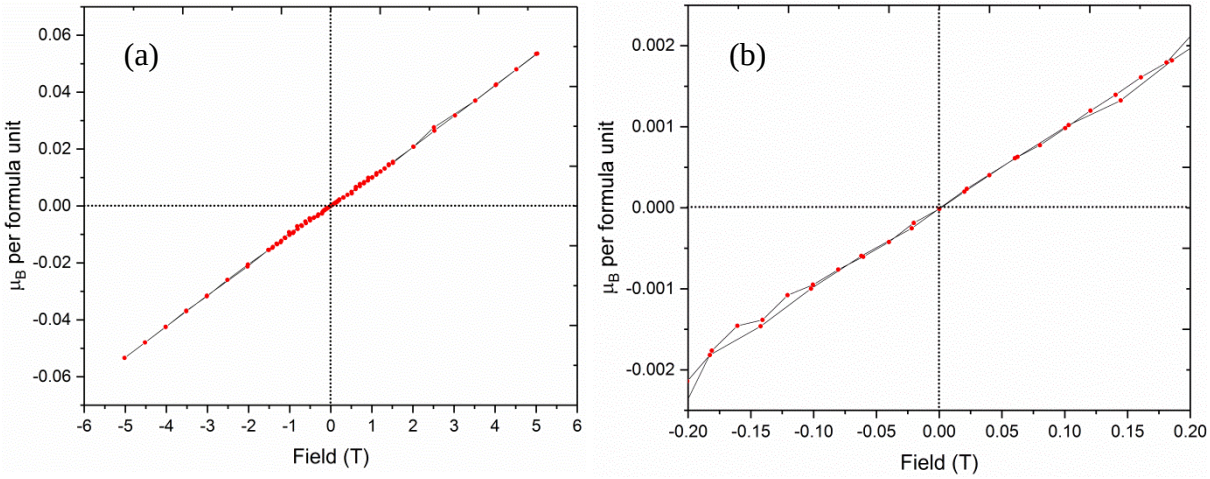

Figure 6.21: a) Magnetic moment per Cr ion of Sr_2CrO_3CuSe as a function of applied magnetic field, measured at 5K in the range -5 ≤ H (T) ≤ +5; b) Zooming in the range of -0.2 T to 0.2 T

6.3.4 Variable temperature PND

Given the appearance of antiferromagnetic ordering at approximately 60 K in the magnetic susceptibility measurements, a further PND measurement at 4 K was performed on D2B to fully characterise the magnetic behaviour of Sr_2CrO_3CuSe. In comparison with its room temperature PND data, several very small magnetic Bragg reflections marked with (*) are present in the diffraction pattern at 5 K (Figure 6.22). The appearance of additional magnetic Bragg peaks at high *d*-spacing is consistent with those magnetic reflections observed in

Sr_2FeO_3CuSe and Sr_2MnO_3CuSe, indicating the presence of antiferromagnetic ordering of Cr^{3+} in the oxide layers.

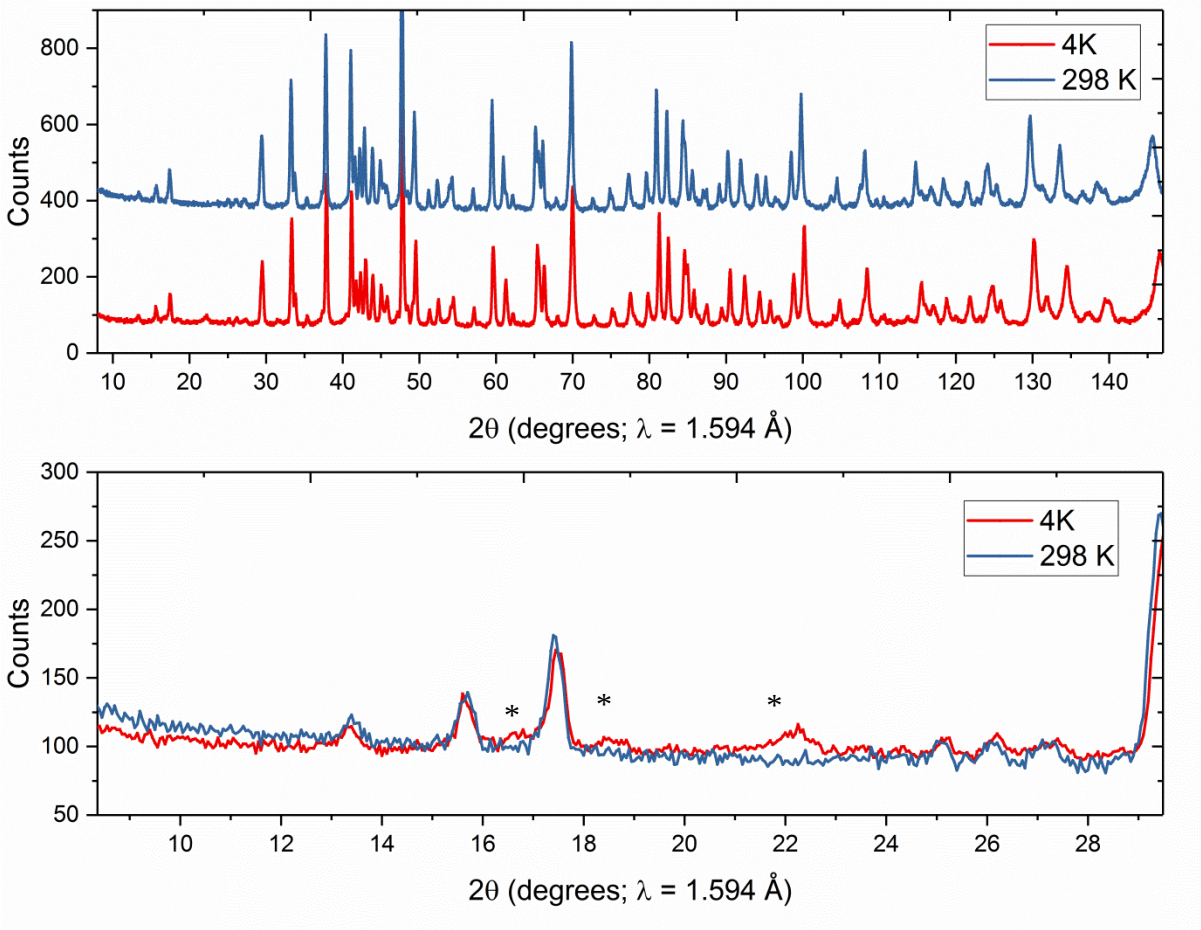

Figure 6.22: Comparison of PND data of Sr_2CrO_3CuSe collected on the D2B diffractometer at 4 and 298 K; The asterisks (*) indicate that the magnetic reflections present at 4 K

These magnetic reflections of Sr_2CrO_3CuSe could then be indexed to a magnetic cell with a $\sqrt{2}a \times \sqrt{2}a \times c$ expansion of the nuclear unit cell, suggesting that these magnetic peaks are from the main product phase. Starting with a magnetic subgroup *P*1(1.1), the web-based software ISODISTORT[56] was applied to help the deduction of the magnetic models before the Rietveld refinement, where all possible magnetic symmetry modes were tried to fit the intensity of the magnetic Bragg reflections. During the refinement, the fit between the observed and calculated data could also be significantly improved by applying a Stephens-type anisotropic broadening function. The intensity of all magnetic peaks at 4 K is very low

for this sample and the best fitting for these peaks was obtained using a single magnetic mode mM1(a) with a highest-symmetry magnetic space group of $P_c2_12_12$ (18.23) on the Cr sites.[56] The Rietveld refinement using mM1(a) magnetic mode at 4 K is plotted in Figure 6.23 with $\chi^2 = 3.59$, $R_{wp} = 8.83$.

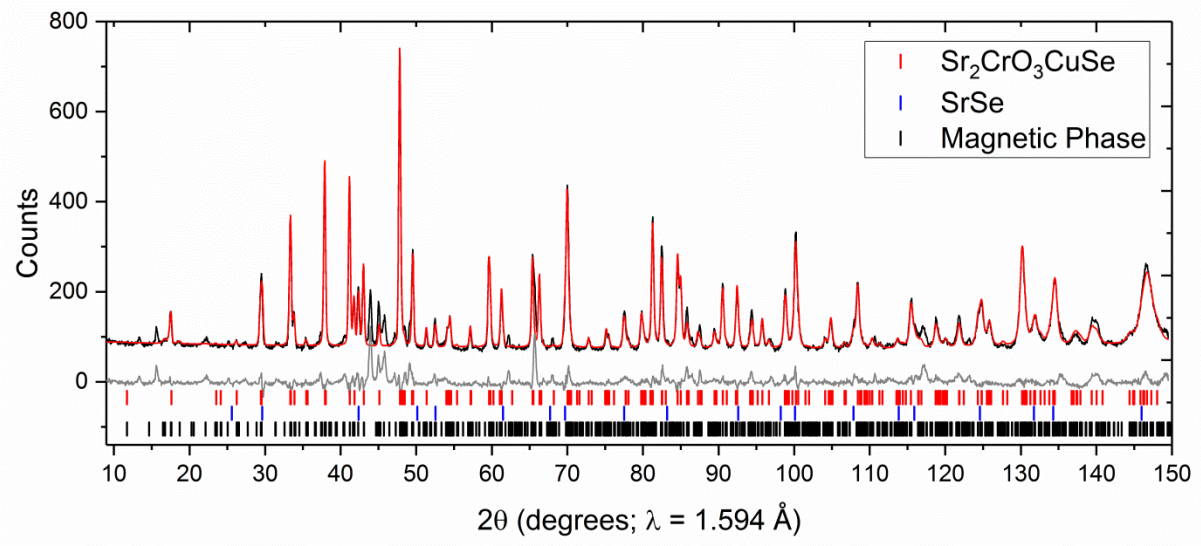

Figure 6.23: Rietveld refinement of Sr_2CrO_3CuSe (XX198C) collected at 4 K ($\chi^2 = 3.58$, $R_{wp} = 8.82$)

Different to its Mn analogues (Sr_2MnO_3CuSe, Sr_2MnO_3CuS and $Sr_2MnO_3Cu_{0.94}S$) discussed in chapter 5, the mM1(a) magnetic mode of Sr_2CrO_3CuSe represents the nearest-neighbour Cr^{3+} magnetic spins in the oxide planes are coupled antiferromagnetically with their moments aligned within the *ab*-plane. The $\sqrt{2}a \times \sqrt{2}a \times c$ expansion gives a doubled volume of the new magnetic unit cell, where the antiferromagnetic alignment of Cr^{3+} in adjacent layers related by the vector *c*/2 is aligned antiparallel, together with the AFM ordering of Cr^{3+} magnetic moments within the planes. The resultant magnetic model of Sr_2CrO_3CuSe is plotted in Figure 6.24. The refined magnetic moment of Cr^{3+} is 1.45(8) $\mu B/Cr^{3+}$ at 4K, which is significantly less than the expected saturated spin-only ordered

magnetic moment of a Cr^{3+} of 3 μB and probably due to the covalency of the Cr–O and Cr-Se bonds in the oxide layers.

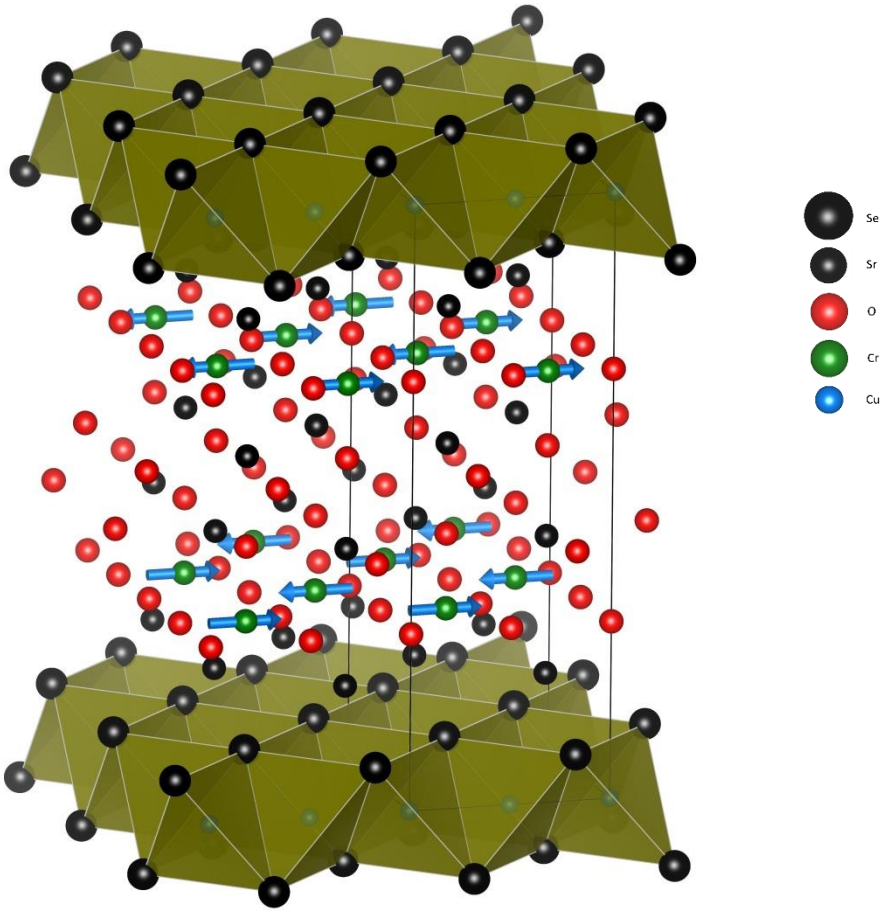

Figure 6.24: The ordering of Cr^{3+} magnetic moments in a magnetic model of Sr_2CrO_3CuSe

As previously discussed in section 6.3.1, the sample of Sr_2CrO_3CuSe (XX198C) still contains SrSe and some other unindexed impurity phases. Therefore further analysis of this compound to explore the evolution of the magnetic scattering would require a purer sample.

6.4 Discussion

The magnetic susceptibility measurements and low-temperature PND carried out on the compounds of Sr_2CrO_3CuSe, Sr_2MnO_3CuSe (chapter 5.2) and Sr_2FeO_3CuSe indicate that the

magnetic moments of these transition metal ions are all antiferromagnetically ordered within the oxide layers below their transition temperatures. This antiferromagnetic ordering is due to the super-exchange interaction through the overlap between the metal *d*-orbitals and the filled O *p*-orbitals, leading to the simultaneous transferring of electron density between the M^{3+} and O^{2-} (see Figure 6.25). Note that the π-type superexchange will also be antiferromagnetic.

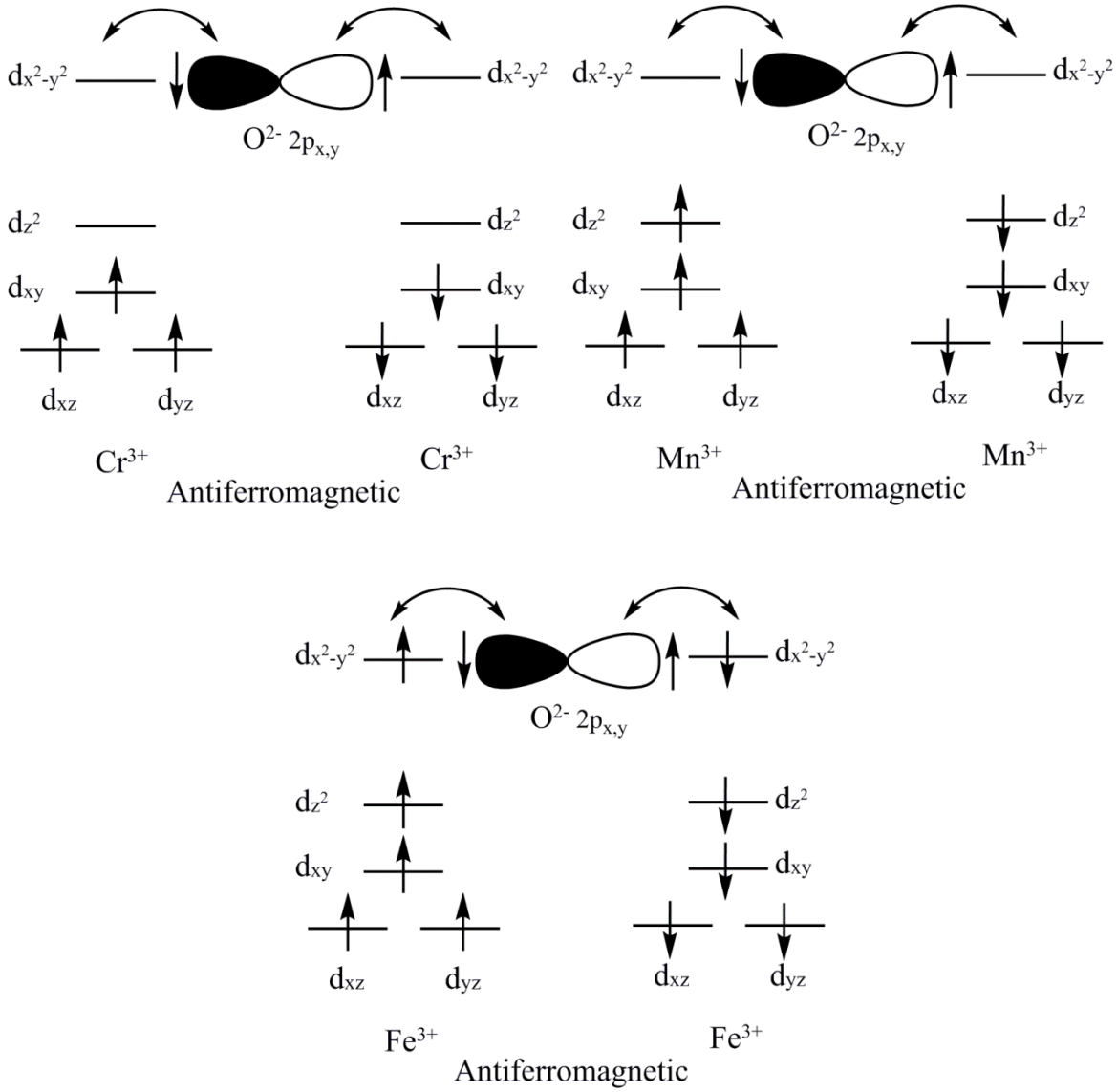

Figure 6.25: Schematic of antiferromagnetic super-exchange interactions between the metal ions and intermediary O^{2-} ligands

The refined magnetic and structural results of Sr_2CrO_3CuSe, Sr_2MnO_3CuSe and Sr_2FeO_3CuSe are listed in Table 6.11 to investigate the relationship between their structures and magnetic behaviour.

Compound	Sr_2CrO_3CuSe	Sr_2MnO_3CuSe	Sr_2FeO_3CuSe
Diffractometer	D2B (ILL)	D2B (ILL)	WISH (ISIS)
T (K)	4	4	3
Oxidation state	+3	+3	+3
Electronic configuration	d^3	d^4	d^5
Moment(μ_B per M ion)	1.5(8)	3.76(6)	4.08(8)
Spin orientation	Within the *ab*-plane	Along the *c*-axis	Reorientation
a (Å)	3.93868(9)	3.87189(4)	3.93702(2)
c (Å)	15.7109(6)	16.3080(2)	15.9685(1)
V (Å^3)	243.72(1)	244.482(6)	247.513(3)
M–O(1) (Å) [×4]	1.9938(19)	1.9571(6)	1.9956(4)
M–O(2) (Å) [×1]	1.826(14)	1.993(4)	1.890(3)
M–Se (Å) [×1]	3.372(13)	3.475(4)	3.460(3)
Cu–Se (Å) [×4]	2.514(4)	2.5043(12)	2.5113(11)
Se-Cu-Se (°)$_{ax}$ [×4]	112.74(12)	113.73(4)	112.68(4)
Se-Cu-Se (°)$_{eq}$ [×2]	103.1(3)	101.26(7)	103.23(7)

Table 6.11: Magnetic and structural results measured for the Sr_2MO_3CuSe-type compounds containing Cr, Mn and Fe

All the 1st-row transition metals (Cr, Mn and Fe) in these compounds are in the highly distended octahedral environment MO_5Se, with the elongated M-O(2) and M-Se distances along the c axis. In contrast to the perfect octahedral coordination environment, the highly distended octahedral environment around both Cr and Mn ions gives the loss of degeneracy of the d-orbitals, leading to a significant quenching of the orbital angular momentum of d electrons. For Sr_2FeO_3CuSe (Fe is in a d^5 configuration), the orbital angular momentum doesn't contribute to any magnetic moment regardless of the ligand field effects. For these three compounds, the magnitude of the magnetic moments of transition metal ions can be estimated by the number of spins, which corresponds to the measured results collected from

low-temperature PND data: the ordered magnetic moment of Fe^{3+} (4.08(8) μ_B) has the biggest value compared with those in both Cr (1.5(8) μ_B) and Mn (3.76(6) μ_B) analogues.

Another contrast between these compounds is the orientation of the magnetic moments of metal ions in the oxide layers. The magnetic moments of Cr^{3+} (d^3) in Sr_2CrO_3CuSe was found to lie within the *ab*-plane. But for Sr_2MnO_3CuSe, the preferred orientation of the magnetic Mn^{3+} (d^4) moments is along the *c*-axis. From 1.5 K to 230 K, the magnetic ordering of Fe^{3+} (d^5) showed a spin reorientation transition in Sr_2FeO_3CuSe with the tilted magnetic moments (having the components in the directions along both *c*-axis and *ab*-plane) completely reorienting to lie in the *ab* plane by 230 K. The different preferred spin orientations of these transition metal ions can be rationalised by considering the spin-orbit coupling in terms of the HOMO(highest occupied orbital) – LUMO(lowest unoccupied orbital) interaction between *d*-orbitals, which was described in chapter 3. For the high-spin Mn^{3+} ($3d^4$, $S = 2$) ions in Sr_2MnO_3CuSe, the distended octahedral environment MnO_5Se with elongated Mn-O_{ax} and Mn-Se distances gives the split *d*-orbitals as shown in Figure 6.26. There are four unpaired electrons on the split *d*-orbitals, where the HOMO is the d_{z^2} orbital and the LUMO is the $d_{x^2-y^2}$ orbital. The difference $|\Delta L_z|$ between the two orbitals is 2 and this means they are not interacting under spin-orbit coupling. The nearest filled *d*-orbital that can interact with the LUMO is the d_{xy} orbital. So the new $|\Delta L_z|$ is 0 now between the $d_{x^2-y^2}$ and d_{xy} orbitals, suggesting that the preferred orientation of the magnetic moments of Mn^{3+} ions lies along the *c*-axis. This calculated result is in a good agreement with the spin orientation observed in Sr_2MnO_3CuSe at low temperatures by neutron diffraction refinements. The same $3d^4$-configuration Mn^{3+} ions are also found in the sulfide analogues Sr_2MnO_3CuS and $Sr_2MnO_3Cu_{0.94}S$ (chapter 5.3 and 5.4), where the refined orientations of their magnetic Mn^{3+} spins always lie along the *c*-axis. Another similar case is the Ruddlesden-Popper-type

compound $LaSrMnO_4$.[110] The Mn^{3+} ions ($3d^4$, $S = 2$) here are in the Jahn-Teller-distorted MnO_6 octahedral coordination with two elongated Mn–O bonds directed along the *c*-axis. For this compound, the Mn^{3+} magnetic moments are found by the PND refinements to lie parallel to the principal *c*-axis, in line with the predictions for other Mn^{3+} compounds.

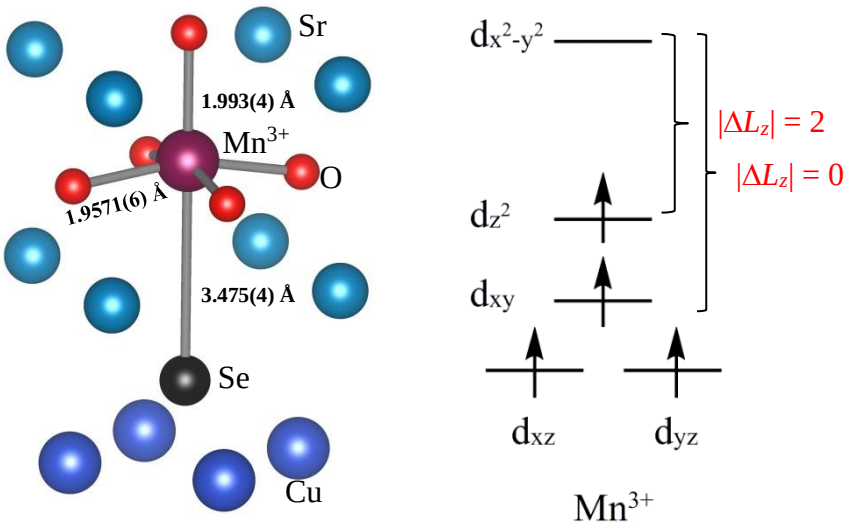

Figure 6.26: The high-spin electron configuration of Mn^{3+} ($3d^4$, $S = 2$) in the axially elongated MnO_5Se coordination environment in Sr_2MnO_3CuSe

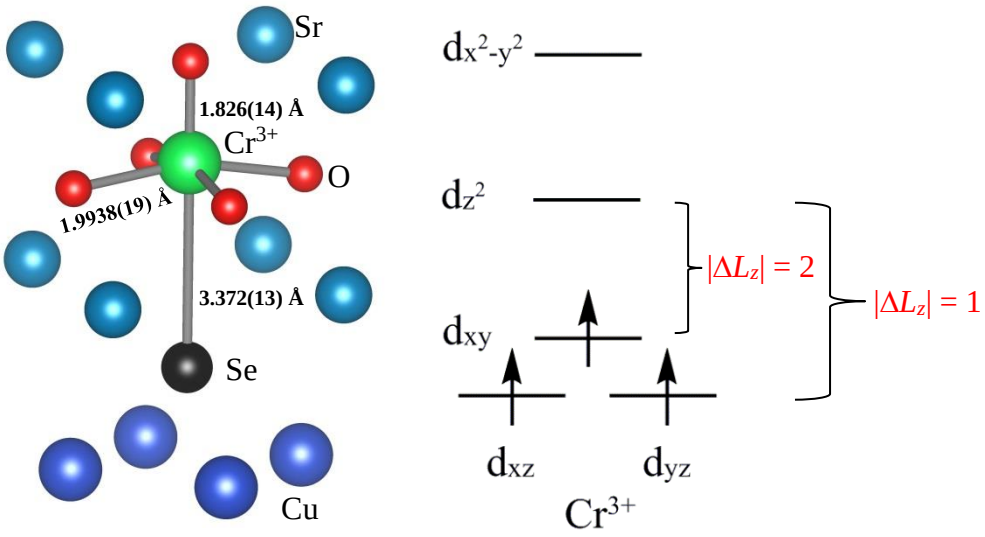

Figure 6.27: The high-spin electron configuration of Cr^{3+} ($3d^3$, $S = 3/2$) with the distorted CrO_5Se coordination environment in Sr_2CrO_3CuSe

In the case of Sr_2CrO_3CuSe, the high-spin Cr^{3+} ions ($3d^3$, S = 3/2) are in the distorted octahedral environment CrO_5Se with slightly shortened Cr-O_{ax} bond and elongated Cr-Se distance. In comparison to the split *d*-orbitals in its Mn analogue, the shortened Cr-O_{ax} bond in Sr_2CrO_3CuSe lifts the d_z^2, d_{xz} and d_{yz} orbitals and thus decreases the energy gap between d_z^2 and $d_{x^2-y^2}$ as well as between d_{xz}, d_{yz} and d_{xy} as shown in the Figure 6.27. The split d_{xy} and d_{xz}, d_{yz} orbitals are now occupied by three unpaired electrons, where the LUMO is the unoccupied d_z^2 orbital and the HOMO is the occupied d_{xy} orbital. Between these two orbitals, applying the previous spin-orbit coupling rule, the difference $|\Delta L_z|$ is 2 (L_z= 0 for d_{z^2}, L_z= ±1 for d_{xz} ,d_{yz} and L_z= ±2 for d_{xy}, $d_{x^2-y^2}$) and they do don't interact with each other. So the difference is calculated again between the LUMO (d_z^2) and its closest filled d_{xz} and d_{yz} orbitals. Now, the $|\Delta L_z|$ is 1, indicating the moment of Cr^{3+} ions lies perpendicular to the *c* direction (i.e. within the *ab*-plane). This predicted orientation exactly matches the refined results collected on Sr_2CrO_3CuSe from PND, with the nearest-neighbour Cr^{3+} magnetic spins in the oxide planes coupled antiferromagnetically within the *ab*-plane. The related *ab*-plane-orientation of Cr^{3+} ions are also observed in Sr_2CrO_3FeAs, in which the Cr^{3+} is in a similar distorted octahedral environment with shortened Cr-O_{ax} bond (compared to Cr-O_{eq}) and elongated Cr-As distance.[100] The magnetic structure of Sr_2CrO_3FeAs is shown in Figure 6.28.

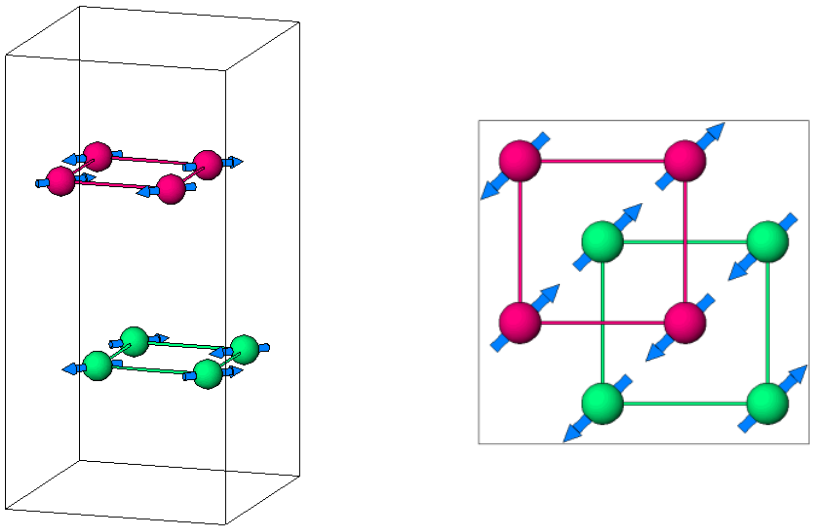

Figure 6.28: The magnetic ordering of the antiferromagnetic Cr^{3+} moments in the oxide layers of Sr_2CrO_3FeAs; The graph was taken from Dr A J Corkett's thesis[99]

This method is much weaker when it is used to explain the orientation of Fe^{3+} magnetic moments. This is because the high-spin d^5 configuration (S = 5/2) possesses no orbital angular momentum no matter how the distended octahedral environment is affected by the ligands. Experimentally, the d^5 Fe^{3+} ions in $LaSrFeO_4$ were in the similar axially distorted octahedral coordination.[111] The Fe^{3+} magnetic moments were reported to be directed within the *ab*-plane, without any observation of spin reorientation. In the case of Sr_2FeO_3CuSe, an obvious spin reorientation of Fe^{3+} moments is found between 1.5 K and 230 K in the low-temperature PND data. This reorientation is complete at 230 K, after which all the moments are aligned within the *ab*-plane until the transition temperature (400 K). It is also found that the refined magnetic moment (4.96(1) μ_B/ Fe^{3+} collected by PND) of Fe^{3+} ions in $LaSrFeO_4$ at 10 K is much bigger than that (4.07(8) μ_B/ Fe^{3+} collected by PND) in Sr_2FeO_3CuSe at 1.5 K. The Fe–O_{eq} distance (1.93545(6) Å) in $LaSrFeO_4$ is only 3.01(2) % shorter than that (1.9956(4) Å) in Sr_2FeO_3CuSe, but the Fe–O_{ax} bond length (2.149(3) Å) in $LaSrFeO_4$ is 13.7(3) % longer than that (1.890(3) Å) in Sr_2FeO_3CuSe. Therefore, the lower magnetic moment of Sr_2FeO_3CuSe is probably because of the Fe-Se interaction and the much shorter

$Fe–O_{ax}$ bond distance, which leads to the greater delocalisation of the unpaired spin density through the covalency of the axial Fe–O and Fe-Se bonds.

Chapter 7

Synthesis and characterisation of Sr_2CrO_3CrAs

7.1 Introduction

The synthesis and characterisation of the first chromium-based layered oxypnictide, $Sr_2CrO_2Cr_2As_2$, was reported by Jiang and co-workers in 2015.[77] The Cr^{2+} ions are stabilised in tetrahedral coordination by arsenide and in a distended octahedral environment CrO_4As_2, which is even more highly distended than the Jahn-Teller-distorted CrX_6 coordinations often found for Cr^{2+}. Its magnetic behaviour and complex spin-reorientation transitions were later investigated by our group using the variable-temperature PND measurements at the WISH diffractometer. As part of work on $Sr_2CrO_2Cr_2As_2$, a small amount of a new phase (Sr_2CrO_3CrAs) with thicker oxide layers was discovered in the TEM image of the sample (Figure 7.1– data from Maria Batuk and Joke Hadermann, University of Antwerp), where Cr^{3+} ions were found in the pyramidal sites in these oxide layers. Sr_2CrO_3CrAs contains Cr^{2+} in the tetrahedral environment by arsenide (as in $Sr_2CrO_2Cr_2As_2$), but in the oxide layer, Cr^{3+} ions generate the double layers in a pyramidal coordination CrO_5, with a weaker sixth bond to an arsenide ion which may allow the interaction between the Cr^{2+} and Cr^{3+} sublattices. Figure 7.2 compares the crystal structure of $Sr_2CrO_2Cr_2As_2$ with Sr_2CrO_3CrAs.

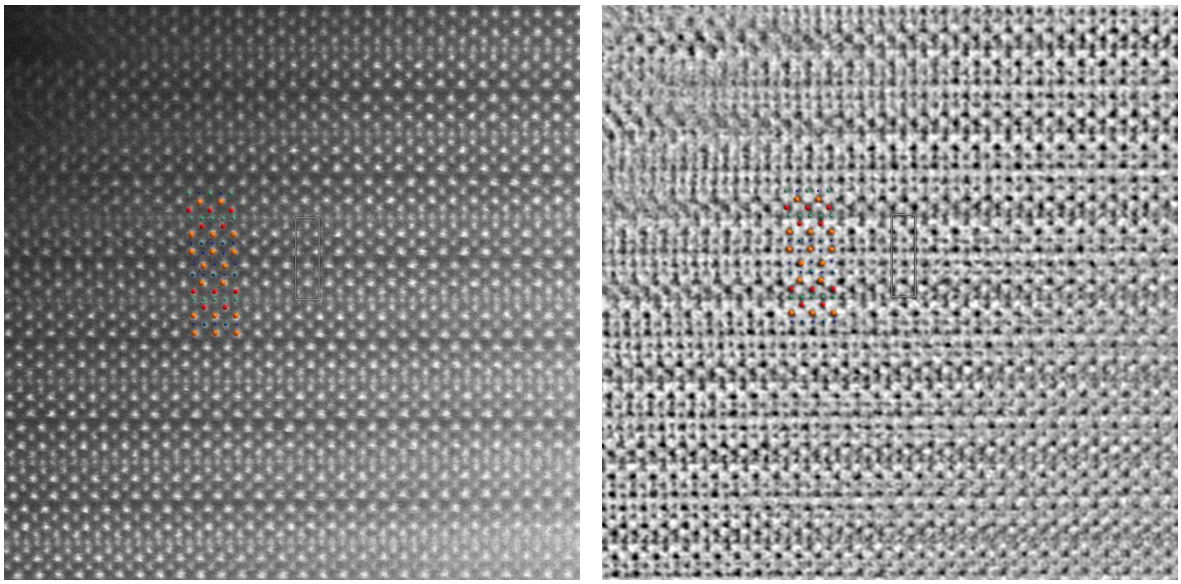

Figure 7.1: The novel structure discovered from TEM image in the measurement of $Sr_2CrO_2Cr_2As_2$, with the composition estimated as $Sr_4Cr_4O_6As_2$

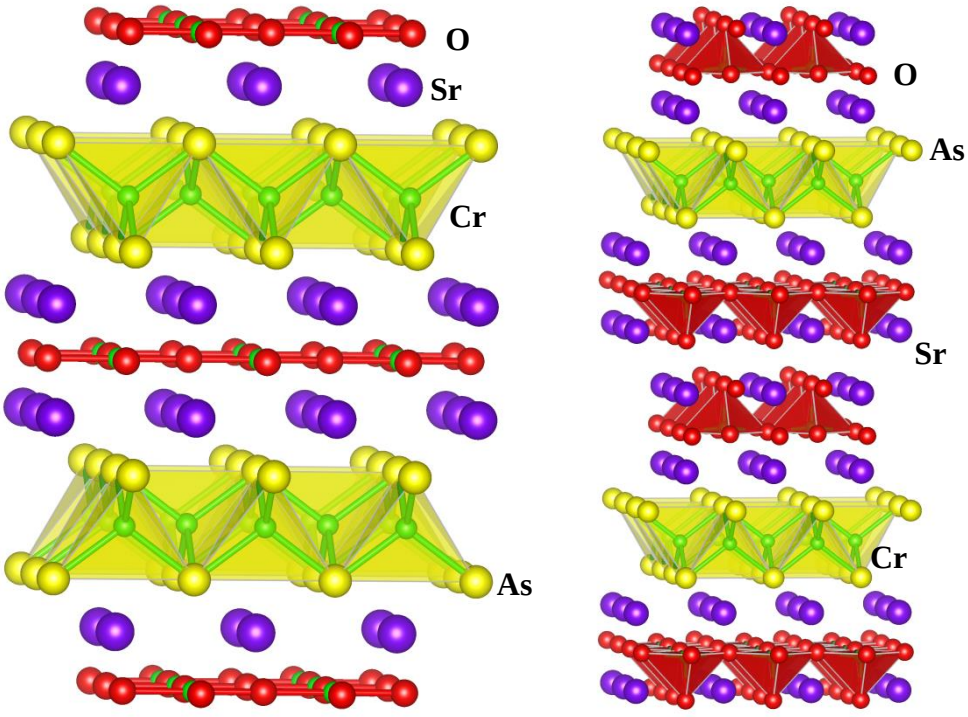

Figure 7.2: Crystal structure of $Sr_2CrO_2Cr_2As_2$ (left) and the new phase Sr_2CrO_3CrAs (right)

Sr_2CrO_3CrAs is also isostructural to the Sr_2MO_3CuCh-type compounds (discussed in chapter 5 and 6), which have similar oxide layers separated by diamagnetic Cu*Ch* layers. All of those

Cu-containing compounds have been found to give antiferromagnetic ordering transitions at similar temperatures and previous PND measurements have proved that the magnetic moments are always antiferromagnetically ordered in the oxide layer. Similar magnetic properties have also been observed in the isostructural arsenide analogue Sr_2CrO_3FeAs,[99, 112] where the oxide-layer Cr^{3+} moments are ordered antiferromagnetically in a checkerboard fashion at 36 K and directed within the ab-plane.

In this chapter, it was found that once the appropriate synthesis conditions were applied, Sr_2CrO_3CrAs could be synthesised with high purity. The composition, structure and magnetic behaviour of this compound were then studied using powder X-ray diffraction, neutron powder diffraction and magnetic susceptibility measurements. Low-temperature PND has revealed the appearance of long-range antiferromagnetic magnetic ordering in Sr_2CrO_3CrAs, which is very different from those magnetic properties reported in Sr_2CrO_3FeAs and some other Sr_2CuGaO_3S-structure-type solids.

7.2 Synthesis and characterisation of Sr_2CrO_3CrAs

Synthesis of a phase-pure sample of Sr_2CrO_3CrAs proved difficult to achieve, with many attempts yielding the competing phase $Sr_2CrO_2Cr_2As_2$ and other impurity phases. Many different synthesis temperatures, reaction times and cooling methods were attempted.

The samples with the composition of Sr_2CrO_3CrAs were prepared by grinding together SrO, Cr_2O_3 (Alfa, 99.6 %), Cr (Alfa, 99.95 %) and As (Alfa, 99 %) in the molar ratio 6: 1: 4: 3 in the glove box. SrO was prepared by thermal decomposition of $SrCO_3$ (Alfa, 99.99 %) at 1100 °C described in section 2.1.3.1 and Cr_2O_3 was pre-dried under vacuum to avoid hydrolysis of the compound by water. It was found that low synthesis temperatures (below

1200 °C) favoured $Sr_2CrO_2Cr_2As_2$ with significant amounts of other unindexed impurity phases. This is shown in the Rietveld refinement of XX142 in Figure 7.3, where the sample was heated to 1100 °C for 24 hours at a slow rate of 2 °C/min. The appearance of SrO is also observed in the diffraction pattern, indicating the reaction is not complete.

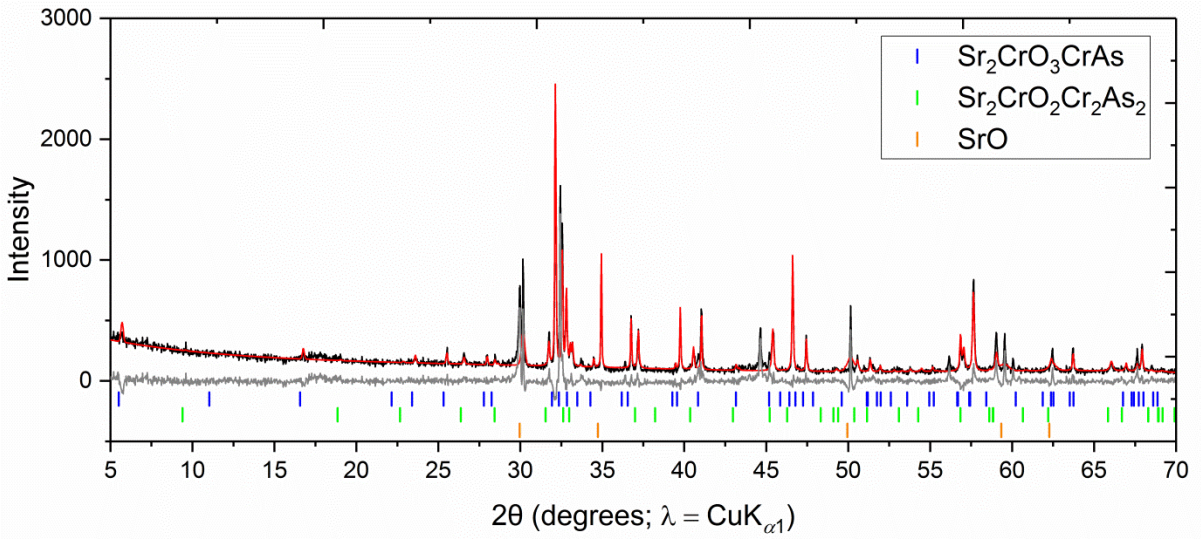

Figure 7.3: Rietveld plot of the sample XX142 (Sr2CrO3CrAs), measured at RT using the PANalytical Empyrean diffractometer; Sample was heated to 1100 °C for 24 hours and cooled in the furnace

A purer sample of Sr_2CrO_3CrAs (XX139) was obtained when the starting materials were heated to 1200 °C and cooled in the furnace. However, the product was still contaminated by a small amount of $Sr_2CrO_2Cr_2As_2$, together with some other unidentified peaks (Figure 7.4). Further reheats of the product at 1200 °C did not give better purity but led a decomposition of the Sr_2CrO_3CrAs phase. After many attempts, it was finally found the quality of the product could be further improved if the solid was quenched quickly in an ice bath after the process of heating.

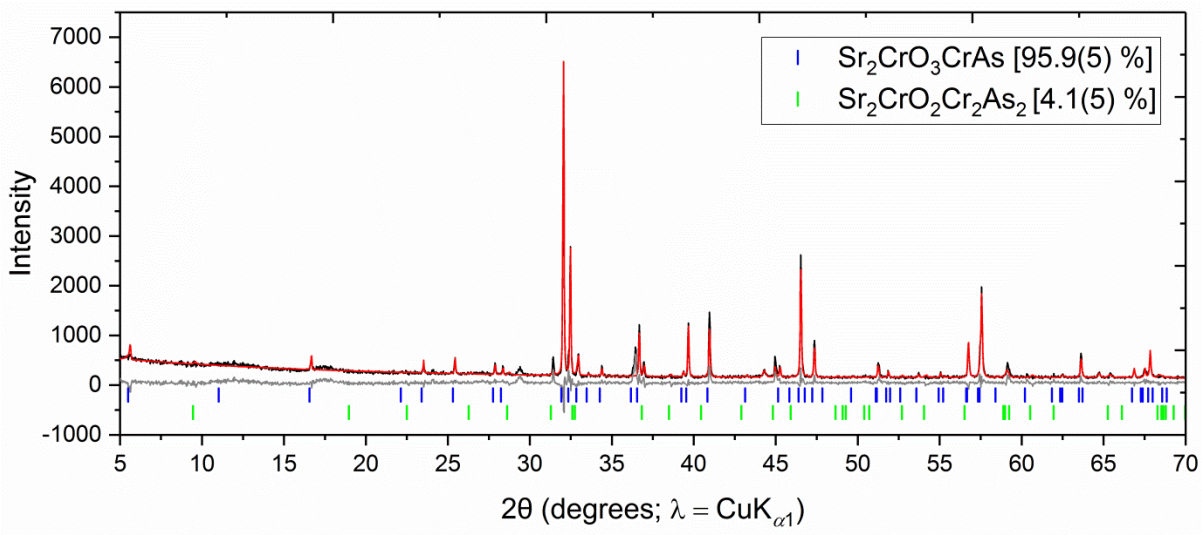

Figure 7.4: Rietveld plot of the sample XX139 (Sr2CrO3CrAs), measured at RT using the PANalytical Empyrean diffractometer; Sample was heated to 1200 °C for 24 hours and cooled in the furnace

The best-quality sample of Sr_2CrO_3CrAs was made by heating the mixture to 1200 °C at a rate of 10 °C/min followed by quenching the reaction in an ice bath very quickly after about 24 hours. The solid was treated as air-sensitive at all stages in the synthesis (although no decomposition of Sr_2CrO_3CrAs was observed on exposure to the air).

7.2.1 Powder X-ray diffraction

High-resolution synchrotron powder X-ray diffraction (MAC detector on the I11 beamline) was performed on the best sample of Sr_2CrO_3CrAs (XX153) synthesised by the method described above. Rietveld refinement against the collected PXRD pattern is plotted in Figure 7.5, showing that the product still contains some very small additional peaks which cannot be indexed with any known impurity phase in the database. The compound (Figure 7.6) is isotypic to Sr_2FeO_3CuSe and Sr_2CrO_3CuSe (discussed in chapter 6) with the Sr_2CuGaO_3S structure type in the space group *P*4/*nmm*. The anti-PbO-type CrAs layers are separated by an oxide layer with the Cr^{3+} cation in a square pyramidal environment, which is significantly thicker than the oxide layer observed in $Sr_2MO_2M_2As_2$. The structural parameters, selected

atomic distances and bond angles for Sr_2CrO_3CrAs are summarised in Table 7.1 in section 7.2.2.

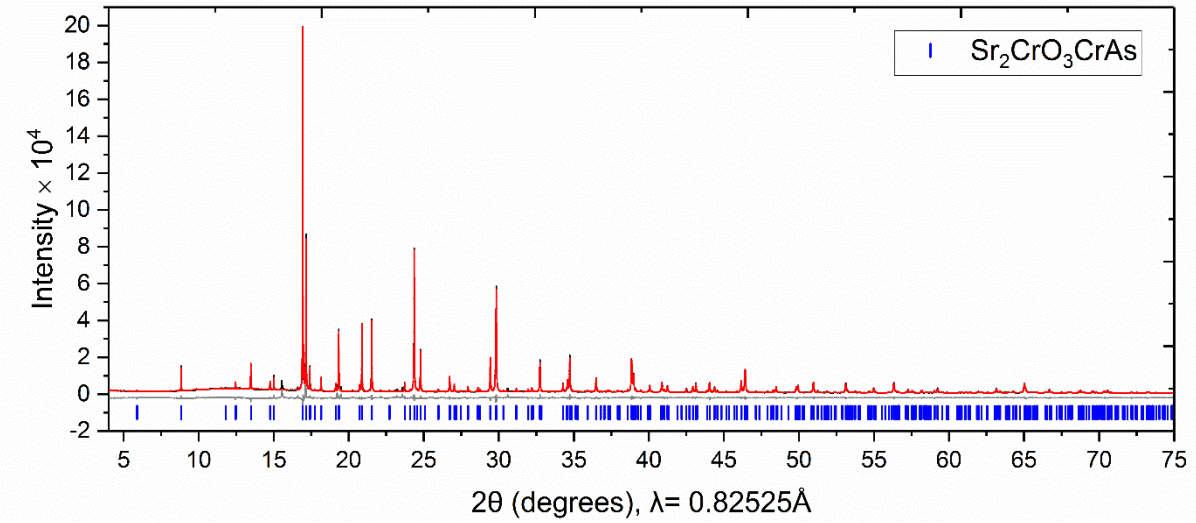

Figure 7.5: Rietveld refinement of Sr_2CrO_3CrAs (XX153) against synchrotron PXRD data measured at room temperature using MAC detector on the I11 beamline

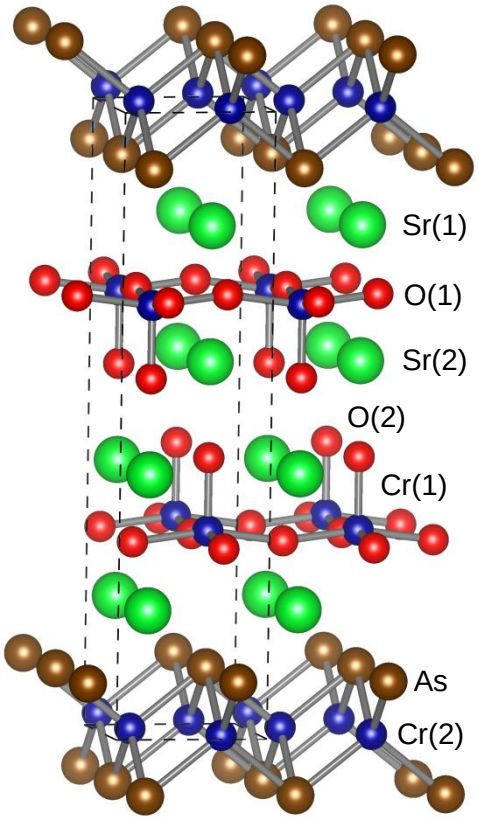

Figure 7.6: The crystal structure of Sr_2CrO_3CrAs

7.2.2 Room temperature PND

Time of flight PND was measured on a 1 g sample of Sr_2CrO_3CrAs (XX153) at room temperature on the WISH diffractometer at ISIS. The Rietveld plot of Sr_2CrO_3CrAs against room temperature PND data is depicted in Figure 7.7 (the magnetic ordering in the diffraction pattern will be discussed in 7.2.4), giving a good agreement between observed data and calculated model. The refinement results show that both Cr(2) and O(1) sites in Sr_2CrO_3CrAs are fully occupied by Cr and O atoms, however, the compound has a deficiency of approximately 4 % on Cr(1) atoms and a 1 % oxygen deficiency on O(2) atoms, which are different to those observed in the PXRD data (where the Cr(1) sites are fully occupied and the deficiency of O(2) sites were refined to be about 20 %). Since Cr is a relatively weak neutron scatterer and O atom has low sensitivity of PXRD, one may suggest that there is actually no deficiency on Cr(1) atoms and the deficiency of the O(2) site is very small. The refined structural parameters from PND data show fair agreement with those derived from PXRD data. Both of them are compared in Table 7.1.

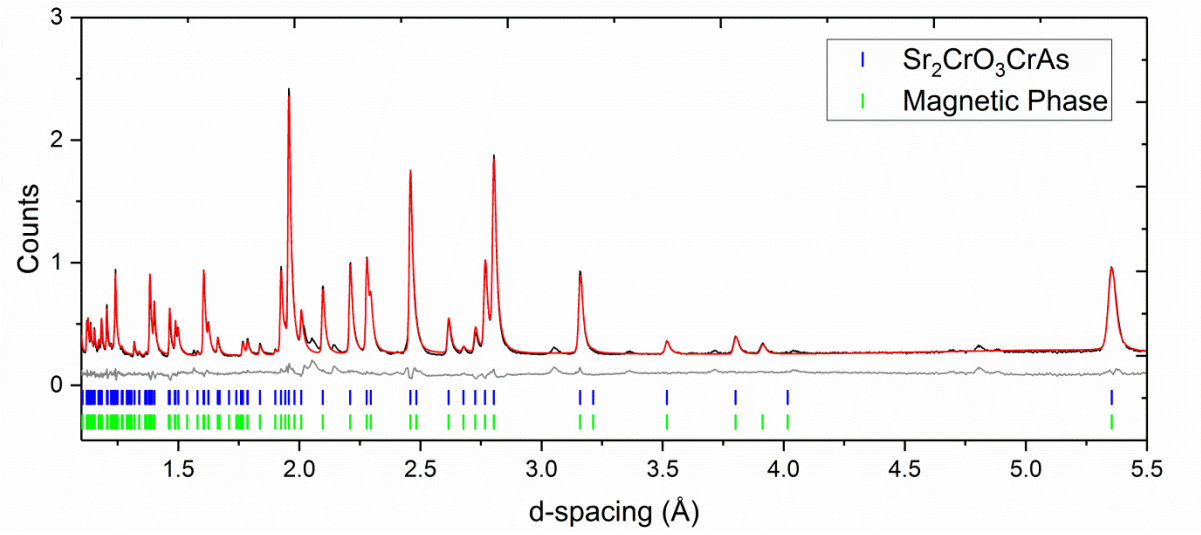

Figure 7.7: Rietveld refinement against PND pattern of Sr_2CrO_3CrAs (XX153), measured at 293 K using the bank 3 and 8 of WISH diffractometer, R_{wp} = 4.49

	Sr_2CrO_3CrAs	
Diffractometer	WISH (ISIS)	I11 (MAC)
Wavelength (Å)	white beam	0.824869
Temperature (K)	293	298
Space group	*P4/nmm*	
a (Å)	3.91270(3)	3.909900(13)
c (Å)	16.0639(2)	16.05407(7)
V (Å^3)	245.925(4)	245.424(2)
z[Sr(1)]	0.19778(13)	0.19943(5)
z[Sr(2)]	0.41633(10)	0.41637(5)
z[Cr(1)]	0.3120(2)	0.31296(8)
z[As(1)]	0.09662(13)	0.09633(5)
z[O(1)]	0.29903(9)	0.29536(19)
z[O(2)]	0.43065(14)	0.4295(3)
Sr(1) U_{11} (Å^2)	0.0029(7)	0.0053(3)
Sr(1) U_{33} (Å^2)	0.0033(11)	0.0098(6)
Sr(2) U_{11} (Å^2)	0.0030(9)	0.0067(3)
Sr(2) U_{33} (Å^2)	0.037(2)	0.0078(5)
Cr(1) U_{11} (Å^2)	0.0053(18)	0.0040(5)
Cr(1) U_{33} (Å^2)	0.000(4)	0.0068(8)
Cr(2) U_{11} (Å^2)	0.0046(13)	0.0076(5)
Cr(2) U_{33}(Å^2)	0.025(2)	0.0098(8)
As U_{11} (Å^2)	0.0146(11)	0.0069(4)
As U_{33} (Å^2)	0.000(2)	0.0080(5)
O(1) U_{11} (Å^2)	0.0144(9)	0.014(1) [a] [U_{iso} (Å^2)]
O(1) U_{22} (Å^2)	0.0118(11)	
O(1) U_{33} (Å^2)	0.0097(11)	
O(2) U_{11} (Å^2)	0.0034(11)	0.010(1) [a] [U_{iso} (Å^2)]
O(2) U_{22} (Å^2)	0.010(2)	
O(2) U_{33} (Å^2)	0.000(2)	
Cr(1)–O(1) (Å) [×4]	1.9674(4)	1.9754(5)
Cr(1)–O(2) (Å) [×1]	1.906(4)	1.872(5)
Cr(1)–As (Å) [×1]	3.460(4)	3.4783(16)
Cr(2)–As (Å) [×4]	2.4974(13)	2.4926(5)
As-Cr(2)-As (°) [×4]	112.73(4)	112.635(16)
As-Cr(2)-As (°) [×2]	103.14(8)	103.31(3)
Cr(1) occupancy	0.958(6)	0.996(3)
O(2) occupancy	0.987(4)	0.803(6)

Table 7.1: Selected refined parameters of Sr_2CrO_3CrAs (XX153) from both PND (WISH) and synchrotron PXRD (MAC) data at RT; [a] O atoms were refined isotropically

7.2.3 Magnetic susceptibility measurements

The *M vs H* curve measured at the low field for the sample of Sr_2CrO_3CrAs (XX153) was not linear at room temperature (Figure 7.8(a)), suggesting the appearance of a small amount of ferromagnetic impurity in the product. It was also observed the curve would be linear above 6000 Oe, where the contribution from the ferromagnetic impurity had saturated. Therefore, a 3 T/4 T subtraction experiment (Appendix D) was applied and the resultant magnetic susceptibility curve (Figure 7.8(b)) shows a broad antiferromagnetic transition at around 75 K, which is comparable to the antiferromagnetic feature observed at about 35 K in the Fe analogue Sr_2CrO_3FeAs,[100, 113] where the Cr is substituted by Fe in the arsenide layers.

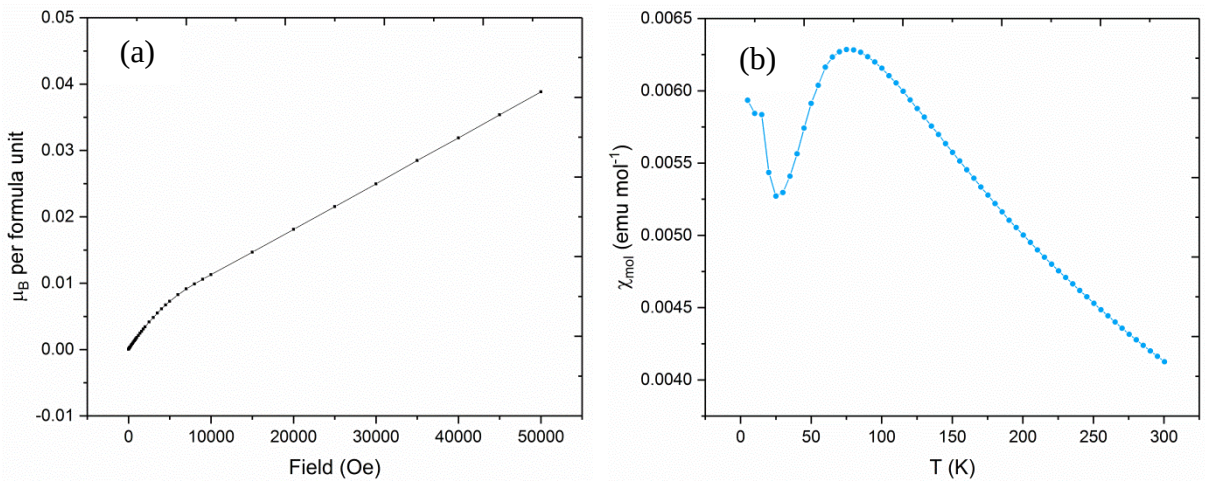

Figure 7.8: (a) Magnetic moment per formula unit of Sr_2CrO_3CrAs (XX153) as a function of applied magnetic field, measured at 300 K; (b) Field-cooled magnetic susceptibility of Sr_2CrO_3CrAs (XX153) measured using a 3 T/4 T subtraction

7.2.4 Variable temperature PND

In order to fully understand the magnetic behaviour of Sr_2CrO_3CrAs as a function of temperature, 1 g sample of the compound (XX153) was measured using PND on WISH at

temperatures between 7 K and 478 K. It was found several antiferromagnetic-ordering reflections appeared at low temperatures and the intensities of these reflections decreased consistently on warming until 478 K, where no additional peaks could be observed in the diffraction pattern. Figure 7.9 shows the evolution of Bragg intensities of the magnetic reflections as a function of temperature from banks 3 and 8.

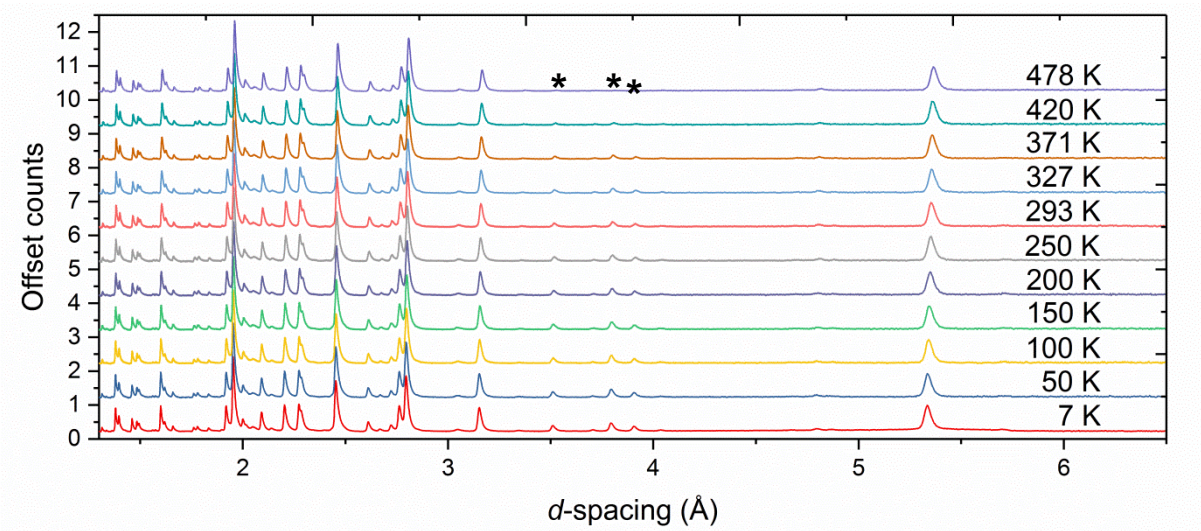

Figure 7.9: WISH PND data of Sr_2CrO_3CrAs (XX153) in the range of 7 K to 478 K from banks 3 and 8; The asterisks (*) indicate the sets of magnetic reflections which are present until warming to 478 K

These magnetic reflections could be well indexed on a tetragonal nuclear-structure unit cell with dimensions $a \times a \times c$, which was loaded in the ISODISTORT[56] to perform the magnetic mode analysis using the magnetic space group $P1$ (1.1) before searching for a higher symmetry space group. It was found that all the magnetic intensity could be accounted for by applying the mGM2$^-$(a) mode, showing that the antiferromagnetic moments are aligned along the c-axis in the arsenide layers. A magnetic space group $P4'/n'm'm$ (129.416) was then calculated from ISODISTORT to allow the refinement of mGM2$^-$(a) mode, yielding a magnetic model (Figure 7.10) to fit these magnetic peaks well in the PND data. Furthermore, some very small additional magnetic peaks were also observed at the temperatures below 371 K (Figure 7.11). They were indexed as the magnetic reflections of $Sr_2CrO_2Cr_2As_2$,

suggesting that although the quick quenching method described in chapter 7.2 eliminated the appearance of $Sr_2CrO_2Cr_2As_2$ impurity phase in PXRD data, there was still a slight amount of this impurity detected by PND, where serveral small nuclear peaks of $Sr_2CrO_2Cr_2As_2$ were found to overlap with the nuclear phase of Sr_2CrO_3CrAs and the magnetic peaks of $Sr_2CrO_2Cr_2As_2$ were present at high *d*-spacings. Additionally, there are still a few nuclear reflections in the PND patterns which could not be indexed with any known impurity phase in the database.

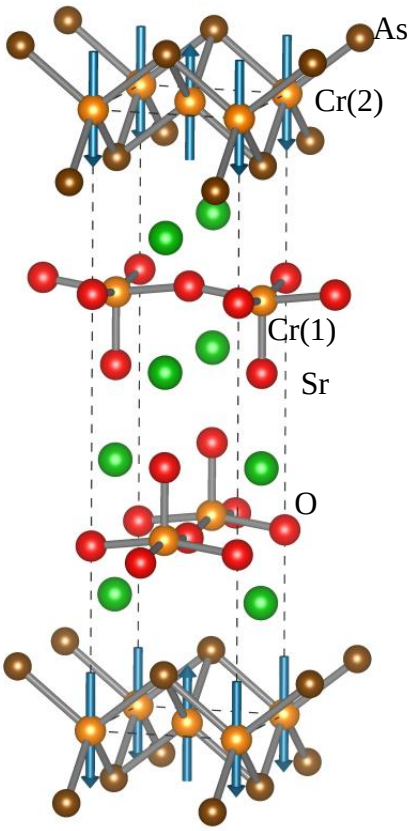

Figure 7.10: The magnetic model with mGM2$^-$(a) mode in the space group *P*4'/*n*'*m*'*m* (129.416)

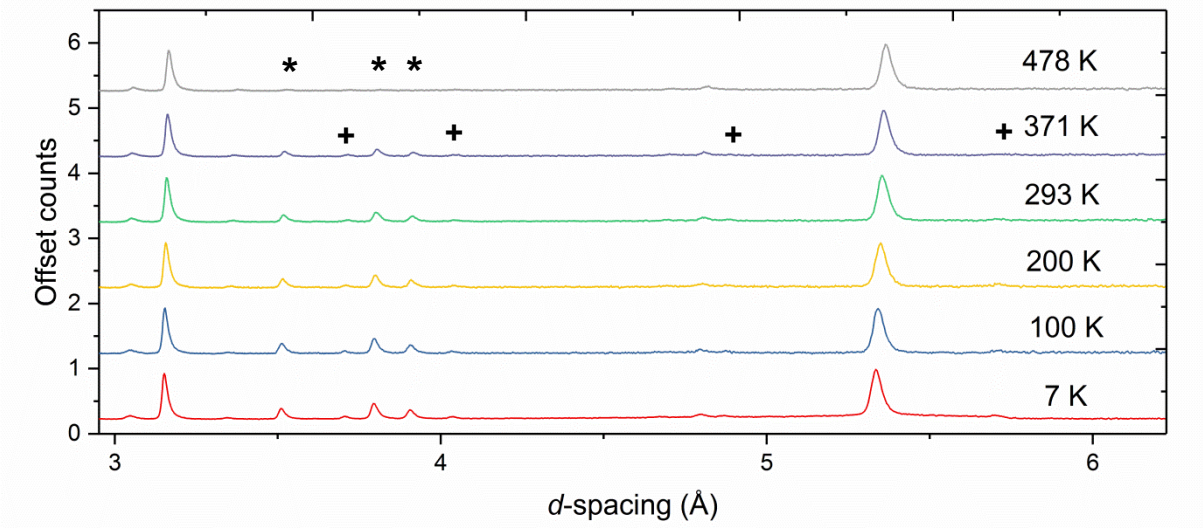

Figure 7.11: WISH PND data of Sr_2CrO_3CrAs (XX153) in the temperature range of 7 K to 478 K, measured at the *d*-spacings between 3 Å to 6 Å; The magnetic peaks marked with (*) represent the magnetic ordering in Sr_2CrO_3CrAs, while the magnetic peaks labelled with (+) correspond to the magnetic ordering in $Sr_2CrO_2Cr_2As_2$

The Rietveld plot of a magnetic refinement against the PND data at 7 K is shown in Figure 7.12 and the refined magnetic parameters are listed in Table 7.2.

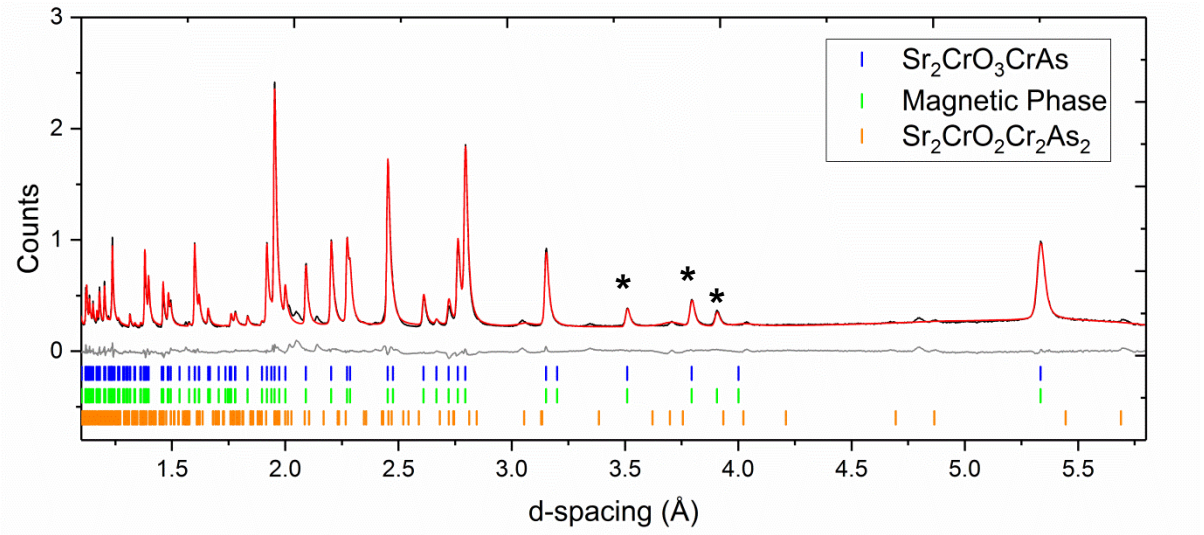

Figure 7.12: Rietveld refinements of Sr_2CrO_3CrAs against PND patterns collected from bank 3 and 8 at 7 K on WISH; The magnetic reflections with asterisks (*) represent the antiferromagnetic magnetic moments observed in arsenide layers

Diffractometer	WISH (ISIS)
Temperature (K)	7
Magnetic space group	*P4′/n′m′m* (129.416)
$\lvert\mu\rvert(\mu_B)$	2.12(3)
R_{wp}	4.69

Table 7.2: Refined parameters for the antiferromagnetic magnetic ordering in the arsenide layers of Sr_2CrO_3CrAs, when it was measured at 7 K by PND

For the analogue with Fe in the arsenide layer, Sr_2CrO_3FeAs, it was found that several additional magnetic peaks appeared in the PND patterns below 38 K (Figure 7.13),[99] representing that the moments were antiferromagnetically ordered in the *ab*-plane of oxide layers (also like the magnetic ordering in the oxide layer of Sr_2CrO_3CuSe discussed in chapter 6). In the sample of Sr_2CrO_3CrAs, sharp Bragg peaks due to long-range magnetic ordering of oxide-layer moments were not detected by PND at low temperatures, but the magnetic ordering is suggested by the magnetometry measurements where a broad maximum is observed at about 75 K. There is a broad diffuse magnetic peak appearing at the *d*-spacing of 5.33 Å below 40 K in Sr_2CrO_3CrAs, the position of which is comparable to the main magnetic reflections observed in Sr_2CrO_3FeAs. Figure 7.14 shows the presence of this diffuse magnetic peak and compares it with the simulated magnetic Bragg peaks if the moments of Sr_2CrO_3CrAs are assumed to order antiferromagnetically within the *ab*-plane of oxide layers (like Sr_2CrO_3FeAs).

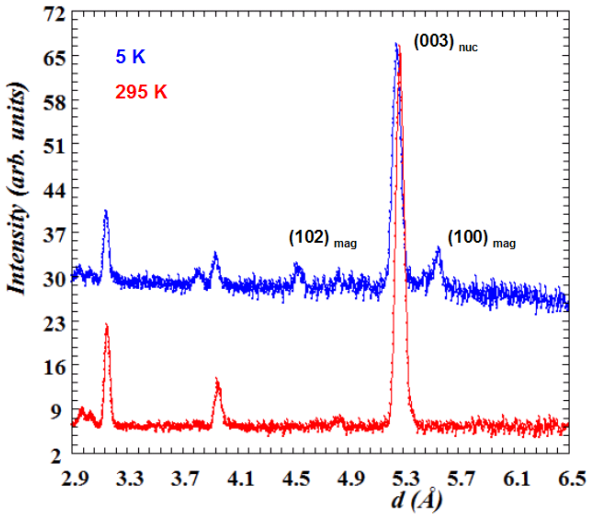

Figure 7.13: The presence of two magnetic peaks in Sr_2CrO_3FeAs, measured at POLARIS diffractometer. The graph was taken from Corkett's DPhil Thesis[99]

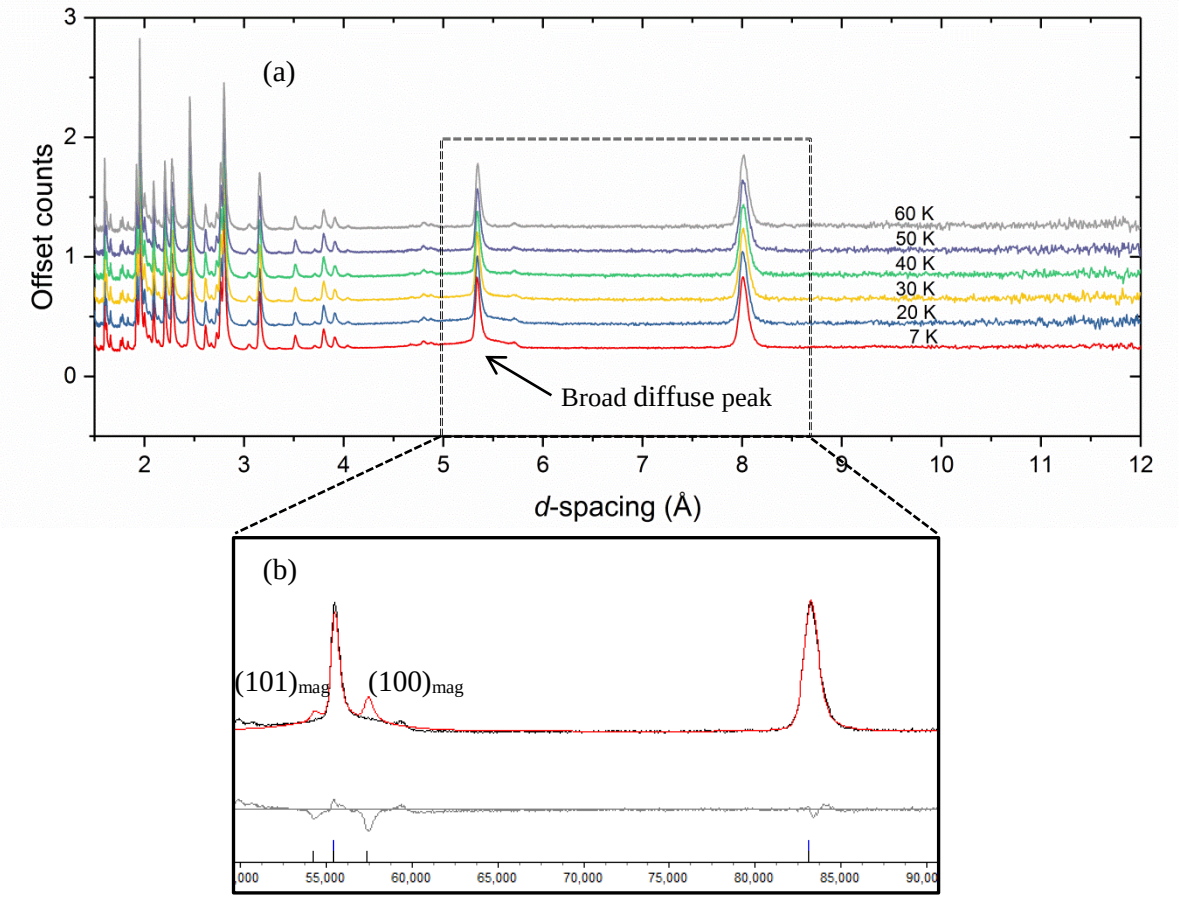

Figure 7.14: (a) The diffuse magnetic peak observed in NPD data from banks 3 and 8 in the temperature range of 7 K to 60 K; (b) The simulated magnetic peaks of Sr_2CrO_3CrAs when moments in the oxide layer align in a similar way to Sr_2CrO_3FeAs

7.3 Discussion

7.3.1 Crystal structures

Compound	Sr_2CrO_3CrAs	Sr_2CrO_3FeAs[99]	Sr_2ScO_3FeAs[9]	Sr_2VO_3FeAs[99]
T (K)	298	300	295	293
a (Å)	3.91270(3)	3.91334(3)	4.0496(3)	3.9313(2)
c (Å)	16.0639(2)	15.7604(1)	15.804(1)	15.6895(1)
c/*a*	4.10558(8)	4.02735(6)	3.9026(5)	3.9909(2)
V (Å^3)	245.925(4)	241.359(5)	259.18(4)	242.49(3)
M(1)–O(1) (Å) [×4]	1.9674(4)	1.9733(2)	2.0513(4)	1.9798(3)
M(1)–O(2) (Å) [×1]	1.906(4)	1.882(1)	2.002(4)	1.903(4)
M(2)–As (Å) [×4]	2.4974(13)	2.4122(5)	2.4143(7)	2.4169(7)
β As-*M*(2)-As (°) [×4]	112.73(4)	110.00(2)	114.00(5)	108.84(5)
α As-*M*(2)-As (°) [×2]	103.14(8)	108.42(3)	107.25(2)	109.79(2)

Table 7.3: Lattice parameters, selected atomic distances and bond angles for several Sr_2CuGaO_3S -structure-type compounds

Table 7.3 compares Sr_2CrO_3CrAs with several other similar compounds adopting the same Sr_2CuGaO_3S-type crystal structure in the space group *P*4/*nmm*. The substitution of *M*(1) and *M*(2) sites with different first-row transition metals results in the significant change of lattice parameters, bond lengths and bond angles. Table 7.4 gives the ionic radii of Sc, V, Cr and Fe, showing that decreasing the size of *M*(1) from Sc to Cr and increasing the size of *M*(2) from Fe to Cr leads to a contraction in *a* lattice parameter (thus the *M*(1)–O(1) bond distance), but has an increase in the *c*/*a* ratio. For Sr_2CrO_3FeAs and Sr_2CrO_3CrAs, the *c* lattice parameter increases by 1.93 % on substituting Cr^{2+} for Fe^{2+}, however, the corresponding *a* lattice parameter decreases only marginally (0.02 %). The *M*(2)–As distance in the arsenide layers increases by 3.53 % by replacing Fe^{2+} with Cr^{2+}, giving a more

distorted MAs_4 tetrahedral environment, from β As-Fe-As (represented in Figure 7.15) = 110.00(2) ° in Sr_2CrO_3FeAs to β As-Cr-As = 112.73(4) ° in Sr_2CrO_3CrAs.

Ion	Radius (Å)
Sc^{3+}	0.745
V^{3+}	0.640
Cr^{3+}	0.615
Fe^{2+}	0.63
Cr^{2+}	0.80

Table 7.4: Comparison of the size of ionic radii for selected first-row transition metal ions[105]

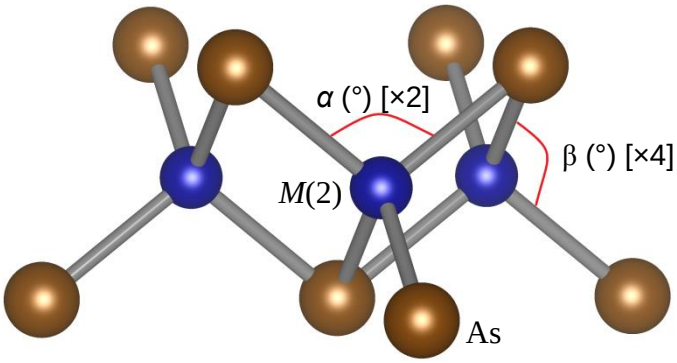

Figure 7.15: Definition of the α and β tetrahedral angles

7.3.2 Magnetic ordering

The observation that the Cr(2) moments in the arsenide layer of Sr_2CrO_3CrAs order antiferromagnetically in a checkerboard fashion is comparable to the observations for arsenide-layer Cr^{2+} moments in $Sr_2CrO_2Cr_2As_2$ between 348 K and 598 K. Figure 7.16 shows the magnetic structures of these two compounds, where the Cr^{2+} moments in the arsenide layers direct along the *c*-axis. The lower ordering temperature for the Cr(2) moments in the arsenide layer in Sr_2CrO_3CrAs (478 K) than $Sr_2CrO_2Cr_2As_2$ (600 K) is

probably due to the much longer interplanar distance (thicker oxide layers in Sr_2CrO_3CrAs) between the adjacent arsenide layers, which leads to weaker interplanar exchange interactions. By comparison, there is not so much difference between the intraplanar exchange interactions in Sr_2CrO_3CrAs and $Sr_2CrO_2Cr_2As_2$, considering that both of them have similar Cr(2)–Cr(2) and Cr(2)–As distances within the arsenide layers (Cr(2)–Cr(2) = 2.76670(3) Å, Cr(2)–As = 2.4974(13) Å in Sr_2CrO_3CrAs and Cr(2)–Cr(2) = 2.83738 (3) Å, Cr(2)–As = 2.5180(4) Å in $Sr_2CrO_2Cr_2As_2$). This is different with $Ba_2CrO_2Cr_2As_2$, where the longer Cr(2)–Cr(2) and Cr(2)–As distances result in a weaker intralayer exchange interaction and thus make arsenide-layer Cr undergo magnetic long-range ordering at a lower temperature (470 K) than in $Sr_2CrO_2Cr_2As_2$. Furthermore, the refined value for the ordered Cr moment in the arsenide layer of 2.12(3) μB/Cr^{2+} at 7 K in Sr_2CrO_3CrAs is comparable to that in $Sr_2CrO_2Cr_2As_2$ (2.703(7) μB/Cr), all of which are lower than 4 μB/Cr expected for a d^4 Cr^{2+}, and are likely reduced by the effects of covalency.

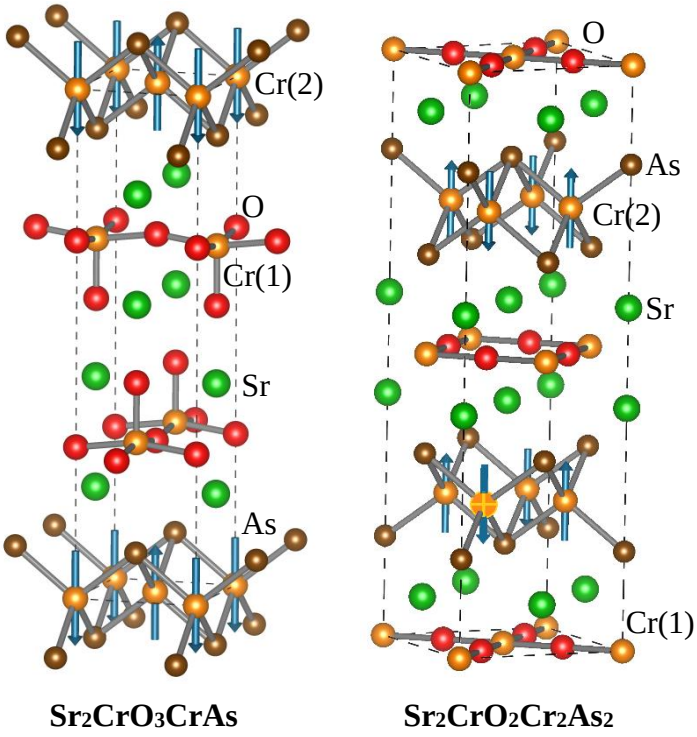

Figure 7.16: The ordering of arsenide-layer Cr^{2+} moments in Sr_2CrO_3CrAs (below 478 K) and $Sr_2CrO_2Cr_2As_2$ (between 348 K and 598 K)

However, only short-range magnetic ordering is evident in the oxide-layer Cr^{3+} in Sr_2CrO_3CrAs and these moments do not contribute to sharp Bragg peaks. This is clearly different from the long-range magnetic behaviour seen in some other Sr_2MO_3CuCh-type analogues (Sr_2CrO_3FeAs and Sr_2CrO_3CuSe) with their oxide layers fully occupied by Cr^{3+} ions. In both Sr_2CrO_3FeAs[99] and Sr_2CrO_3CuSe (chapter 6), the nearest-neighbour Cr^{3+} magnetic spins in the oxide planes are coupled antiferromagnetically with their moments aligned within the *ab*-plane but this type of long-range magnetic order was not observed in Sr_2CrO_3CrAs. Figure 7.17 shows the magnetic ordering of Cr^{3+} ions in the oxide layers of Sr_2CrO_3CrAs, Sr_2CrO_3FeAs and Sr_2CrO_3CuSe, where the refined values for oxide-layer Cr moment are 1.95(7) μB/Cr^{3+} at 1.5 K in Sr_2CrO_3FeAs[99] and 1.5(8) μB/Cr^{3+} at 4 K in Sr_2CrO_3CuSe.

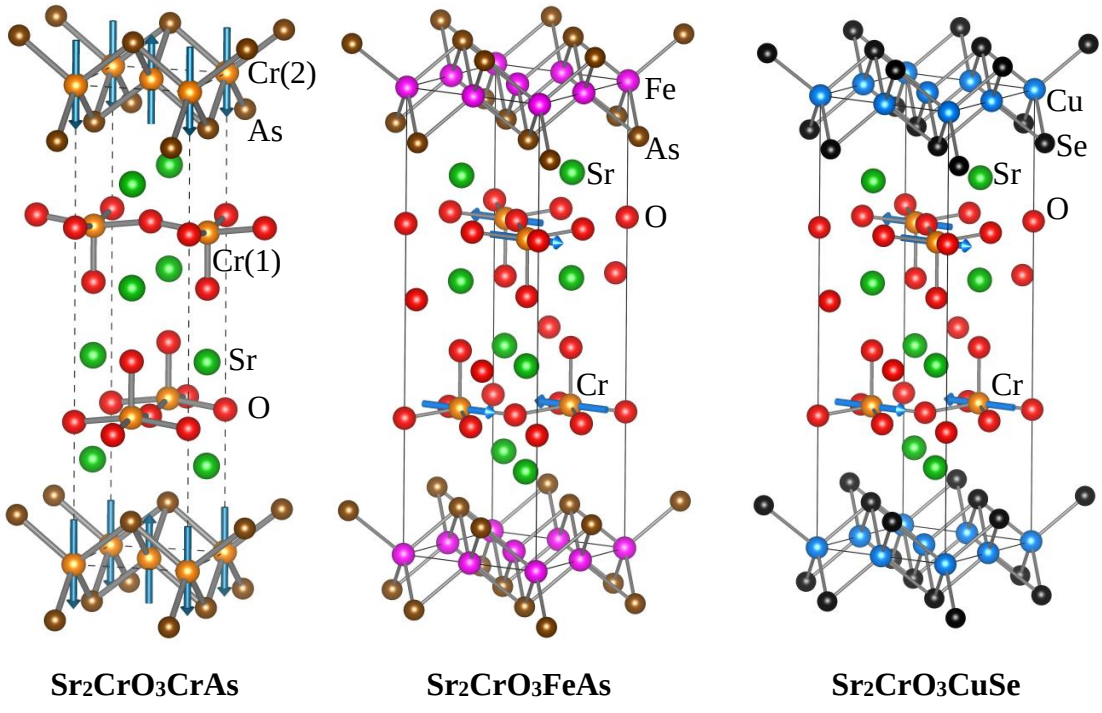

Figure 7.17: The magnetic ordering of Cr^{3+} moments in the oxide layers of Sr_2CrO_3CrAs, Sr_2CrO_3FeAs and Sr_2CrO_3CuSe

Magnetometry measurements performed on Sr_2CrO_3CrAs also suggest that the broad transition occurs on cooling at 75 K, characteristic of short-range two-dimensional magnetic

ordering. Moreover, there are also some precedents in the $Sr_2Mn_3O_2Sb_2$-type compounds (such as $Sr_2MnO_2Mn_2As_2$) where the oxide Mn ions don't seem to engage in long range order (previously discussed in section 4.5.2).

Chapter 8

Summary

In this thesis the structures and magnetic properties of the layered oxyarsenides $A_2M_3As_2O_2$ (A=Sr, Ba and M = Cr, Mn) and layered oxychalcogenides Sr_2MO_3CuX (M = Cr, Mn, Fe and X= S, Se) have been studied. These materials are synthesised with different choices of the transition metal cations and it has been demonstrated that the nature of the metals can strongly influence the magnetic properties of these layered solids.

In this work a novel Cr-based oxypnictide $Ba_2CrO_2Cr_2As_2$ has been successfully synthesised. This compound crystallises in space group *I4/mmm* and is isostructural with $Sr_2CrO_2Cr_2As_2$ except for Ba-substitution of Sr-site, in which the Ba-containing layers are separated by alternating $Cr_2As_2^{2-}$ and CrO_2^{2-} layers. Variable temperature powder neutron diffraction reveals checkerboard-type long range antiferromagnetic ordering of the Cr^{2+} ions in both oxide and arsenide layers below 248 K and 470 K respectively and the magnetic moments in both layers are aligned along the *c*-axis, where the two independent Cr^{2+} sublattices order with two different propagation vectors k = (½ ½ 0) in the oxide layer and k = (1 1 1) in the arsenide layer. It has been shown that the substitution of Sr^{2+} with the larger Ba^{2+} increases both parameters *a* and *c* of the crystal structure and thus leads to the larger distances both in and between the CrO_2 and Cr_2As_2 layers, which results in lower ordering temperatures in both layers in $Ba_2CrO_2Cr_2As_2$ compared with $Sr_2CrO_2Cr_2As_2$. The magnetic moments of both chromium layers grow slowly in magnitude as the sample is cooled down to 5.5 K, at which point the Cr^{2+} ions in the arsenide layers reach a value of 2.298(8) μB/Cr^{2+} whilst

those in the oxide planes reach 3.30(1) μB/Cr^{2+}, reflecting greater covalency in the arsenide layer. In contrast to the Sr analogue, the two Cr^{2+} sublattices behave as independent magnetic systems in $Ba_2CrO_2Cr_2As_2$ and this is a valuable contrast with the unusual behavior of $Sr_2CrO_2Cr_2As_2$ which shows a spin reorientation transition of one Cr sublattice on the onset of the magnetic ordering of the other.

In chapter 4 the synthesis of several new Cr/Mn mixed compounds with the compositions $Sr_2Cr_{3-x}Mn_xAs_2O_2$ and $Ba_2Cr_{3-x}Mn_xAs_2O_2$ has been described to investigate the effect of cation substitution on the structural and magnetic properties in the $Sr_2Mn_3O_2Sb_2$-type oxypnictides. All members in this series show that the more oxophilic Cr^{2+} has a strong preference to reside in the oxide layers and Mn^{2+} prefers the site in the arsenide layers. All of these compounds were found to be antiferromagnetic and variable temperature neutron powder diffraction enabled the magnetic structures to be determined. The most characteristic feature of the magnetic properties in these compounds is the appearance of two magnetic structures. For $Sr_2Cr_{0.79}Mn_{0.21}O_2Mn_{1.76}Cr_{0.24}As_2$ and $Ba_2CrO_2Mn_{0.98}Cr_{1.02}As_2$, two similar magnetic structures are present from 210 K to 383 K and 200 K to 215 K respectively, except that the magnetic spins in adjacent arsenide layers related by the vector $\boldsymbol{c}/2$ are aligned parallel in one structure compared with antiparallel in the other one. Similarly, in $Sr_2Cr_{0.93}Mn_{0.07}O_2Mn_{0.92}Cr_{1.08}$ two magnetic structures are obtained below 230 K, where the magnetic spins in adjacent oxide layers related by the vector $\boldsymbol{c}$ are aligned either parallel or antiparallel. Furthermore, similar to $Sr_2CrO_2Cr_2As_2$, a spin-reorientation of the moments is found in the arsenide layer of the Cr-rich compound $Sr_2Cr_{0.93}Mn_{0.07}O_2Mn_{0.92}Cr_{1.08}$, where the *M*(2) moments rotate from the *c*-axis to lie within the *ab*-plane in a two times bigger magnetic unit cell with a $\sqrt{2}a \times \sqrt{2}a \times 2c$ expansion. This is probably due to the slight incommensurability of the magnetic structure with the crystal structure that makes the coupling interaction between the *M*(1) and *M*(2) sublattices possible. A further analysis of

the magnetic properties is probably required using single crystal neutron diffraction and electron microscopy to disentangle the complex magnetism in these phases; they certainly contrast in different ways with the all-Mn and all-Cr analogues.

In chapter 5 a new Sr_2GaO_3CuS-structure-type compound Sr_2MnO_3CuSe has been synthesised for the first time, in which the anti-PbO-type CuSe layers are separated by two oxide layers that resemble a portion of the K_2NiF_4 structure, with the Mn^{3+} cation in a square pyramidal geometry. Powder neutron diffraction data reveal long-range AFM ordering in the oxide layers, with the moments directed along the *c*-axis in a magnetic unit cell with a $\sqrt{2}a \times \sqrt{2}a \times c$ expansion. In replacing Se^{2-} by S^{2-} in Sr_2MnO_3CuSe, another sample Sr_2MnO_3CuS has been prepared in this work. Magnetometry measurements on Sr_2MnO_3CuS reveal a broad maximum in the susceptibility at 95 K, similar to that seen in Sr_2MnO_3CuSe (100 K), which is attributed to long-range AFM ordering of Mn^{3+} moments. While PND measurements performed on the sample of Sr_2MnO_3CuS show that the neighbouring moments are coupled antiferromagnetically in a checkerboard fashion with their moments directed perpendicular to the *ab*-plane, the resultant magnetic unit cell is doubled along the *c*-axis and the magnetic structure is different in detail to that of the selenide analogue. Surprisingly, Sr_2MnO_3CuS also has a much lower ordered magnetic moment (2.83(6) μ_B/Mn^{3+}) than that for the Sr_2MnO_3CuSe (3.76(2) μ_B/Mn^{3+}). However, the oxidative deintercalation of just 6% of the Cu from Sr_2MnO_3CuS changed the crystal structure slightly and not only resulted in adoption of the same magnetic structure as found for the selenide analogue, but also led to a much larger ordered moment than in stoichiometric Sr_2MnO_3CuS with a value approaching that of Sr_2MnO_3CuSe. A possible reason for this is that the Mn^{3+} ions in Sr_2MnO_3CuS were slightly reduced by electrons that transferred from the sulfide ions to the transition metal ions. This would introduce some Mn^{2+} ions and lead to moment reduction due to frustration.

In chapter 6 an improved synthetic route has been established to Sr_2FeO_3CuSe, without the presence of any impurity phases (e.g. Fe_3O_4 and $Cu_{1.8}Se$) and unindexed peaks, which allows the investigations into its magnetic properties to be performed. Low temperature PND measurements performed on Sr_2FeO_3CuSe have revealed a spin reorientation transition between 1.5 K and 230 K with the tilted Fe^{3+} magnetic moments in the oxide planes gradually reorienting to lie in the *ab* plane by 230 K. While Sr_2CrO_3CuSe demonstrates antiferromagnetic ordering of Cr^{3+} in the oxide layers with their moments aligned within the *ab*-plane. Rietveld refinements against PND data as well as results obtained from PXRD show that Sr_2CrO_3CuSe still contains a significant amount of impurity peaks, suggesting there is a slight non-stoichiometry in the sample. Therefore, further analysis of this compound to explore the evolution of the magnetic scattering would require a purer sample.

As part of work on $Sr_2CrO_2Cr_2As_2$, a small amount of a new phase (Sr_2CrO_3CrAs) with thicker oxide layers was discovered by our group in the TEM image of the sample. In chapter 7 the synthesis of this challenging compound Sr_2CrO_3CrAs has been successful, which is isostructural to the Sr_2MO_3Cu*Ch*-type compounds. The Cr^{3+} ions in Sr_2CrO_3CrAs generate the double layers in a pyramidal coordination CrO_5, and with a weaker sixth bond to an arsenide ion. Variable temperature powder neutron diffraction reveals long range antiferromagnetic ordering of the Cr^{2+} ions in the arsenide layer, with their moments directed along the *c*-axis, comparable to those observations for arsenide-layer Cr^{2+} moments in $Sr_2CrO_2Cr_2As_2$ between 348 K and 598 K. However, only short-range magnetic ordering is evident in the oxide-layer Cr^{3+} in Sr_2CrO_3CrAs and these moments do not contribute to sharp Bragg peaks. This is clearly different from the long-range oxide-layer magnetic behaviour seen in some other Sr_2MO_3Cu*Ch*-type analogues (Sr_2CrO_3FeAs and Sr_2CrO_3CuSe), where the nearest-neighbour Cr^{3+} magnetic spins in the oxide planes are coupled antiferromagnetically with their moments aligned within the *ab*-plane. Magnetometry

measurements performed on Sr_2CrO_3CrAs also suggest that the broad transition occurs on cooling at 75 K, characteristic of short-range two-dimensional magnetic ordering.

Clearly a great wealth of magnetic properties is offered by the oxyarsenides $A_2M_3As_2O_2$ and oxychalcogenides Sr_2MO_3Cu*X* in this work and the ability to substitute ions between and within both layer types enables property modification in a controlled manner. Despite the similarities in the structural blocks of these solids, it has been found that their crystal structures and magnetic properties are significantly dependent on the identity of the transition metal *M*.

References

1. M. Eckert, *Annalen der Physik*, 2012, **524**, A83-A85.
2. W. H. Bragg and W. L. Bragg, *Proceedings of the Royal Society of London. Series A, Containing Papers of a Mathematical and Physical Character*, 1913, **88**, 428-438.
3. J. G. Bednorz and K. A. Müller, *Zeitschrift für Physik B Condensed Matter*, 1986, **64**, 189-193.
4. M. K. Wu, J. R. Ashburn, C. J. Torng, P. H. Hor, R. L. Meng, L. Gao, Z. J. Huang, Y. Q. Wang and C. W. Chu, *Physical Review Letters*, 1987, **58**, 908-910.
5. P. Dai, B. C. Chakoumakos, G. F. Sun, K. W. Wong, Y. Xin and D. F. Lu, *Physica C: Superconductivity*, 1995, **243**, 201-206.
6. H. Kamerlingh-Onnes, *Communication from the Physical Laboratory of the University of Leiden*, 1911.
7. H. Takahashi, K. Igawa, K. Arii, Y. Kamihara, M. Hirano and H. Hosono, *Nature*, 2008, **453**, 376.
8. R. C. Che, L. Wang, Z. Chen, C. Ma, C. Y. Liang, J. B. Lu, H. L. Shi, H. X. Yang and J. Q. Li, *EPL (Europhysics Letters)*, 2008, **83**, 66005.
9. F. Zheng, M. Kotobuki, S. Song, M. O. Lai and L. Lu, *Journal of Power Sources*, 2018, **389**, 198-213.
10. P. G. Bruce, *Chemical Communications*, 1997, 1817-1824.
11. H. Liu, Y. Yang and J. Zhang, *Journal of Power Sources*, 2007, **173**, 556-561.
12. K. M. Shaju, G. V. Subba Rao and B. V. R. Chowdari, *Electrochimica Acta*, 2002, **48**, 145-151.
13. T.-H. Kim, J.-S. Park, S. K. Chang, S. Choi, J. H. Ryu and H.-K. Song, *Advanced Energy Materials*, 2012, **2**, 860-872.
14. H. M. Xie, R. S. Wang, J. R. Ying, L. Y. Zhang, A. F. Jalbout, H. Y. Yu, G. L. Yang, X. M. Pan and Z. M. Su, *Adv. Mater.*, 2006, **18**, 2609-2613.
15. J. B. Goodenough and Y. Kim, *Chemistry of Materials*, 2010, **22**, 587-603.
16. G. Bate, *Journal of Magnetism and Magnetic Materials*, 1991, **100**, 413-424.
17. J. H. Judy, *Journal of Magnetism and Magnetic Materials*, 2005, **287**, 16-26.
18. R. E. Cohen, *Nature*, 1992, **358**, 136-138.
19. H. O. Pastore, S. Coluccia and L. Marchese, *Annual Review of Materials Research*, 2005, **35**, 351-395.
20. A. K. Cheetham, C. N. R. Rao and R. K. Feller, *Chemical Communications*, 2006, 4780-4795.
21. C. B. Dartt and M. E. Davis, *Catalysis Today*, 1994, **19**, 151-186.
22. H. Yamane, M. Shimada, S. J. Clarke and F. J. DiSalvo, *Chemistry of Materials*, 1997, **9**, 413-416.
23. J. Nagamatsu, N. Nakagawa, T. Muranaka, Y. Zenitani and J. Akimitsu, *Nature*, 2001, **410**, 63-64.
24. R. Marchand, Y. Laurent, J. Guyader, P. L'Haridon and P. Verdier, *Journal of the European Ceramic Society*, 1991, **8**, 197-213.
25. R. E. Loehman, *Journal of Non-Crystalline Solids*, 1983, **56**, 123-134.

26. D. L. Sidebottom, M. A. Hruschka, B. G. Potter and R. K. Brow, *Journal of Non-Crystalline Solids*, 1997, **222**, 282-289.
27. S. J. Clarke, P. Adamson, S. J. C. Herkelrath, O. J. Rutt, D. R. Parker, M. J. Pitcher and C. F. Smura, *Inorganic Chemistry*, 2008, **47**, 8473-8486.
28. V. Johnson and W. Jeitschko, *Journal of Solid State Chemistry*, 1974, **11**, 161-166.
29. J. H. Albering and W. Jeitschko, *Zeitschrift für Naturforschung B*, 1996, **51**, 257-262.
30. M. Palazzi, *Comptes Rendus De L Academie Des Sciences Serie Ii*, 1981, **292**, 789-791.
31. K. Ueda and H. Hosono, *Thin Solid Films*, 2002, **411**, 115-118.
32. K. Ueda and H. Hosono, *Journal of Applied Physics*, 2002, **91**, 4768-4770.
33. H. Hiramatsu, K. Ueda, H. Ohta, T. Kamiya, M. Hirano and H. Hosono, *Applied Physics Letters*, 2005, **87**, 211107.
34. Z.-A. Ren, G.-C. Che, X.-L. Dong, J. Yang, W. Lu, W. Yi, X.-L. Shen, Z.-C. Li, L.-L. Sun and F. Zhou, *EPL (Europhysics Letters)*, 2008, **83**, 17002.
35. E. Brechtel, G. Cordier and H. Schäfer, *Zeitschrift für Naturforschung B*, 1979, **34**, 777-780.
36. T. C. Ozawa, S. M. Kauzlarich, M. Bieringer, C. R. Wiebe, J. E. Greedan and J. S. Gardner, *Chemistry of Materials*, 2001, **13**, 973-980.
37. M. Enjalran, R. T. Scalettar and S. M. Kauzlarich, *Physical Review B*, 2000, **61**, 14570-14580.
38. S. L. Brock, N. P. Raju, J. E. Greedan and S. M. Kauzlarich, *Journal of Alloys and Compounds*, 1996, **237**, 9-19.
39. S. L. Brock and S. M. Kauzlarich, *Inorganic Chemistry*, 1994, **33**, 2491-2492.
40. M. M. O. T. Ozawa, S. L. Brock, S. M. Kauzlarich and D. M. Young, *Chemistry of Materials*, 1998, **10**, 392-396.
41. W. Zhu and P. Hor, *Journal of Solid State Chemistry*, 1997, **130**, 319-321.
42. Z. A. Gál, O. J. Rutt, C. F. Smura, T. P. Overton, N. Barrier, S. J. Clarke and J. Hadermann, *Journal of the American Chemical Society*, 2006, **128**, 8530-8540.
43. W. Zhu and P. Hor, *Journal of Solid State Chemistry*, 1997, **134**, 128-131.
44. W. Zhu and P. Hor, *Inorganic Chemistry*, 1997, **36**, 3576-3577.
45. W. Zhu and P. Hor, *Journal of Solid State Chemistry*, 2000, **153**, 26-29.
46. D. R. Lide, *Handbook of Chemistry and Physics*, 2nd edn.
47. C. N. R. Rao, *The Journal of Physical Chemistry B*, 2000, **104**, 5877-5889.
48. G. Brauer, *Handbook of Preparative Inorganic Chemistry*, 1965.
49. W. L. Bragg, *Proceedings of the Cambridge Philosophical Society*, 1912, 17.
50. J. Karle and H. Hauptman, *Acta Crystallographica*, 1950, **3**, 181-187.
51. D. Sayre, *Acta Crystallographica*, 1952, **5**, 60-65.
52. A. L. Patterson, *Physical Review*, 1934, **46**, 372-376.
53. G. Oszlanyi and A. Suto, *Acta Crystallographica Section A*, 2004, **60**, 134-141.
54. *https://www.ncnr.nist.gov/resources/n-lengths/*.
55. A. Coelho, *Journal of Applied Crystallography*, 2018, **51**, 210-218.
56. B. J. Campbell, H. T. Stokes, D. E. Tanner and D. M. Hatch, *Journal of Applied Crystallography*, 2006, **39**, 607-614.
57. http://manchesterhistory.net/architecture/2000/diamondlight.html.
58. http://pd.chem.ucl.ac.uk/pdnn/inst2/work.htm.
59. http://pd.chem.ucl.ac.uk/pdnn/inst2/insert.htm.
60. S. P. Thompson, J. E. Parker, J. Potter, T. P. Hill, A. Birt, T. M. Cobb, F. Yuan and C. C. Tang, *Review of Scientific Instruments*, 2009, **80**, 075107.
61. *Beamline I11 User Manual*.

62. http://pd.chem.ucl.ac.uk/pdnn/inst3/pulsed.htm.
63. R. I. Smith and S. Hull, *User Guide for the POLARIS Diffractometer at ISIS*.
64. G. Caglioti, A. Paoletti and F. P. Ricci, *Nuclear Instruments*, 1958, **3**, 223-228.
65. *ISIS Neutron Training School Booklet*, 2017.
66. *The OSIRIS User Guide, 3rd Edition*.
67. A. C. Hannon, *Nuclear Instruments and Methods in Physics Research Section A: Accelerators, Spectrometers, Detectors and Associated Equipment*, 2005, **551**, 88-107.
68. S. Hull, R. I. Smith, W. I. F. David, A. C. Hannon, J. Mayers and R. Cywinski, *Physica B: Condensed Matter*, 1992, **180-181**, 1000-1002.
69. D. Duxbury, D. Khalyavin, P. Manuel, D. Raspino, N. Rhodes, E. Schooneveld and E. Spill, *Journal of Instrumentation*, 2014, **9**, C12008-C12008.
70. https://www.ill.eu/users/scientific-groups/diffraction/instruments/.
71. https://www.ill.eu/users/instruments/instruments-list/d2b/how-it-works/simulated-experiment/.
72. H. M. Rietveld, *Acta Crystallographica*, 1967, **22**, 151-152.
73. H. M. Rietveld, *Journal of Applied Crystallography*, 1969, **2**, 65-71.
74. G. Pawley, *Journal of Applied Crystallography*, 1981, **14**, 357-361.
75. http://hyperphysics.phy-astr.gsu.edu/hbase/Solids/Squid.html#c1.
76. J. Clarke, *Scientific American*, 1994, **271**, 36.
77. H. Jiang, J.-K. Bao, H.-F. Zhai, Z.-T. Tang, Y.-L. Sun, Y. Liu, Z.-C. Wang, H. Bai, Z.-A. Xu and G.-H. Cao, *Physical Review B*, 2015, **92**, 205107.
78. J. Liu, J. Wang, J. Sheng, F. Ye, K. M. Taddei, J. A. Fernandez-Baca, W. Luo, G.-A. Sun, Z.-C. Wang, H. Jiang, G.-H. Cao and W. Bao, *Physical Review B*, 2018, **98**, 134416.
79. N. N. Greenwood and A. Earnshaw, *Chemistry of the Elements, 2nd edn*.
80. D. R. Lide, *Handbook of Chemistry and Physics*, 2003-2004.
81. M. Jones, *Part II Thesis, University of Oxford*, 2015.
82. S. L. Brock, N. Raju, J. Greedan and S. M. Kauzlarich, *Journal of Alloys and Compounds*, 1996, **237**, 9-19.
83. S.-W. Park, H. Mizoguchi, K. Kodama, S.-i. Shamoto, T. Otomo, S. Matsuishi, T. Kamiya and H. Hosono, *Inorganic Chemistry*, 2013, **52**, 13363-13368.
84. K. A. Filsinger, W. Schnelle, P. Adler, G. H. Fecher, M. Reehuis, A. Hoser, J.-U. Hoffmann, P. Werner, M. Greenblatt and C. Felser, *Physical Review B*, 2017, **95**, 184414.
85. H. Von Schnering and B. H. Brand, *Zeitschrift für Anorganische und Allgemeine Chemie*, 1973, **402**, 159-168.
86. B. Li, A.-V. Mudring and J. D. Corbett, *Inorganic Chemistry*, 2003, **42**, 6940-6945.
87. E. B. Brackett, T. E. Brackett and R. L. Sass, *The Journal of Physical Chemistry*, 1963, **67**, 2132-2135.
88. C. J. Howard, B. J. Kennedy and C. Curfs, *Physical Review B*, 2005, **72**, 214114.
89. M.-H. Whangbo, E. E. Gordon, H. Xiang, H.-J. Koo and C. Lee, *Accounts of Chemical Research*, 2015, **48**, 3080-3087.
90. R. Nath, V. O. Garlea, A. I. Goldman and D. C. Johnston, *Physical Review B*, 2010, **81**, 224513.
91. M. A. McGuire and V. O. Garlea, *Physical Review B*, 2016, **93**, 054404.
92. S.-W. Park, H. Mizoguchi, K. Kodama, S.-i. Shamoto, T. Otomo, S. Matsuishi, T. Kamiya and H. Hosono, *Inorganic Chemistry*, 2013, **52**, 13363-13368.

93. K. A. Filsinger, W. Schnelle, P. Adler, G. H. Fecher, M. Reehuis, A. Hoser, J.-U. Hoffmann, P. Werner, M. Greenblatt and C. Felser, *Physical Review B*, 2017, **95**, 184414.
94. W. J. Zhu and P. H. Hor, *Inorganic Chemistry*, 1997, **36**, 3576-3577.
95. Y. Kamihara, M. Matoba, T. Kyomen and M. Itoh, *Journal of Applied Physics*, 2002, **91**, 8864-8866.
96. W. J. Zhu and P. H. Hor, *Journal of Solid State Chemistry*, 1997, **134**, 128-131.
97. D. Berthebaud, O. I. Lebedev, D. Pelloquin and A. Maignan, *Solid State Sciences*, 2014, **36**, 94-100.
98. D. O. Charkin, A. V. Sadakov, O. E. Omel'yanovskii and S. M. Kazakov, *Materials Research Bulletin*, 2010, **45**, 2012-2016.
99. A. J. Corkett, *DPhil Thesis, University of Oxford*, 2012.
100. M. Tegel, F. Hummel, Y. Su, T. Chatterji, M. Brunelli and D. Johrendt, *EPL (Europhysics Letters)*, 2010, **89**, 37006.
101. A. J. Corkett, D. G. Free, S. J. Cassidy, S. Ramos and S. J. Clarke, *Journal of Solid State Chemistry*, 2014, **216**, 91-98.
102. F. Hummel, Y. Su, A. Senyshyn and D. Johrendt, *Physical Review B*, 2013, **88**, 144517.
103. S. L. Wang, W. L. Li, G. F. Wang, D. Y. Dong, J. J. Shi, X. Y. Li, P. G. Li and W. H. Tang, *Powder Diffraction*, 2013, **28**, S3-S6.
104. W. J. Zhu and P. H. Hor, *Journal of Solid State Chemistry*, 2000, **153**, 26-29.
105. R. Shannon, *Acta Crystallographica Section A*, 1976, **32**, 751-767.
106. P. Stephens, *Journal of Applied Crystallography*, 1999, **32**, 281-289.
107. A. L. Goodwin, M. G. Tucker, M. T. Dove and D. A. Keen, *Physical Review Letters*, 2006, **96**, 047209.
108. C. F. Smura, D. R. Parker, M. Zbiri, M. R. Johnson, Z. A. Gál and S. J. Clarke, *Journal of the American Chemical Society*, 2011, **133**, 2691-2705.
109. L. Todd, *Part II Thesis, University of Oxford*, 2018.
110. D. Senff, P. Reutler, M. Braden, O. Friedt, D. Bruns, A. Cousson, F. Bourée, M. Merz, B. Büchner and A. Revcolevschi, *Physical Review B*, 2005, **71**, 024425.
111. N. Qureshi, H. Ulbrich, Y. Sidis, A. Cousson and M. Braden, *Physical Review B*, 2013, **87**, 054433.
112. M. Tegel, F. Hummel, S. Lackner, I. Schellenberg, R. Poettgen and D. Johrendt, *Zeitschrift für Anorganische und Allgemeine Chemie*, 2009, **635**, 2242-2248.
113. M. Tegel, F. Hummel, S. Lackner, I. Schellenberg, R. Pöttgen and D. Johrendt, *Zeitschrift für Anorganische und Allgemeine Chemie*, 2009, **635**, 2242-2248.
114. S. J. Clarke, *DPhil Thesis, University of Oxford*, 1994.

Appendix A: Units in magnetometry

DC magnetic susceptibility measurements were performed to investigate how responsive a material is to an applied magnetic field. In the SI units system, the magnetic susceptibility of a material at a particular temperature is:

$$\kappa = \frac{M(\mathrm{Am^{-1}})}{H(\mathrm{Am^{-1}})} \tag{A.1}$$

For a SQUID magnetometer, the applied magnetic field described above is actually the flux density B_0 in the unit of Tesla. The relationship between H and B_0 is:

$$H(\mathrm{Am^{-1}}) = \frac{B_0(\mathrm{T})}{\mu_0(\mathrm{TmA^{-1}})} \tag{A.2}$$

where μ_0 is the vacuum permeability and thus:

$$\kappa = \frac{M(\mathrm{Am^{-1}})\mu_0(\mathrm{TmA^{-1}})}{B_0(\mathrm{T})} \tag{A.3}$$

A SQUID magnetometer actually doesn't measure the magnetisation directly, but rather the magnetic moment *m*. The magnetisation is the magnetic dipole moment per unit volume. Therefore, the susceptibility can be written by substituting the moment for the magnetisation in the *eqn* 2.26:

$$\chi(\mathrm{m^3}) = \frac{m(\mathrm{Am^2})\mu_0(\mathrm{TmA^{-1}})}{B_0(\mathrm{T})} \tag{A.4}$$

This is the susceptibility of the actual sample loaded in the SQUID. It is usually to use the molar susceptibility χ_{mol} in the magnetic susceptibility measurements:

$$\chi_{mol}(\mathrm{m^3mol^{-1}}) = \frac{m(\mathrm{Am^2})\mu_0(\mathrm{TmA^{-1}})}{B_0(\mathrm{T})n(\mathrm{mol})} \quad \text{(A.5)}$$

where n is the number of moles from the measured sample. It is often more convenient to use c.g.s units for magnetism, where μ_0 is 1 and magnetic moment as well as susceptibility are in electromagnetic units, emu. The molar susceptibility in c.g.s units (emu $\mathrm{mol^{-1}}$) is then obtained:[114]

$$\chi_{mol}(\mathrm{emu\ mol^{-1}}) = \frac{m(\mathrm{emu})}{B_0(\mathrm{g})n(\mathrm{mol})} \quad \text{(A.6)}$$

The units of emu $\mathrm{mol^{-1}}$ are equivalent to $\mathrm{cm^3mol^{-1}}$, so the conversion between $\chi_{mol}(\mathrm{SI})$ and $\chi_{mol}(\mathrm{cgs})$ is:

$$\chi_{mol}(\mathrm{SI})[\mathrm{m^3mol^{-1}}] = \chi_{mol}(\mathrm{cgs})[\mathrm{cm^3mol^{-1}}] \times 4\pi \times 10^{-6} \quad \text{(A.7)}$$

Appendix B: Variable temperature PND (WISH) on $Sr_2CrO_2Cr_2As_2$

Variable Temperature PND measurements were performed on a 2.5 g sample of $Sr_2CrO_2Cr_2As_2$ (MAJ047, prepared by the group's previous Part II student Michael Jones) using the WISH diffractometer at the ISIS Facility, UK. The samples were contained inside a 6 mm diameter vanadium cylinder and measured in the temperature range 1.5 K – 320 K in a helium cryostat, and separately in the range from room temperature to 623 K in a resistance furnace. Cadmium metal was used to mask the steel part of the sample container below room temperature, while gadolinium foil was used for the same purpose above RT. PND measurements on $Sr_2CrO_2Cr_2As_2$ revealed that there were intense diffraction peaks present at ambient temperature which were not predicted by the structural model although these diminished to the background level on warming the sample above 600(10) K and were most intense at long *d*-spacings suggesting that they arose from long range magnetic ordering. Measurements below a Neél temperature estimated as 600(10) K down to 1.5 K revealed dramatic changes in the relative intensities of these reflections around room temperature as shown in Figure B.1.

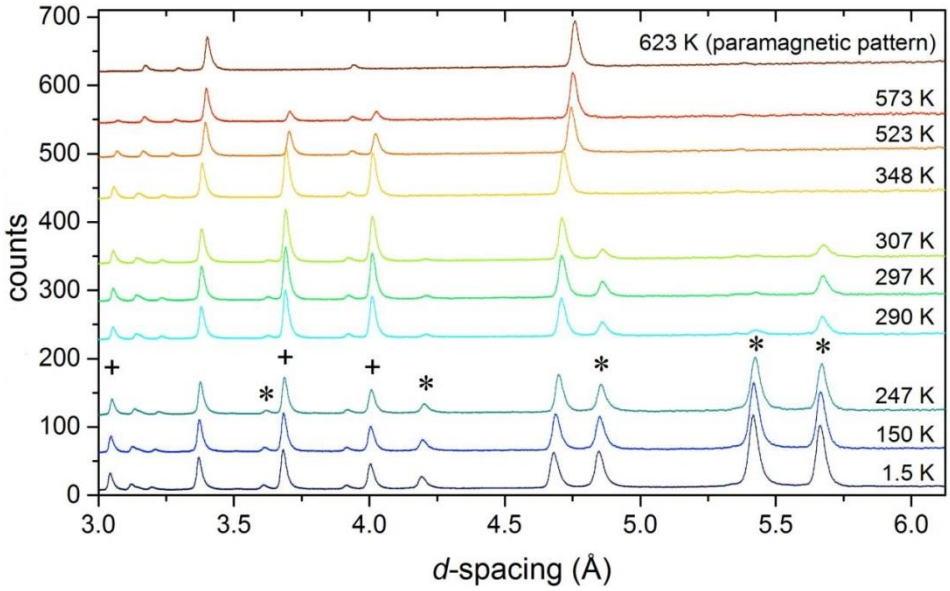

Figure B.1: WISH PND data of $Sr_2CrO_2Cr_2As_2$ in the range 1.5 to 623 K (combination of banks 3 and 8). Several magnetic peaks marked with (+) disappear until 600 K

Appendix C: Bond valence calculations

The bond valence method supposes that the valence (V) of an atom is the sum of the individual valences (v_i) surrounding the atom:

$$V = \sum(v_i) \tag{C.1}$$

The individual bond valences are calculated from the observed bond lengths:

$$v_i = \exp\left(\frac{R_0 - R_i}{b}\right) \tag{C.2}$$

where R_i is the observed bond length between a cation and an anion, R_0 is the valence parameter tabulated based on observations on a large series of standard compounds (the values relevant for this thesis are listed in Table C.1) and b is a constant, typically 0.37 Å.[1]

	(Mn-O)	(Mn-S)
Bond valence parameter	1.790[2]	2.22[2]

It is a method which takes into account the distribution of anions around a cation and enables determination of the apparent valence based on comparison with a wide range of known compounds.

1. I. D. Brown and D. Altermatt, *Acta Crystallographica Section B*, 1985, **41**, 244-247.

2. *bvparm2016.cif*, 2016.

Appendix D: 3 T/4 T subtraction

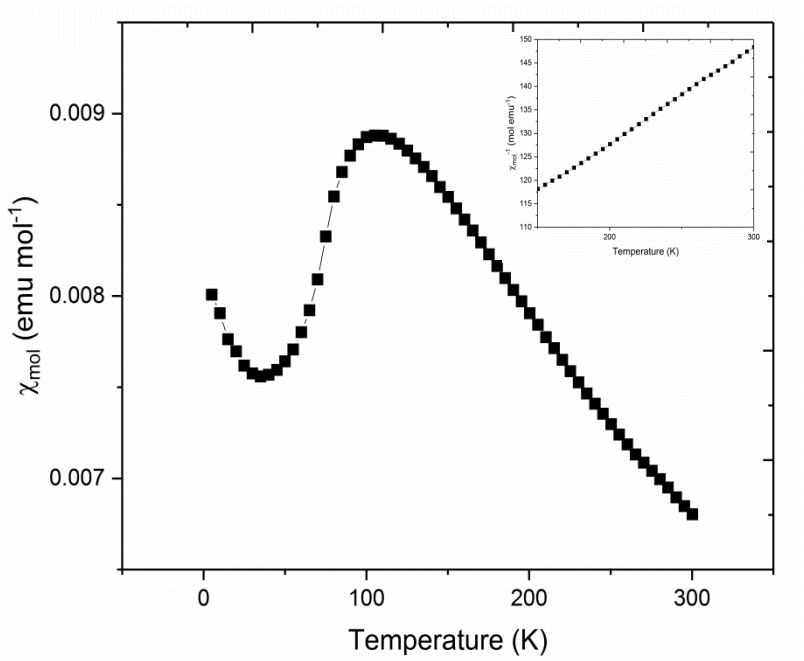

Figure D.1: The magnetic susceptibility of Sr_2MnO_3CuSe (XX211C) obtained using a 4 – 3 T subtraction. The inset shows the inverse magnetic susceptibility with line of best fit (150-300 K), from which the effective magnetic moment and Weiss temperature were derived

A non-linear magnetisation curve was sometimes found on a sample at the low applied field for the *M vs H* measurement at 300 K. This was normally due to the presence of a ferromagnetic impurity, which was too little to be detected by PXRD but sufficient to be observed in the magnetometer because of the enormous susceptibility of ferromagnets. In these cases a more accurate magnetic susceptibility measurement of the sample could be performed by running the experiment at two fields both higher than the saturation field of the ferromagnetic impurities. Two applied fields, 3 and 4 T (1 T is equivalent to 10 000 Oe) were used in this thesis and the new susceptibility of the sample was determined by:

$$\chi_{mol} = \frac{M(H_2) - M(H_1)}{(H_2 - H_1)n} = \frac{M(4\mathrm{T}) - M(3\mathrm{T})}{10000n} \qquad \text{(D.1)}$$

Figure D.1 shows the magnetic susceptibility curve of Sr_2MnO_3CuSe (XX211C) measured using a 3 T/4 T subtraction.

Appendix E: Variable temperature powder X-ray diffraction on Sr_2MnO_3CuSe

The variable-temperature PXRD was performed on the sample of Sr_2MnO_3CuSe (XX211C) using the Mythen detector of the instrument I11 at the Diamond Light Source. The sample was measured in the temperature range of 100 to 300 K since the lowest easily accessible temperature using the cryostream is 100 K. It is hoped that this could help the investigation of the change of lattice *c* at the temperatures higher than the magnetic transition. The sample was loaded into a 0.5 mm borosilicate glass capillary, which was first cooled to 100 K and then warmed up to 300 K. The collected data were well refined by using the original nuclear structure with the space group of *P*4/*nmm* at all temperatures. The lattice parameters, unit cell volume and *c*/*a* ratio extracted from the refinements are plotted against temperature in Figure E.1 with those derived from D2B PND measurements at the temperatures below 100 K.

The lattice parameter *a* of Sr_2MnO_3CuSe shows a smooth increase on warming up from 100 K to 300 K. It also obeys the thermal expansion below 100 K, with bigger *a* values as the temperature increases. But the expansion in the lattice parameter c is less below the magnetic transition temperature (100 K), even with a bigger c at 4 K than 100 K. A small curve is also observed for the change of *c* between about 100 and 120 K, which suggests the value of lattice parameter c would reach the minimum at T_N (100 K). Therefore it is found that the unusual change in lattice parameter c is coincident with the magnetic ordering in the compound. This is probably due to the repulsion between the two magnetic layers below the

Neél temperature, which gives the longest lattice parameter c at 4 K with the maximum magnetic moment of Mn^{3+}.

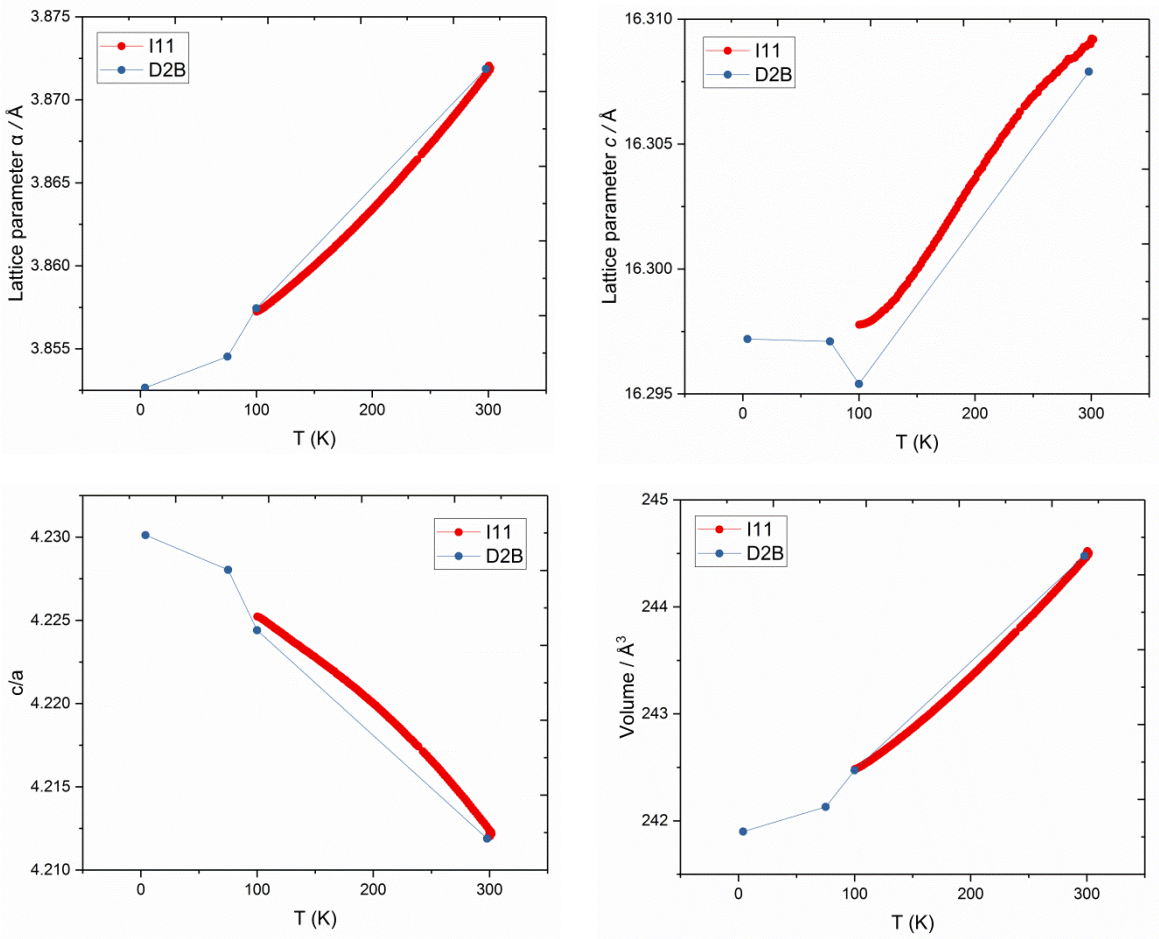

Figure E.1: The change of lattice parameters a and c, c/a ratio and unit cell volume of Sr_2MnO_3CuSe (XX211C) on warming from 1.5 K to 300 K, measured by D2B diffractometer and Mythen detector at I11